

Stress relaxation of nickel-based superalloy springs

Thesis submitted for the degree of Doctor
of Philosophy at the University of
Leicester

By

Marc-Antony Coster

Department of Engineering
University of Leicester

September 2018

Acknowledgements

The work presented in this thesis was carried out at the Department of Engineering of the University of Leicester, under the supervision of Dr Simon Gill. This work is to the best of my knowledge original, except where reference and acknowledgement is made to previous work.

I would like to thank the EPSRC CDT and Alstom/GE for the funding for this project, without which none of this would be possible.

Thanks are due to Gordon McColvin, for the beneficial discussion had at Alstom/GE and the Nimonic 90 spring samples provided for the stress relaxation tests.

I would like to thank all of the technical staff at the Materials Lab in the Department of Engineering, such as Vinay Patel, for assisting in the training for EBSD analysis and sample preparation, and guidance in setting up in-situ stress relaxation experiments using the furnace. Graham Clark and Alex Frost must be thanked for guidance in experimental technique, training and all manner of requests throughout the years.

I must also thank Dr Simon Gill for his support, supervision, and advice throughout the project. Your guidance, expertise and support were invaluable to me these past years. Our discussions on the behaviour of high temperature modelling of nickel superalloys will be missed. Thank you for believing in me.

I would like to thank Charlotte Ratcliffe, the heart of the IMPaCT CDT, for making everything happen as and when it needed to.

Finally, I would like to thank my family and friends, your support and love has gotten me through the difficult times, the frustrating times, and made the good times better.

For my father, for everything.

Abstract

In recent years there has been a move to increase operating temperatures in steam turbines for power generation. This leads to increased efficiencies but also new challenges for material choice and design. One such challenge is the stress relaxation (reduction of reaction force when held at constant displacement) of materials being far more severe when moving from 600°C to 700°C. This work focuses on helical springs utilised in support of steam turbine casings, which are composed of nickel-based superalloy wire of radius 1.25mm coiled into a spring 28.5 mm in height.

This project utilises Finite Element (FE) modelling and mechanical testing to inform development of an analytical model for stress relaxation utilising a modified Dyson creep model, which allows microstructural properties of the nickel superalloy to inform macrostructural creep and stress relaxation phenomena. Dislocation density, γ' volume fraction and particle radius are included in the models, assuming climb/glide flow mechanism.

Preliminary testing of helical samples of Nimonic 90, a medium volume fraction (approx. 20%) γ' alloy, produced stress relaxation results faster than expected from FE and analytical analysis calibrated from uniaxial creep test data, by up to three orders of magnitude. It is proposed this is a result of the helical geometry containing many Geometrically Necessary Dislocations (GNDs), induced as a result of winding the wire into a coil. By predicting this higher dislocation density improved correlation is found between model and data. Enhancing the model by the addition of back-stress hardening via build-up of dislocations at the γ/γ' interface improves the correlation further.

Microstructural and mechanical testing of stress relaxation specimens is conducted through the use of SEM, EBSD and Vickers hardness tests on the heat treated and thermomechanically treated samples. The geometrically necessary dislocations are calculated at each time period during a stress relaxation test from misorientation maps, and the values are compared with the predicted dislocation density from modelling software, to be generally favourable. Evidence of recovery processes are presented from the EBSD data for annealing twins, dislocation density and grain boundary misorientation varying during relaxation testing.

The FE model is used to propose a thermomechanical process map at high temperature. The predictions for the improvement in stress relaxation behaviour are compared with coil springs undergoing the new process and are found to be in agreement. Significant increases in the resistance to stress relaxation are predicted from the proposed process.

Contents

Acknowledgements	i
Abstract	iii
Contents.....	v
Chapter 1: Introduction	1
1.1 Problem.....	2
1.2 Aims and Objectives.....	5
Chapter 2: Nickel-based Superalloys.....	9
2.1 Nickel Based Superalloys.....	9
2.2 Why Nickel Superalloys?	10
2.3 History of Nickel Superalloy Development	11
2.4 Strengthening Mechanisms of Nickel Superalloys.....	13
2.41 Solution Treatment and γ phase.....	14
2.42 Precipitation treatment.....	17
2.43 γ' phase	18
2.44 Carbides.....	19
2.45 TCP phases.....	20
2.46 Defects in γ FCC phase and deformation mechanism.....	20
2.47 Summary of strengthening mechanisms.....	23
2.5 Material.....	24
Chapter 3: Creep and stress relaxation	27
3.1 Creep definition.....	27
3.2 Stress relaxation definition	29
3.3 Empirical creep rate modelling.....	31
3.4 Physics-based creep rate models	32
3.41 Dyson model.....	32
3.42 Secondary creep model.....	33
3.43 Introduction of primary creep and back-hardening	36
3.44 Stress Relaxation of Coil Springs.....	37
Chapter 4: Helical springs	40
4.1 Spring wire.....	40
4.2 Elastic deformation of springs.....	41

Contents

4.3 Effect of wire curvature	43
3.31 Shear stress for straight wire and coil spring	44
4.4 Dyson Creep Equation.....	46
Chapter 5: Stress relaxation test methodology	49
5.1 Nut and bolt tests	49
5.2 In-situ testing.....	51
5.21 Calibration of load cell.....	53
5.3 Summary	58
Chapter 6: FE modelling of stress relaxation of springs	60
6.1 FE simulation of structural deformation	60
6.2 COMSOL simulation of stresses in an elastic spring	61
6.3 Calculation of spring force in COMSOL	62
6.4 FE stress relaxation model for a helical spring	64
6.5 Summary	70
Chapter 7: Analytical models of stress relaxation in coil springs	72
7.1 Polylogarithmic analytical model.....	72
7.2 A simplified physical model.....	75
7.3 Summary	78
Chapter 8: Calibration of stress relaxation models for a coil spring	80
8.1 Model predictions against results	80
8.2 Calibrations of FE and simplified physical models.....	83
8.21 Particle coarsening.....	84
8.23 Origins of Geometrically Necessary Dislocations.....	85
8.24 FE model to calculate GND density during winding.....	87
8.25 Effect of enhanced dislocation density on stress relaxation model	90
8.26 Back-stress hardening	91
8.27 Finite difference model	92
8.28 Dislocation multiplication.....	92
8.3 Calibrated stress relaxation models against results	94
8.4 Conclusions.....	97
Chapter 9: Investigating methods for improving the stress relaxation resistance of coil springs	99
9.1 Multiple-Stage Loading	99
9.11 Initial model validation with test	100
9.12 Predictions of FE model for thermomechanical process.....	103
9.2 Consequences of thermomechanical treatment on material microstructure	105
9.3 Results against model with thermomechanical treatment.....	109

Contents

9.4 Predictions for changing displacement and temperature of thermomechanical process.....	111
9.5 Stress Relaxation Discussion	112
9.6 Conclusions.....	114
Chapter 10: Microstructural and Mechanical Characterization.....	116
10.1 SEM imaging	117
10.2 Vickers Hardness Test	121
10.21 Spring wire surface Vickers hardness test	121
10.23 Cross-section Vickers hardness test	124
10.24 Hardness test discussion	127
10.3 EBSD operation	130
10.4 EBSD Sample Preparation and Methodology	132
10.5 EBSD Results	133
10.51 Effect of heat treatments on microstructure	134
10.52 Heat treatment effect on grain size and shape	136
10.53 Stress relaxation effect on microstructure	142
10.54 Dislocation calculation from misorientation maps	152
10.6 Conclusions.....	158
Chapter 11: Discrete Dislocation Interaction Model	161
11.1 Dislocation Interaction	162
11.2 Full model.....	166
11.21 Boundary Conditions.....	168
11.22 Gamma Prime precipitates.....	169
11.23 Frank-Read Sources.....	170
22.24 Strain rate calculation	170
11.3 Results	171
11.31 Stress relaxation simulation	173
11.32 Creep simulation	176
11.33 Stress relaxation and creep simulation summary.....	178
11.34 Multiple stage thermomechanical processing.....	179
11.4 Conclusions.....	180
Chapter 12: Conclusions and further work.....	183
12.1 Stress relaxation modelling	183
12.2 Microstructural and mechanical characterization.....	184
12.3 Dislocation interaction model	185
12.4 Further work.....	186
12.4 Comparison of coil spring and leaf spring	187

Contents

12.11 Analytical prediction for number of coil springs to number of helix springs	192
12.2 Geometry Comparison Summary	193
Appendices.....	203
Appendix 1 finite difference equations	203
Appendix 2 Discrete dislocation interaction model	204

Chapter 1: Introduction

Nickel-based superalloys have been in use in the aerospace and power generation industries since their emergence in the 1940's and 1950's [1], as a result of continuous alloy development throughout the 19th century and first half of the 20th century to find increasingly efficient methods of engine and gas/steam turbine design. Current developments in steam turbine design include increasing temperature from around 600°C at 30MPa steam pressure to so-called 'ultrasupercritical' steam conditions of 700°C at 37.5MPa. These more extreme conditions lead to an increase in the thermodynamic cycle efficiency from approximately 42%-45% up to 50%-60% respectively [2, 3]. It is of great importance to note that the efficiency gained allows for a reduction in fossil fuel consumption for the required demand, which in turn is expected to lead to a net drop in CO₂ emissions from a given steam turbine.

Nickel based superalloys, designed for high temperature and stress conditions, have exceedingly good high temperature creep-resistant properties that arise from a complex microstructure that ensure long component lifetimes at high homologous temperatures. By manipulating the microstructure through solid solution strengthening and heat treatments, one can affect the mechanical strength, resistance to corrosion, and required ductility [4, 5]. By increasing the operating temperatures of steam turbines, however, new challenges are placed upon the materials that have until now been utilised, which may lead to new processing techniques or entire chemistries of alloys being utilised. Modelling the long-term behaviour of the materials in service at these higher temperatures is therefore of great value.

In this chapter an outline of the projects aims and objectives, will be given, along with an introduction to Nimonic 90, the alloy studied in this thesis, and the microstructural strengthening mechanisms that allow for its high creep resistance. Following this, a literature review of creep and stress relaxation modelling will be discussed, and the context of this work will thus be given. Finally this section will close with a segment on a model for a wire in torsion, the effect of the wire curvature and the introduction of Geometrically Necessary Dislocations (GND's) into the material through mechanical forming.

1.1 Problem

A key component of a steam turbine is the metallic helical coil springs utilised in surface control clearance systems to exert pressure against the steam turbine casing, shown in Figure 1, and in some designs to press an abradable sealant onto the casing. The coil spring is thus compressed at high temperature when the turbine is active. Torsional stresses experienced by the springs under compression are known to be high even under small compressions and thus stress relaxation of springs at high temperature is a significant problem.

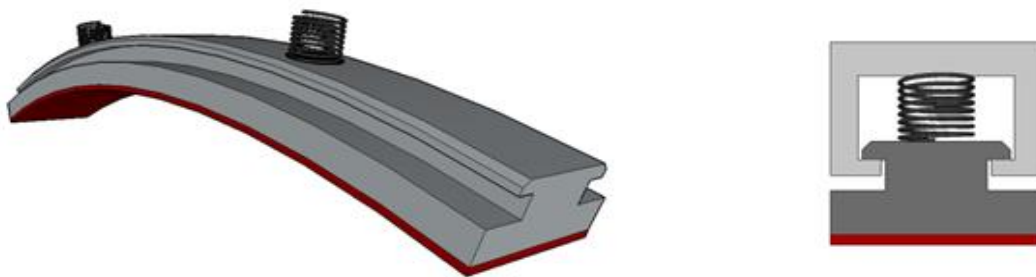


Figure 1: Image of steam turbine casing with placement of springs, along with a cross section of the casing

Stress relaxation is defined according to ASTM standards as ‘the time-dependant decrease in stress of a solid under given constraint at constant conditions’ [6]. This manifests itself on a macroscopic scale as a reduction in reaction force upon constraint and displacement. The spring will then no longer provide the reaction force required and is not suitable for service. Stress relaxation is a phenomenon related to creep and thus both will be described in depth in chapter 3. Simply put, a stress relaxation test has similarities with a traditional creep test. In a creep test the applied stress is kept constant and the deformation over time at heightened temperature is measured. Conversely, for a stress relaxation test, the displacement/deformation of a material is held constant at heightened temperature, and the reaction force or stress of a material is determined, and its reduction over time plotted.

Currently the alloy utilised by G.E for these coil springs at 600°C is Nimonic 90, a medium γ' nickel superalloy that is considered to have good cost to effectiveness in resisting creep at the current operating conditions. Increasing the temperature, however, may lead to this material

no longer being suitable. Previous modelling work has been accomplished on Nimonic 90 springs in the same condition using a creep rate model calibrated to uniaxial tensile creep data, such as the top graph in Figure 2, for an extruded section subsequently 'cold rolled' at room temperature. The top graph shows the required stress to generate strains of 0.1%, 0.2% and 0.5% at different times. The model fits well to the uniaxial tensile creep data, but as can be seen from the bottom graph in Figure 2, the reaction force ratio, P/P_0 for the previous model is not well-calibrated or currently suitable for the coil springs utilised by GE.

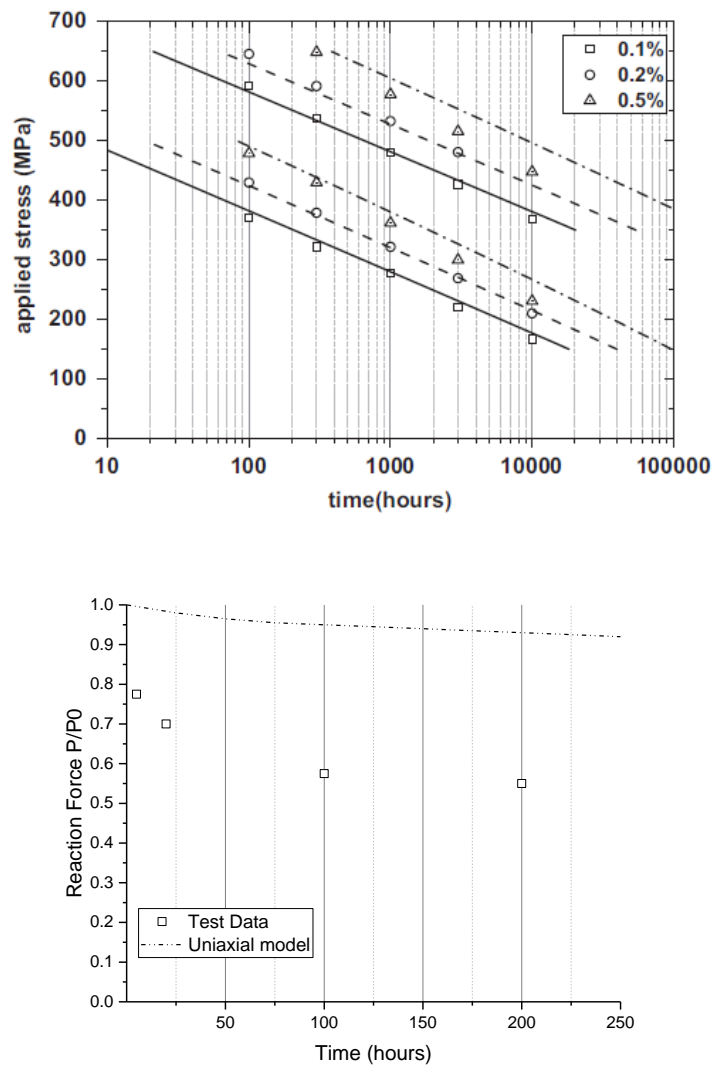


Figure 2: Top: calibration of uniaxial creep model for extruded bar of Nimonic 90, subsequently cold rolled. The graph shows the required stresses to generate 0.1%, 0.2% and 0.5% strain. The top 3 data sets are for 600°C and the bottom 3 sets are for 700°C. The bottom graph shows the same uniaxial calibrated model for the Nimonic 90 coil springs, displaced 9mm, at 600°C, adapted from [76]

This thesis will attempt to propose and calibrate a model to take the coiling of wire into a spring into account, along with the micro-mechanisms of creep that may affect creep rate in the temperature and stress regime.

Traditional creep models are thought to be insufficient based on macro-scale observation and fitted curves [7]. Creep rate equations have in the past relied only on arbitrary power laws, based only upon the stress applied. It is well known that creep rate is affected by the stress, temperature and previously accumulated plastic strain, and the microstructure of a material at heightened temperature can be expected to evolve over time, with a material perhaps increasing its dislocation density through activation of Frank-Read sources, and through precipitate growth which can inhibit dislocation glide and climb mechanisms. These can interact in complex ways to increase or reduce the creep rate of a material. Hence bridging the gap between macroscopic viscoplastic models and the microstructure by creating a model with microstructurally sensitive parameters is of great importance [8] .

As current models are not inherently physical there are naturally inaccuracies incurred in using such methods. While over the long time periods typically associated with creep and stress relaxation (of the order of 1 – 40 years) these simpler power laws have been deemed accurate enough for industrial application, ever improving models will potentially open new avenues of material processing and design, specifically in short term thermomechanical processing.

Understanding how the environmental pressures interact and change the microstructure, and developing a multi-scale model to describe the creep rate and thus the stress relaxation at operating stresses and temperatures, and the effect on lifetime expectancy is the main goal of this thesis. Materials characterisation during stress relaxation at the increased operating temperature will allow for validation of any model along with an insight into the effect of increased strains and any changes in grain structure or precipitation of new carbides and other phases.

1.2 Aims and Objectives

The main objective of this thesis is to understand the generally poor stress relaxation performance of coil springs compared with their uniaxial counterparts, which has been found to be 1-3 orders of magnitude faster by GE during testing, and therefore to propose methods to extend the lifetime of springs in high temperature applications.

The secondary objectives of the project are as follows:

- 1) Create a microstructurally sensitive stress relaxation model using a Finite Element Analysis (FEA) software package, with the goal of achieving accurate calculation of the reduction in reaction force of a Nickel Superalloy coil spring. The inclusion of an analytical torsional model to validate the computational model and experimental data will allow for circular improvement of the model.
- 2) Perform stress relaxation tests at the newly proposed increased operating temperature of 650°C on coil spring samples and compare with computational and analytical model
- 3) Perform microstructural analysis on the stress relaxation samples and examine the evolution of strain and microstructure during the test. The method chosen for this is Electron Back Scattered Diffraction (EBSD), through which the strain in a material can be visualised and other microstructural properties such as grain size and orientation can be calculated utilising software packages.
- 4) Develop a processing methodology to improve the stress relaxation behaviour of Nickel Superalloy sample. A simple thermomechanical process is described that can utilise back-stress hardening phenomena to reduce the relative amount of reaction force lost in a stress relaxation experiment.
- 5) Adapt the FE stress relaxation model to predict the reduction in reaction force calculated in the thermomechanical process.

- 6) Investigate the dislocation-dislocation interaction during stress relaxation and model the effect of an applied stress on a sample on such a scale.

1.3 Thesis Outline

This thesis is segmented into 12 chapters. Chapter 2 will introduce nickel superalloys in order to contextualise the research performed in this project. The high temperature strength mechanisms are described along with the history of superalloy development. Following the description of nickel superalloys in general, is a description of the microstructural properties and strengthening mechanisms that are utilised to improve the strength and creep resistance of the alloy in question.

Chapter 3 defines creep and stress relaxation with a description of the Dyson creep rate model and the component parts. This creep rate model will form the basis of the stress relaxation models in the thesis.

Chapter 4 describes the torsional model that is used to calculate the reaction force of a spring under compression. The effect of bending a wire into a coil is considered, with the change in the stress calculated between a straight wire under torsion and a coil spring. The stress, along with temperature and time, is compared with a creep mode map to determine the type of creep involved in the samples under the conditions specified.

Chapter 5 lists the methodologies of stress relaxation testing for mechanical test data in this thesis. It is split into the calibration of an in-situ short-term stress relaxation test setup and a longer term (up to 1000 hours) test using the nut and bolt method.

Chapter 6 explains the FE model utilised in this thesis to calculate stress relaxation. The model begins as a simple coil spring that calculates the stress state after deformation. After this is validated, creep is introduced to allow for time-dependant studies of the reduction in stress at high temperature.

Chapter 7 derives an analytical model for the stress relaxation based upon introducing the Dyson creep rate model to an equation for torsion of a wire spring. The model is then improved by observations made from the FE model, and re-derived to form a simplified physical model which allow for the 'plastic creep zone' to be taken into account.

Chapter 8 is the stress relaxation results chapter. This chapter is segmented into 3 main sections. The first is the basic FE and simplified physical models compared with each other and in-situ stress relaxation data. The discrepancies are noted and calibrations made in the second section, accounting for particle coarsening, dislocation density, and the addition of back-stress hardening to the FE and simplified physical model. After the calibrations a 1000 hour stress relaxation test is performed to compare with the models.

Chapter 9 introduces methods to improve the stress relaxation resistance of the samples, by proposing a thermomechanical process to increase the back-stress hardening prior to the stress relaxation experiments. The effects of this additional step to the heat treatments is modelled, and an experiment is performed to test the FE model with the thermomechanical process against regularly heat treated samples.

Chapter 10 considers the microstructural characterisation of the Nimonic 90 samples. Scanning Electron Microscope (SEM) imaging of the samples is performed with Energy-Dispersive X-ray spectroscopy (EDX) mapping of samples is performed with the data compared and analysed. Vickers Hardness testing of the 1000 hours stress relaxation samples is accomplished and the change in hardness over the course of the test is analysed. The chapter then continues the microstructural characterisation with Electron Back-Scattered Diffraction (EBSD) imaging of the samples, which are taken to demonstrate the effect of stress-relaxation on the orientation of grains, grain area, and the strain in the material. A method to estimate the GND density using pixel colour gradient and the Nye equation is given, with results compared with previous estimations using FE modelling.

Chapter 11 gives a description of a computational, microstructural model for dislocation climb and glide within a grain, and the interaction between dislocations, precipitates and Frank-Read sources are considered. The question of the difference between stress relaxation and creep is posed, with the model set to answer.

Chapter 12 is the conclusion and further work chapter. The work accomplished in this thesis is summarised and conclusions drawn. Some proposals for future research on this topic are given, including a rudimentary comparison between the stress relaxation resistance of coil springs against a leaf spring geometry.

Chapter 2: Nickel-based Superalloys

2.1 Nickel Based Superalloys

While there exists no strictly determined definition of Superalloys, there is general acceptance that one may define one as an ‘...alloy developed for elevated temperature service, usually based on group VIII elements...where high surface stability is required’ [9]. They are typically utilised in high temperature, high stress applications due to their large resistance to creep. The title of ‘Superalloy’ can apply to nickel, iron-nickel, and cobalt based [10] alloys. Complex in nature, a superalloy may contain up to 10 alloying elements, with each component constituting the microstructure and phases in the alloy. Superalloy composition is typically comprised of an austenitic gamma (γ) Face-Centred Cubic (FCC) phase matrix from the base transition metal element, along with a solid solution strengthening elemental addition and/or precipitation hardening [11] , Figure 3 shows a typical example of a high volume fraction of γ' polycrystalline Nickel Superalloy, with the cuboidal γ' precipitates clearly visible, along with the carbide phase $M_{23}C_6$ at grain boundaries.

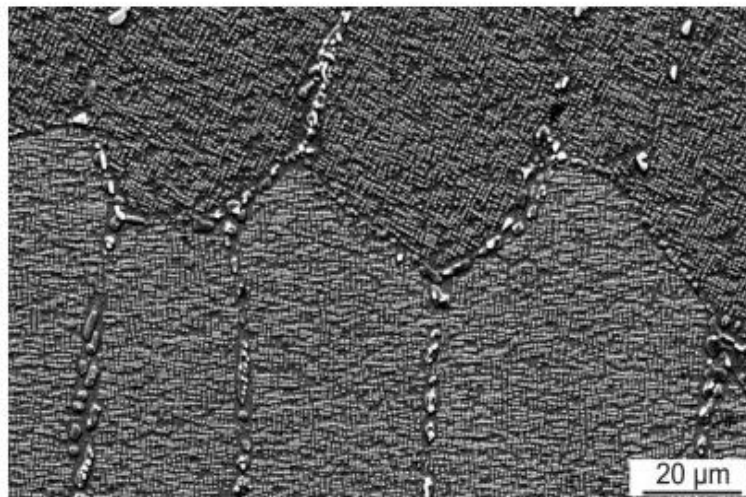


Figure 3: Microstructure of a polycrystalline nickel-based superalloy [12]. The cuboidal L12 ordered FCC γ' precipitate can be seen throughout the grains

The FCC matrix allows for good ductility and toughness for a metal, for example Nickel will maintain acceptable toughness up to its melting point of 1453⁰C [10], with good resistance to phase transformation. The main strengthening phase that Superalloys are known for is the cuboidal L12 ordered FCC γ' phase within the γ matrix, along with carbides at grain boundaries, which prevent grain boundary migration, while contributing to creep resistance [13].

2.2 Why Nickel Superalloys?

The high solubility of alloying elements within a Ni matrix is well known [12], and the ability to control the solidification and grain structure has allowed for increased creep resistance at high temperatures and stresses. While cobalt-based Superalloys were considered to be of great importance in early superalloy development, and have typically greater hot-corrosion resistance than Nickel superalloys [14], they have inferior strength and creep resistance properties to Nickel-based superalloys at high temperature, due to unstable γ' (formed from Co₃Ti). This poor thermal stability is a result of transformation of the matrix at high temperatures [15].

While iron is much cheaper than nickel, it has an electronic structure that has a far greater tendency to promote embrittling Topologically Closed Packed (TCP) phases such as Laves and σ , leading to lower volumes of alloying elements being viable [16]. Iron is known to have a lower oxidation resistance than nickel, which makes it less suitable for high temperature conditions. Finally Iron does not favour the formation of γ' ; it is typically only a metastable phase and is formed only in a narrow band of Al and Ti ratios [17]. For these reasons, Nickel-based superalloys have become the ubiquitous in high temperature power generation and aerospace industries.

2.3 History of Nickel Superalloy Development

As stated above, the early superalloys were first popularised in the 1940's, however the origins can be traced back much earlier. The first example of the γ matrix alloy is in the range of transistors and heating elements patented in 1906 by Albert Marsh [18]. This patent emphasised the superior oxidation resistance found in the binary Ni-Cr system. This was taken further in France prior to the first world war due to demand for more corrosion and creep resistant alloys for aircraft engines using a newly developed alloy; Fe-60%Ni-11%Cr with W and C additions [16]. The following 20 years saw other developments such as the so-called ATV alloy by Chevenard to combat corrosion issues in steam turbine blade steels for use with impure steam [19], increasing the nickel content to 34%Ni along with 11%Cr. The increased solubility of Ni allowed for 0.3%C, giving additional strength). The 0.3% C also helped to prevent the formation of deleterious carbides that were believed to be responsible for poor corrosion resistance in Fe-Ni steels utilised at the time. From this alloy Chevenard made further improvements to mitigate the effect of chromium carbides by precipitation hardening. In 1929 a patent and paper were submitted to cover austenitic Fe-Ni-Cr steels emphasising the hardening effect of Al and Ti additions. The same year, P. Merica developed and filed a patent (to be published in 1936), the earliest example of Inconel 600, through development of a nickel based stainless alloy for kitchen use, containing 75%Ni-15%Cr-8%Fe [20, 21], also making mention of the hardening effect of Al and Ti. While the strengthening effects discussed by Chevenard and Merica, neither indicated the high temperature creep resistance of the new alloys, which were investigated by The Mond Nickel Company, designing an alloy derived from Chenard's work, filing a patent for Nimonic 80 in 1940 [22].

The 1940's and 1950's saw great pressure to increase the maximum temperature of jet engines, and a steep increase in the working temperature was made between 1940 and 1950 by optimising elemental composition and heat treatments, as seen in Figure 4 however for the blading application in a jet engine the further increases were made possible by changing from wrought to conventional casting utilising then-modern methods of vacuum induction.

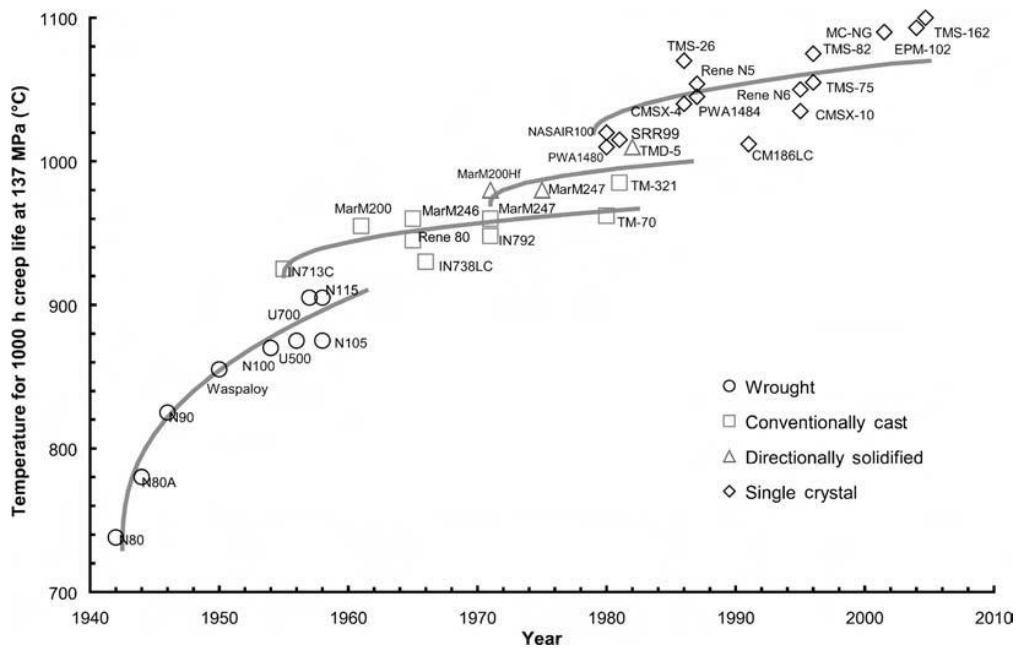


Figure 4: The evolution of high temperature creep life of superalloys between 1940 and 1960[1]

The third class of superalloys found further improvement by the work of VerSnyder [23] the introduction of directional solidification, utilising the process known as ‘investment casting’ or ‘lost wax’ [24], after which the introduction of the Bridgman process, whereby a large casting is withdrawn from the furnace, at an average speed of a few centimetres per hour, ensuring the liquid/solid interface travels along the cast from the base to tip. This process creates long grains in the direction of the withdrawal, and removes transverse grains from the material. In the context of a turbine blade the largest stresses are along the leading and trailing edges. Thus, the perpendicular grain boundaries tend to be the crack initiation sites. By removing these grain boundaries the lifetime of the component is increased.

Another advantage of this casting method is the reduction in number of grains, creating far larger grains that share the same orientation, $\langle 001 \rangle$. This will increase creep resistance for Coble and Nabarro Herring diffusional mechanisms, while increasing the resistance to thermal fatigue cracking.[25]

Finally, the fourth set of superalloys can be seen as a natural progression of the directional solidification approach. Full removal of grain boundaries utilising a grain selector is achieved leaving a single crystal. While the increased grain size gives further paths for diffusional creep, the method also allows for the removal of grain boundary strengthening elements such as C,

B, Zr, and Hf, which can form phases with low melting points [25]. Removing these elements allows for further solution treatment at higher temperatures by increasing the solidus temperature to beyond the γ' solvus, allowing for high temperature homogenization with finely distributed precipitates. Removing particular elements from the alloy also allowed an increase in the volume fraction of γ' forming elements for further creep resistance. The three crystal structures derived from cast, directionally solidified, and single crystal growth are shown in Figure 5.

In summary, since their inception in the first half of the 20th Century, nickel-based superalloys have been continuously improved. Through breakthroughs in the understanding of the microstructure and processing, along with new casting techniques, nickel superalloys have been at the core of high temperature gas, steam and jet turbine technology, and continue to be today.

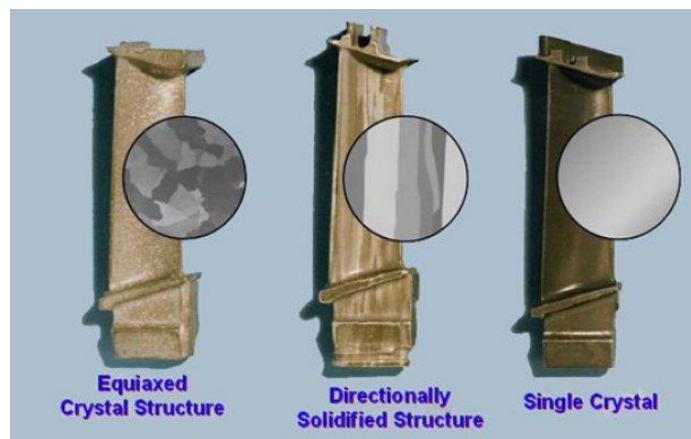


Figure 5: Images of cast (equiaxed grains), directionally solidified and single crystal grain structures insert against blades [26]

2.4 Strengthening Mechanisms of Nickel Superalloys

Nickel superalloys employ multiple mechanisms to improve the mechanical properties and creep resistance of the alloy. Typical modern nickel superalloys contain a mixture of alloying additions in solid solution, to increase the strength of a material, along with elements for carbide precipitation for increased mechanical properties (typically at grain boundaries),

precipitation hardening for creep resistance (such as the γ' phase) and elemental additions for oxidation resistance. These will be discussed below in this section.

2.41 Solution Treatment and γ phase

Solid solution strengthening is a method through which the strength of a pure metal may be increased by the inclusion of additional atoms (known as the solute atoms) of an element added to the crystalline lattice of another element. The non-uniformity of the lattice due to size differences in the atoms creating localised compressive or tensile stresses [27]. For a lattice with an additional atom with an atomic size significantly less than the host atoms (greater than 15% size difference), is known as an interstitial solution, while an atom of similar size or larger is known as a substitutional atomic solution, demonstrated in Figure 6. Due to the size difference needed for an interstitial solution, only very small atoms can be considered, typically C, H and B, while metallic atoms similar in size to Ni will create substitutional solutions.

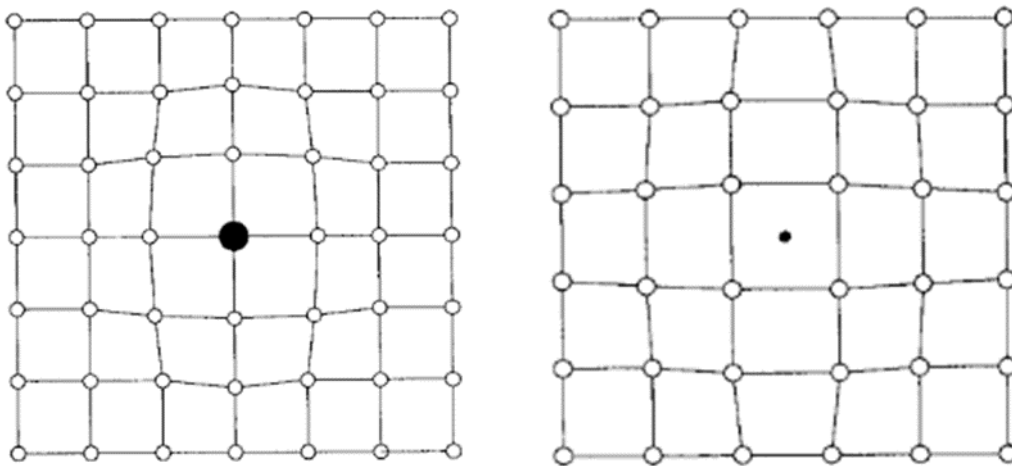


Figure 6: Shown left: a sketch of a substitutional atom creating a positive strain field in the lattice. b) A sketch of a substitutional atom creating a negative dilation strain in the lattice, [28]

The nickel superalloy γ matrix is a solid solution strengthened fcc phase as shown in Figure 7, where the crystal structure is shown to be a random distribution of atoms, the majority of

solutionising elements are shown in Table 1 under ‘Matrix Class elements’, with other classes of elements to be discussed below.

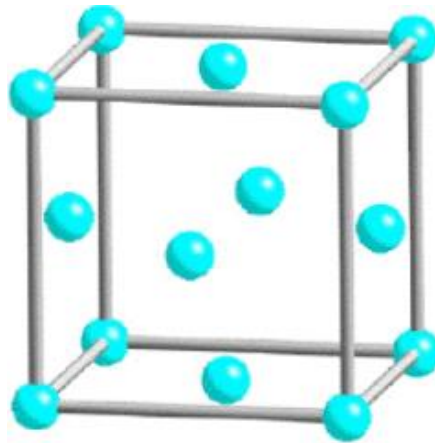


Figure 7: Crystal structure of FCC γ phase lattice, with random distribution of atom species [29]

Solution heat treatment

Solidification of an alloy while casting can lead to segregation of elements based upon the liquidus temperature of each element. This can cause issues such as non-homogenous precipitate distribution, and formation of deleterious secondary phases between solidifying dendrites.

A solution heat treatment is designed to heat a nickel superalloy above the γ' solvus but below the solidus in order to prevent incipient melting. The typical temperature chosen is about 1300°C [16, 30], however it will vary alloy to alloy, along with the required time for the solution treatment to be carried out. Cr can be added to reduce the incipient melting points, along with the liquidus, solidus and solvus temperatures, which allows for lower solution treatment temperatures [31]. The rate of cooling from the solution treatment temperature will determine the precipitate morphology, with fast quenched morphologies resembling spherical nuclei, and slower continuously cooled resembling a more cubic structure. More complex morphologies are possible, such as the octodendritically diced cube (f) and star-shaped octodendrite and dendrite structures (c and d) [32], shown in Figure 8. Solution heat

treatments, at the correct temperature, can also be used to relieve residual stresses within the material.

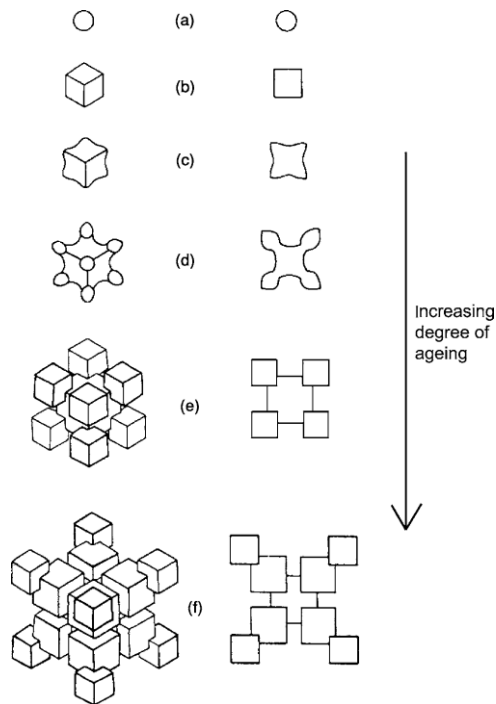


Figure 8: Diagram illustrating the gradual evolution from spherical nuclei (a), to larger, more complex cuboidal structures (b-f). [1]

Stress relief heat treatments

The final use of a solution treatment in the case of a nickel superalloy spring is that winding a spring can induce many GND's which can create residual stresses in the coiled wire, along with SSD's they may create compressive stresses at the outside radius of a wire, and tensile stresses at the inside radius. These residual stresses may be reduced with a stress relief treatment that annihilates a portion of the dislocations, for example, a 400 °C treatment for 20 minutes on a high strength steel spring can be modified from 681.9 MPa and -593 MPa at the interior and exterior respectively, to 124MPa and -63.2 MPa [33]. One limitation of such treatments, however, is that most of the annihilated dislocations will be SSD's, as GND's are all of the same sign, they will be more resistant to such treatments.

2.42 Precipitation treatment

Following the solution treatment, a precipitation treatment is often accomplished. This treatment is typically at a lower temperature than the solution treatment, and is designed to encourage growth of the now-homogenized particles in the matrix. Known as ‘ageing’ the alloy, the growth of particles comes at a cost of reducing the particle spacing to volume fraction ratio. i.e., the maximum number of nucleated precipitates are formed in the solution treatment, and the precipitation treatment encourages the larger precipitates to grow at the expense of smaller precipitates. It is important not to over-age a metal as there is a reduction in ductility as the strength of the material increases, and there is a maximum radius of particle size for material strength, at which the optimal size and distribution of particles is achieved. Growth of particles beyond the optimal radius leads to poor distribution due to the spacing increasing, and lack of coherency with the alloy matrix. [34]. A sketch of the ageing increase in hardness is shown in Figure 12.

A precipitate increases the hardness of a metal by creating stress fields around the precipitate due to strain in the lattice produced in much the same way as the substitutional and interstitial atoms mechanism described above. The stress field will repel or attract dislocations based upon whether the stress field is compressive or tensile. Regardless of stress fields, the precipitate acts as an obstacle to climbing and gliding dislocations moving through the lattice under an applied stress. The coarsening of particles is called ‘Ostwald Ripening’, and has been derived in many ways throughout the years [35], however many may be described by some modified version of the equation derived by Lifshitz, Slyozov and Wagner (LSW theory):

$$r^3(t) - r^3(0) = K(Q)t \quad (2.10)$$

where $r(t)$ and $r(0)$ are the particle radii at time, t , and $t = 0$. $K(Q)$ is a function of the interfacial energy of particles, elemental concentrations within the particle and matrix, the volume diffusion coefficient of the main element in a particle, and the temperature. As K is sensitive to many factors, designing a precipitation heat treatment to obtain the desired volume fraction and particle size of particles within an alloy can be a complex process, and when operating at high temperatures, particles may be expected to continue to coarsen, as in the case for the single crystal nickel superalloy CMSX-4 which has been found to have a

significant decrease in Vickers Hardness within a hundred hours at 950⁰C [36] due to over-aging.

2.43 γ' phase

The γ' precipitate is an L12 ordered FCC intermetallic phase Ni₃(Al,Ti), where the main difference between this phase and the γ matrix is that the matrix contains a random arrangement of atoms in the FCC lattice, while the γ' phase has the Ni atoms inhabit the cubic face-center, while the Al or Ti atoms inhabit the cube corners. Both crystal structures are shown in Figure 9 for comparison.

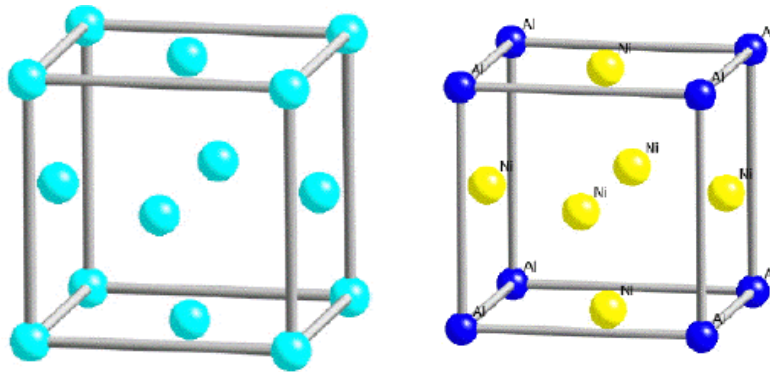


Figure 9: Left: crystal structure of γ matrix, right: crystal structure of γ' for a Ni₃Al chemistry [29]

As both the matrix and precipitate have the same cubic structure with approximate lattice parameters, the γ' will precipitate be coherent with the matrix. Due to a phenomena discussed in section 2.46 dislocations have difficulty entering into γ' , which leads to the high temperature creep strength superalloys are known for. The misfit of between γ and γ' can be described by the equation [37]:

$$\delta = \frac{2 \cdot a(\gamma') - a(\gamma)}{a(\gamma') - a(\gamma)} \quad (2.11)$$

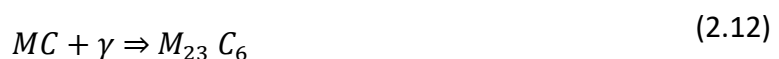
where a is the lattice parameter. The misfit is deemed to be positive if the γ' has a larger lattice parameter than γ , and conversely if the γ lattice is larger, the misfit is negative. Misfit can have a large affect upon the internal stress state of a nickel-based superalloy [38]

There is typically a small misfit between the matrix and γ' [39] which can be affected by cooling rates and aging methods [37]. A lower misfit implies a small interfacial energy at the γ/γ' interface. As particle coarsening is driven by minimisation of total interfacial energy, there is stronger coherency between the particles and matrix, which allows for a stable microstructure, even at higher temperatures. The degree of lattice misfit between γ and γ' can be affected by the alloying elements, such as the platinum group metals which are known to affect either the lattice parameters of the matrix or particle phases [40].

2.44 Carbides

By introducing a small amount of C into the alloy, the precipitation of carbon-based phases can be controlled. These precipitates are ordinarily desired at grain boundaries to limit grain growth, leading to increased reduction in grain boundary sliding [41]. Carbides are thus more common in polycrystalline nickel superalloys than single crystal, where grain boundary strengthening is not required. Chen and Knowles [42] were able to demonstrate that a small amount of C (0.1 wt%) and B (0.01wt%) were enough to encourage formation of MC carbides within and significantly increase time to creep rupture in a modified second generation nickel superalloy, which they attributed to the formation of blocky $M_{23}C_6$ at grain boundaries.

The two main phases concerned in this thesis are the MC and $M_{23}C_6$ carbides, where M is the metal atom. $M_{23}C_6$ is a carbide with a complex cubic structure, nucleating in alloys with significant Cr content [43] and are known to improve the creep properties of a material. TiC is known to be less stable and can decompose during heat treatment or during service into other $M_{23}C_6$ [1]



2.45 TCP phases

Topologically Closed Packed (TCP) phases are typically undesirable phases that are formed during heat treatments or during service at high temperature. A common TCP phase in nickel superalloys is σ -phase, a tetragonal structure with the composition of AB_7 to A_7B , where A is a transition metal from group VIIA or VIIIA, and B is from group VIIA or VIIIA [44]. Taking the shape of platelets or needles, the phase is known to lead to a depletion in γ and γ' forming elements, which can lead to a reduction in alloy strength. The phase shares a similar structure to $M_{23}C_6$, and σ -phase can be found to nucleate sympathetically from $M_{23}C_6$. It is a brittle phase that can lead to the initiation of cracks, and due to its Cr affinity for the phase, can reduce the oxidation resistance. Another common TCP phase in nickel superalloys is the μ -phase. This phase is based on the composition A_6B_7 with a rhombohedral cell containing 13 atoms, such as W_6Co_7 and Mo_6Co_7 . Though different in composition, the phase leads to similar mechanical issues as σ -phase.

2.46 Defects in γ FCC phase and deformation mechanism

There are three distinct types of defects present within crystalline FCC solids. These can be classified as: stacking faults and other planar defects, dislocations, and point defects such as vacancies interstitials and anti-site defects. It is important to understand the mechanism of stacking faults, anti-phase boundaries and dislocation movement in order to grasp the strengthening mechanism of γ' particles. There are two primary variants of dislocation; edge dislocations and screw dislocations. In this thesis, screw dislocations are neglected and all dislocations are treated as having edge character.

An edge dislocation can be described as an extra half plane of atoms, travelling horizontally on a slip plane, where the dislocation line is perpendicular to the direction slip. A sketch of an edge dislocation is shown in Figure 10.

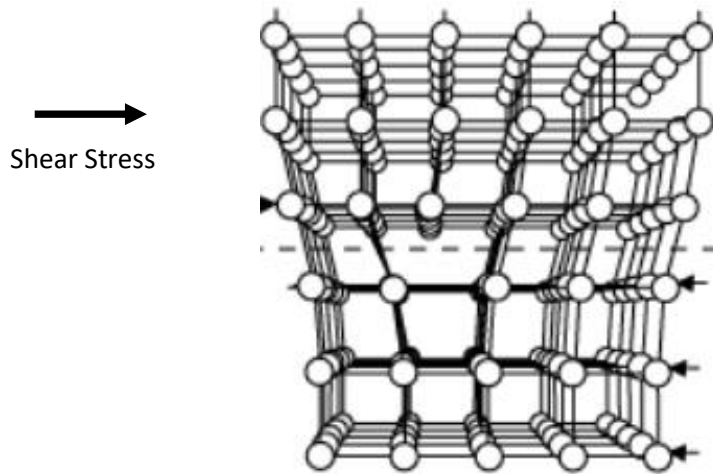


Figure 10: Sketch of an edge dislocation within a crystal lattice under a shear stress [45]

Dislocations in a nickel superalloy are assumed to travel along the Burgers vector $(a/2)\langle 110 \rangle$, residing on the $\{111\}$ planes, where a is the lattice spacing. The lattice vectors can be seen in Figure 11. The Burgers vector is a lattice vector and so the slip does not affect the structure of γ . Conversely, for γ' , $(a/2)\langle 110 \rangle$ is not a lattice vector. Rather, $(a/2)\langle 110 \rangle$ is a primitive cubic lattice vector. This means that the $(a/2)\langle 110 \rangle$ dislocation entering γ' from the γ matrix will disrupt the order, leading to an 'anti-phase domain boundary' (APB), which is a crystallographic defect in which the atoms in a region of a crystal are arranged in the opposite order to the perfect lattice system, forming anti-phase boundaries with the rest of the lattice. An initial $(a/2)\langle 110 \rangle$ dislocation will disrupt the γ' lattice, however, passing a second dislocation through on the same slip plane will restore the atomic order. It is therefore clear that the penetration of γ' has to be achieved with pairs of dislocations from γ . Known as 'Super dislocations' or 'Shockley partials', a larger dislocation, 'b' will dissociate into b_1 and b_2 with an APB between them [46] so long as it is energetically favourable, according to (2.13-2.15).

$$b_1^2 + b_2^2 \leq b^2 \quad (2.13)$$

$$b = \frac{a}{2} [110] \quad (2.14)$$

$$b_1 + b_2 = \frac{a}{6} [21\bar{1}] + \frac{a}{6} [121] \quad (2.15)$$

The two partial dislocations are of same sign and thus repel one another. The area between them, the 'stacking fault' is of higher energy than the surrounding matrix, and its size depends upon the force of elastic repulsion between the partial dislocations. The requirement for

pairing requires more energy, and therefore increases the resistance to creep deformation. It is important to note that there are two mechanisms of strengthening in γ' linked to the distance between the super dislocation pairs. Known as 'weakly coupled' and 'strongly coupled' [47] where the weakly coupled case applies to dislocation pairs with large distance between them compared to γ' particle size, ie a large stacking fault area. This mode is typically associated with underaged alloys. Conversely, with large γ' particles the spacing of dislocation partial pairs is small compared with particle size, meaning that the two dislocation partials may both inhabit a particle at the same time.

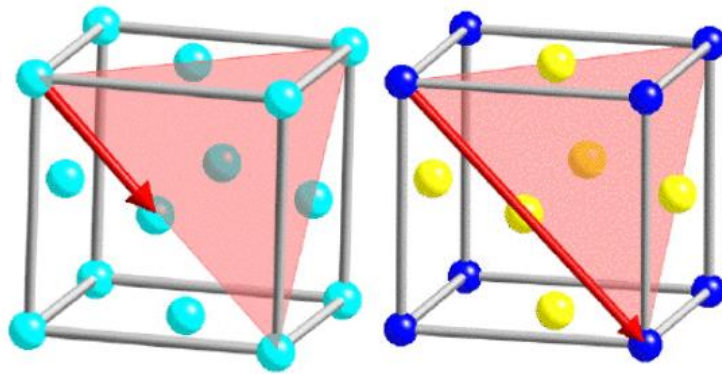


Figure 11: Lattice vectors along the $\langle 110 \rangle$ directions, residing on the $\{111\}$ planes. Left: γ matrix with random distribution of Ni and other alloying elements. Right: γ' lattice with Ni atoms residing at the face-center [48]

Particle coarsening has an effect on the mode of interaction between dislocations and precipitates. These modes are Orowan Bowing and Particle Shearing. There is an optimum yield strength for the material that is achieved at a critical particle radius, r_p , approximately 20nm in Nickel superalloys [49]. Figure 12 demonstrates the change from cutting to bowing of dislocations and the link to weak and strong coupling.

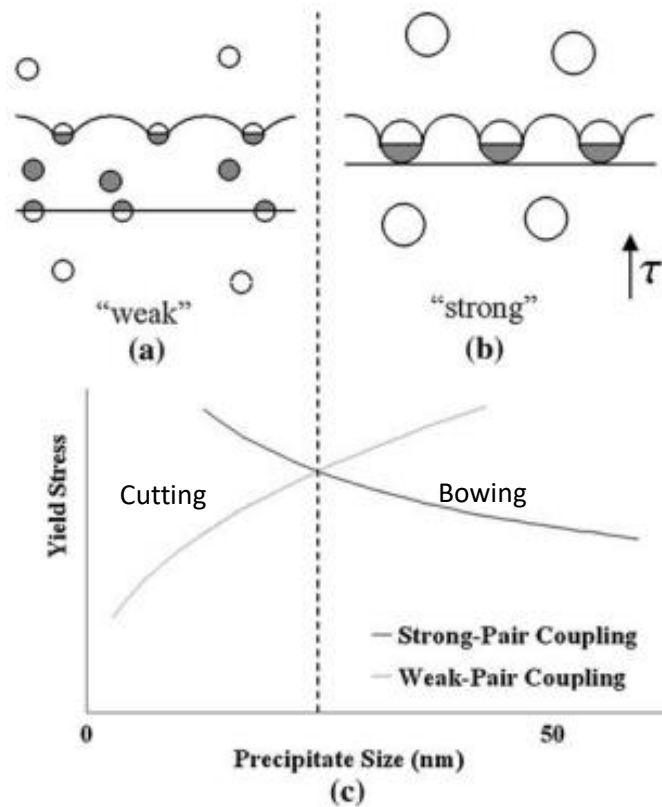


Figure 12: Cutting/Orowan bowing of dislocations in a precipitation strengthened material; r_c is shown by the dashed line and denotes the optimum particle radius for largest strength [49]

2.47 Summary of strengthening mechanisms

Nickel-based superalloys design includes multiple mechanisms for improvement of mechanical properties, including solid solution strengthening, heat treatments to create fine dispersal of elemental additions and precipitates, and precipitation treatments to coarsen precipitates to a desired size. The alloying elements effect on the microstructural properties are summarised in Table 1. The formation of γ' by elemental additions of Al and Ti to form the ordered L12 fcc structure lead to additional creep strengthening that increases the difficulty of dislocations gliding through the matrix.

	Element	Function
Matrix-class elements	Co, Fe, Cr, Mo, W, V, Ti, Al	Solid solution strengthening (Al and Cr, Corrosion resistance)
γ'-phase forming elements	Al, Ti, Nb, Ta	Precipitation Strengthening
Carbide-forming elements	Cr, Mo, W, V, Nb, Ta, Ti, Hf	Reduction in grain boundary sliding
Grain-boundary-active elements	Zr, B	Enhancement of creep strength and rupture ductility

Table 1: Elements grouped by contribution to microstructural properties [14]

2.5 Material

The material utilised in-service as steam turbine surface control clearance systems is Nimonic 90, a medium γ' volume fraction (20-40%) Nickel-based Superalloy, which gives a compromise between creep strength (high γ') and formability (low γ'), the composition of which is shown in Table 2

Alloy	Ni	Cr	Co	Mo	Al	Ti	Fe	Mn	Si	C	B
Nimonic 90	53	19.5	18	-	1.4	2.4	3	1	1.5	0.13	-

Table 2 composition of Nimonic 90 Nickel Superalloy [50]

Nimonic 90 is an age-hardened alloy designed for temperatures up to 920°C, for use in turbine discs, turbine blades, and ring-sections within high-temperature steam turbines, with a liquidus temperature $T_L=1370^\circ\text{C}$ [50]. Although designed for some uses at temperatures as high as 920°C, Nimonic 90 has poor creep resistance in the region of 650°C-700°C, showing a

suggested reduction in creep rupture time by a factor of 10^2 hours between 600°C and 700°C at constant operating stresses above 350 MPa [51], making it potentially the incorrect choice for the application concerned in this thesis, investigating and modelling this behaviour thus will allow an informed decision on its suitability.

Nimonic 90 contains a large amount of Cr, which leads to the creation of a protective oxide layer of Cr_2O_3 on the surface when heat treated in an oxidising environment, the optimum amount is found to lay between 15-30% [52], a small amount of silicon is added for additional oxidation resistance. Al, Ti are included to promote formation of γ' precipitates ($\text{Ni}_3(\text{Al},\text{Ti})$) and alongside Ta and Nb add to the flow stress and ultimate tensile stress of the alloy. Finally C is utilised to form carbides with Ti and Cr, to promote carbide growth.

In summary, Nickel-based superalloys are utilised in high temperature, high stress applications, due to their high creep resistance. The mechanics and basis of creep modelling and stress relaxation modelling are considered in the following chapter.

Chapter 3: Creep and stress relaxation

3.1 Creep definition

Creep can be described as the plastic deformation experienced by a material while subjected to a constant stress below its yield stress. Creep typically occurs above $0.4 - 0.5 T_m$, where T_m is the melting temperature [54]. Creep of a material can be split into three distinct phases: primary, secondary and tertiary. Figure 13 shows an example of a typical strain-time graph. It can be seen that in the first stage, the creep strain rate ($\dot{\epsilon}$) of the material reduces with time and strain. This is typically associated with an increase in dislocation density and the development of a dislocation substructure similar to that seen in work hardening. This increases with strain, but due to dislocation interactions these substructures can be viewed as 'tangles' or 'forests', restricting continual dislocation glide, and lead to dislocation climb becoming the rate controlling process. The transition from the glide to climb can be seen as the transition from primary to secondary creep [54, 55]. The secondary creep is roughly constant, with the majority of component life spent in this regime. The microstructure will evolve in a steady state, with the steady state creep rate $\dot{\epsilon}_{ss}$ a minimum unchanging

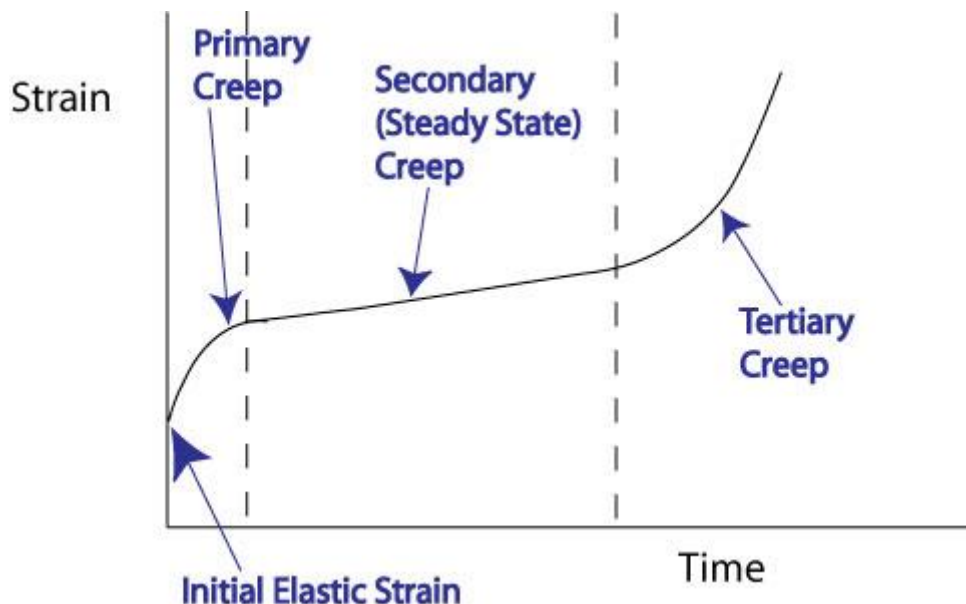


Figure 13: Sketch of simple strain-time graph demonstrating primary, secondary and tertiary creep, adapted from [53]

value. The modes of softening and hardening are assumed to be in a state of balance, keeping dislocation density approximately constant [56].

Finally, the tertiary regime of creep shows a continuous increase in the creep rate, leading to fracture of the component. The transition from secondary to tertiary creep can be caused by multiple changes in the microstructure, such as cavitation at grain boundaries. The rate at which the strain can reach the tertiary regime can vary non-linearly with small changes to the applied stress at constant temperature [57] or at relatively small changes in temperature. Various methods of modelling creep have been employed, and these will be discussed in the literature review.

There are several possible mechanisms for creep and these depend upon the microstructure of the alloy in question, the temperature, and applied stress. These factors will determine whether the material will undergo creep dominated by dislocation glide, dislocation climb, or diffusional flow mechanisms (Nabarro-Herring and Coble creep). Both Nabarro-Herring Creep and Coble Creep are diffusion controlled, occurring at low stresses.

The factor deciding whether it is Nabarro- Herring or Coble creep that dominate is the temperature. Lower temperatures typically result in Coble creep, which is diffusion along grain boundaries. At higher temperatures Nabarro-Herring Creep can dominate, which allows for diffusion within the grains. By increasing the grain size, one may increase the creep resistance to diffusional creep by increasing the length of the diffusion paths.

Dislocation creep occurs at higher stresses than diffusion creep, and describes the movement of a dislocation via gliding along a 'slip plane' of close-packed atoms in the lattice, with the rate-dependant step of dislocation creep being the climb process. Dislocation climb is the movement of an edge dislocation out of a slip plane onto the plane either directly above or below it. Climb is more temperature dependant than glide, and thus dominates at higher temperatures [58]. At very high stresses, dislocations can cut through particles.

In the case of the model presented in this thesis a combination of climb and glide is modelled, in which a dislocation is expected to glide through the matrix on a glide plane, until it comes into contact with a particle, at which point it is able to climb by vacancy emission and absorption, shown as 'e' and 'a' respectively in Figure 14.

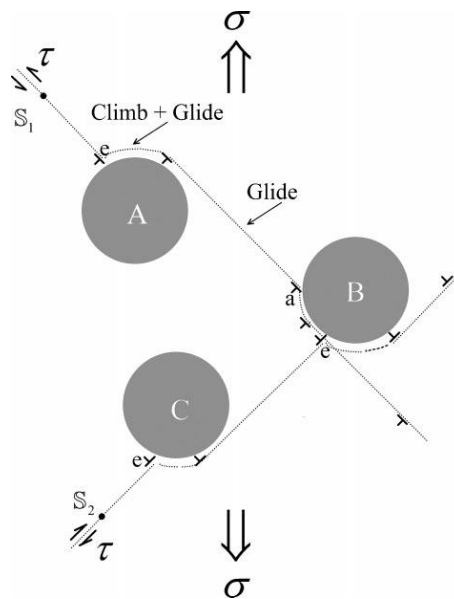


Figure 14: Illustration of precipitate strengthened alloy, experiencing creep by dislocation climb and glide. Dislocation sources S_1 and S_2 get past particles A and C through climb by vacancy emission, 'e' and bypass particle B by vacancy absorption 'a' and emission 'e' [7].

3.2 Stress relaxation definition

As mentioned in section 1.1 stress relaxation is the time-dependant decrease in stress of a solid under given constraint at constant conditions. A stress relaxation test differs from a creep test in that during a creep test, the measured stress of the sample is kept constant, by fixing the load on the sample during the test. This test essentially has constant stress, while measuring the strain response. Conversely, a stress relaxation test keeps the strain constant, leading to a reduction in the stress response over time. When a sample is subjected to a tensile or compressive load, a reaction force response may be measured. This stress state initially leads to elastic strain, distorting the crystal lattice of the material. Over time, at elevated temperatures, this elastic strain may become plastic strain, through the movement of dislocations. The sample undergoes permanent deformation and no longer exerts the reaction force it did previously. The ratio of reaction force at time, t to the initial reaction force $\frac{P(t)}{P_0}$ can be plotted to measure the reduction in the stress over time. A sketch of a typical stress relaxation curve is shown in Figure 15.

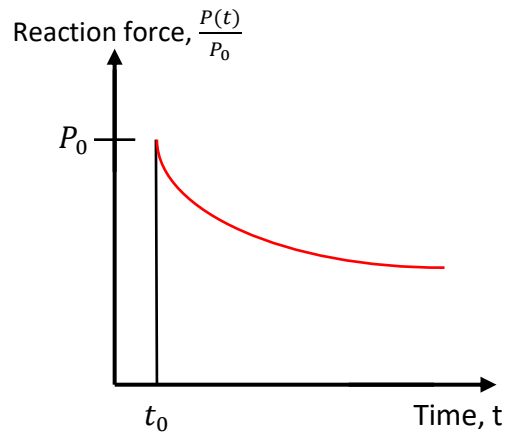


Figure 15: Sketch of typical stress relaxation curve. Loading occurs at time, t_0 , and the stress relaxes from P_0 over time. Initial relaxation is rapid leading to a steady-state response.

It is well accepted that stress relaxation can be considered to be a particular type of creep, being well represented using existing creep laws [59]. This is corroborated by Zhang et al [60] who performed thermomechanical fatigue tests on the single crystal nickel based superalloy TMS-82, and investigating the microstructural evolution of the alloy using SEM, TEM and Optical Microscopy, concluding that stress relaxation is a result of three separate mechanisms:

- 1) Primary stress relaxation is caused by the filling in of γ channels between γ' precipitates of dislocations and the cutting of γ' cuboids by dislocations
- 2) The steady state stress relaxation is related to the annihilation of dislocations produced during deformation, leading to a steady state of dislocation density
- 3) Tertiary stress relaxation is due to de-twinning of deformation twins

These three mechanisms are similar to creep mechanisms, which gives strength to the argument that creep and stress relaxation are inextricably linked and can be described using the same models.

An early model of stress relaxation considering the dislocation behaviour in the matrix was accomplished by Gupta et al [61] as an example of utilising dislocation glide mechanics within a stress relaxation model based upon a creep power law. While this model does not account for precipitate size and distribution, it does take into account the internal stress within the

material leading to work hardening effects and the effective stress acting upon any mobile dislocations. This model is the basis for later stress relaxation models such as Chaboche [62] and Zhan [63]

3.3 Empirical creep rate modelling

The prediction of creep, and the design of components and materials to resist creep has existed for a long time. Traditionally empirically-driven power law expressions have been used to fit numerical expressions to data. While these models do have some physical basis, taking into account creep mechanisms such as dislocation density affecting glide and lattice diffusion, these features are often included indirectly through adjusting the power value, n , depending on the assumed creep rate mechanism. These methods also assume simple alloys and pure metals without precipitates [128], which makes them unsuitable to more complex materials like Nickel superalloys, where the γ' volume fraction is known to have a significant effect on the creep rate. They do not typically incorporate the effect of microstructural features such as grain size, precipitates and dislocation densities.

E.Orowan [64] described the various forms of creep failure mechanisms that were understood in the 1940's. He described the creep rate of materials in terms of the strain rate which depended on the stress applied to a material. He stated that, at low strain rates, a metal will behave as a Newtonian viscous material, with creep rate given by

$$\dot{\epsilon} = \frac{\sigma}{3\eta} \quad (3.10)$$

Where η is a constant of viscosity and σ is the applied stress.

Although there are many different creep models, varying in complexity, most classic creep models take the form [65] :

$$\dot{\epsilon}_{ij} = \frac{3}{2\sigma_e} S_{ij} A \exp\left[-\frac{Q_{sd}}{kT}\right] (\sigma_{ss})^n \quad (3.11)$$

where A is material constant, Q_{sd} is the activation energy for self-diffusion, k is Boltzmann's constant, and σ_{ss} is the applied stress during the steady state creep. The exponent ' n ' is

typically in the range 3-10, and varies depending on the alloy in question. The deviatoric stress, $s_{ij} = (\sigma_{ij} - \delta_{ij}\sigma_{kk}/3)$ and the effective stress, $\sigma_e = \left(\frac{3s_{ij}s_{ij}}{2}\right)^{1/2}$. This allows for the creep rate to be calculated for a multiaxial stress state, which can be utilised in a more complex geometry like a coil spring [74]. Equation (3.11) is based upon the work of Norton [66]. This model is essentially phenomenological and does not physically relate to the microstructural changes that occur during high temperature creep. Models of this format are optimised for a particular alloy, over a particular temperature and applied stress range, and can therefore not be extended to different alloys, or even heat treatments, without performing additional creep tests and recalibrating the model from scratch each time. It is therefore challenging to use these models for alloy development or to extrapolate creep data to similar materials. Ideally the underlying creep mechanisms should be understood and accounted for in any possible model. These are described as physics-based models.

3.4 Physics-based creep rate models

The evolution of microstructure and the interaction between particles, particle size, matrix, grain size, dislocation density and coarsening is complex, requiring computer programs to make continuous calculations of constitutive equations. The late 1980's and 1990's saw computation increasingly used for research purposes using Finite Element Modelling. For example, the creep of nickel-based superalloys, consisting of a γ matrix with embedded γ' precipitates, was first studied in this way by Cailletaud et al [67], inserting constitutive equations for strain rate into a macro-scale model.

3.4.1 Dyson model

The early 'two-phase' creep models for nickel superalloys were a product of modern computational techniques developed in the 1980's and early 1990's. The so-called 2-phase models of creep have been used to describe the strain rates of nickel-based superalloys by considering the γ and γ' phase. An early model for this is described by Pollock and Argon (1992) in which the nickel superalloy CMSX-3 was studied. The conclusions, along with such

works as of Muller et al (1992) on SRR 99 exploring the stress distribution between γ and γ' , found that during steady-state creep the matrix channels between γ' particles develop three-dimensional networks of dislocations with three Burgers vectors $\frac{a}{2} \langle 1\bar{1}0 \rangle$ lying in the $\{111\}$ plane, and that the substantial climb occurs in this system [68, 69]. The models of this type assume the rate-controlling mechanism is dislocation climb and typically replaces the stress term σ_{ss} with $(\sigma - \sigma_0)$, where σ_0 is a temperature-dependant threshold stress below which climb cannot take place.

Osgerby and Dyson [70] first proposed a physics-based creep law for precipitate-strengthened alloys in 1993. They used a conceptual model of the glide and climb process, illustrated in Figure 14, resulting in a model for how the internal stress redistributed over time from matrix to particles during creep that depends on the precipitate volume fraction, precipitate size and dislocation density. The basic equation for the secondary creep rate under uniaxial tension takes the form:

$$\dot{\epsilon}_{ij} = \frac{3}{2\sigma_e} S_{ij} \dot{\epsilon}_0 \sinh \left[\frac{\sigma}{\sigma_0} \right] \quad (3.12)$$

where $\dot{\epsilon}_0 = k' \rho_m \phi_p^{\frac{1}{2}} (1 - \phi_p) (1 - \phi_p^{\frac{1}{2}}) c_j D_m$ and $\sigma_0 = \frac{KTF(\phi_p)\sigma_{or}}{Gb^3}$, where K' is a constant of order unity, ρ_m is the mobile dislocation density, ϕ_p is the particle volume fraction, c_j the jog density, D_m the matrix diffusivity, G the shear modulus and σ_{or} the Orowan stress for particle bypass. $F(\phi_p)$ is a function of the stress redistribution around particles, increasing from unity to a maximum during steady state creep as $F(\phi_p) = 1 + 2 \phi_p$.

3.42 Secondary creep model

Also pertinent to this thesis, more recent work on creep rate equations has been completed by Dyson [7] on Nimonic 90, in which the creep rate is considered as a 'dispersion controlled' kinetic creep model, that is, the model is dependent upon the particle volume fraction, f , and the 'dispersion parameter' of the inter-particle spacing, λ_p and the applied stress σ . Many physically based models utilise the Orowan-Bailey equation that links the shear strain rate $\dot{\gamma}$ to the dislocation density ρ , burgers vector b and gliding velocity v_g :

$$\dot{\gamma} = \rho b v_g \quad (3.13)$$

Dyson separates the gliding and 'pinned' at γ' particles dislocations, dividing the total dislocation density into two parts, $\rho = \rho_g + \rho_c$, where ρ_c is the density of pinned dislocations that are climbing over a particle. The dislocation densities have corresponding velocities $v_g \rho_g$ and $v_c \rho_c$. The Orowan-Bailey equation was therefore written as

$$\dot{\gamma} = b(\rho_g v_g + \rho_c v_c) \quad (3.14)$$

Pinned dislocations must climb slowly over a dislocation to 'escape' and continue to glide, which is considerably faster. According to Dyson there will always be a fraction $\frac{b}{r_p}$ of pinned particles able to escape or 'jump' with frequency Γ_e . This means that the rate of gliding dislocations will increase with $\rho_c \phi_p \left(\frac{b}{r_p}\right) \Gamma_e$, and are immobilised at the next particle after gliding at a rate $\rho_g \frac{v_g}{\lambda_p}$, with λ_p as the interparticle spacing, Dyson writes that the rate of change of gliding dislocations may then be written as:

$$\dot{\rho}_g = \rho_c \phi_p \left(\frac{b}{r_p}\right) \Gamma_e - \rho_g \frac{v_g}{\lambda_p} \quad (3.15)$$

By substituting $\rho_c = \rho - \rho_g$ and integrating (3.15), while keeping ϕ_p and r_p constant and setting $\rho_g = 0$ at $t = 0$, one may reach

$$\rho_g v_g = \frac{\lambda_p \phi_p \left(\frac{b}{r_p}\right) \Gamma_e}{v_g + \lambda_p \phi_p \left(\frac{b}{r_p}\right) \Gamma_e} \rho v_g \quad (3.16)$$

By taking the limit $v_g \gg \lambda_p \phi_p \left(\frac{b}{r_p}\right) \Gamma_e$, that the glide in the matrix is fast and the rate controlling mechanism for creep is the release of dislocations from the particle dispersion, then one reaches the 'dispersion controlled shear strain rate':

$$\dot{\gamma}_{d/c} = \rho b \lambda_p \phi_p \left(\frac{b}{r_p}\right) \Gamma_e \quad (3.17)$$

With square particle spacing λ_p becoming the square lattice spacing $\lambda_p = 1.6 r_p \left[\left(\frac{\pi}{4\phi}\right)^{\frac{1}{2}} - 1\right]$. Dislocations may climb by vacancy emittance or absorbance, and so Γ_e is taken as the average of the rate of vacancy emittance and absorbance, where the vacancy absorption rate is:

$$\Gamma_{e,a} = \frac{c_j D_s}{b^2} \left(1 - \exp \left(-\frac{b \lambda_p}{KT} b \tau_d \right) \right) \quad (3.18)$$

Where c_j is the dislocation line jog density, D_s is the diffusion coefficient, and $b \tau_d$ is the shear force on a dislocation. The vacancy emission rate is:

$$\Gamma_{e,e} = \frac{c_j D_s}{b^2} \left(\exp \left(-\frac{b \lambda_p}{KT} b \tau_d \right) - 1 \right) \quad (3.19)$$

As the number of vacancies and emissions are expected to be approximately equal, one may take the average of (3.18) and (3.19) and obtain:

$$\Gamma_e = \frac{c_j D_s}{b^2} \sinh \left(\frac{b^2 \lambda_p}{KT} \tau_d \right) \quad (3.20)$$

Inserting (3.20) into (3.17) Dyson obtains:

$$\dot{\gamma}_{ij} = A \sinh \left(\frac{\alpha \tau}{\bar{M}} \right) \quad (3.21)$$

where $A = \frac{\phi_p \rho \eta}{\bar{M}} (1 - \phi_p) D_s$, and $\alpha = \frac{b^2 \lambda_p}{\bar{M} k T}$, where $\bar{M} = \frac{\sqrt{3}}{3} \approx 1.6$ is the Taylor factor for polycrystalline metals, a constant relating average ratio of shear strain, $\dot{\gamma}$ to macroscopic strain, $\dot{\epsilon}$, while ϕ_p is the particle volume fraction. D_s is the constant for self-diffusivity, η is the particle spacing to radius ratio where $\eta = 1.6 \left[\left(\frac{\pi}{4 \phi_p} \right)^{\frac{1}{2}} - 1 \right]$. The stress component within the sinh term includes the applied stress, τ , the internal stress, τ_i , related to the back-stress hardening of dislocations piling up on particles, evolving with time. $\hat{\tau}_{net}$ is the minimum stress required for activation of Frank-Read sources to generate dislocations that may then glide in the matrix. Finally the inter-particle spacing is defined as $\lambda_p = r_p \eta$, where r_p is the particle radius.

This model, equation (3.21), maintains the earlier origins of the hyperbolic sine function in (3.12), with microstructural phenomena such as particle coarsening, matrix solute concentration and dislocation multiplication. The minimum creep rate calculations from this model for Nimonic 90 for varying temperatures can be seen in Figure 16, with the applied stress equal to the calculated 0.1% proof stress at each temperature. It is clear that the model reproduces the general trends well at 750°C, and was verified by others such as Basoalto [71] for conventionally cast and single-crystal nickel superalloys IN738LC and CMSX4 respectively.

It would therefore be expected to give acceptable results in the temperature regime of 650°C in this thesis, so long as the dominant creep rate mode is climb and glide. An analysis of the stress in the spring wire, taking curvature into account, is completed in chapter 4 to determine the creep mode using a creep deformation map.

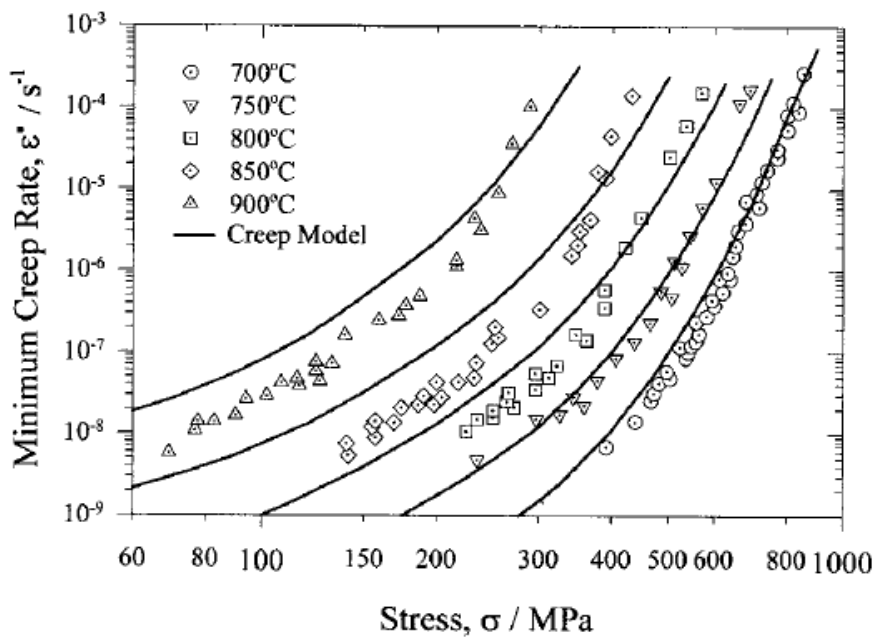


Figure 16: A comparison of the Dyson model minimum creep rate dispersion-controlled model against industry data for Nimonic 90 in a uniaxial creep test [7]

3.43 Introduction of primary creep and back-hardening

Although not strictly applicable to the steady state creep models presented in this thesis, it is worth noting that in order to move from secondary to tertiary creep one must include new terms into the model that accelerate the creep rate. Conversely, movement from primary to secondary creep requires a term to slow the initial creep rate down to a steady, constant value. Continuum Damage Models (CDM), originally based upon the work of Kachanov and Rabotnov in the 1950's, use a single 'damage' parameter, D , within a power law creep rate formulation to describe the tertiary creep and failure [72]. This relates the strain rate to two evolving state variables which represent primary and tertiary creep respectively. Introducing the back-stress hardening parameter, H , to represent stress redistribution during primary

creep due to dislocation pile-up on particles, and damage parameters to include microstructural change during creep eventually leading to tertiary creep and failure.

Mustata et al [73] created an FE model based upon the CDM work of Kachanov and Rabotnov, to investigate three-dimensional creep of a steel cylinder-cylinder branched pressure vessel welded connection, utilising a three-dimensional CDM-based creep model of the form:

$$\dot{\varepsilon}_{ij} = \frac{3s_{ij}}{2\sigma_e} A \sinh \left[\frac{B\sigma_e(1-H)}{(1-\phi)(1-\omega)} \right] \quad (3.22)$$

$$\dot{H} = \left(\frac{h\dot{\varepsilon}_e}{\sigma_e} \right) \left(1 - \left(\frac{H}{H^*} \right) \right) \quad (3.23)$$

with state variables, H , ϕ and ω . \dot{H} describes the strain hardening during primary creep saturating at a maximum value H^* when transitioning to secondary creep. ϕ is the evolution of particle spacing between precipitates, and ω is the inter-granular cavitation damage parameter. The major difference of interest to this thesis is the inclusion of the deviatoric stress $s_{ij} = (\sigma_{ij} - \delta_{ij}\sigma_{kk}/3)$ and the effective stress, $\sigma_e = \left(\frac{3s_{ij}s_{ij}}{2} \right)^{1/2}$ included as before, while $\varepsilon_e = \left(\frac{2\varepsilon_{ij}\varepsilon_{ij}}{3} \right)^{1/2}$ is the effective creep strain. It is important to note that in the stress relaxation in this thesis there is a disparity between the expected and measured time scales for relaxation. The springs relax on an order of minutes/hours to unacceptable levels, compared with the expected weeks/month. Microstructural changes can thus be ignored over this time frame. Tertiary creep will not be expected to be a factor and over short enough time scales, perhaps not even secondary creep, considering that the hardening parameter may not have enough time to saturate, and that the strains are expected to be small, of the order 0.1% and fixed at this small level throughout the relaxation tests.

3.44 Stress Relaxation of Coil Springs

The prediction of stress relaxation in a coil spring was investigated by Chang [6] who constructed a model for stress relaxation of a stainless steel wire based upon the principle that all plastic strain is a result of shear strain, and that a bi-linear shear stress-strain curve may be constructed from a uni-axial tensile stress-strain curve. Calculating the residual stresses due to pre-setting of the springs allowed for a calculation of the residual stress in a

wire cross-section from the center to wire radius. The model was not effectively validated, however, as only one data point for relaxation in a spring at 1000 hours was obtained. The model also takes no account of microstructural features of the spring, and their affect upon the strain. The assumption of a bi-linear stress-strain response allows for a simple, if not entirely physical, model.

Building upon the Chang model, Kobolev [74] created stress relaxation models for coil springs utilising the Norton Bailey model and the Garofalo hyperbolic sine model, amongst others. The limitations of these creep models discussed in section 3.42 above remain here. Derivation of the stress relaxation over time using Garafalo creep is given as a polylogarithmic function that is not validated within the paper. No account of creep strain mechanism is taken, and no back-stress hardening is considered within the models presented.

By measuring the stress across a spring wire cross section it is possible to calculate the reduction in reaction force of the spring over time at high temperature utilising FEA computational methods. One such example is the work of Jiang et al [75] where the stress distribution across a cross section of metallic rope wire was investigated. The non-uniform stress distribution demonstrated that the stress is higher towards the center radius of winding curvature, and that the strand closest to the center of the wire has the highest values of stress. It is also clear that the wire surface has a more uniform stress, with generally higher values than the cross section. It would be expected that a similar stress distribution would be present in the coil springs in this work.

Gill, Strang and McColvin [76] measured the relaxation of spring reaction for Nimonic 90 coil springs at varying temperatures and displacements. Observing the stress relaxation results against their proposed model based upon the work of Lewthwaite and Smith [77], it was found that the springs tended to relax much faster than predicted. The reason why this occurs and a method to prevent it are issues that have not yet been resolved. By performing similar stress relaxation tests in this thesis the possible causes of the disparity between expected and observed stress relaxation will be discussed and a method of adapting the proposed model to account for the disparity will be presented.

Chapter 4: Helical springs

This chapter will introduce the geometry of the helical spring samples investigated in this thesis, before discussing the simple elastic torsion of a wire commonly used to estimate its stiffness. Winding a wire into a coil spring will clearly have effects on the stress response of a spring, and so the effect of the shear stress response at different temperatures is investigated. The creep rate model that was chosen for this work was the Dyson model, selected as it is physically based and assumes a glide-climb creep mechanism. This chapter finishes with a short investigation to justify that choice. The coil springs stress response is compared with a creep deformation map to determine the expected creep rate mechanism that can be expected during the stress relaxation testing in this work.

4.1 Spring wire

The springs supplied by GE were supplied in the so-called ‘as-tempered’ state, that is, initially solution treated and given a post winding precipitation heat treatment after being cold-drawn at room temperature to 2.5mm diameter and cold-wound to the geometry required using a mandrel. Both heat treatments are shown in Table 3. A series of springs without the post-winding precipitation treatment were also supplied for later tests in this thesis. The solution treatment is utilised to reduce the internal stresses induced during the wire winding into a coil, and to evenly distribute the γ' forming elements across the material. The precipitation treatment is utilised to grow γ' to a particle radius $r_p = 0.01 \mu\text{m}$.

Alloy	Wire Solution Treatment	Spring Precipitation Treatment
Nimonic 90	0.5 hours 1150°C Rapid Cool	4 hours 750 degrees air cooled

Table 3 Nimonic 90 Nickel Superalloy solution and precipitation treatments

The dimensions of the springs used are as follows:

Inside coil radius, $R_i=8.25$ mm and maximum wire radius $a=1.25$ mm, with r representing any distance between the wire center and a . The springs were approx. 28.5 mm in height, W_s ,

with approximately five coils with the addition of tapered ends. A diagram of an example spring may be seen in Figure 17.

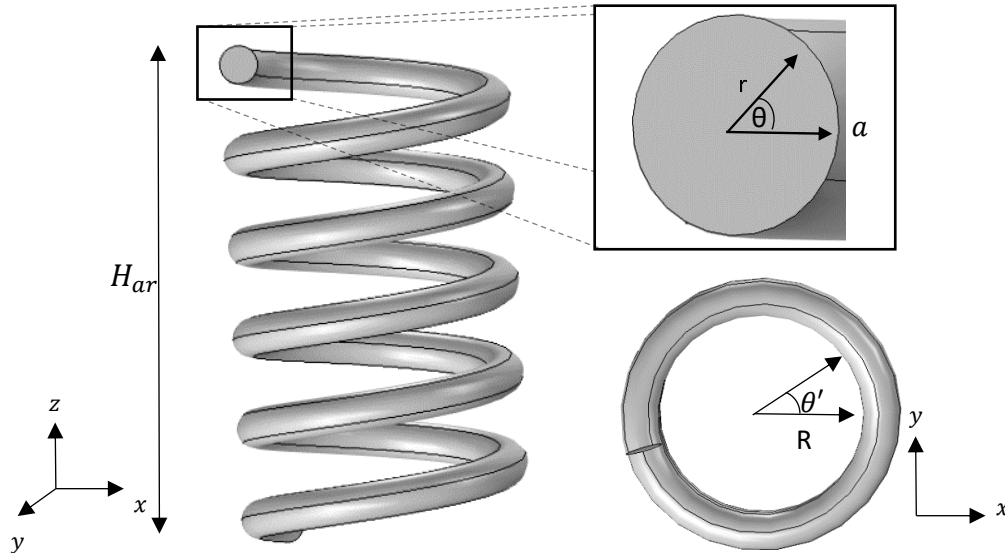


Figure 17: Diagram of sample spring with as-received height, H_{ar} . The expanded view of the wire cross-section shows radius, r , and maximum radius a . A top-down view of the helix coil is shown with coil radius R , with a small segment of angle θ' in the x - y axis.

It is important to note that the microscopic shear strain may be affected by the crystal anisotropy. That is, the grain orientation. It is shown later in Chapter 10 that the grain size is very large, and lenticular, and so it is possible that highly orientated grains may lead to anisotropic effects on internal stresses between grains, effectively inhomogenous macro plasticity. However, this is not considered in the models presented in this thesis.

4.2 Elastic deformation of springs

Spring wire carries a compressive load on the spring principally by torsion. The derivation of a stress relaxation model will thus begin for a coil spring by first considering the torque on a simple straight wire, neglecting coiling effects of pitch and winding curvature. This is the approach that Lewthwaite and Smith [77] took to describe their model, and it is reproduced here. An end displacement δ induces a torque, T , in the spring wire. This is applied around

the longitudinal axis of a cylindrical wire of radius, a and length L held in position at one end, rotated through an angle, θ at the other end. If R is the coil radius of a spring then the rotation is given by

$$\tan \theta = \frac{\delta}{R} \approx \theta \quad (4.10)$$

An elastic shear strain of $\gamma_{\theta r} = \frac{r\theta}{L}$ is induced in the wire as it twists, where r is the radial distance from the centre of the wire. The shear stress is related to the shear strain through the shear modulus G such that

$$\tau_{\theta r} = G\gamma_{\theta r} = \frac{Gr\theta}{L} \quad (4.11)$$

The torque on the wire required to generate this distribution of shear stress can be determined by summing the rotational moments due to the shear stress acting on a cross-sectional area of the wire

$$T = \int_A r\tau dA = \int_0^a 2\pi r^2 G \frac{r\theta}{L} dr = \frac{2\pi G\theta}{L} \int_0^a r^3 dr = \frac{\pi G\theta a^4}{2L} \quad (4.12)$$

We can therefore relate the applied torque to the rotation by

$$T = GJ\phi \quad (4.13)$$

where G is the shear modulus, $J = \frac{1}{2}\pi a^4$ is the second polar moment of the area of cross section, and $\phi = \frac{\theta}{L}$ is the rotation per unit length. For a spring coil of radius R and number of coils, N , the length of the wire is $L = 2\pi RN$, and therefore $\phi = \frac{\delta}{2\pi R^2 N}$.

Torque is due to the moment of the applied force, P_0 . Assuming the load acts vertically down the centre of the spring, the induced moment is

$$T = P_0 R \quad (4.14)$$

The reaction force of a spring, P_0 , can thus be described by substituting equation (4.14) into (4.12) giving

$$P_0 = \frac{1}{2R} \pi G \phi a^4 = K\delta \quad (4.15)$$

where K is the spring constant [N/m]. By rearranging:

$$K = \frac{Ga^4}{4R^3N} = \frac{P_0}{\delta} \quad (4.16)$$

demonstrating the linear dependence of the reaction force upon the displacement δ of the spring. Upon examination of the samples it is apparent that the coil spring wire has flattened ends that taper to a point on either end of the spring. It is for this reason that the idea of an 'effective' number of coils is used. The total effective number of coils, N , can be calculated by taking K from equation (4.15) and comparing it with the measured spring stiffness of 17.5 N/mm. With the given geometry of $a = 1.25$ mm and $R=8.25$ mm, and taking the room temperature shear modulus of Nimonic 90 as $G_0 = 82.5$ GPa one may calculate from equation (4.16) that the effective number of coils, $N=5.12$. From equation (4.16) it is quite clear that the reaction force is quite sensitive to the values of R and a and as such wire thickness and coil radius are clearly very important considerations in spring design for any given property.

Having discussed a simplified model assuming only a straight wire, the effect of curvature has been neglected. The effect that the curvature has on response of the spring in torsion should be investigated in order to create a reliable model that takes into account the true geometry of the sample. The following sections in this chapter will discuss the effect that winding the wire into a coil spring has on the macroscopic stress response, and the effect the plastic winding process will have on the dislocation density.

4.3 Effect of wire curvature

To create the necessary geometry for a coil spring the wire is taken and bent and twisted into a helix. This cold working of the wire induces a strain gradient across the wire cross-section. The coiling of the wire induces a radial curvature and a pitch. The effect of the radial curvature is considered first.

Thus far only a straight wire has been considered for the model as the majority of compressive force is due to torsion. For a straight wire the maximum shear strain due to torsion along the distance of the longitudinal axis of the wire, s , is calculated from equation (4.10) as $\gamma_{\theta s}^{max} = a\phi$. To take curvature into account we observe a small segment of angle θ from the coil center, as shown in the top-down image in Figure 17. The variation in the width of this

chosen arc segment from the inside edge of the wire to the outside edge relative to the mean width is $1 + \left(\frac{r}{R}\right) \cos \theta'$ [76]. Therefore the variation of the strain throughout the curved arc segment is

$$\gamma_{\theta_s}(r, \theta) = \frac{r\phi}{1 + \left(\frac{r}{R}\right) \cos \theta'} \quad (4.17)$$

By using a 1st order correction to this model in equation (4.17), one can may rewrite the maximum strain as $\gamma_{\theta_s}^{max} = \left(\frac{c}{c-1}\right) a\phi$, with $c = R/a$ as the spring index and the curvature correction factor $\frac{c}{(c-1)}$ [78]. Given the spring geometry in this thesis the value of spring index is $c = 6.6$, giving a correction factor of 1.179.

Now consider the effect of the pitch of the wire coil. This affects the radius of curvature, R by increasing it to $\frac{R}{\cos \psi}$ where $\psi = \sin^{-1}\left(\frac{h}{L}\right)$ is the pitch. The given height of the springs is $H_{ar} = 28.5$ mm so the effect of the pitch correction factor, $\frac{1}{\cos \psi} = 1.0058$. Therefore, we can conclude that the pitch has a negligible effect on the stress in the spring. It would thus be expected that the stresses within a zero-pitch toroid to be very similar to a small-pitch helical spring. Neglecting the pitch correction, but including the stress correction factor into the equation (4.13) gives

$$T = \int_0^a 2\pi r^2 G \gamma_{\theta_s} \left(1 + \left(\frac{r}{R}\right) \cos \theta\right) dr = \frac{\pi G \theta a^4}{2L} \quad (4.18)$$

where (4.18) is identical to (4.12), which would indicate that the net macroscopic effect on the reaction force of a spring in compression is a small second order effect in c , despite the stress distribution being effected by the curvature.

3.31 Shear stress for straight wire and coil spring

Along with the torsional shear stress one must account for the shear stress $\tau_{zs} = P_0 A_z$ to oppose the shear force P_0 , where A_z is the cross-sectional area of the spring wire normal to the z direction, found as $A_z = \frac{\pi a^2}{\cos \psi}$. As the pitch effect is essentially negligible the total

effective shear stress at a given point is $\tau = \sqrt{\tau_{\theta_s}^2 + \tau_{zs}^2}$. Taking the ratio of these two shear

stresses to find the contribution of the shear stress due to shear force $\left(\frac{\tau_{zs}^2}{\tau_{\theta s}^2}\right) = \left(\frac{1}{4c^2}\right) = 0.005$.

This implies that only 0.5% of the load carried by the spring is due to the shear force, while 99.5% is due to the torsion of the wire. In summary, this means that in the analytical model presented in this thesis the contribution of shear force will be deemed negligible and not included. Therefore, for this thesis the nomenclature of the shear strain and shear stress shall be $\gamma = \gamma_{\theta s}$ and $\tau = \tau_{\theta s}$ respectively.

For the multiaxial approach to stress relaxation and creep one must consider the effective creep strain ε_e and effective Von Mises stress. These are

$$\varepsilon_e = \frac{\gamma}{\sqrt{3}} \quad (4.19)$$

$$\sigma_e = \sqrt{3}\tau \quad (4.20)$$

For a displacement of 6mm this leaves an effective strain of $\varepsilon_e^{max} = 0.34\%$ for a straight wire, compared with $\varepsilon_e^{max} = 0.41\%$ for a curved spring at 6mm compression, and of $\varepsilon_e^{max} = 0.45\%$ for a straight wire at 8mm displacement, compared with $\varepsilon_e^{max} = 0.54\%$ for a coil spring under 8mm compression.

To calculate the effective stresses one must take account of the shear modulus G at a given temperature. By assuming G halves as the temperature T_m goes from room to melting one may write

$$G(T) = G_0 \left(1 - \left(T - \frac{300}{2(T_m - 300)} \right) \right) \quad (4.21)$$

Taking $T_m = 1370$ gives a good match to published data for temperatures between 600 °C and 700°C for $G(T)$ [50]. Applying this value for Nimonic 90, one obtains $\sigma_e^{max} = 382$ MPa for 6mm compression of a straight wire, compared with $\sigma_e^{max} = 449$ MPa for a curved spring. Increasing compression to 8 mm it is calculated that for a straight wire $\sigma_e^{max} = 511$ MPa and for a coil spring $\sigma_e^{max} = 602$ MPa, which is approaching the 0.1% proof stress of about 700 MPa at 600 °C. It is important to note then, that the curvature of a wire into a spring leads to high stresses even at relatively low loads, with P_0 between 90 N and 150 N for 6 mm and 8 mm displacements.

Increasing the displacement to 10 mm leads to an effective stress $\sigma_e^{max} = 752$ MPa for a coiled spring compared to a straight wire $\sigma_e^{max} = 638$ MPa, which would suggest yielding at

some points on the spring. However residual stresses in the spring wire may counteract this as no evidence of yielding has been found at this displacement on identical springs [76].

4.4 Dyson Creep Equation

One of the most important decisions to make when creating a creep rate equation is to come to a conclusion on the mechanism of creep that would be expected at the stresses and temperatures that the material will be operating at. Observing the creep deformation mode map of Nimonic 90 taken in Figure 18 shows the calculated maximum stress of $\sigma_e^{max} = 449$ MPa for 6mm compression for between 600 and 700°C clearly delineated in red, well within the particle shearing/climb regime. The 8 mm appears along the border of shear/climb and the 10 mm displacement sits well into the particle shearing regime. Both are treated here as having climb as the dominant rate-controlling mechanism as the relaxation is found to be fast, with the 10 mm case expected to drop into the climb domain relatively quickly in the areas with the highest stress (much of the stress in the material is expected to be lower than the maximum calculated, and so the creep regime will likely sit lower than predicted here). The majority of the specimen lifetime will therefore be spent in the climb-controlled regime. The creep deformation map was created by Harrison, Evans and Winstone [79]. While this is similar to an Ashby map it is based upon steady state and creep rupture data for varying stresses and temperatures. It is important to note that the Nimonic 90 in the paper underwent a different heat treatment to that in this thesis, and thus the γ' particle radius was 0.05 μm as opposed to the predicted 0.01 μm in the model here. That said, the map gives a good predictive indication of the behaviour one may expect from the Nimonic 90 springs used here.

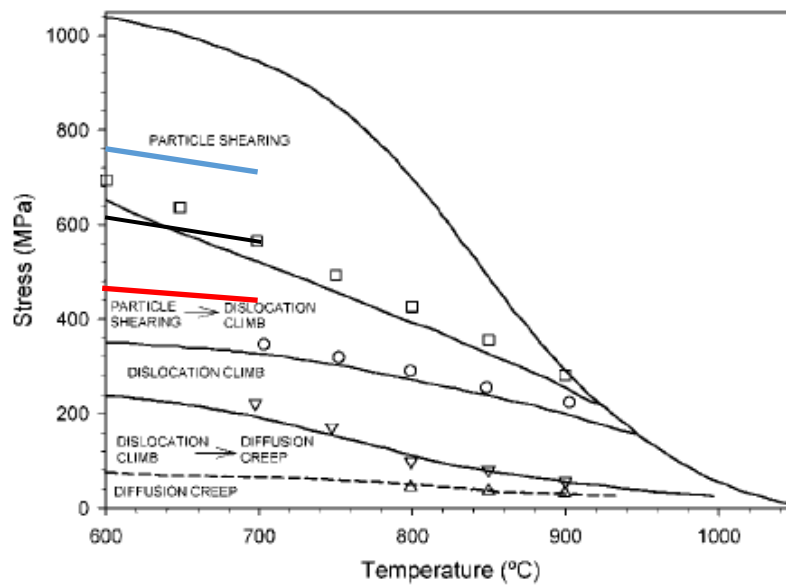


Figure 18: Creep deformation map for Nimonic 90 based upon the operating processes. The predicted maximum stress for a coil spring displaced by 6mm is labelled in red, 8 mm in black, and 10 mm in blue. [79]

As a result of expecting the creep to be dominated by dislocation climb, the Dyson creep rate equation (3.21) was chosen as a basis for the stress relaxation models in this thesis.

In summary, the curving of a straight wire into a coil induces tensile and compresses strains and thus has a significant effect on the stresses that need to be calculated for the stress relaxation model. The effect of pitch is found to be negligible and thus will not be included in models presented here. The curvature of the wire is taken into account when determining the creep mechanism in the stress and temperature regime being investigated. By comparing the operating conditions of the springs to the expected creep mechanism at the expected temperatures and stresses, it is determined that the climb and glide creep rate model proposed by Dyson [7] is suitable for the stress relaxation models proposed in this thesis.

Chapter 5: Stress relaxation test methodology

In this chapter the methods of measuring stress relaxation in coil springs to compare with F.E and analytical models are discussed. Stress relaxation tests may be performed in multiple different ways, from multiple compressions in order to observe cyclic fatigue effects on a material, to single-displacement tensile or compressive tests on bars or more complex geometries. Utilising modern computer systems and modified tensile testing equipment with a load cell, it is possible to measure the reduction in reaction force of a material in real time at elevated temperature. This is not without its challenges, however. Other, mechanically simpler tests may be performed on samples to measure the reaction force before and after a stress relaxation test, but do not give as many data points as the in-situ methods. The two main methods in this thesis are the in-situ testing of direct reaction force and the 'nut-and-bolt' method. The nut and bolt method is described below, along with the in-situ test setup and calibration.

5.1 Nut and bolt tests

One method of measuring the stress relaxation of springs is the so-called 'nut and bolt' test. This test constrains a coil spring by constraining the spring on a bolt and tightening the nut until the spring is displaced to the required height. The spring is then placed within a furnace at the required temperature. After a given time period the spring is removed and allowed to cool in air. The nut and bolt are taken off and the height of the spring is measured utilising Vernier callipers, utilising Hooke's Law to calculate the reaction force. An example of a constrained spring is given in Figure 19.



Figure 19: Photograph constrained by nut-and-bolt method, compressed by tightening the nut

With deformation of the spring due to stress relaxation, the unloaded spring is expected to permanently reduce in height. One may thus calculate the reduction in reaction force by measuring the new displacement required to reach the original compressed height at δ , known as H_c , as shown in Figure 20. By calculating the reduced difference between the post stress relaxation height, H_{pr} and the compressed height H_c and finding the ratio of this reaction force P/P_0 one may re-write equation (4.15) for the reaction force ratio as

$$\frac{P}{P_0} = \frac{H_{pr} - H_c}{(H_{ar} - H_c)} \quad (5.10)$$

Where H_{ar} is the as-received spring height.

The spring constant, K is predicted to have minimal change during the stress relaxation testing [76, 80], and as such any change may be neglected in the ratio of reaction force calculations. While this method is rather simple it does not allow for 'real-time' in-situ calculations of the reaction force, giving only single data points for any given time period, as the experiment must be ended to remove the spring from the furnace and constraints of the nut and bolt. Therefore, many springs must be used to obtain a variety of data points at different time scales, which may not give a fully accurate description of events between each

data point. For this reason, a real time in-situ tests method has also been developed. This is described in the next subsection.

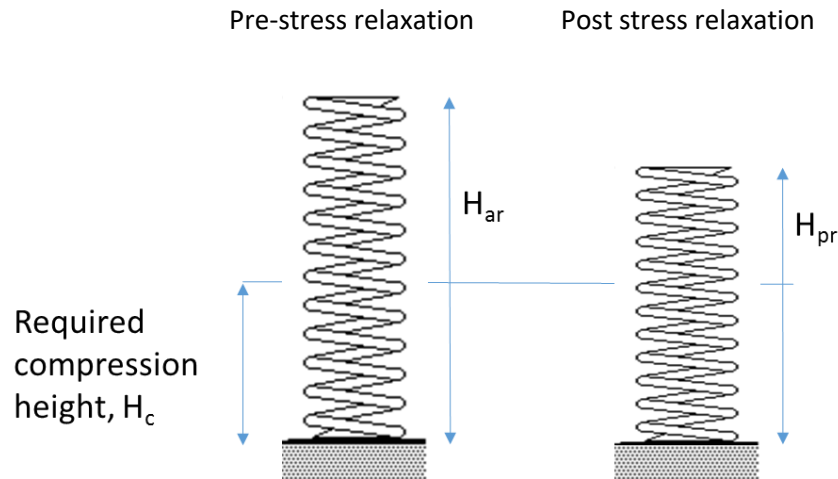


Figure 20: Left: spring prior to stress relaxation, displaced from height H_{ar} by δ to height H_c . Right: post stress relaxation with new reduced height, with smaller required displacement δ to reach H_c

5.2 In-situ testing

The in-situ testing of samples of Nimonic 90 were conducted in the hydraulic powered Mechanical Testing Machine (MTS) 810 equipped with a 100kN MTS 681 load cell as shown in Figure 21, utilising specially designed actuators to accommodate springs of the size used. A high temperature furnace was used to heat the springs to temperature and the lower actuator displaced the spring to the required distance. Three separate thermocouples were utilised to measure the temperature of the sample, the temperature at the load cell and the ambient temperature. Heat resistant wool was used to close gaps in the furnace.

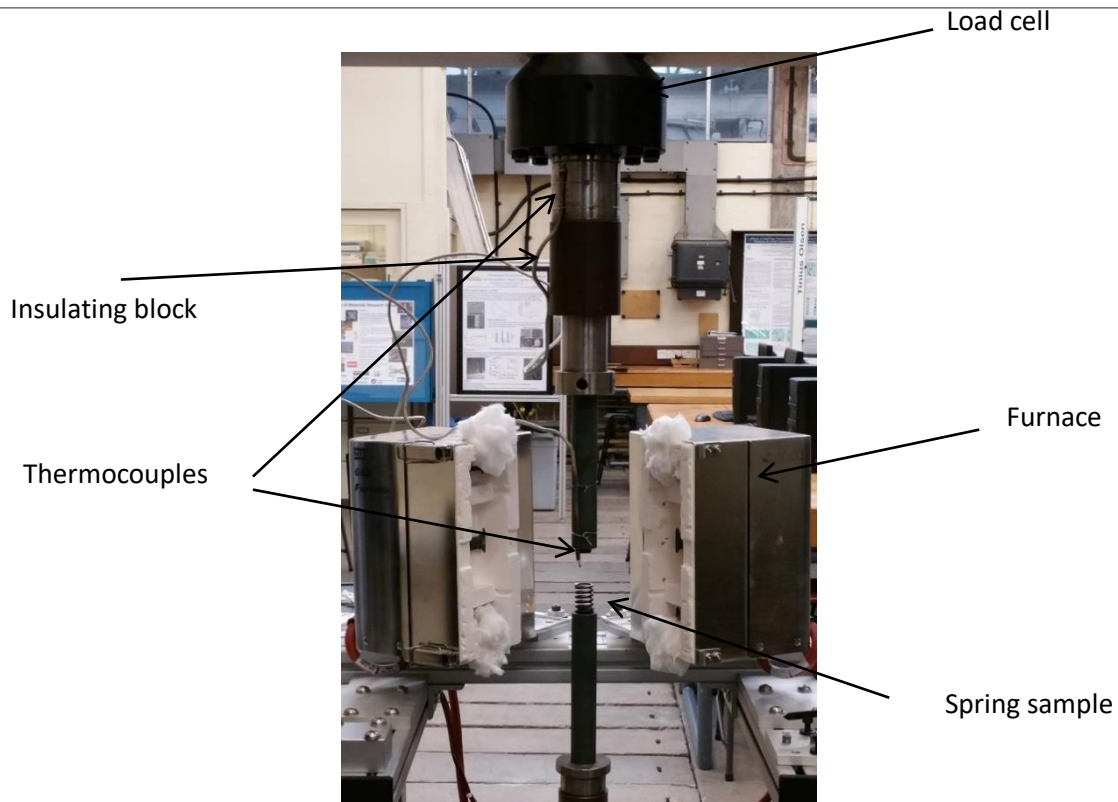


Figure 21: MTS setup in laboratory with furnace and insulating block. The spring is fit into the actuators and heated, then compressed.

The spring specimen was measured for length and the furnace heated to temperature, and held for two hours in order to stabilize. The spring was then placed in the furnace efficiently in order to avoid as much heat loss as possible.

The MTS software package was then utilised to program the sufficient dwell time at the specified temperature for the sample, and to record stress and force response from the sample via the load cell and plot in Excel, in this case it would record a value every 90 seconds. Once the testing was complete the actuators were slowly parted to allow the spring to decompress and the final spring length is measured and compared to the original length.

The load cell utilizes a strain gauge to measure the stress response of the sample as in Figure 22, the load cell is designed to measure the electrical resistance between two points on a thin conductive strip that may be physically displaced by applied tension or compression.

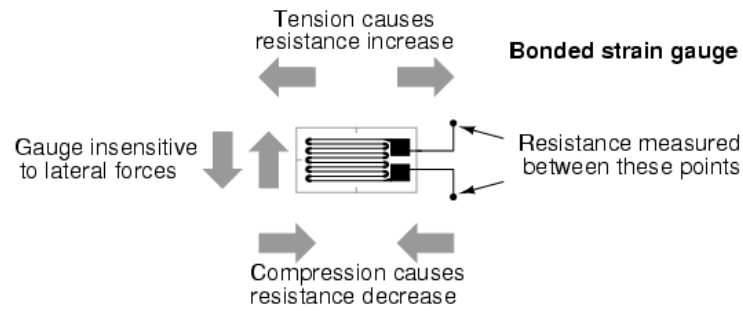


Figure 22: Diagram of a strain gauge [127]

Note the insulating block in Figure 21 installed into the top actuator, in order to reduce conduction of heat into the load cell in order to reduce the impact of temperature upon the stress readings. As the load cell is sensitive to changes in temperature, the strain gauge will expand and distort, in effect creating an addition to the errors involved in measurement. The insulating block material is a phenolic paper based laminate, with low thermal conductivity and a high T_m .

5.21 Calibration of load cell

Some issues with measurement of data were met in early testing of the MTS and so calibration of the machine and achievement of accurate results was a prime concern. This was achieved by testing a spring first for 24 hours without pre-heating the furnace.

This was followed by a series of tests for 24 hours under 10mm displacement for the spring. The data collected in the early tests proved to be unphysical and inaccurate. As a result of this an investigation into the improvements that could be implemented to the MTS and testing practice was made.

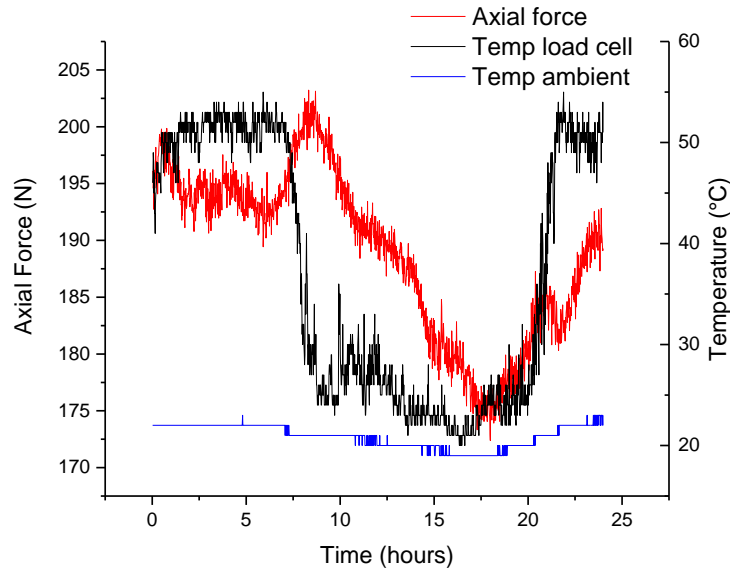


Figure 23: Data set of stress relaxation (P/P_0) of 10 mm displaced Nimonic 90 spring with temperature of load cell, test beginning at 14.00.

The temperature at the load cell was found to be very high compared to the ambient temperature, and the axial force is much higher than the expected 140N for 10mm displacement, beginning the experiment between 190 N and 200 N. This may have been due to the radiating heat from the furnace below heating up the load cell to approximately 50 °C. It is interesting to note the trend of the load cell temperature dropping rapidly approximately 7 hours into the experiment and rising again at 19 hours in Figure 23. This is believed to be due to overnight temperature reduction within the mechanical testing lab, as can be seen where the load cell temperature follows the trend of the ambient temperature, a difference of 3°C having a large effect on the load cell temperature and thus reducing the calculated reaction force by up to about 25N. It was deemed necessary to utilize a method to stabilize the temperature of the load cell to achieve more reasonable results.

Stabilisation of the load cell temperature was achieved by designing an insulation box with a Carel IR33V7HR20 PID controller attached to two 'RS 245-534' 7.5 W heating mats within, to encompass the entire load cell, shown in Figure 24.

The PID controller was set to 'reverse' mode so that if the temperature should decrease below the setpoint, it will attempt to revert to the setpoint by activating the heat mats, with a differential of 0.1 °C, that is to say, if the temperature dropped below 0.1 °C from the

setpoint, the heat mats would activate. If the temperature was for any reason on or above the setpoint, the heat mats would deactivate.

This would monitor overnight temperature drop and compensate accordingly. The box is made of sheet aluminium cut, folded and screwed together to make the net shape of height: 17 cm, length 30 cm and width 17 cm. The hole to accommodate the load cell was 14 cm in diameter. To both avoid damage to the load cell and maintain constant temperature, packing foam was used to line the box inside walls. To install and remove the insulation box it was designed as two blocks that are screwed together around the load cell.

Figure 25 shows one example of the calibration tests with set point of 25 °C. Variance is an average of <math><1\text{ }^{\circ}\text{C}</math> and the stress relaxation curve is clearly improved from the previous data in Figure 23.



Figure 24: Left: insulation box, right: implementation around load cell (shown in red)

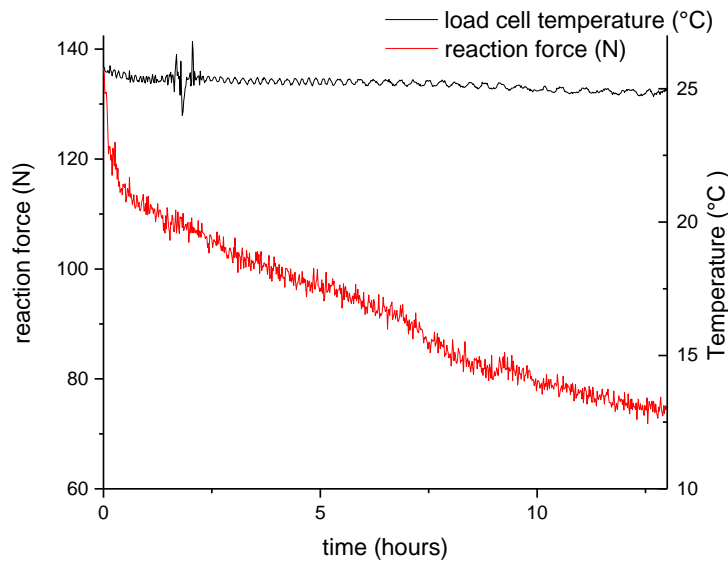


Figure 25: 10mm displacement Nimonic 90 with temperature of furnace 700°C, test beginning at 14.00 and running for 14 hours

While the in-situ experiments have the advantage of offering real-time data for the stress relaxation tests, there are drawbacks. The setup of the furnace ensured that the only way to insert a spring was to open the furnace at the desired temperature, fit the spring in to the actuators, and then close the furnace. This would lead to some lost heat, with the temperature of the furnace returning to the setpoint over the next 20-30 minutes before the spring was compressed and the experiment could begin. This could possibly have effects on the microstructure of the spring and act as a type of precipitation heat treatment, which could have moderate effects on the final results.

Due to the nature of the experimental in-situ rig setup in a laboratory with high demand for equipment, only short-term stress relaxation tests were possible. Thus high temperatures and compression were needed to ensure swift stress relaxation during this time-frame to be able to generate an observable effect to the model. For benchmarking against proposed analytical and FE models, 3 springs were compressed to 10 mm in the furnace at 700 °C and relaxed for 15 hours. The average of the data was taken, shown in Figure 26, where the value of the reaction force at the given time is $P(t)$ and the initial reaction force is P_0 . It is clear that relaxation at this temperature is very rapid, with almost instantaneous reduction to 0.7 of the

initial reaction force. This data has a good correlation with data obtained in previous published tests by the nut and bolt method up to 10 hours [76] and so is deemed acceptable.

The nut and bolt data for benchmarking is shown in Figure 27. It is important to note that these experiments were accomplished at 6mm compression at 650 °C, as this is the most likely temperature and compression in service, and is applicable to climb glide and small strain conditions assumed under the Dyson creep rate model in this thesis. This also allowed for thermomechanical treatments to be applied to the existing springs as seen in chapter 6. The results of the initial 1000 hour nut and bolt tests have good correlation with previous data [76]. It is interesting to see that there is very little change within the first 10 hours of this data, with the exception of the initial drop within the first hour. This behaviour appears to be similar to that found in the in-situ data set, albeit with a larger initial drop. Due to the large amount of stress relaxation within the first hour, the short-term in-situ testing would be suitable to calibrate the analytical and F.E models proposed in this thesis, and the longer term behaviour of the nut and bolt tests will be compared latterly once the initial drop in stress relaxation has been modelled correctly to ensure longer-term behaviour is accurate.

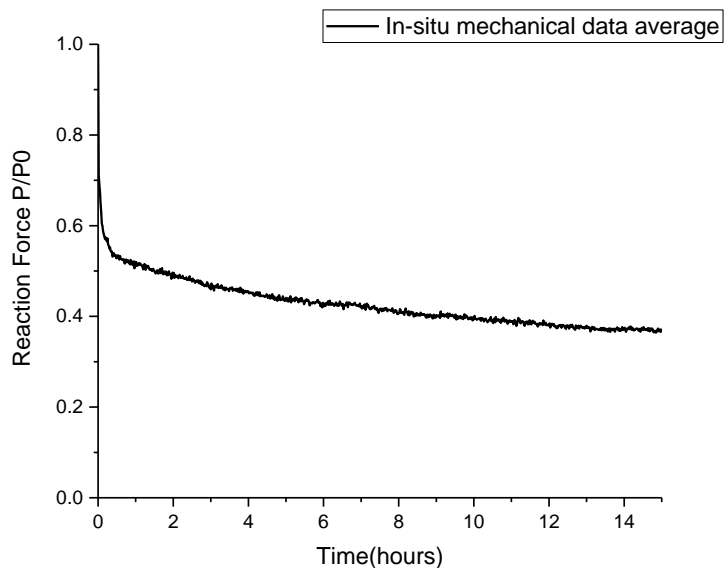


Figure 26: Average data for 3 springs compressed by 10mm and relaxed for 15 hours at 700°C

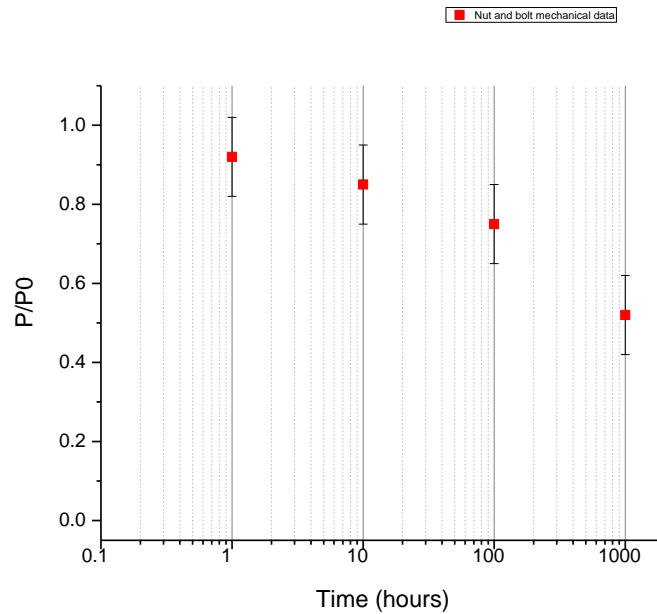


Figure 27: Nut and bolt test data for 6mm compression at 650°C for up to 1000 hours

5.3 Summary

To summarize, the two mechanical testing methodologies have been described here. The in-situ testing was found to be challenging due to the temperature changes affecting results from the load cell, and a solution was proposed by designing and implementing an insulation box with PID temperature control. The in-situ tests were considered to be suitable for short-time testing, while the nut and bolt method has been selected for longer time periods up to 1000 hours.

Chapter 6: FE modelling of stress relaxation of springs

In this chapter the FE model for the stress relaxation of a coil spring will be described. Simple FE models observing stresses in springs have been presented in the past, such as the work of Jiang et al [75] or by Mulla [81]. However, FE models such as these are designed only to determine the time-independent stress response to applied load. Designing a time-dependant stress response model sensitive to the effects of stress relaxation is thus of great worth. An unmodified version of the Dyson creep rate model is utilised by adapting the hyperbolic-sine ‘Garafalo’ creep rate model option in Comsol Multiphysics 4.4 to resemble the Dyson climb-glide creep rate model. An FE model for a full helical spring is introduced first, along with the methodology for choosing the geometry of a representative small toroidal element to increase calculation efficiency. The methodology of calculating the reaction force over time is then discussed.

6.1 FE simulation of structural deformation

In order to create the geometry of the spring the program Comsol Multiphysics 4.4 was selected. This program is a F.E analysis package capable of solving a wide variety of conventional physics-based problems. With this program the effects of stress relaxation in the nickel superalloy springs may be observed, by creating a three dimensional geometric shape, and, with suitable boundary conditions, exerting a displacement in the Z-direction, it is possible to simulate and record the Von-Mises stress distribution across the geometric shape as time progresses. Using the FE program, one may observe the evolution of both stress and strain over space and time, and the net applied force over time. FE modelling also allows one to visualise the location of stress and strain concentrations within a helical spring. In a helical spring, for example, the stress on compression is higher on the inside of the spring than at the outside, and these stress concentrations can be seen later in this chapter in Figure 30, where a coil spring with 5.12 coils and mechanical properties of room-temperature (21°C)

Nimonic 90, is compressed by 6mm in the z-direction, with the bottom coil end held using the 'fixed constraint' function, preventing movement.

The objective of the Comsol simulation is to recreate the stress relaxation conditions that are performed experimentally and compare the results. Using this method it will be possible to calibrate the model to the experimental results by comparing the data and thus determine the accuracy of the FE model. The process of creating the geometry and boundary integration are described below.

6.2 COMSOL simulation of stresses in an elastic spring

For all initial testing the acting temperature was chosen to be room temperature (21⁰C), latterly increased for comparison with analytical data. Translating the model to a three-dimensional shape adds complexity. Following the above methodology, a helical geometry is selected to mirror the coil spring shape described in section 3.2 with the necessary factors listed in Table 4

Name	Expression	Description
δ	-0.006 m	Displacement applied on spring
N	5.12	Number of effective coils
R	0.00825 m	Radius of coils of spring
a	0.00125	Wire radius
ϕ	$d/(2*\pi*R*N)$	Amount of rotation per unit length
ψ	0.0075	Pitch of coil spring

Table 4: FE full coil spring geometrical components

The number of effective coils is selected as 5.12 as discussed in section 4.2 using equation (4.16), and the displacement, δ , is selected as 0.006 m for the initial test.

A prescribed downward displacement on one face of the coil, $-\delta$, is applied to the highlighted black surface in Figure 28, whilst a 'fixed constraint' is applied to the blue surface of the cross

section of wire on the opposite end. This prevents movement of the spring coil in space and allows for compression against the applied displacement. The next important choice to make is the mesh size. For this model, tetrahedral elements were chosen, with quadratic shape functions, with a total of 83812 elements across the entire geometry.

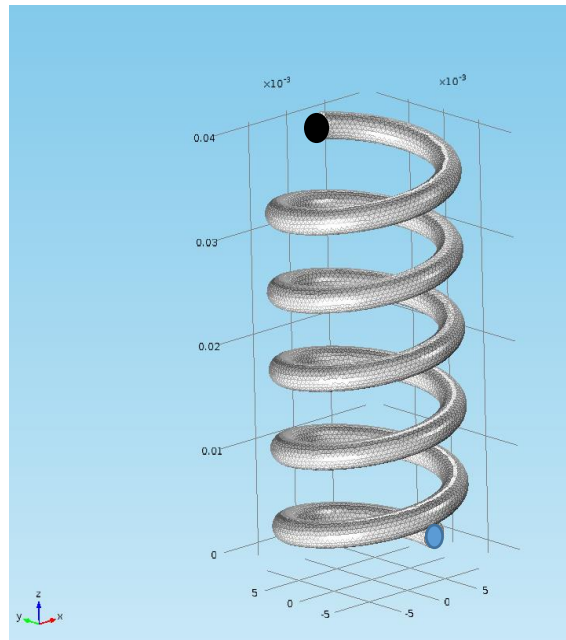


Figure 28: Application of displacement to black surface on spring geometry

6.3 Calculation of spring force in COMSOL

After setting the geometry and mesh size a stationary time-independent study is performed. Firstly the spring constant K is calculated from a reaction force against displacement plot, to compare the FE result with the measured value. In order to calculate the reaction force of a spring under vertical displacement in Comsol 4.4 the 'boundary Integration' feature is utilised. As described in (4,12) the torsion of a spring may be calculated from:

$$T = \int_A r\tau dA \quad (6.10)$$

over a cross-sectional area A . As $T = P_0R$ a value for the reaction force may be given by the FE software.

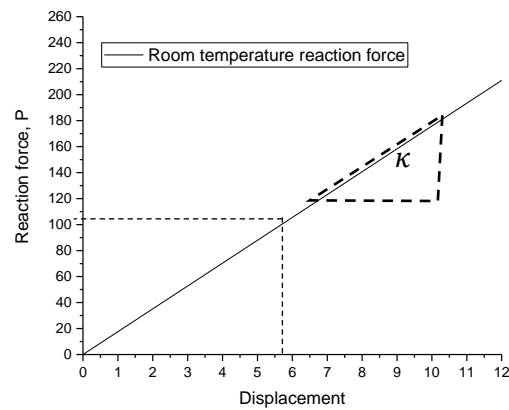


Figure 29: Reaction force at room temperature against displacement for elastic model

By performing this integration on a coil spring compressed by 6mm a value of $P_0=105.51$ N is given, along with compression between 1 and 10 mm with the corresponding reaction forces in Figure 29. The reaction force increases linearly with displacement, as expected. According to equation (4.16), the spring constant K will be the gradient of the force-displacement graph, which gives a value of $K=17.58$ N/mm. This gives a very good comparison with elastic predictions from equation (4.16) in section 4.2, where K was calculated to be 17.5N/mm using the torsional of a wire model prediction.

The stress distribution across a wire cross-section is expected to vary. The Von Mises stress distribution for a 6 mm displacement on the coil wire at room temperature is shown in Figure 30. As can be seen the stress is more intense on the inside surface of the spring, due to the curvature of the geometry. In the second figure, a close up of the cross section of the spring can be seen, where a minimum of stress can be seen in the centre, increasing with the radius. This is due to the centre of the wire displacing far less than the outside, which undergoes a greater torsional force. The stress distribution is uniform across the different coils, with no discernible change from the middle coils to the end-coils.

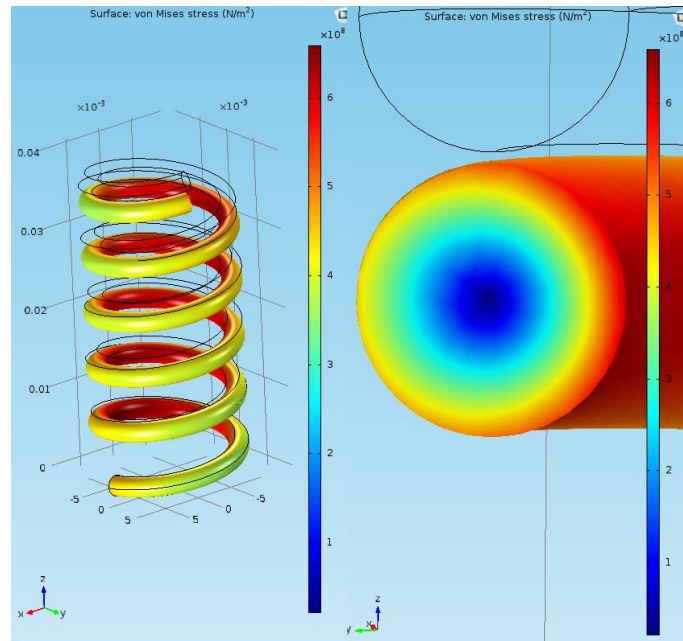


Figure 30: Distribution of Von-Mises stress in a spring under compression in Comsol 4.4, under 6mm compression. Left: distribution of Von-Mises stress across entire spring surface, right: cross section at top-end of spring.

Taking the average Von-Mises stress across the cross section of the spring wire gives a value of 342 MPa, while the inside surface average is 472 MPa. As the expected maximum effective stress from section 4.3 is $\sigma_e^{max} = 449\text{MPa}$, this is not an entirely unreasonable value for a 6 mm compression.

6.4 FE stress relaxation model for a helical spring

By examination and in accordance with model predictions the stress distribution along the length of the coil spring wire is approximately uniform as expected. Therefore, in order to simplify the FE model and to reduce computation time a simpler geometry was chosen for the creep model, as creep simulation is much more computationally intensive.

Following the example given by Watanabe [82] and Gill [76] whereby the full coil spring is not considered, instead a toroid geometry is created by drawing a helix in Comsol with pitch of 0.0075, all parameters given below in Table 5

Name	Expression	Description
Delta	-0.006 m	Displacement applied on spring
N	0.02	Number of effective coils
R	0.00825 m	Radius of coils of spring
a	0.00125	Wire radius
d	Delta*N/5.12	Effective displacement
Pitch	0.0075	Pitch of coil spring
Phi	$d/(2*\pi*R*R*N)$	Amount of rotation per unit length
T	973	Temperature [K]
L	$2*\pi*N*R$	Length of Sample
Sigma	d/L	Pitch rotation of sample
Theta	$2*\pi*N$	Segment angle
G0(T)	$(83590000000)*(1-((T-300)/(2*(1643-300))))$	Temperature-dependant Shear Modulus
E(T)	$E0*(1-(T-273)/(1643-300)/2)$	Temperature-dependant Elastic Modulus

Table 5: Geometrical components of spring coil toroid segment

A section of the toroid is isolated along the new parameter: segment angle $\theta = 2\pi N$. For the x-axis this is $R\cos\theta$ and for the y-axis this is $R\sin\theta$. The new parameter 'Sigma' is also added, which is the pitch rotation of the sample, i.e. the change in pitch that occurs when the spring is compressed. A small coil section is created, with the number of coils $N = 0.02$, giving 2% of a full coil. The resulting geometry is shown in Figure 31.

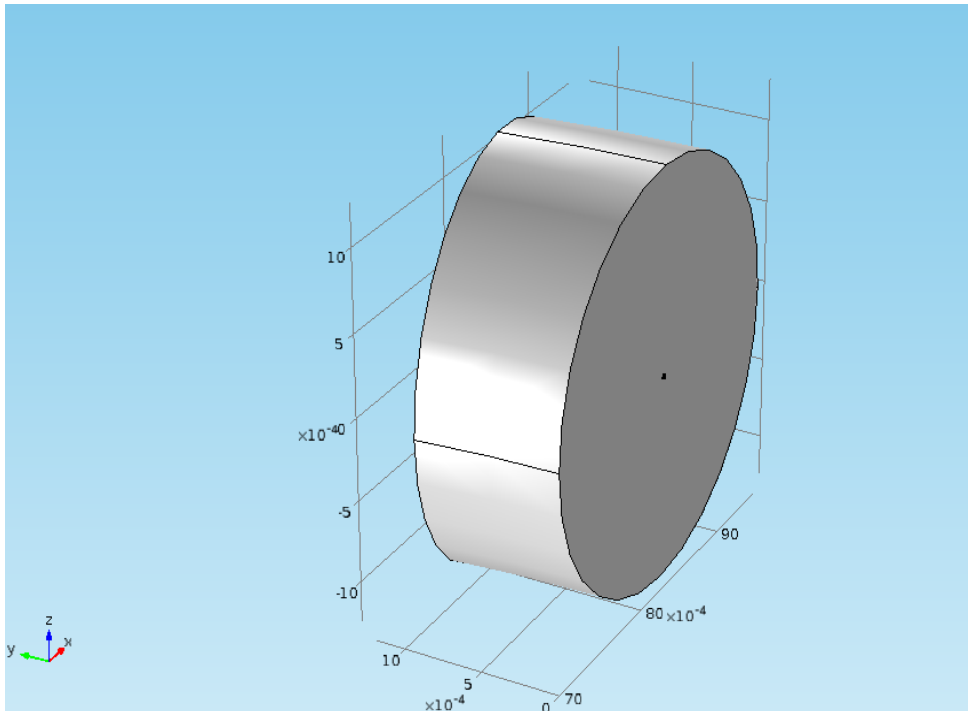


Figure 31: Toroidal section used for F.E analysis

The boundary conditions must be applied carefully to avoid end effects in such a small sample. They are applied to both cross sectional areas of the toroid using the 'rigid connector' function in Comsol 4.4, which keeps the ends planar but allows them to displace and rotate

The axis of rotation is asymmetrical as although the pitch of a basic toroid would be 0, the model is to be replicating a spring with one end held rigidly and the other being displaced in the $-z$ direction. Therefore, the cross sectional area facing the $+y$ direction has a prescribed displacement of $(-d/2)$ in the Z direction, axis of rotation of $\cos(\theta)$ in the x direction and $\sin(\theta)$ in the y -direction, 0 in the z -direction. The angle of rotation of the pitch angle is $-\text{Sigma}$.

The cross-sectional area facing the $-y$ direction has a prescribed displacement of $(+d/2)$ in the z -direction and the axis of rotation is (1) in the x -direction, 0 in the y -direction and 0 in the z -direction. The pitch angle of rotation is $-\text{Sigma}$.

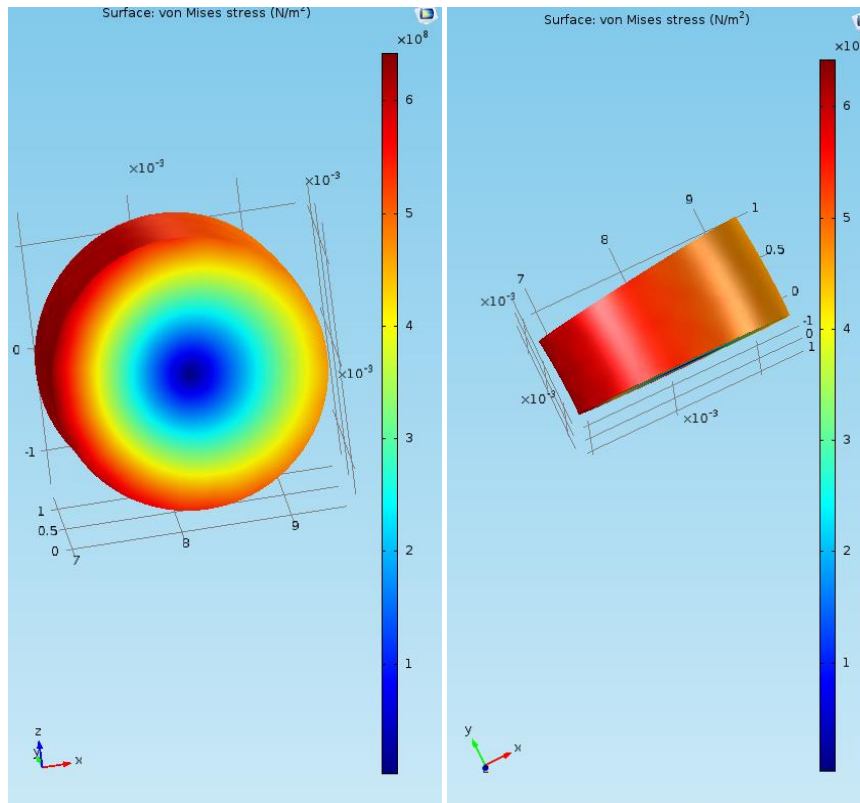


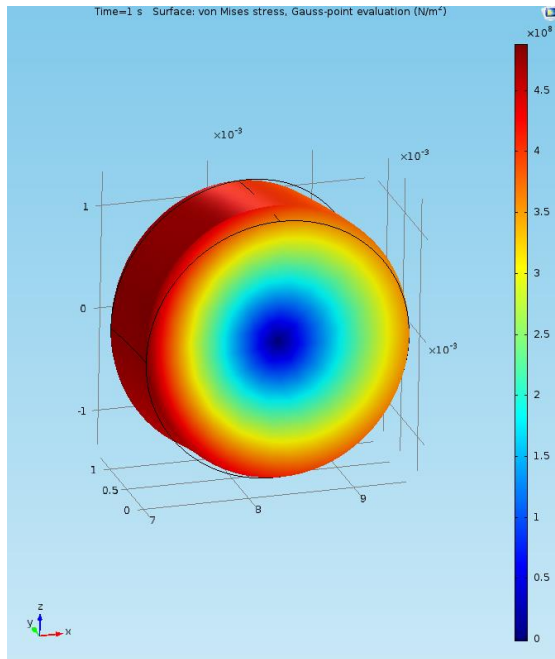
Figure 32: Toroidal segment under 6mm displacement von Mises stress distribution. Left: cross section surface of spring wire, right: top-down image of surface of spring wire

Under a 6mm displacement an instantaneous stationary study for Nimonic 90 gives the stress distribution in Figure 32 with the average on the cross sectional surface equal to $\sigma_{average} = 360.46$ MPa which matches the full helical spring calculation well. The reaction force $P_0 = 114.2$ N is close to the full helical calculation, with a difference of approximately 7 N. The difference is due to the higher mesh resolution that is possible when considered a small section rather than a whole spring.

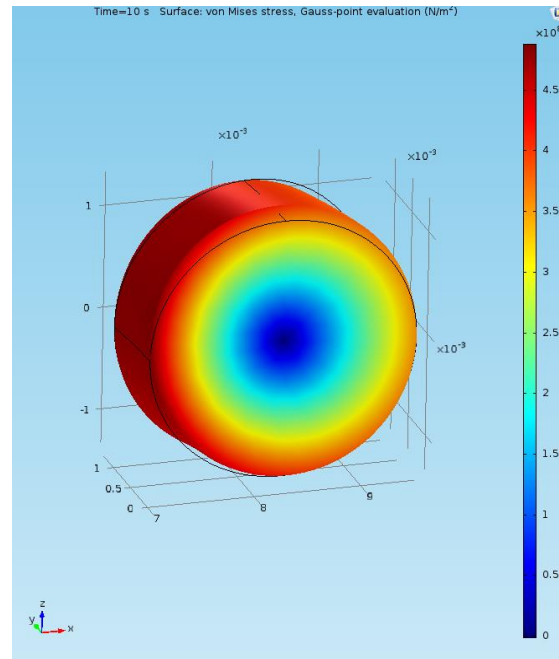
It is useful to be able to calculate instantaneous stresses under load, to be able to calculate stress relaxation of the spring over a prolonged period under load gives insight into behaviour in service and so is investigated. Extending the instantaneous study to a time-dependant study for Nimonic 90 at 600 °C and 6mm compression is implemented by using the creep function in the solid mechanics module and selecting the Garofalo hyperbolic sine function. The Garofalo creep rate model is used

$$\dot{\epsilon} = A \left[\sinh \left(\frac{\sigma_{eff}}{\sigma_{ref}} \right) \right]^n \left[\frac{3S}{2\sigma_{eff}} \right] \quad (6.11)$$

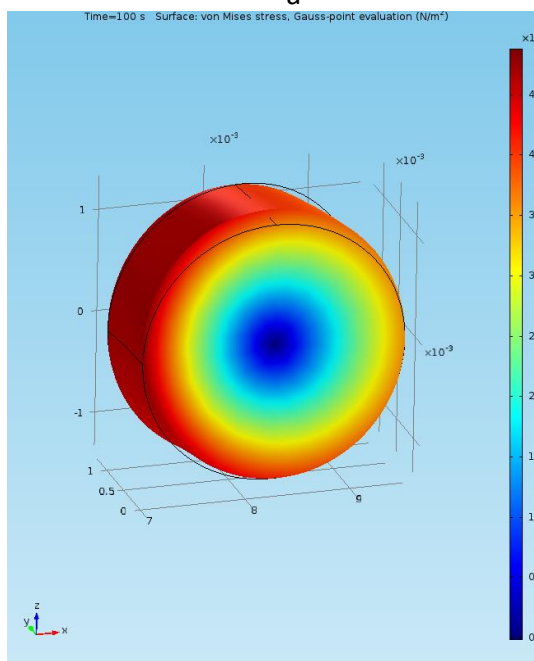
where $[s]$ is the deviatoric stress and $A = \frac{\phi_p \rho^n}{\bar{M}} (1 - \phi_p) D_s$. To fit the Dyson model (3.21) the reference stress is $\sigma_{ref} = \frac{1}{\alpha}$ and the power parameter $n = 1$. The pre-factor A defines the timescale, which may be chosen to fit the observed timescales of minutes/hours rather than weeks/months. The stationary reaction force is calculated and then the time-dependant study is computed for 10^6 seconds. Figure 33 illustrates the evolution of the effective Von Mises stress across the spring segment during the stress relaxation process.



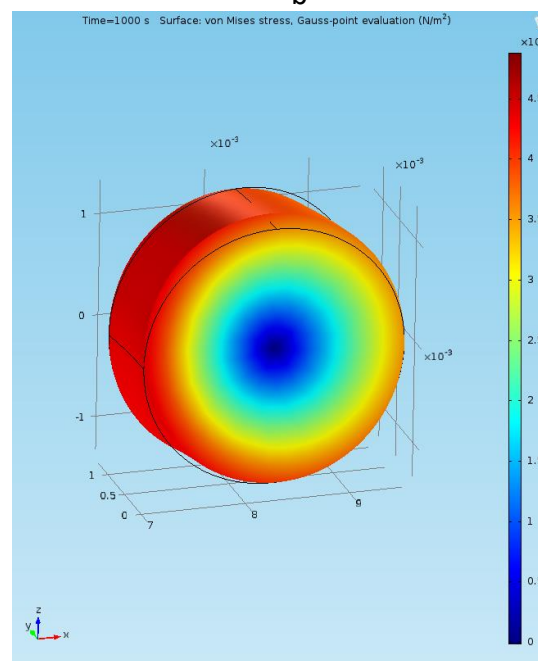
a



b



c



d

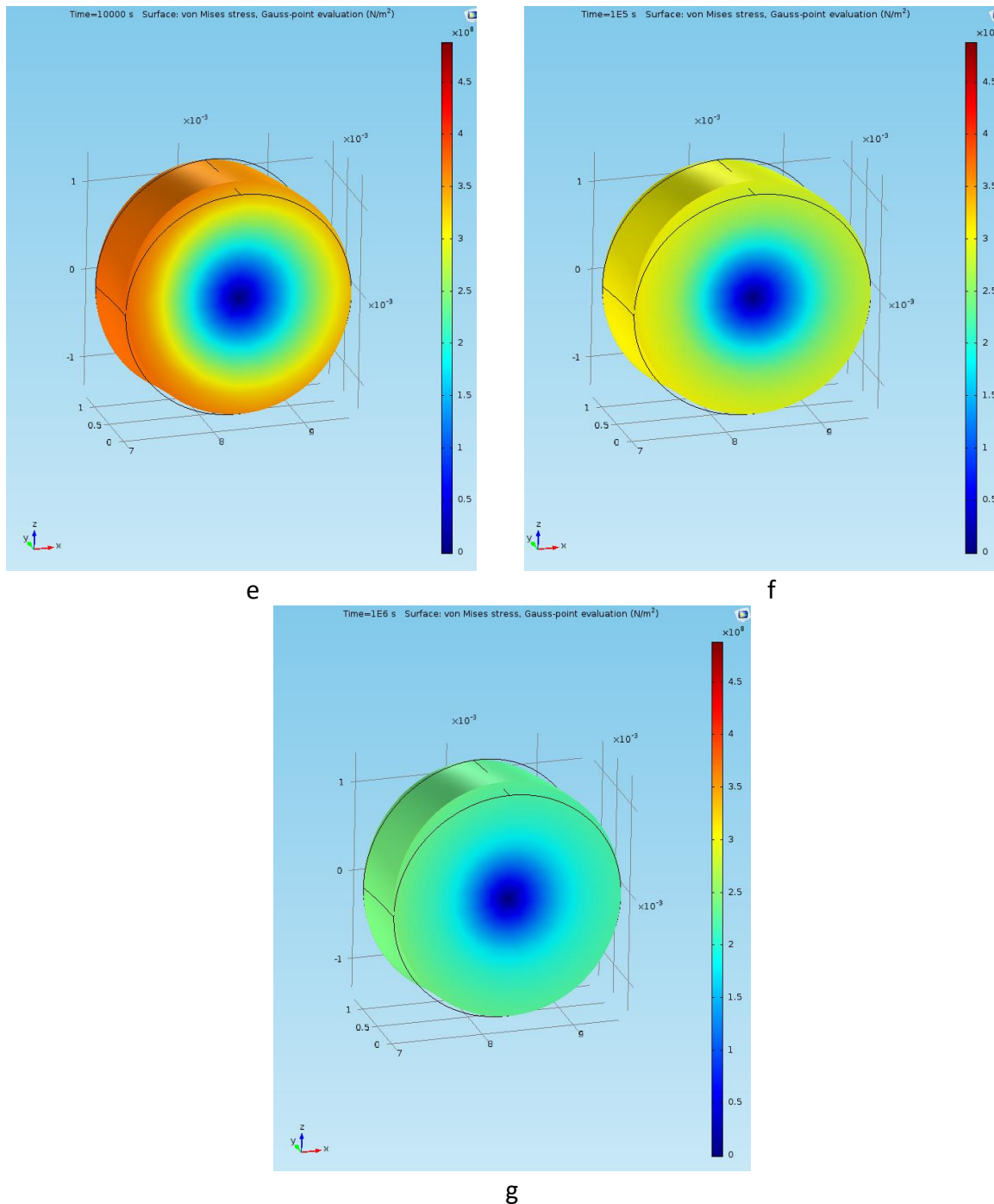


Figure 33: Stress relaxation for 6mm compression at 600°C for a) 1, b) 10, c) 100, d) 1000, e) 10000, f) 10^5 and g) 10^6 seconds

Note the wire frame represents the original position of the coil segment, as can be seen there has been displacement over time as a result of the initial elastic deformation and then the stress relaxation phenomena. The average stress of the wire has been reduced from $\sigma_{average} = 360.5$ MPa to $\sigma_{average} = 109.6$ MPa. The stress distribution appears far more uniform, with the majority of the cross-section of the spring wire approaching the new, lower,

maximum stress $\sigma_{max} = 120$ MPa, implying that the stress relaxation incurred during the test begins at the surface of the wire and over time moves toward the centre of the spring. The calculated stress relaxation curve for this case is shown in Figure 34. Mirroring the Von Mises stress calculations in Figure 33, there is little change in the reaction force within the first 1000 seconds of relaxation, but significant drops in $\frac{P(t)}{P_0}$ can be seen at the later time periods. Comparing the stress relaxation curves of the FE and analytical models with mechanical test data is accomplished in chapter 8.

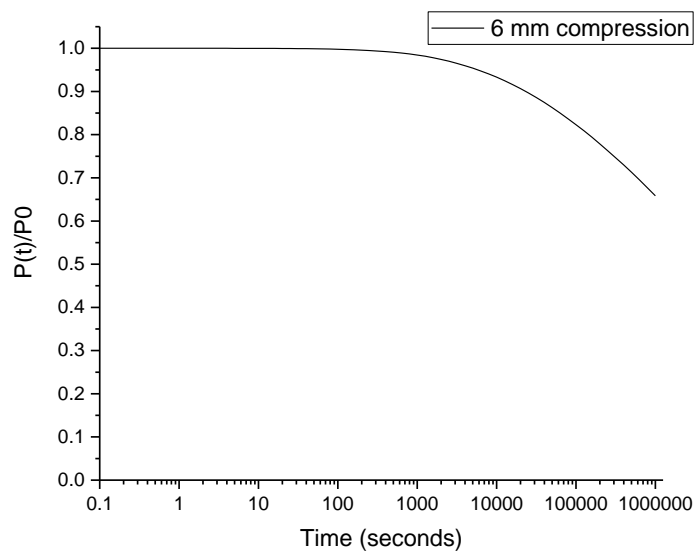


Figure 34: $P(t)/P_0$ for COMSOL model of toroid for 6mm compression at 600 °C.

6.5 Summary

Two FE models have been developed, demonstrating the method of preserving the correct end conditions whilst reducing the geometry from a full helix to a small toroidal segment. This was shown to give similar values for the calculated stresses, and allows for improved calculation speed. The Dyson creep rate model selected for the F.E model is a modified Garafalo model which is shown to reduce the stress from the outside surface of the spring towards the centre over time. After 10^6 seconds of relaxation for a 6mm displacement at 600 °C, the spring is shown to have a reduced, more uniform Von Mises stress distribution. More complex versions of this model will be developed and used later in the thesis, including the back-stress hardening. In the next chapter, an analytical model of the stress relaxation discussed here is developed to gain more fundamental insight into the process.

Chapter 7: Analytical models of stress relaxation in coil springs

In this chapter an analytical solution for the stress relaxation simulated in the previous chapter is presented based upon inserting a creep rate equation into a torsional model. This model then has improvements made to make it more physical based upon observations from the FE simulation.

7.1 Polylogarithmic analytical model

Beginning with the exact solution proposed in chapter 4, equation (4.15) is reproduced here

$$P_0 = \frac{1}{2R} \pi G \phi a^4 \quad (7.10)$$

As a result of expecting the creep to be dominated by dislocation climb, the Dyson creep rate equation (3.21) was chosen. Described first in Chapter 3, the Dyson creep rate equation can be written simply as

$$\dot{\varepsilon} = A \sinh(\sigma \alpha) \quad (7.11)$$

where $A = \frac{f \rho \eta}{M} (1 - f) D_s$, $\alpha = \left(\frac{b^2 \eta r_p}{MKT} \right)$ and $\eta = 1.6 \left[\left(\frac{\pi}{4f} \right)^{\frac{1}{2}} - 1 \right]$ is the particle size to spacing ratio. The shear stresses and shear strains replace the regular stress and strain utilising the relations $\varepsilon_e = \frac{\gamma}{\sqrt{3}}$ and $\sigma_e = \sqrt{3}\tau$, in order to be applied to the torsional case of a coil spring giving the creep shear strain rate in terms of the local shear stress as

$$\dot{\gamma}_c = \sqrt{3} A \sinh(\sqrt{3}\tau \alpha) \quad (7.12)$$

For this model the assumption of Atkinson and Gill (2012) [83] is used for A , where $A = \frac{\rho}{M} (1 + \eta)(1 - f)$. This allows for glide and climb in the model, taking account of the expected large amount of strain incurred during small time periods after load has been applied, during which dislocations would be predicted to glide from their positions to precipitates and other obstacles in order to become pinned.

First we begin by taking the total shear strain as the sum of both the elastic and creep strain total $\gamma_{total} = \gamma_e + \gamma_c$ and assuming that the shear stress $\tau = G\gamma_e$, where γ_e is the elastic shear strain and γ_c is the permanent creep shear strain, such that (7.12) becomes

$$\frac{d\gamma_c}{dt} = \sqrt{3}A \sinh[\sqrt{3}\alpha G(gr\phi - \gamma_c)] \quad (7.13)$$

where $\gamma_{total} = gr\phi$, as described in equation (4.17), is the total effective shear strain taking the wire radius, twist and geometrical factor contributing to curvature $g = \frac{1}{1 + (\frac{r}{R})\cos\theta}$ into account. Making the assumption that $\sinh x \approx \frac{1}{2}[e^x - 1]$ for $x \gg 1$, one may rewrite (7.13) as

$$\frac{d\gamma_c}{dt} = \frac{1}{2}A_0[\exp(\beta(gr\phi - \gamma_c)) - 1] \quad (7.14)$$

where the constants $A_0 = \frac{\rho_0}{M}(1 + \eta)(1 - f)$, where ρ_0 is the initial dislocation density and $\beta = \sqrt{3}Gb^2\eta r_p / (MK_B T) = \sqrt{3}G\alpha$. By integrating (7.14) one obtains:

$$\gamma_c(r, t) = gr\phi + \frac{1}{\beta} \ln \left[1 - \exp\left(-\frac{1}{2}A_0\beta t\right) (1 - \exp(-\beta gr\phi)) \right] \quad (7.15)$$

By taking this equation for the creep rate at given time, t , one may insert (7.15) into the simple torsional model equation (4.12) and then dividing by P_0 described in equation (4.16) to achieve the ratio of relaxation at a given time $P(t)/P_0$

$$T = P(t)R = G \int_0^{2\pi} \int_0^a r^2 (gr\phi - \gamma_c(r, t)) \left(1 + \frac{r}{R}\cos\theta\right) dr d\theta \quad (7.16)$$

$$\frac{P(t)}{P_0} = -\frac{2}{\beta\pi\phi\alpha^4} G \int_0^{2\pi} \int_0^a \frac{r^2}{g} \ln \left[1 - \exp\left(-\frac{1}{2}A_0\beta t\right) (1 - \exp(-\beta gr\phi)) \right] dr d\theta \quad (7.17)$$

By assuming the value of the geometrical factor g has a negligible effect and setting it to $g = 1$, one may solve the integral in equation (7.17), which gives an unwieldy sum of polylogarithmic functions as the solution. To first order this can be approximated as

$$\frac{P(t)}{P_0} \approx -\frac{4}{3h} \ln(1 - y) \quad (7.18)$$

where $h = \beta\alpha\phi$ is a group of dimensionless constants, and $y = \exp\left(-\left(\frac{1}{2}\right)A_0\beta t\right)$.

By examining the behaviour of equation (7.18) it becomes apparent that it is not suitable for short time periods as $P \rightarrow \infty$ as $t \rightarrow 0$. Assuming $A_0\beta t \ll 1$ allows further simplification to

$$\frac{P(t)}{P_0} \approx -\frac{4}{3h} \left[\ln(t) + \ln\left(\frac{1}{2}A_0\beta\right) \right] \quad (7.19)$$

which is a straight line on a $\frac{P}{P_0}$ vs $\ln(t)$ plot. Given the range of assumptions taken in deriving this expression it is predicted to only be applicable in the case of $0.3 < (P/P_0) < 0.7$. Therefore, one may expect the stress relaxation data from this model to appear as in the sketch in Figure 35. The sketch shows the expected range of values for $\frac{P}{P_0}$ where the polylogarithmic model would be expected to coincide with real stress relaxation data on a $\log t$ graph. The advantage of (7.19) is that it allows for the creep parameters A and β to be interpreted directly from the slope and intercept of the fit to the linear section of the stress relaxation plot.

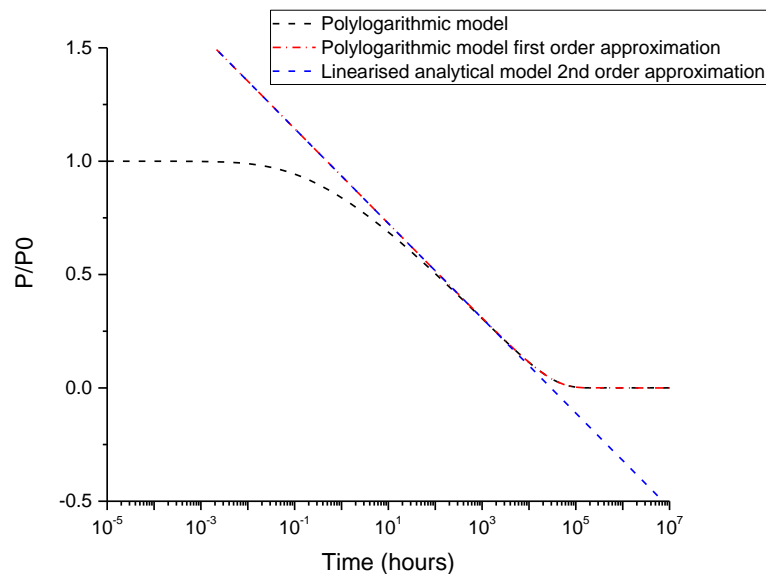


Figure 35: Sketch of linearised analytical model of (7.19) (dashed blue line) against a sketch of a full solution of the stress relaxation curve of (7.17) (black line) and first order approximation (7.18) (red line).

7.2 A simplified physical model

The linearized analytical model in equation (7.19) was derived using a number of simplifying assumptions. These mean that the model is valid only in a certain time range, i.e. it does not have the correct asymptotics as $t \rightarrow 0$ or as $t \rightarrow \infty$. This is problematic as stress relaxation at higher temperatures can be swift, and have large effects even at very small values of t . In order to solve this issue another approach is taken to derive P/P_0 . Observations from the Comsol FE simulations suggest that the strain field across the spring wire cross section may be approximated by a simplified form. To do this, a new radial parameter, b , is introduced. This represents the expanding size of the plastic creep zone over time during creep.

Under torsion and over time at high temperature creep will occur within a wire. The wire cross section will experience elastic deformation only at first, which will change to a plastic creep zone over time. The plastic zone will begin at the area of highest stress, which is in this case the outside surface of the wire. Over time, the elastic zone will shrink as the plastic creep zone grows towards the centre of the wire. A sketch of the process is shown in Figure 36.

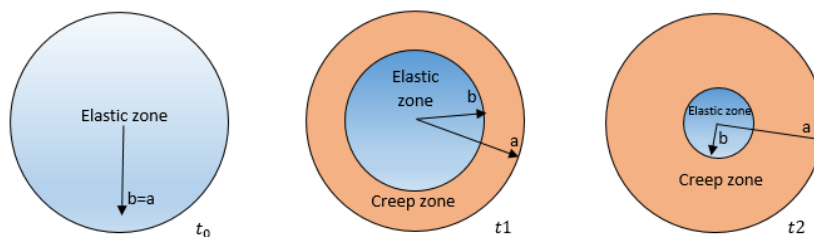


Figure 36: Wire cross section under torsion at 3 separate times, t_0 , t_1 , t_2 , as t increases the creep zone becomes larger and the radius of elastic zone, b , becomes smaller.

As t increases the elastic creep reaches a maximum at b . As b reduces over time this will reduce the overall elastic strain while increasing the creep strain as $\gamma_{total} = \gamma_{elastic} + \gamma_{creep}$, as shown schematically in Figure 37.

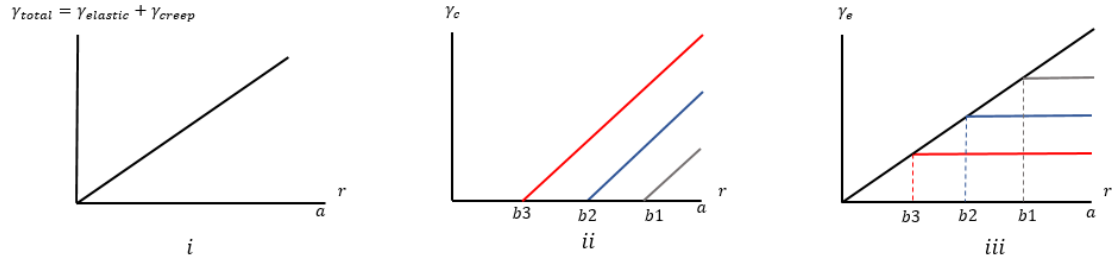


Figure 37: Sketch of elastic and plastic creep radii; showing *i*) a linear graph of total strain with δt . *ii*) the radius, b_1, b_2, b_3 , at which the plastic creep zone begins, where b reduces with δt and *iii*) demonstrates the maximum elastic strain boundary at each b value

As before, we have

$$PR = 2\pi \int_0^a G(\gamma_{total} - \gamma_c)r^2 dr. \quad (7.20)$$

As $\gamma_{total} = r\phi$, the maximum value for $\gamma_e^{max} = b\phi$ for any given t is shown in Figure 38.

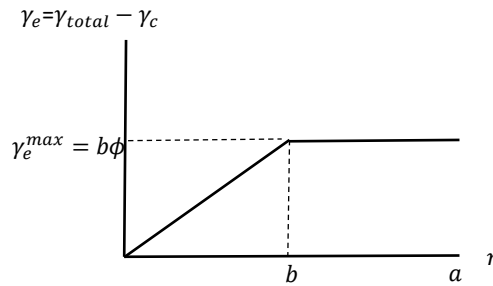


Figure 38: Diagram of maximum elastic strain $\gamma_e^{max} = b\phi$ at given b and t . Between $r = 0$ and b the value of γ_e is assumed to increase linearly, saturating at maximum value of $b\phi$.

Therefore

$$PR = 2\pi G \left[\int_0^b r\phi r^2 dr + \int_b^a b\phi r^2 dr \right] \quad (7.21)$$

which gives

$$P = \frac{1}{6R} \pi G \phi b (4a^3 - b^3). \quad (7.22)$$

or

$$\frac{P(t)}{P_0} = \frac{1}{3} \left(\frac{4b(t)}{a} - \frac{b(t)^4}{a^4} \right) \quad (7.23)$$

which reduces as $b(t)$ decreases from $b(0) = a$ over time. Now we must define b in terms of t in order to calculate the stress relaxation.

As $\gamma_e = \tau/G$ then $\tau = Gb\phi$. As $\gamma_{total} = \gamma_c + \gamma_e$, and the rate of change of γ_{total} is zero for a fixed displacement, δ , it is clear that $\dot{\gamma}_c = -\dot{\gamma}_e = -\dot{b}\phi$. Inserting this into the Dyson Model leads to

$$\dot{\gamma}_c = A \sinh(\alpha G b \phi) = -\dot{\gamma}_e \quad (7.24)$$

therefore,

$$\frac{db}{dt} = \frac{-A \sinh(\alpha G b \phi)}{\phi} \quad (7.25)$$

Solving using Maple 18, a mathematical software package, gives

$$b(t) = \frac{1}{\beta} \left[\frac{(1 + f(t))}{(1 - f(t))} \right] \quad (7.26)$$

where,

$$f(t) = \exp \left[\frac{-A\beta t}{\phi} + \ln \left(\frac{\exp(\beta a) - 1}{\exp(\beta a) + 1} \right) \right] \quad (7.27)$$

and $\beta = \alpha G \phi$.

Comparing the two analytical models, equations (7.23) and (7.19) for a 10 mm compression at 700 °C for approximated values of $A = 4.14 \times 10^{-10} \text{ s}^{-1}$ and $\alpha = 4.72 \times 10^{-8} \text{ m}^2 \text{ N}^{-1}$ gives the stress relaxation curve in Figure 39. As can be seen the values between the two analytical models are nearly identical between 1 and 10 hours, and so the effect of adding b has appeared to have negligible results on the stress relaxation compared to the previous model. However, the new model now includes the correct asymptotic as $t \rightarrow 0$.

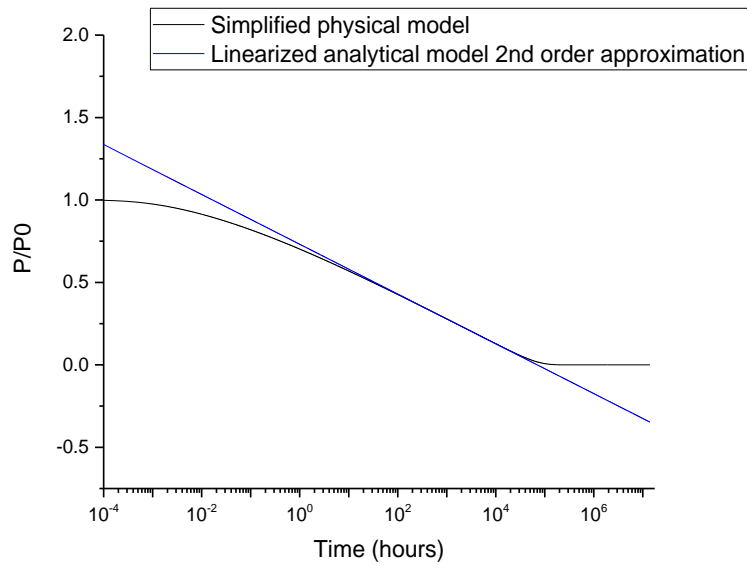


Figure 39: Simple physical model with dynamic creep radius parameter $b(t)$ and linearized analytical model for 10 mm displacement at 700 °C

7.3 Summary

A full analytical model for stress relaxation based upon inserting the Dyson creep rate equation into a torsional model for reaction force of coil springs has been developed, assuming glide-climb creep rate mechanism, taking into account physical mechanics of dislocation density, γ' volume fraction and particle radius, and assuming small strain and therefore neglecting damage. The exact solution is an unwieldy sum of polylogarithmic functions. This solution is linearised through a number of assumptions. Although the short and long time asymptotics of this solution are incorrect, it predicts a linear regime in the middle of the force vs $\log(\text{time})$ stress relaxation plot. This is useful as the slope and intercept of this regime can be used to infer the creep parameters of the Dyson model. Observations of the evolution of the creep strain field during stress relaxation have led to the proposal of a simple analytical model with the correct asymptotics. This models the creep zone growing from the outside radius to the centre of the spring wire over time. This model, along with the Comsol FE simulation, are compared with mechanical test data in the next chapter and calibrated accordingly.

Chapter 8: Calibration of stress relaxation models for a coil spring

In this chapter the stress relaxation response of a Nimonic 90 coil spring is investigated. This is initially achieved using short term in-situ measurements to calibrate the FE and analytical models discussed in Chapter 5. Then nut and bolt stress relaxation test results are used to confirm the model validity at longer times. Calibration of the model includes investigating the effect of particle coarsening, a calculation of the GND density through analytical and FE models, and the introduction of back-stress hardening to the analytical model and FE model. This is done through the introduction of a back-stress hardening parameter, H , which represents the transfer of load from the γ matrix to γ' precipitates through dislocation build-up on the particles due to glide. This reduces the effective stress in the sample, and thus can be used to model the reduction in creep rate from primary to secondary creep. In order to model the back-stress more simply, a simple finite difference analytical model is then proposed in order to accommodate the back-stress hardening differential equation.

8.1 Model predictions against results

For the calibration of the FE and simple physical models, a short-term stress relaxation test was performed in-situ according to the method in section 5.2, with a spring compression of 10 mm at 700 °C. Three springs were tested and the average values for reaction force were measured. The furnace was heated to 700 °C prior to the springs being placed within, and took approximately 15 minutes to stabilise to 700 °C due to heat loss from opening and placing in the springs. The springs were heat treated as according to Table 3 before being placed in the furnace. The FE and analytical models utilised the initial values according to [76] for the hyperbolic sine creep rate equation. Note Table 6 is split into two sections: those parameters that were kept constant and unadjusted, and those that were manipulated to fit the experimental data

Parameters Kept Constant		
Parameter	Value	Description
δ	0.01 m	Displacement applied on spring
N	5.21	Spring coil
N_{eff}	0.02	Number of effective coils in FE segment
R	0.00825 m	Radius of coils of spring
a	0.00125 m	Wire radius
d	$\delta * \left(\frac{N_{eff}}{N}\right)$	Effective displacement
ψ	0.0075	Pitch of coil spring
ϕ	$\frac{d}{2 * \pi * R * R * N_{eff}}$	Amount of rotation per unit length
T	973 K	Temperature [K]
L	$2 * \pi * N_{eff} * R$	Length of Sample
β	d/L	Bending rotation of sample
θ	$2 * \pi * N_{eff}$	Segment angle for FE geometry
$G_0(T)$	$(8.359 \times 10^{10}) * \left(1 - \left(\frac{T - 300}{2 * (1643 - 300)}\right)\right)$	Temperature-dependant Shear Modulus
$E(T)$	$E_0 * \left(1 - \left(2 * \frac{T - 273}{1643 - 300}\right)\right)$	Temperature-dependant Elastic Modulus
$D_s(T)$	$D_s = \left(10^{-4}\right) * \left(\exp\left(\left(\frac{-3.2 * (10^5)}{(8.3144) * T}\right)\right)\right) = 6.62 \times 10^{-22}$	Constant of self-diffusivity
C_0	0.057	Combined molar concentration of γ' forming elements (Al and Ti)
ϕ	$2.74 = \frac{d}{(2 * \pi * R * R * N_{eff})}$	Amount of rotation per unit length
$f(T)$	$\frac{C_0 - C_e}{0.23 - C_e} = 0.225$	Volume fraction of γ'
b	0.25 nm	Burgers vector
$C_e(T)$	$17 \exp\left(-\frac{7250}{T_{heat}}\right) = 0.00987$	Combined equilibrium matrix concentration
Parameters and derived values used to Calibrate Model		
ρ_0	$0.3 \times 10^{10} \text{ m}^{-2}$	Initial dislocation density
r_p	12.5 nm	Particle radius
η	1.4645	Particle spacing to radius ratio
α Analytical	$\alpha = \left(\sqrt{3} * b^2 * \eta * \frac{r_p}{K_b * T}\right) = 3.92 \times 10^{-8}$	Sinh term constant α
α F.E	$\alpha = \left(b^2 * \eta * \frac{r_p}{K_b * 3 * T}\right) = 2.26 \text{E-}8$	Sinh term constant α
A_0 Analytical	$A_0 = \frac{\sqrt{3}}{M} * \rho_0 (1 + \eta) (1 - f(T)) * D_s(T) = 2.22 \times 10^{-12}$	Pre-sinh term A_0
A_0 F.E	$A_0 = \frac{(\rho_0 (1 + \eta) (1 - f(T)) * D_s(T))}{M} = 3.84 \times 10^{-12}$	Pre-sinh term A_0

Table 6: Parameters for analytical model and FE model for 10 mm compression of spring with at 700 °C

The value of $\rho_0 = 0.3 \times 10^{10}$ was chosen as the value for the Dyson model fitting the standard tensile creep results of uniaxial extruded and subsequently cold rolled Nimonic 90 samples [76], initially neglecting the effect of winding and torsion on the dislocation density. The calculations for the volume fraction, f , of the material come from the equation

$$f = \frac{C_0 - C_e}{0.23 - C_e} [76] \quad (8.10)$$

where C_0 is the total mol% concentration of the γ' forming elements in the nickel superalloy, in this case Al and Ti. C_e is the total combined matrix concentration at equilibrium, given by

$$C_e = 17 \exp\left(-\frac{7250}{T}\right) \quad (8.11)$$

The value of $r_p = 12.5$ nm comes from the approximate average value calculated utilising the parameters for the precipitation treatment the alloy has undergone in JMatPro to calculate the particle diameter. JMatPro is a physically based multi-component materials modelling software, capable of predicting the phase growth during service of various alloy types. As can be seen in Figure 40 the diameter of the γ' particles is expected to be approximately 12.5 nm after 4 hours at 750 °C, giving a radius of about 6.25 nm. The particles were expected to be of the order of 10 nm and after some initial testing 10 nm was found to be a good fit.

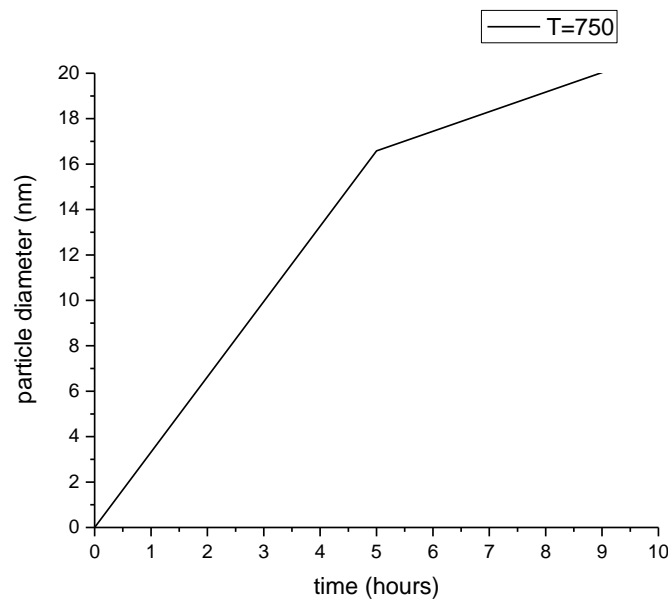


Figure 40: JMatPro prediction for γ' diameter during precipitation treatment of 4 hours at 750 °C followed by air cooling.

The initial stress relaxation model values are shown in Figure 41 for the extreme case of high load and high temperature; 10 mm compression at 700 °C for 15 hours. The FE model is shown in black and the simplified physical model from section 7.2 in red. Within the first hour it is found that the mechanical test data is reduced to approximately 0.5 of its original reaction force, while the FE and simplified physical models are at approximately 0.73 and 0.70, respectively. While both models have a fair correlation with one another, the reduction in reaction force for the mechanical tests are much higher than that of either model. The general shape of the curves for the models is acceptable but there is too little initial drop before reaching a less inclined steady state at about 4 hours of relaxation.

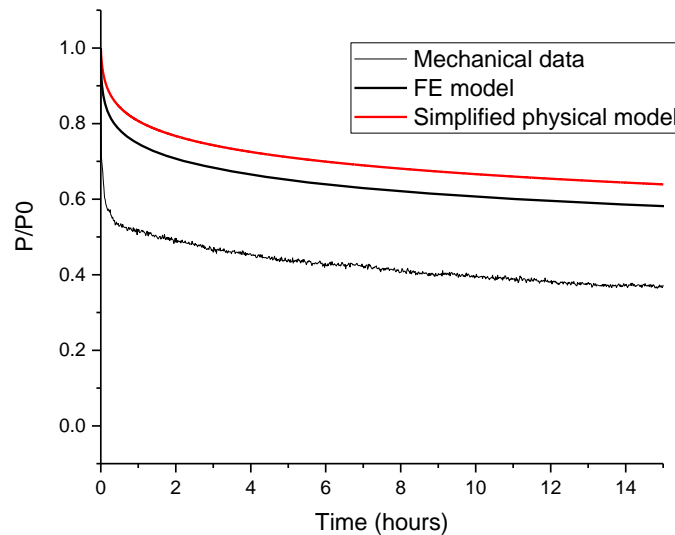


Figure 41: Initial stress relaxation test results for 10 mm compression, 700 °C for 15 hours.

8.2 Calibrations of FE and simplified physical models

In this section the models so far presented are calibrated to the mechanical data. This section is separated into three parts. Firstly, the effect of particle coarsening of γ' in the alloy is considered using modelling software. Secondly, the dislocation density is calculated both analytically and with an FE model to give more accurate initial dislocation density values, as

the models are very sensitive to this initial condition. Finally, the effect of back stress hardening is added to the models, to allow for transition from primary to secondary creep, and better match physical data.

8.21 Particle coarsening

The initial reduction in the reaction force for the mechanical data was explored in the context of particle radius, r_p . The models are very sensitive to the A term and α terms, with the variables for dislocation density (ρ) and γ' particle radius r_p being the simplest to change to make a fit to the mechanical data. As the particle diameter of γ' is expected to change by about 2.5 nm within the 15 hours of testing at 700 °C, shown in Figure 42, this is an increase of 1.25 nm in r_p , which, while enough to make a difference to initial values, there is little change within the first few hours, which would suggest particle coarsening does not have a direct effect on the initial drop in reaction force.

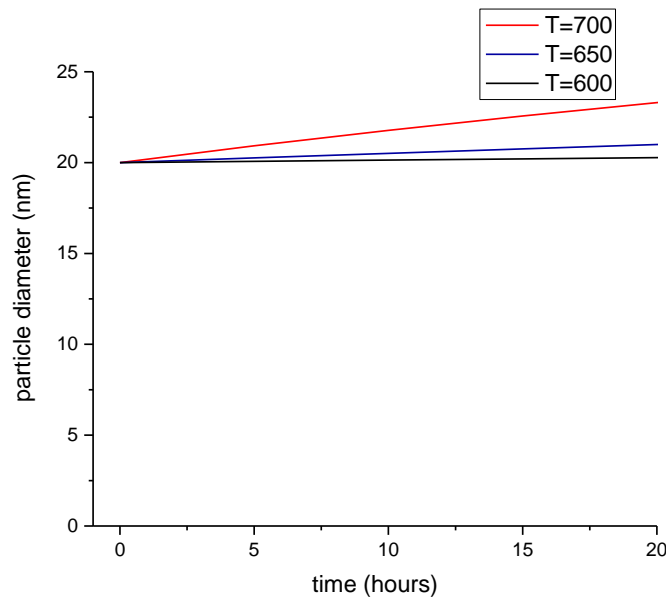


Figure 42: JMatPro 8 predictions for Nimonic 90 γ' coarsening at 600, 650 and 700 °C showing increased growth with temperature and time.

Looking at further time periods beyond the first 4 hours the particle coarsening becomes more significant at 700 °C, and so including particle coarsening within the model to account

for the increase in size may be important. For the initial 20 hour model, however, the particle coarsening was considered to be negligible as the majority of stress relaxation was seen within the first 1-2 hours, and so $r_p = 12.5$ nm was kept as a constant for this test.

The remaining major adjustment factor was to change the *sinh* pre-factor A_0 by increasing the value of the initial dislocation density, ρ_0 , which is generally not well known. It has been shown that A_0 is dependant on the dislocation density, volume fraction of gamma prime, and diffusivity. The diffusivity is unlikely to change compared with the original uniaxial tests, and the volume fraction is fixed with the heat treatments. This leaves only the dislocation density as the other parameter to change A_0 . Initial work hardening leads to an increase in the dislocation density, and so a change in the dislocation density during winding of the spring is entirely possible, and thus an increase in the rate of stress relaxation is possible through this and by scaling A_0 with the dislocation density, which will effectively just rescale the time x-axis of a stress relaxation plot. The value originally used ($\rho_0 = 0.3 \times 10^{10} \text{ m}^{-2}$) is fitted to the uniaxial creep test data of a straight wire, which does not take into account the Geometrically Necessary Dislocations (GND's) that arise from the plastic bending and torsion of the straight wire into a coiled helical spring. The origins of GND's and methods to calculate them analytically and implement them into an FE model will be discussed in the following section.

8.23 Origins of Geometrically Necessary Dislocations

A dislocation is a crystallographic defect found within a crystal structure, and as it glides through the lattice of a material, contributes to the creep rate. A higher density of dislocations therefore leads to a larger creep rate. Under deformation, the crystal lattice in a material would be expected to generate GND's in order to accommodate plastic strain. The curvature of a spring wire into a coil would therefore be expected to induce strain gradients within the material that would increase the dislocation density significantly. As dislocation density has a large impact on the creep response of the samples, being able to calculate an accurate value for the dislocation density is paramount.

Dislocations may be separated into two distinct varieties: Statistically Stored Dislocations (SSD) and Geometrically Necessary Dislocations (GND's), where $\rho_{total} = \rho_{SS} + \rho_{GN}$. SSDs are

thought to occur as a result of random trapping processes that occur during plastic deformation [84] and dislocation multiplication under stresses high enough to activate Frank Read and other sources. The GND's typically arise due to strain gradients induced by deformation of a material, such as the winding of a straight wire into a spring. GND's are necessary to accommodate the plastic deformation of the metal crystal lattice that occurs, and are typically of the same burgers vector in a given area. SSDs are not strictly necessary and have a random distribution of burgers vectors. Hence SSDs are more easily removed by the annihilation of dislocations of opposite burgers vector during solution heat treatments near the melting temperature of the material, in contrast to GND's.

One may estimate the density of GND's induced due to bending and torsion of wire utilising the method of Fleck et al [85] whereby

$$\rho_{GN} = \frac{1}{b_0} \left| \frac{d\varepsilon_p}{dx} \right| \quad (8.12)$$

where b_0 is the burgers vector and $\left| \frac{d\varepsilon_p}{dx} \right|$ is the plastic strain gradient.

The GND's are split into those created by bending, torsion and stretching

$$\rho_{GN} = \rho_{GN}^{bend} + \rho_{GN}^{torsion} + \rho_{GN}^{tension} \quad (8.13)$$

where for bending $\rho_{GN}^{bend} = \frac{\kappa}{b_0} = \frac{1}{Rb_0}$ and $\kappa = \frac{1}{R}$ is the wire curvature. Similarly, the contribution from twisting is $\rho_{GN}^{torsion} = \frac{\phi_0}{b_0} = \frac{H_{ar}}{LRb_0}$, where ϕ_0 is the plastic rotation per unit length, H_{ar} , L and R are the height, length, and coil radius of the resulting spring. The contribution from stretching is $\rho_{GN}^{tension} = 0$ as this induces no gradients in the strain field.

The origins of the SSDs is due principally from the work hardening arising from plastic bending of the spring wire. Dyson [7] proposes

$$\rho_{ss} = 300 \times 10^{10} |\varepsilon_{ep}| \text{ m}^{-2} \quad (8.14)$$

where elastic strains are neglected as small and

$$\varepsilon_p \approx \kappa y = \frac{y}{R} = 0.15 \left(\frac{y}{a} \right) \quad (8.15)$$

and y is the distance from the center of the wire, different from r as y may be negative in the center-half of the wire, and positive in the outer half, as shown in Figure 43.

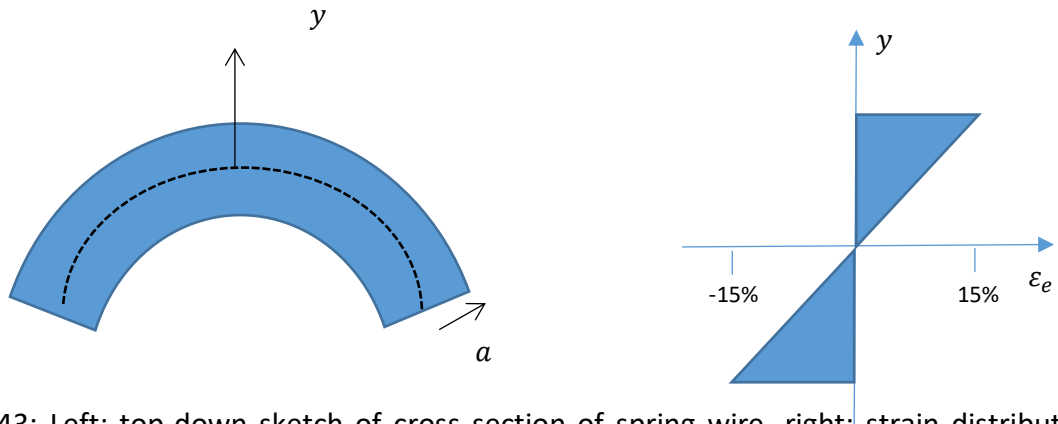


Figure 43: Left: top-down sketch of cross section of spring wire, right: strain distribution across wire cross-section

$$\rho_{ss} = 45 \times 10^{10} \left| \frac{y}{a} \right| \text{ m}^{-2} \quad (8.16)$$

The total dislocation density is the sum of all contributions

$$\rho_{GN} + \rho_{ss} = \frac{1}{Rb_0} + \frac{H_{ar}}{LRb_0} + 45 \times 10^{10} \left| \frac{y}{a} \right| = 55 \times 10^{10} \text{ m}^{-2} + 45 \times 10^{10} \left| \frac{y}{a} \right| \text{ m}^{-2} \quad (8.17)$$

As the springs are solution treated after winding it would be expected that a large portion of the SSD's will be annihilated, along with a portion of the GND's as the temperature is close to the melting point. For this reason, the SSD contribution will be neglected.

8.24 FE model to calculate GND density during winding

An FE model was designed in Comsol to simulate the winding process of the spring wire to provide an additional estimate for the value of ρ_{GN} . This was accomplished by creating a wire of length $L = 0.05$ m and radius $a = 0.00125$ m and a winding block of radius 0.0076 m. The mechanical properties of the wire were chosen to be that of Nimonic 90 at room temperature. The wire was split into two domains, one where contact was expected between the wire and the block, and one where no contact would be achieved within the prescribed deformation. The contact domain contained a finer mesh of 2138 tetrahedral elements and the remaining domain had a coarser mesh of 773 tetrahedral elements. The geometry is shown in Figure 44.

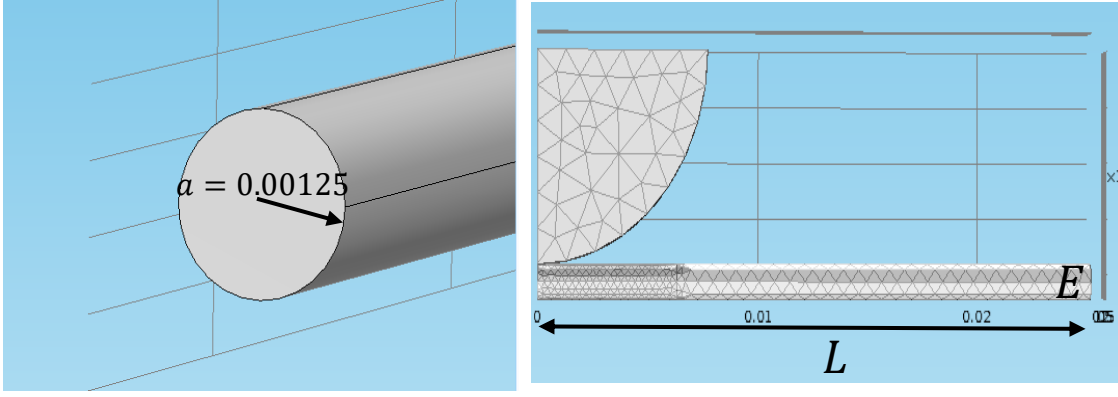


Figure 44: Geometry of wire to be coiled around forming block. Left: the wire cross section of radius a . Right: the length, L of the wire and forming block in the x-y plane

The end of the wire at point E in Figure 44 was moved along a circular arc defined by $[-L\sin(\theta\eta), -L(1 - \cos(\theta\eta)), \psi\eta]$, where the bending angle θ was 45° and the pitch ψ was chosen to be a small value of 0.3° . This caused the coil wire to wrap around the cylindrical moulding block as η is increased from 0 to 1. The material is assumed to be perfectly plastic (i.e. no hardening due to GNDs) with a yield stress of 730×10^6 Pa. The GND population is therefore part of the post-processing calculation. It is calculated utilising the Nye dislocation tensor [86-88]

$$\rho_{GN} = \frac{1}{b_0} \|\text{curl}[F^p]\| \quad (8.18)$$

which describes GNDs as arising from plastic rotations in the crystal lattice, where $[F^p]$ is the plastic deformation tensor and b_0 is the burgers vector.

Compatibility of the overall deformation $[F] = [F^e][F^p]$ requires $\text{curl}[F] = 0$. This arises from symmetry of second derivatives of overall displacement field eg. $u_{x,xz} = u_{x,zx}$. If there is no plastic strain, ie $[F^p] = [I]$, then no GNDs result.

Assuming plastic rotations are small for an isotropic plasticity model results in the plastic deformation tensor $[F^p] \approx [F^p]^T$ being symmetric [89].

Now, plastic strain is defined as

$$[\varepsilon^p] = \frac{1}{2} ([F^p] + [F^p]^T) - [I] = [F^p] - [I] \quad (8.19)$$

implying that all rotations are elastic in nature.

Therefore equation (8.18) may be written as

$$\rho_{GN} = \frac{1}{b_0} \|\text{curl}[\varepsilon^P]\| \quad (8.20)$$

describing GNDs arising from plastic rotations in the crystal lattice. In rectangular coordinates this can be expressed as

$$\rho_G = \frac{1}{b} \sqrt{(\varepsilon_{xz,y}^p - \varepsilon_{xy,z}^p)^2 + (\varepsilon_{yz,y}^p - \varepsilon_{yy,z}^p)^2 + (\varepsilon_{zy,z}^p - \varepsilon_{zz,y}^p)^2 + (\varepsilon_{xx,z}^p - \varepsilon_{xz,x}^p)^2 + (\varepsilon_{yx,z}^p - \varepsilon_{yx,z}^p)^2 + (\varepsilon_{zx,z}^p - \varepsilon_{zz,x}^p)^2 + (\varepsilon_{xy,x}^p - \varepsilon_{xx,y}^p)^2 + (\varepsilon_{yy,x}^p - \varepsilon_{yx,y}^p)^2 + (\varepsilon_{zy,x}^p - \varepsilon_{zx,y}^p)^2} \quad (8.21)$$

The FE model uses equation (8.21) to calculate the GND density. This is shown in Figure 45, where the highest values for the dislocation density are found at the surface of the spring wire, specifically on the inside of the coil due to the larger strain gradient. The calculated average at the surface of the wire for ρ_{GN} is found to be $55.9 \times 10^{10} \text{ m}^{-2}$ which has a very good correlation to the calculated analytical value based on addition of equations (8.12) and (8.14), which calculated a value of $55.0 \times 10^{10} \text{ m}^{-2}$. These values for the GND densities are significantly higher than the uniaxial value of $0.3 \times 10^{10} \text{ m}^{-2}$ and will therefore be expected to have a significant effect on the stress relaxation calculations.

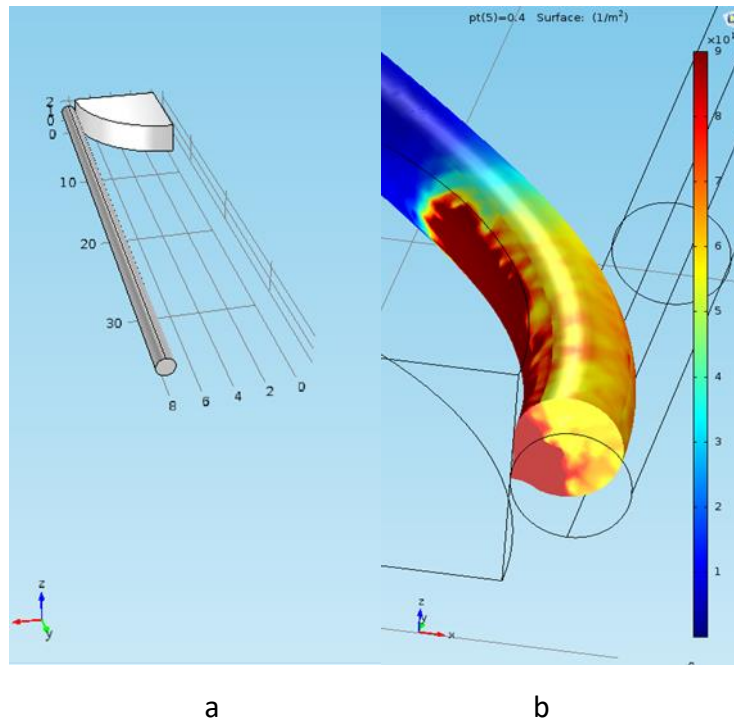


Figure 45: a) F.E model of basic wire geometry wound around curved block and b) the predicted dislocation densities and locations on the wire after bending and torsion

8.25 Effect of enhanced dislocation density on stress relaxation model

Due to both the FE predictions and the results of equation (8.12) calculating a similar value, the initial dislocation density for the springs is taken to be $\rho_0 = 55 \times 10^{10} m^{-2}$ from this point onwards. Stress relaxation for the revised model can be seen in Figure 46. It is observed that the values in the model now align far closer with the mechanical data. However the model now over-estimates the rate of stress relaxation by a consistent margin, levelling out from the steep initial drop a significant amount of time later than the mechanical test. This is likely to be due to the lack of back-stress hardening within the model, which is a phenomena describing build-up of gliding dislocations upon the precipitate/matrix interface, leading to a transfer of load from the matrix to the elastic particle [90]. This in turn leads to an effective reduction in the average matrix stress of the sample, reducing the creep rate and stress relaxation rate. For this reason, hardening is incorporated into the model in the next section.

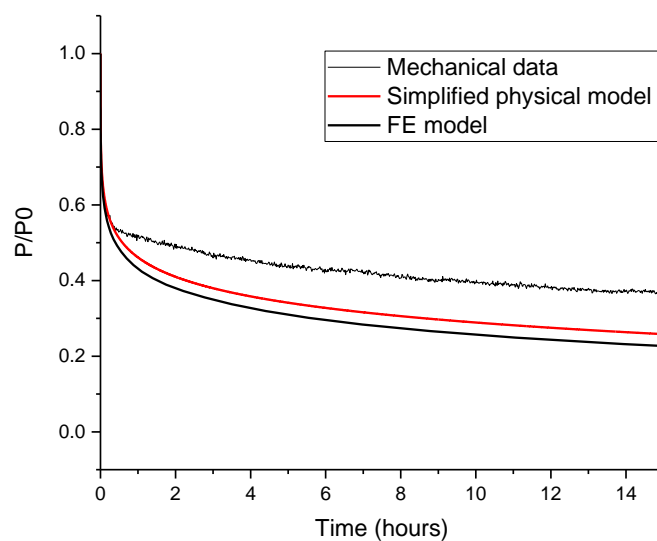


Figure 46: Mechanical test data (700 °C, 10 mm displacement) against FE model and simplified physical model with dislocation density $\rho_0 = 55 \times 10^{10} m^{-2}$.

8.26 Back-stress hardening

As discussed in section 3.33, the back-stress hardening parameter, H , can be introduced to the creep rate equations to simulate the reduction in the effective internal stress within the alloy grain structure. This is modelled as an opposing stress inserted into the hyperbolic sine creep rate model. Proposed by Dyson, based on Ion et al's work [7], the back stress is defined as

$$\sigma_b = H\sigma_e \quad (8.22)$$

where σ_e is the effective stress, H is a hardening parameter and $0 < H < 1$.

The rate of change of back stress is defined as

$$\dot{\sigma}_b = \frac{\varphi_p E}{1 - \varphi_p} \dot{\epsilon}_e \quad (8.23)$$

in which the maximum back stress $\sigma_b^* = H^* \sigma_e$, where $H^* = \frac{2\varphi_p}{(1+2\varphi_p)}$.

During stress relaxation the load does not remain constant so equations (8.22) and (8.23) give

$$\frac{dH}{dt} \tau + H \frac{d\tau}{dt} = \frac{Ef}{3(1 - \varphi_p)} \left(1 - \frac{H}{H^*}\right) \frac{d\gamma_c}{dt} \quad (8.26)$$

Taking $\tau = G(gr\phi - \gamma_c)$ as before gives

$$\left[\frac{Ef}{3(1 - \varphi_p)} \left(1 - \frac{H}{H^*}\right) + HG \right]^{-1} \frac{dH}{dt} = \frac{1}{G(gr\phi - \gamma_c)} \frac{d\gamma_c}{dt} \quad (8.27)$$

Integrating over time leads to

$$H(t) = \frac{H_a}{H_b} \left(1 - \left(1 - \frac{\gamma_c(t)}{gr\phi} \right)^{H_b} \right) \quad (8.28)$$

where $H_a = \frac{2(1+\nu)\varphi_p}{3(1-\varphi_p)}$ and $H_b = \left[\frac{(1+\nu)(1+2\varphi_p)}{3(1-\varphi_p)} - 1 \right]$. The volume fraction of gamma prime, φ_p ,

is critical to H_b , as the value can result in this being positive or negative if φ_p is high enough.

In the case of Nimonic 90 the value of $\varphi_p = 0.214$, which indeed results in a negative value

of H_b , for which the value of $H(t)$ will be expected to rise from zero to $\min\left(\frac{H_a}{H_b}, 1\right)$. Inserting

$H(t)$ into the shear strain rate equation gives

$$\frac{d\gamma_c}{dt} = \sqrt{3}A \sinh[\sqrt{3}\alpha\tau(1 - H(t))] \quad (8.29)$$

where the evolving back-stress parameter will reduce the effective stress within the \sinh term, where as $H(t) \rightarrow 1$ the creep rate will effectively cease, leaving a minimum value for the calculated reaction force.

The back-stress parameter was included in the FE model by use of equation (8.28) as a variable, defining H_a and H_b as appropriate. Implementing the back stress hardening into the full analytical model (7.17) proved to be too complex due to the requirement of solving multiple differential equations in $\dot{\gamma}_c$ and \dot{H} which have an interdependence upon one another.

8.27 Finite difference model

In order to solve this problem the simplified physical model of section 7.2 was adapted, although now in a finite difference form required to iteratively calculate the solutions of the differential equations for the radius of the elastic zone, \dot{b} from equation (7.25), the hardening parameter \dot{H} from equation (8.27) and $\dot{\gamma}_c$ from equation (8.29). The finite difference method works by using a discretised approximation for the function differentials. The method is a form of the Eulers method, in which a first order differential equation may be solved given the initial conditions. By multiplying by a time step, Δt , the solution at iteration $n + 1$ may be found using the form $f_{n+1} = f_n + \dot{f}_n \Delta t$. Finding the correct value of Δt is important, as the smaller the value of Δt the closer the approximation comes to the true value of f_{n+1} . However, it also increases the number of iterations required for a longer-term model with high values of t . The value for the time step was made to increase with time, with $\Delta t = 0.001t$, to allow for accurate, small values of Δt at small t where there is expected to be large change in the reaction force of the spring per second, and at larger time periods the change is expected to be smaller. The full finite difference equations are given in Appendix 1.

8.28 Dislocation multiplication

The SSD density during plastic deformation is expected to increase due to the activation of internal sources. The multiplication of dislocations was introduced into the FE and analytical

models utilising an equation taken from Dyson [7] in which the change in dislocation density is described based on empirical observations as

$$\dot{\rho}_{SS} = K_m \dot{\epsilon}_p \quad (8.30)$$

where the value $K_m = 300\rho_0$ is a constant of multiplication. The differential equation may be integrated to give the total dislocation density

$$\rho(t) = \rho_0 \left(1 + \frac{1}{\sqrt{3}} K_0 \gamma_c(t) \right) \quad (8.31)$$

The dislocation density would not be expected to increase significantly during the 1000 hours of testing experienced here due to the low expected strains as described in section 3.33. By utilising $\rho_0 = 55 \times 10^{10}$ for 650 °C at 6 mm displacement, the FE model gives an average value for the dislocation multiplication over the entire spring segment volume, shown in Figure 47, where the dislocation density is predicted to grow by 1.8 times its initial value within the first 1000 hours.

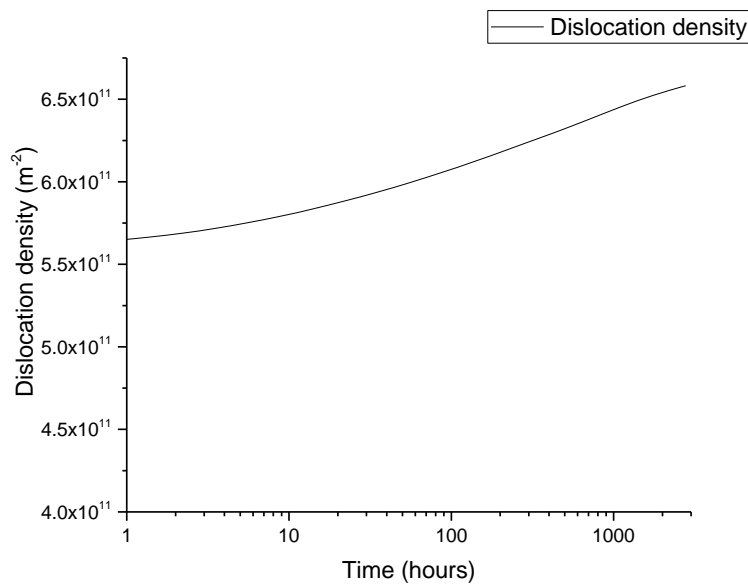


Figure 47: Dislocation density of FE model of Nimonic 90 coil spring segment displaced 6mm at 650°C.

In summary, the FE model and simplified physical models have been calibrated to the mechanical test data by first considering the effects of particle coarsening and dislocation

density. The particle coarsening was considered to have negligible effect during the largest part of the stress relaxation and so the other sensitive initial parameter, the dislocation density, was calculated. It was found to be two orders of magnitude larger than the current uniaxial value. Back stress hardening was then implemented into the FE model, and the simplified physical model was adapted to a finite difference model, which has the following differential equations to solve:

- \dot{b} , the radius of elastic zone within the coil wire equation (7.25)
- \dot{H} , the back-stress hardening parameter equation, rearranged from (8.27)
- $\dot{\gamma}$, the shear creep strain rate, taken from (8.29)

to find $b(t)$, $H(t)$, and $\gamma(t)$ respectively, with the full finite difference equations shown in Appendix 1. The value of $H(t)$ was found to saturate at long time values as expected. Finally, as dislocation multiplication was predicted to have a large effect on the stress relaxation calculations, equation (8.31) was added to the models.

8.3 Calibrated stress relaxation models against results

By including the back-stress hardening into both the analytical model and the FE model and comparing again with the mechanical data for the displacement of 10mm, 700°C sample, it can be seen in Figure 48 that there has been a reduction in the short-term stress relaxation of the models, bringing them closer to the in-situ data. The optimisation of the model appears to match the data well, with the majority of the stress relaxation within the first 2 hours found to be very close, with the FE and analytical models slowly diverging away from the mechanical data with increasing time. This may be due either to experimental error or to slight over-estimation of the back-stress effect on the creep rate for both models. Note there are no fitting parameters for the back-stress model. When plotting $H(t)$ for the FE model the average value across the cross-section was used, to give a good impression of the general increase of $H(t)$ in the specimen. It is important to note, however, that it varies in space due to the strain and is higher at the wire surface than towards the centre. The $H(t)$ values for both the FE and analytical models show good correlation with one-another, increasing rapidly within the first hour, and slowing down thereafter, along with the reaction force. The FE

model shows slightly less growth in $H(t)$ than the analytical counterpart, but becomes larger at 8 hours.

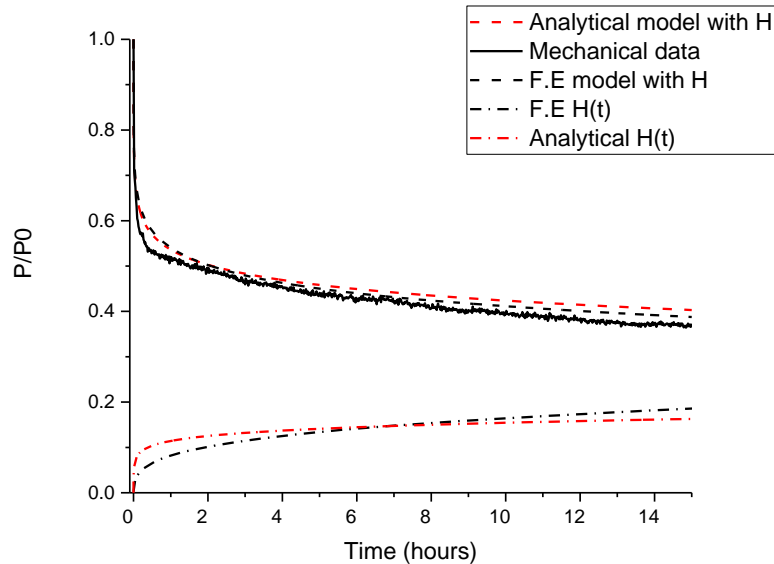


Figure 48: Mechanical test data (700°C, 10mm displacement) against FE model and finite difference model with initial dislocation density $\rho_0=55 \times 10^{10} \text{ m}^{-2}$, back stress hardening, $H(t)$ and dislocation multiplication $\rho(t)$. The back-stress parameter $H(t)$ is shown on the same scale for the FE model and finite difference models.

The longer term calculation of the stress relaxation of the springs was accomplished using the nut-and-bolt method. This was utilised to measure the reaction force of the Nimonic 90 springs up to 1000 hours, taking a value of the height at 1, 10, 100 and 1000 hours. The data in Figure 49 demonstrates the finite difference model and FE model against the nut and bolt method mechanical data for 6mm compression at 650 °C up to 1000 hours. Best fit was found for the FE and finite difference models with a dislocation density $\rho_0 = 20 \times 10^{10} \text{ m}^{-2}$, which is of the same order of magnitude of that calculated using the wire bending FE model to calculate ρ_0 . The value for r_p was reduced from 12.5 nm to 10 nm to calibrate the model to the data. The samples used in the nut and bolt tests were from a different batch, and thus this may be a realistic value for the average particle size, a size distribution change of 2.5 nm is possible even under the same heat treatments. Using the exact solution from the FE model as a reference, the pattern of the finite difference model initially has a larger value of

$H(t)$ and later being overtaken by the FE model, is seen here. The more accurate FE model $H(t)$ shows significantly higher values of $H(t)$ beyond 1000 hours and appears to have the greater correlation with measured results. Hence this is utilised in the following section to calculate the effect of pre-straining coil springs. In summary, the analytical model can be said to have very good accuracy with the FE model generally, however there is a small discrepancy in the calculation of P/P_0 between the models. For reference, published data for similar springs at the same compression and temperature is shown in Figure 49. The values found in the nut and bolt tests here show good agreement with the published values up to 10 hours, with a trend of the published data relaxing faster over time. The FE model predicts a value for $\frac{P}{P_0}$ closer to the published data at 1000 hours, and so it is worth performing more nut and bolt tests to ensure greater accuracy in the data the models are calibrated to.

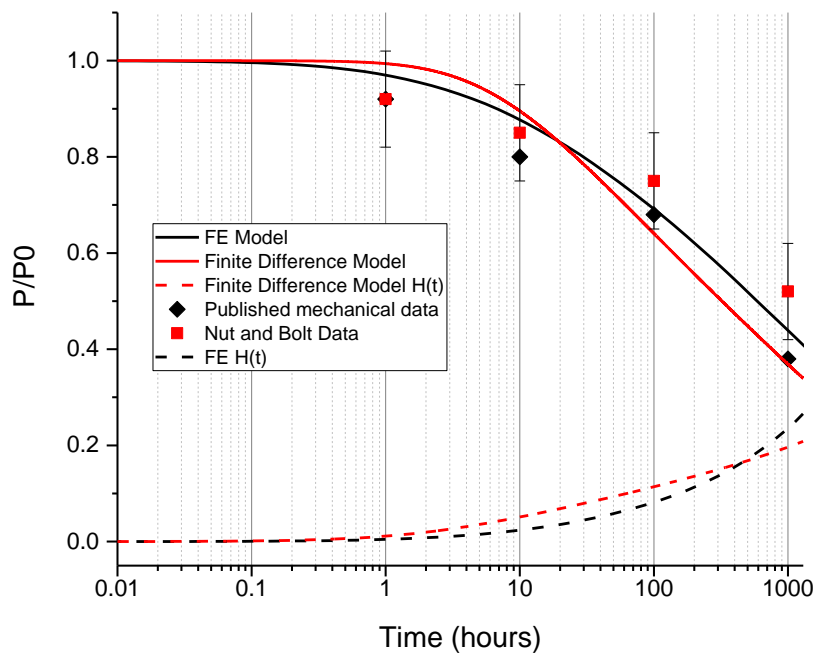


Figure 49: Nut and bolt mechanical test data (650 °C, 6 mm displacement) against FE model and finite difference model with dislocation density $\rho_0=20 \times 10^{10}$, back stress hardening, $H(t)$ and dislocation multiplication $\rho(t)$. The back-stress parameter $H(t)$ is shown on the same scale for the FE model and finite difference models. Published data for 6 mm compression at 650 °C on Nimonic 90 springs of similar geometrical size is shown for reference. [76]

8.4 Conclusions

The FE and simplified analytical model were compared with short-term stress relaxation data in the extreme condition of 10 mm displacement at 700 °C. The models under-predicted the stress relaxation results and it was found by calculating the GND density using analytical and FE methods that the bending of the wire into the spring may be increasing the dislocation density by two orders of magnitude. The new dislocation density resulted in $\rho_0 = 55 \times 10^{10} \text{ m}^{-2}$, two orders of magnitude higher than the uniaxial value of $\rho_0 = 0.3 \times 10^{10} \text{ m}^{-2}$.

Back-stress hardening was then implemented into the models, through use of the hardening parameter, $H(t)$. The value of $H(t)$ represents the rate control of the movement of glide of dislocations during primary creep. An increase in $H(t)$ will reduce the creep rate and slow the creep rate, developing the creep from primary to secondary, in which the rate of climb is balanced by the glide velocity. Dyson [7] discusses a method to model the back-stress hardening in the Appendix, describing it as a ‘stress redistribution that takes place between matrix and particles as inelastic strain accumulates by creep’. Dyson re-writes equation (3.21) and defines as

$$\dot{\epsilon} = A \sinh(\alpha(\sigma - \sigma_i - \hat{\sigma}_{net})) \quad (8.32)$$

Replacing the stress term with $\hat{\sigma}_{net}$ representing the network of interacting dislocations slowing glide, and σ_i the internal stress in the matrix. The load transfer from matrix to particle increases with inelastic strain, and leads to a reduction in the matrix loading and therefore the creep rate. Therefore, $\hat{\sigma}_i$ determines the reduction of the creep rate. The introduction of this into the models created an improved match for both the short and long-term stress relaxation data to a good degree, and the models now include all features of the Dyson creep rate model, allowing for a physically based approach to model the stress relaxation of springs. The next chapter will utilise the understanding gained so far to develop methods to increase the stress relaxation resistance of the coil springs.

Chapter 9: Investigating methods for improving the stress relaxation resistance of coil springs

In the previous chapter the FE model and simple physical model based on an unmodified Dyson creep rate model were calibrated to stress relaxation data and found to be in good agreement with both one another and the data itself at times up to 1000 hours. The models are physically based, including the γ' volume fraction, particle size and dislocation density, assuming a climb/glide mechanism that leads to back-stress hardening over time. In this chapter a combined thermomechanical method of improving the stress relaxation resistance, that is, the time taken for the reaction force to reach a given value during relaxation, is introduced, by inducing back-stress hardening prior to spring service. The consequences of this new treatment are considered using models and experimental data.

9.1 Multiple-Stage Loading

One method by which springs can be prepared before service is by so-called 'hot-setting' [91]. This involves winding a spring with an initial height that is greater than the final required height of the spring desired in-service. The spring is then heated to a particular temperature and compressed in a special jig, after which they are air cooled or quenched depending on the manufacturing needs. [92]. The spring thus undergoes creep during the compression and develops residual stresses that may be modelled as a back-stress. The spring will reduce in height during the process and if planned correctly will reduce to the correct height required for service.

Investigation into a possible pre-treatment for the springs led to manipulation of the back-stress hardening parameter, H , in the F.E model, in order to improve the stress relaxation resistance of springs in service. By initiating primary creep either during or after thermal

treatments on the samples, the dislocations within a grain can be forced to glide to precipitates and grain boundaries, pinning them in position. A sketch is shown in Figure 50.

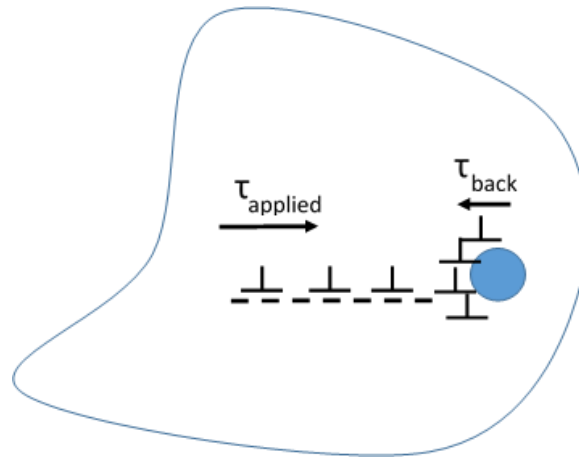


Figure 50: Sketch of a grain with dislocation pile-up on a precipitate. The build-up of GND's creates a forest of same sign dislocations that repel one-another, or lock one another in place, increasing the effective back-stress that opposes the applied stress.

9.11 Initial model validation with test

A method was devised to measure the effect of modelling hot-setting of springs in the FE model. This was achieved by relaxing a spring segment displaced initially by 6 mm at 700 °C, and then allowing stress relaxation to occur for 1 hour. After 1 hour the FE model is used to calculate the required further displacement needed to re-establish the initial spring force. After this second displacement, the spring is allowed to relax again. This process is repeated a total of 4 times; once per hour, during which the hardening parameter, $H(t)$, will increase. During the first deformation a redistribution of dislocations from matrix to precipitate is predicted, via glide caused by strain. The back-stress hardening parameter is related to the thermomechanical history as the dislocation density and their interactions (repulsion of same sign in particular) may reduce introduce additional contributions to hardening. The greatest increase in hardening will be seen in the first hour, as the majority of dislocations glide into contact with precipitates, and further repeated deformations will give smaller additions to the back-stress via additional strain, with diminishing returns as the creep rate slows. The glide and interactions of dislocations in the first and subsequent thermomechanical

displacements will build a resistance to the further stress relaxation of the springs, leading to a shallower stress relaxation curve. Results are shown in Figure 51.

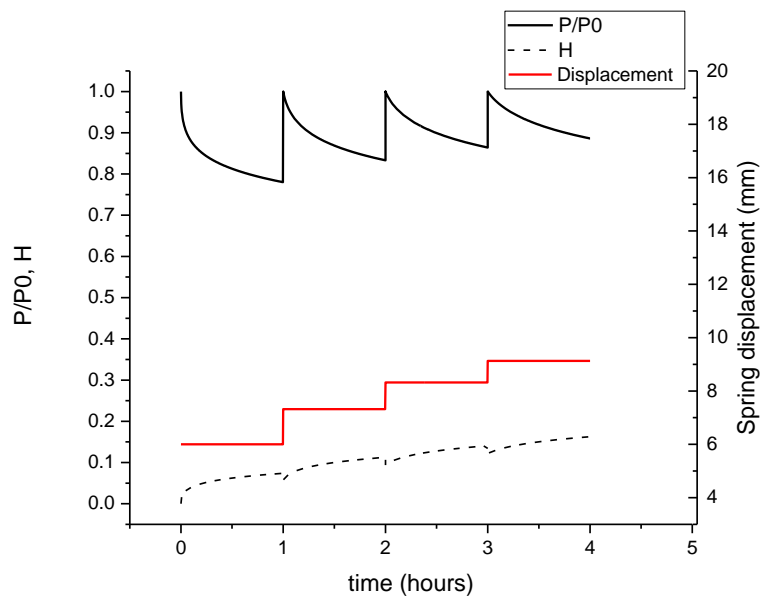


Figure 51: Multiple deformation of Nimonic 90 spring in F.E, beginning with 6mm displacement, and increasing displacement after relaxation to reach initial reaction force at 1, 2, 3, hours. The hardening parameter, $H(t)$, is shown as the dashed line, increasing over time, while the red line shows the increase in the displacement required at each stage, on the right y axis.

The stress relaxation in the first stage over 1 hour reaches a force reduction ratio of 0.78, while in the 4th stage, after multiple deformations and increases in $H(t)$, the stress relaxation over a 1 hour period reaches 0.88 of P_0 , which is a significant improvement.

This was replicated experimentally by displacing a Nimonic 90 spring and measuring the reaction force using the in-situ method. The limiting factor in the repeated deformations is the reduction in spring height, which made a 4th stage difficult to achieve as the spring coils made contact. Ideally taller springs would have been available to more fully test the capacity of hot setting to increase stress relaxation resistance. However, a 3 stage deformation scheme was accomplished, and the results for the 1st and 3rd cycles are shown in Figure 52. This graph shows the increase in stress relaxation resistance is real and simple to accomplish, with the relaxation in the 3rd cycle clearly less than that observed in the 1st cycle. This provides

reasonable validation for further use of the model, as the reduction in stress relaxation between stage 1 and stage 3 is similar between the FE model and the mechanical testing of the spring.

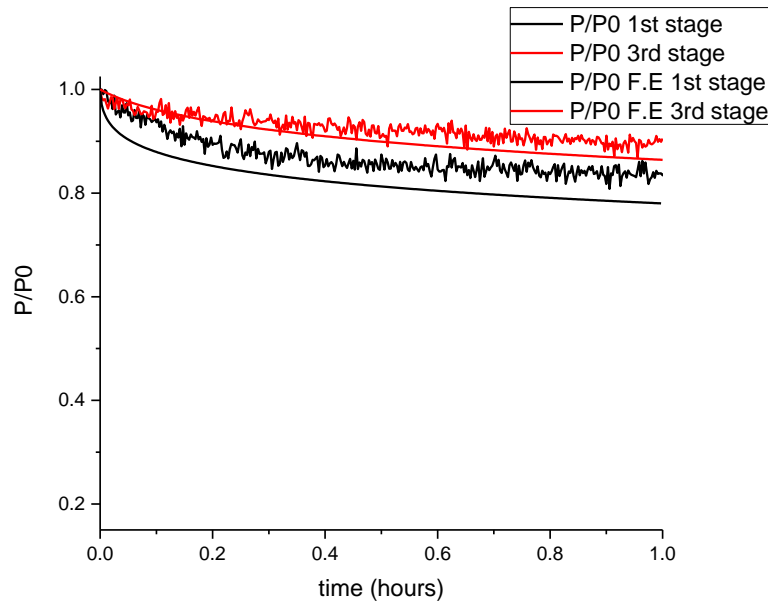


Figure 52: 1st and 3rd stage relaxation for mechanical testing and F.E model.

Figure 52 gives a useful indication that back-stress hardening as a method of improving spring relaxation behaviour can be modelled and replicated in situ. However, the multiple deformation method of back-stress hardening may be impractical as a thermomechanical treatment to be completed alongside thermal treatments currently performed on the springs before service. A more practical method would be a single displacement over a short period of time, utilising a spring with greater height than required for service, and relaxing the spring at high temperature, reducing the height to the in-service requirement. The displacement for the thermomechanical process should thus induce a large amount of creep strain within as short a time period as possible. The process is designed to allow for primary creep to reduce the length of spring during the stress relaxation, with the majority of creep having occurred during the thermomechanical process. Thus, the in-service stress relaxation would then occur after the initial drop shown in Figure 53.

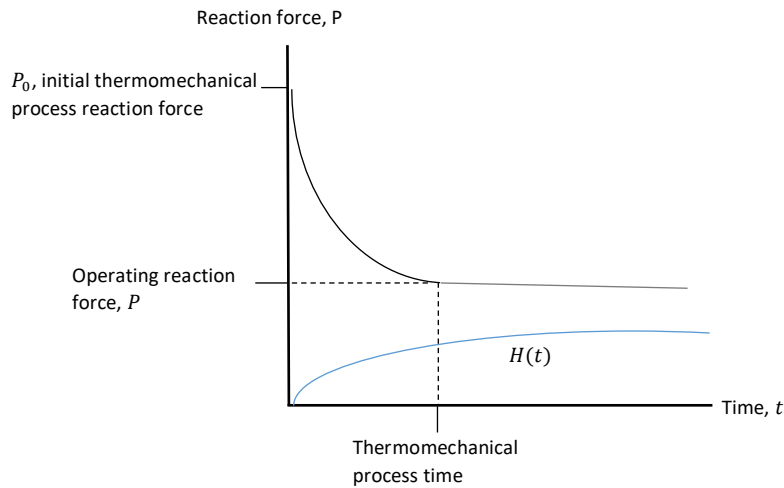


Figure 53: Diagram of proposed thermomechanical process showing initial relaxation leading to shallow curve, at which operation stress relaxation would take place. $H(t)$ can be seen to increase during both processes

9.12 Predictions of FE model for thermomechanical process

The FE model was used to anticipate the values of the stress relaxation and thus the reduction in length of the spring during the thermomechanical process. In order to select a suitable displacement and time period for the thermomechanical process the data in Figure 54 is analysed, in which the temperature chosen was 650 °C, with displacements at 1 mm increments. The hardening parameter is seen to increase more rapidly with the increased displacement, along with increased stress relaxation utilising the FE model will be useful for other similar alloys when attempting to determine suitable thermomechanical processes.

An 8 mm displacement, for 30 minutes at 650 °C, was selected as an initial test of the thermomechanical process as it would allow for a noticeable amount of back-stress hardening within that time-frame, without reducing the spring height to the extent that a further stress relaxation test with available springs could be carried out. Figure 55 demonstrates the predicted height of springs during thermomechanical process from 0.5 to 10 hours, with 8mm

displacement reducing the total spring height from 29 mm to 25.23 mm at 0.5 hours, allowing for a subsequent 6mm displacement stress relaxation test at 650 °C. The dashed line shows the limit of possible height loss, as the coils of the spring will touch at 17mm. All of the simulated compression distances can be used up to 10 hours for back-stress hardening, except for 10 mm, which will cause the coils to come into contact.

The thermomechanical process occurs at 650 °C and the stress relaxation tests also occur at 650 °C. This temperature lies at 41% of the melting temperature (1370 °C) of the sample, and as such is within the warm working regime ($0.3 - 0.5 T_m$); creep active, but below the recrystallization temperature. The optimum hot-working temperature for Nimonic 90 has been found to be 1130°C [93], and thus fewer of the features of hot-working such as deformation twins and recrystallized dislocation-free grains are expected to be seen, while it should maintain some degree of creep-induced dislocation glide, leading to the back stress hardening effect. Warm work allows a reduced back-stress hardening effect compared to cold working. However suitable hardening can still be achieved with a lower application of force with the increased creep effect of a higher temperature.

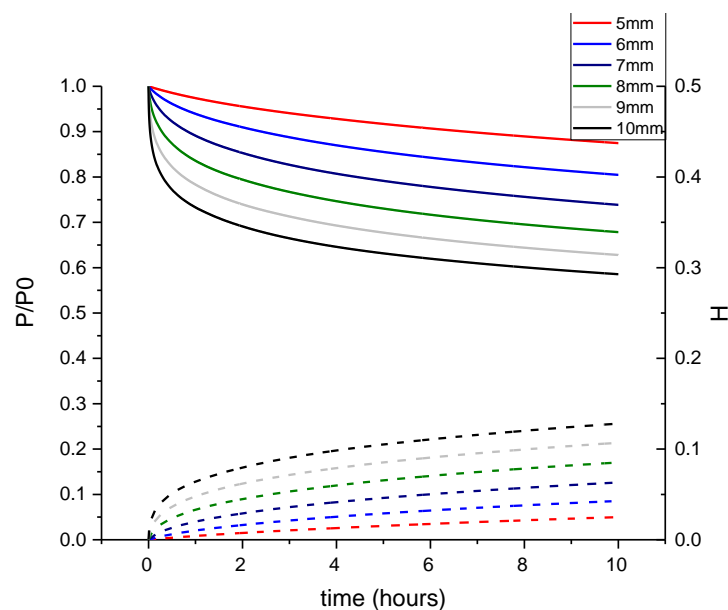


Figure 54: Stress relaxation for displacements during thermomechanical treatment of springs at 650 °C, the hardening parameter, H , is shown as the dashed lines corresponding to the displacement of the same colour, and the value of H is on the y-axis.

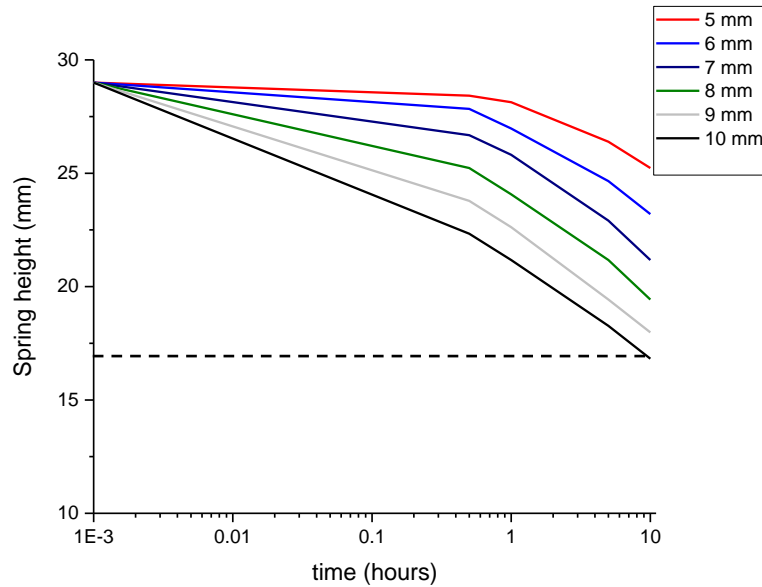


Figure 55: Varying displacement of spring during thermomechanical process in FE model at 650 °C. Increasing displacement leads to further reduction in spring height. The dashed line represents the height at which the coils touch, 17 mm.

9.2 Consequences of thermomechanical treatment on material microstructure

The solution and precipitation treatments that the samples undergo are crucial to the strengthening of the creep properties in the material. An investigation into the predicted volume fraction of γ' was accomplished utilising JMatPro 8. The program is capable of predicting the particle coarsening and volume fraction as a function of alloy composition, temperature, and time. Using a combination of a modified Ostwald ripening equation based upon the work of Lifshitz, Slyozov and Wagner (LSW theory shown in equation (2.10)) to calculate the coarsening rate coefficient $K(t)$, making use of the γ/γ' interfacial energy by CALPHAD (Computer Coupling of Phase Diagrams and Thermochemistry) calculations [94], alloy composition of γ and γ' forming elements, and the diffusion coefficient D_S . The approach used is found to have good approximation to experimental results in multi-component Nickel-based superalloys [95]

Inputting the alloy composition of Nimonic 90, seen in Table 2, into JMatPro 8 gives the precipitation and coarsening of γ' for 600, 650, 700, and 750 °C precipitation treatments lasting up to 1000 hours. These predictions assume a solution treatment of 1150 °C for 30

minutes quench cooled, prior to the precipitation treatment. Figure 57 shows the particle diameter over time. It is clear that the expected diameter grows relatively quickly until it reaches approximately 20 nm when precipitation stops. The particles then experience a slower regime where coarsening occurs. This reduction in rate coincides with the particles reaching their maximum volume fraction due to the particle growth, at which the solid solution is fully saturated as shown in Figure 56. Beyond this point it is expected that large particles will begin to coarsen, at the expense of smaller ones. It can be seen that the effect of temperature chosen for the heat treatment is of great importance. Lower temperatures lead to generally larger equilibrium volume fractions, and smaller particles, which is good for dispersion strengthening of the material. Higher temperatures lead to a smaller volume fraction of larger particles, which will be expected to be less effective for dispersion strengthening.

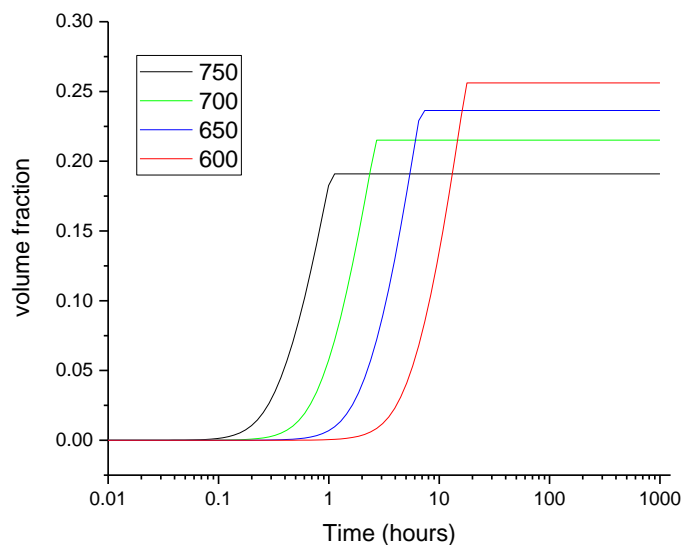


Figure 56: Particle volume fraction of γ' for constant temperature after solution treatment 1150 °C for 30 minutes then quenched.

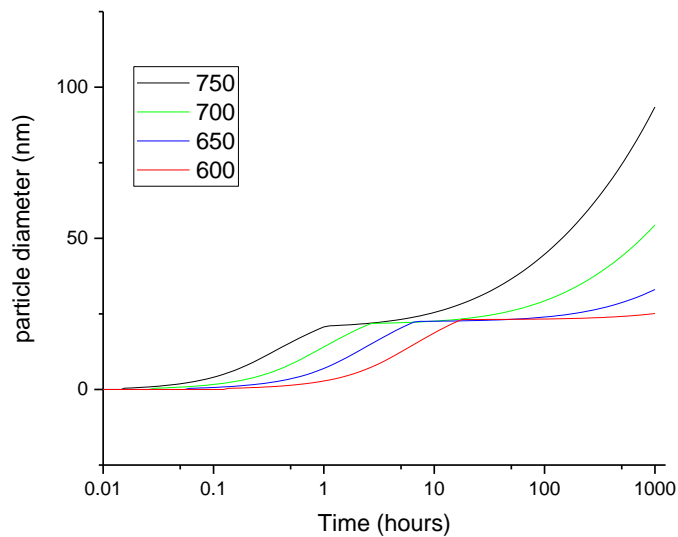


Figure 57: Particle diameter of γ' for constant temperature after solution treatment 1150 °C for 30 minutes then quenched

The stress relaxation models in this thesis are particularly sensitive to particle radius, and so being able to predict the particle radius after the heat treatments and thermomechanical treatments is crucial. This was investigated again in JMatPro 8 by including a third precipitation heat treatment stage after the precipitation treatment at 750 °C for 4 hours. This was calculated at 650 °C for 1000 hours to model the thermomechanical process and subsequent stress relaxation test, as accomplished in later in this section. The volume fraction is demonstrated in Figure 58, where it can be seen that reducing the temperature from 750 °C to the thermomechanical and stress-relaxation test temperature of 650 °C leads to a volume fraction increase from 0.19 to 0.23. The particle diameter is predicted to increase, according to Figure 59, from the end of the precipitation treatment at 22.5 nm, to 34.9 nm during the thermomechanical process and stress relaxation test. The thermomechanical process, being performed for only 30 minutes, is predicted to have only a small effect on the particle size, here predicted to be 0.3 nm, making this time period a suitable one for this third stage heat treatment of the samples. It should be noted that the predictions for the particle radius are indicative of the general behaviour and cannot be taken as an exact determination of the particle radius in a given material as this depends on other factors, such as the number

of nucleation sites for precipitation, which depends on a number of factors which are not included in the software, such as grain size, dislocation density etc.

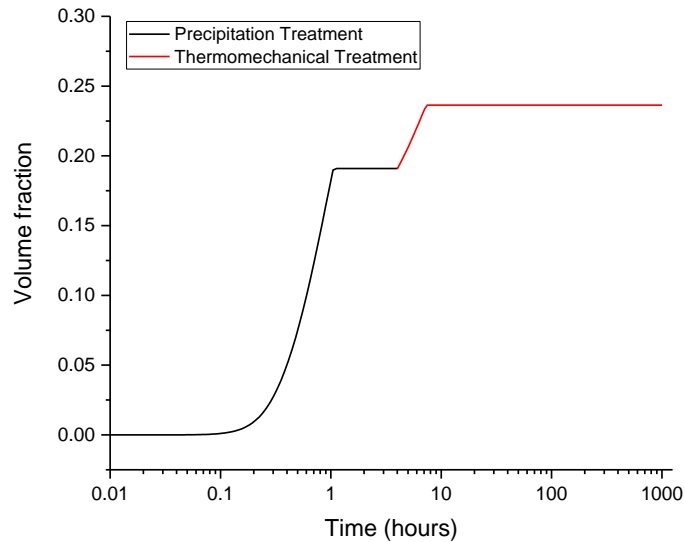


Figure 58: Predictions for γ' volume fraction for 750 °C precipitation treatment for 4 hours (shown in black), followed by thermomechanical process and stress relaxation test for up to 1000 hours at 650 °C (shown in red).

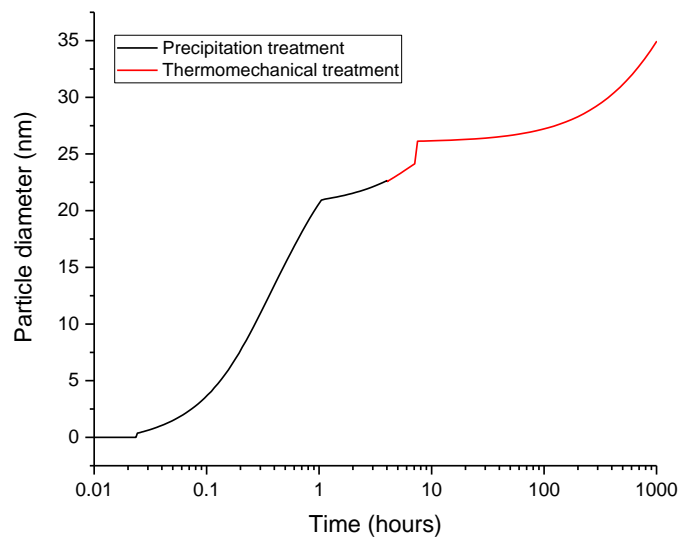


Figure 59: Predictions for γ' particle diameter for 750 °C precipitation treatment for 4 hours (shown in black), followed by thermomechanical process and stress relaxation test for up to 1000 hours at 650 °C (shown in red).

9.3 Results against model with thermomechanical treatment

After selecting the time period and temperature, as-received wire cold-wound into springs were heat treated using the industry-standard treatments; a solution treatment at 1150°C then quenched, followed by a precipitation treatment at 750°C for 4 hours, air cooled, to allow for uniform distribution of γ' . The springs were then thermomechanically creep-hardened by the process described above, displaced utilising the 'nut-and-bolt method', constraining the spring by 8 mm, placing them in a furnace at 650 °C for 30 minutes, and then measuring the height before and after the treatment. The height post-thermomechanical treatment was found to be 27.09 mm, which agrees well with the FE predictions for height loss. Measuring the height before and after the stress relaxation tests allowed for the calculation of the reaction force according to Hooke's Law. The subsequent stress relaxation tests; 6 mm displacement at 650°C, were accomplished using the same method. While this approach prevented in-situ data collection being possible, it allowed for multiple springs to be relaxed simultaneously, and is more suitable for longer time-periods of up to 1000 hours.

To analyse the effects that the heat treatments have upon the springs, the stress relaxation tests were also accomplished upon as-received springs; cold drawn and wound, but with no solution or precipitation treatments. These 'as-wound' springs were then compared with the solution + precipitation only (S+P) springs and the solution + precipitation + thermomechanically-treated (S+P+T) samples.

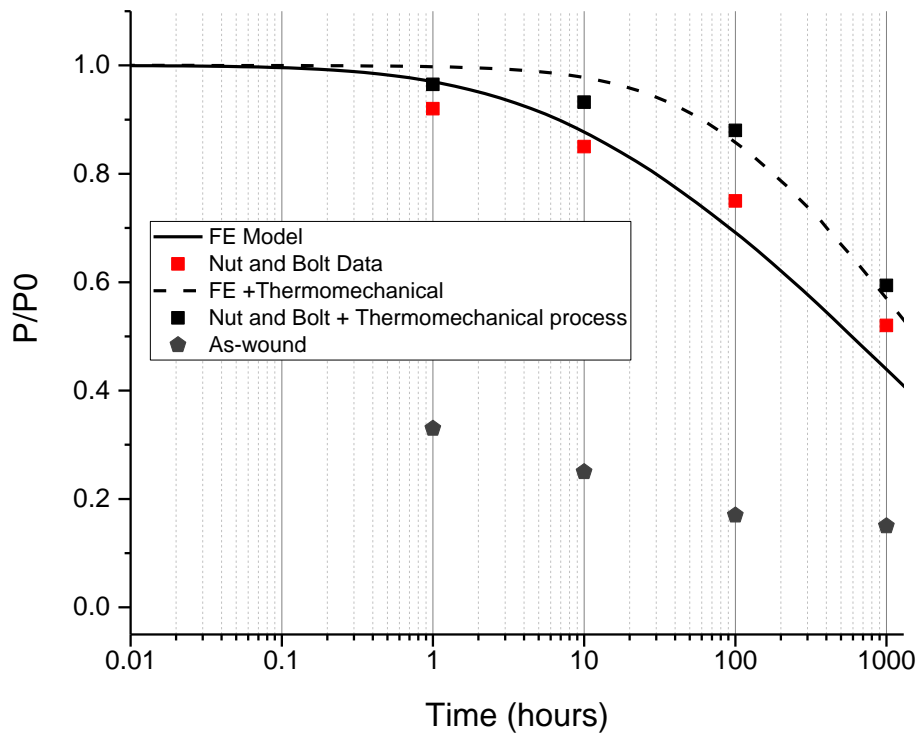


Figure 60: Stress relaxation nut and bolt test data for Nimonic 90 at 650°C, 6mm displacement

The results in Figure 60 show a very significant increase in stress relaxation resistance between the as-received springs (black circles) compared with the S+P only case (red squares). The majority of increase in stress-relaxation resistance is seen here; when relaxed 1 hour, the as-received case drops to 0.33 of the initial reaction force, a value that the precipitation hardened case does not reach even up to 1000 hours of relaxation testing. Significant gains are made by thermomechanically treating the S+P case, with the model predicting between 5 and 10 times increase in stress relaxation resistance (measured as time to reach an equivalent ratio of force reduction) from the S+P treated samples compared to the S+P treated samples (black squares), while the mechanical tests reveal at least a 10 times increase between 1 and 100 hours, and a 2 times increase between 100 and 1000 hours.

9.4 Predictions for changing displacement and temperature of thermomechanical process

As shown in Figure 54, it is predicted that a 10 mm displacement will lead to a higher value of H within the thermomechanical process time. By increasing from 8 mm to 10 mm for the thermomechanical treatment at 650 °C for 30 minutes, and comparing with the FE predictions for the stress relaxation values, it is possible to determine the effect initial strain can have upon the springs long term behaviour. Similarly, increasing the temperature from 650 °C to 700 °C for both the 8 mm and 10 mm thermomechanical cases would determine whether the effect of temperature is greater than displacement. Figure 60 demonstrates that performing a thermomechanical process at 700 °C with an 8 mm displacement for 30 minutes will increase the time required to reach 0.8 of the initial reaction force, P_0 , by a factor of 2.5, compared with a thermomechanical process under the same conditions at 650 °C. Increasing the displacement from 8 mm to 10 mm gives a predicted increase of 3.15. Further improvement can be made by increasing the temperature from 650 to 700 °C for the 10 mm case, giving a ratio of 10 for the time to reach 0.8 of P_0 .

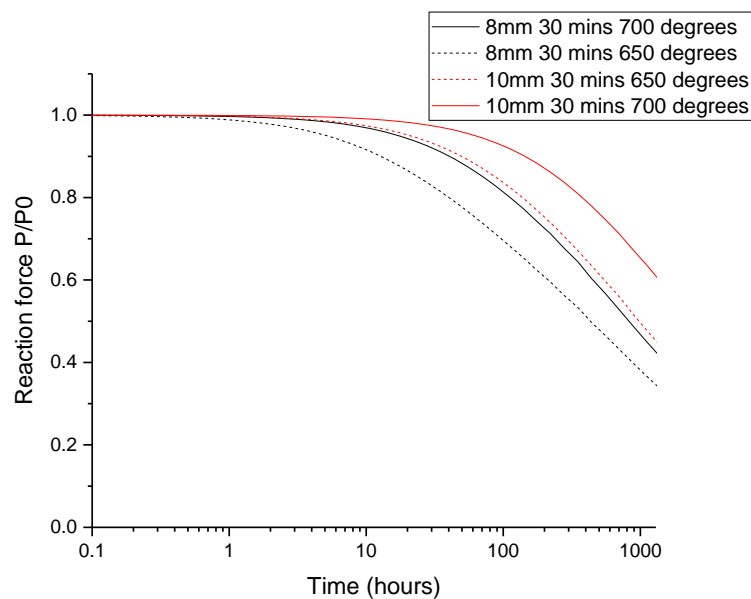


Figure 61: F.E model predication for 8mm, 10mm thermomechanical processes (displaced for 30 mins at 650 °C and 700 °C degrees) then relaxed at 6mm compression at 700 °C.

9.5 Stress Relaxation Discussion

By increasing the back stress hardening of the samples with a thermomechanical process, equivalent to an increase in the hardening parameter, $H(t)$, within the FE model, a significant increase in the stress relaxation resistance of the Nimonic 90 springs has been observed. This is in agreement with the predicted increase in the stress relaxation behaviour of the model. The model may be further calibrated by changing the particle radius size, r_p . However, as r_p is placed within the hyperbolic sine term, a small difference may lead to large changes in behaviour that possibly takes the predictions of the Dyson creep rate model too literally. Obtaining the correct dislocation density based upon the twisting of wire into the form of a coil spring was attempted in section 8.24, and appeared to work at the shorter time periods. This was also true in the nut and bolt experiments, with the mechanical tests appearing to reach steady state creep in smaller time scales than the FE model. It may therefore be most efficient to rescale the initial primary creep drop in reaction force through manipulation of the initial ρ_0 value.

Ageing of nickel superalloys can be expected to have a significant effect on the microstructure, and thus on the material properties at high temperature [1]. Optimum hardening of γ' particles occurs as the particles approach the transition from weak to strong coupling of dislocation pairs within the lattice. These coupled dislocations must overcome the anti-phase boundary energy, γ_{APB} , which is of the order 0.1 J/m^2 [96], where experiments in TEM by Kruml et al showed the cutting stress is approximately 400 MPa, implying that substantial order strengthening is to be expected in the microstructure, which is seen here.

The S+P+T sample is superior in stress relaxation resistance to both the as-wound and S+P samples, with Figure 60 suggesting a full 10 times improvement from the S+P data up to 100 hours, and significant improvement of 2-3 times improvement in relaxation resistance between 100 and 1000 hours. The FE model appears to under-predict the reaction force at 1000 hours for both the S+P and S+P+T cases compared with the mechanical data. This may be due to poor fit with the input parameters chosen for these tests, or under-prediction of the back-stress hardening effect.

The 1000 hour nut and bolt mechanical stress relaxation tests have only been completed at one particular temperature and displacement, with only an 8 mm, 650 °C for 30 minutes thermomechanical process. Significant increases in stress relaxation resistance have been predicted by increasing the thermomechanical compression and temperature as shown in Figure 60, and it can be seen that increasing the compression has a large effect on the increase in stress relaxation resistance by a factor of 5. Increasing the temperature to 700 °C appeared to have a compounding effect, leading to an approximate 10 times increase in stress relaxation resistance. The multiple-stage deformations implemented in Figure 51 could potentially increase the stress relaxation behaviour significantly, however the effect on the microstructure would need to be investigated. The possibility of recrystallization and annihilation of dislocations could potentially reduce the back-stress hardening effect, and other problems such as fatigue and crack-propagation would also need to be investigated to ensure safety of operation. The multiple-stage hardening was not possible for high displacements of springs due to restrictions of a geometrical nature. One possible solution would be to increase the pitch of the spring at the design stage, and to reduce its height and pitch through a thermomechanical process, to the required in-service height. Using the FE models presented here, one may calculate the predicted loss of height during the thermomechanical process and choose the appropriate temperature and time for the relaxation.

9.6 Conclusions

Stress relaxation testing using an F.E and analytical model on nickel superalloy coil springs has been shown to have good correlation with mechanical test data during single-stage deformation. Investigating possible improvements to the stress relaxation behaviour in the springs led to thermomechanical processing at warm-working temperatures for both single-stage and multiple stage deformations on the samples. The following conclusions can be made:

- 1) Both the F.E and the finite-difference analytical model have been shown to give good approximation of the stress relaxation of nickel superalloy coil springs, as calibrated in Chapter 8. Initial tests gave much higher stress relaxation than predicted in uniaxial test data on wire samples. To rescale the stress relaxation from weeks/months to minutes/hours, creep rate prefactor A was modified. The key calibrating factor in A was the assumption that the GND density was much higher in the coiled spring compared with the expected values of dislocation density for a straight bar or wire sample. The subsequent heat treatments after winding the spring would lead to a reduction in SSD's, but would not be expected to reduce the GND population significantly, as they are all of same sign and thus cannot annihilate one-another.
- 2) A simple thermomechanical process of 8 mm compression at 650 °C for 30 minutes can be modelled using FE and comparing with mechanical data it is found that the stress relaxation resistance of the spring can be increased by between 5 and 10 times.
- 3) Short thermomechanical processes are preferred due to cost and manufacturing time, and can also be shown to prevent over-coarsening of γ'
- 4) Increasing the number of deformation stages, temperature and displacement have all been shown to have significant increases in the stress relaxation behaviour of the springs. In order to make the most efficient process, increasing the pitch/height of springs would allow for far better stress relaxation behaviour.

The next chapter will investigate the microstructural effects the stress relaxation and thermomechanical treatments have on the samples up to 1000 hours.

Chapter 10: Microstructural and Mechanical Characterization

In this chapter the effect of stress relaxation on the microstructure of Nimonic 90 is considered. This has been accomplished in two separate ways:

- 1) Scanning Electron Microscopy (SEM) of the spring samples
- 2) The Vickers hardness of the samples is taken at each time step of the nut and bolt stress relaxation test up to 1000 hours
- 3) Electron Back-Scattered Diffraction of samples at different stages of relaxation

SEM was utilised in order to obtain images to characterise the microstructure of the samples, in order to understand the microstructure prior to stress relaxation tests and to give quantitative data about the microstructure for the setup for EBSD, such as step size, and indexing of phases.

Electron Backscattered Diffraction (EBSD) of the samples undergoing thermomechanical treatments and stress relaxation testing was accomplished to identify and analyse the microstructural changes undergone during deformation at increased temperatures. As the samples were warm-worked they would not be expected to have significant amounts of recrystallization involved during the thermomechanical treatment, however the change in the strain, measured as misorientation, is of great interest to this project. EBSD studies on hot deformation of nickel-superalloys have been accomplished recently by Lin et al [97] where it was found that the fraction of low angle grain boundaries decreased with temperature, and at low strain rates.

EBSD allows analysis of the grain size, shape, grain boundary misorientation, grain boundary type (eg $\Sigma 3$ annealing twins, (where the number 3 refers to the ratio of the size of the unit cell measured to a standard FCC unit cell), and sub-grain misorientation. These microstructural features give an insight into the material behaviour under deformation at high temperature.

10.1 SEM imaging

As-received Nimonic 90 springs samples were prepared by grinding the samples in stages from 200 to 1200 grit. The samples were then etched. The etchant used was two-stage. The first stage used a solution of glyceresia (15 ml of HCl, 3ml of HNO₃, 18 ml of Glycerine) to bring out the sample grain boundaries. For the glyceresia etch the sample is submerged for 20-40 seconds which leads to preferential dissolution of the γ' phase and is considered quite aggressive, and in some cases may lead to some structural information being lost [98]. The second stage is an electro-etch in a solution of 1% citric acid and 1% ammonium sulphate at 1.6 V, current density 0.2 Acm⁻². This is to cause preferential dissolution of the γ matrix and restore a level surface whilst keeping internal structural details visible. The sample is submerged and a platinum cathode is moved across the surface of the sample for 45-100 seconds.

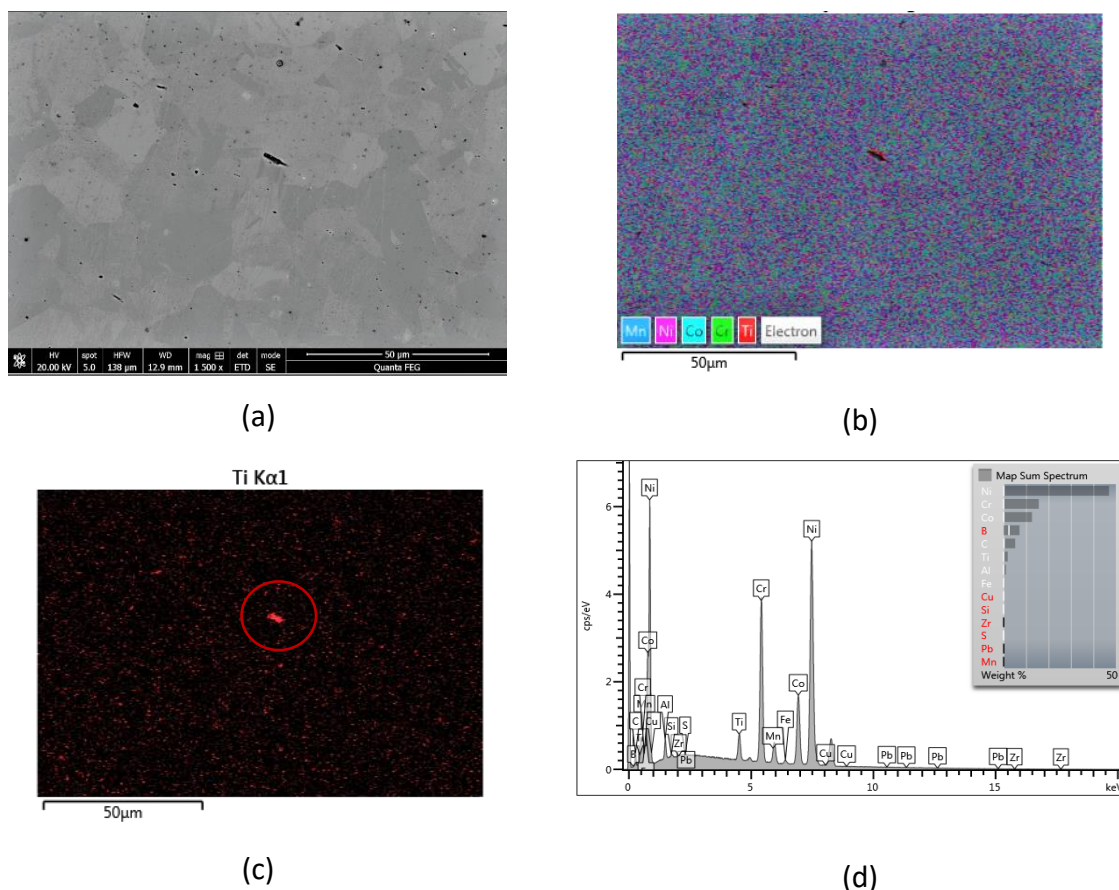


Figure 62: SEM and EDX maps for as-received Nimonic 90 spring surface, with no heat treatment and glyceresia etchant. (a) SEM image, (b) EDX map of all elements detected, (c) EDX map of Ti only, (d) EDX spectra

Figure 62 demonstrates the chemical composition and microstructure of the as-received (A.R) sample with glyceresia etching. Figure 62 (a) shows that the polycrystalline grain structure, with grains typically smaller than $50\ \mu\text{m}$ across. The chemical composition appears to be quite uniform, as shown in Figure 62 (b), with the exception of Ti, which is concentrated in what appears to be an MC carbide, according to the fact that it lies on a grain boundary and appears blocky in nature. The EDX spectra in Figure 62 (d) gives a good approximation to the expected chemical make-up of Nimonic 90, shown in chapter 3, Table 2. The wt% given here also agrees well with the predicted composition.

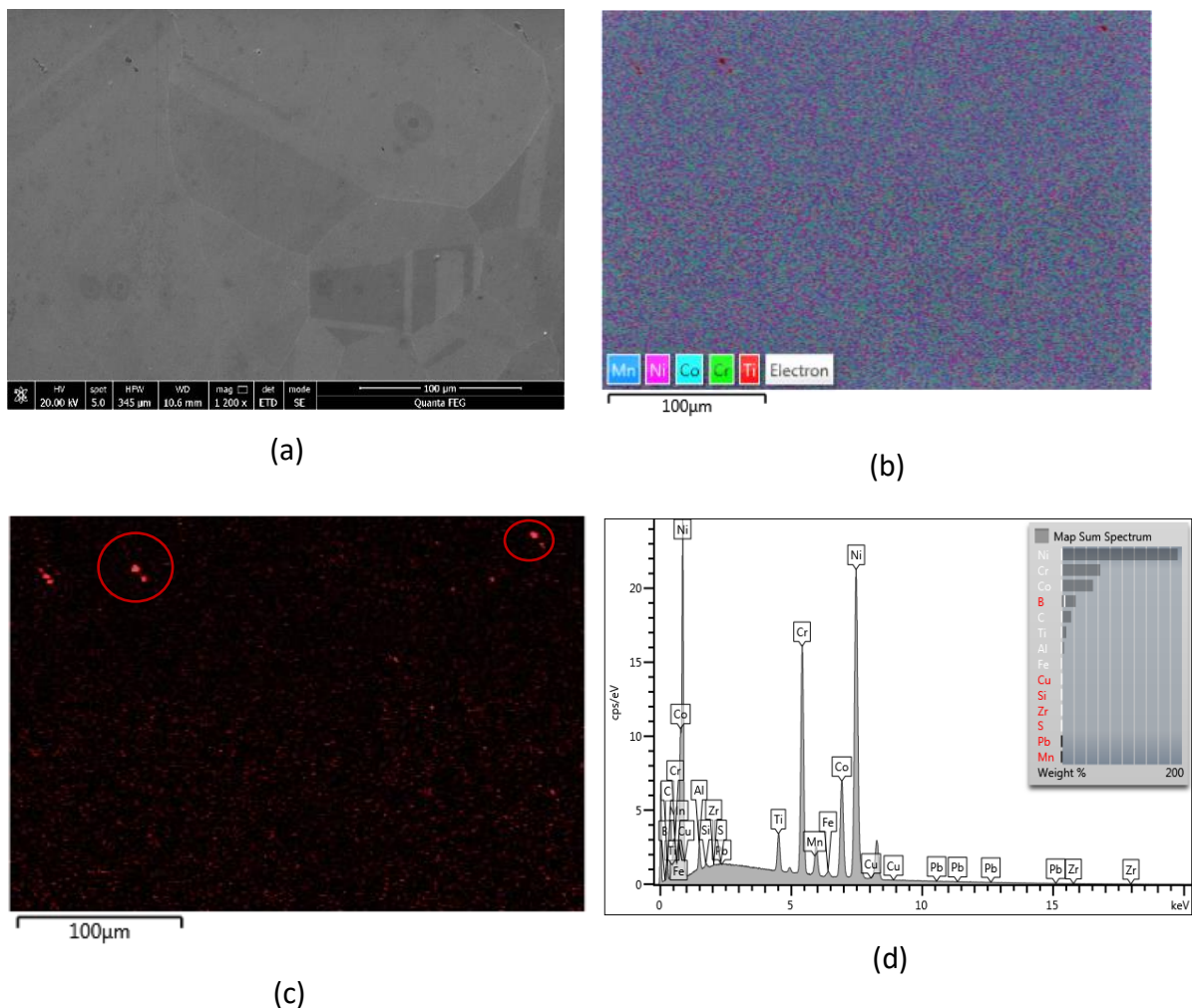


Figure 63: SEM and EDX maps for S+P Nimonic 90 spring surface, glyceresia etchant. (a) SEM image (b) EDX map of all elements detected (c) EDX map of Ti only (d) EDX spectra.

The SEM image in Figure 63 shows far larger grains than the AR sample, with what appear to be annealing twins in some of the grains. The chemical composition is similarly uniform, with some notable peaks of Ti concentrated in blocky particles, shown circled in red in Figure 63 (c) in what again appear to be carbides or nitrides such as TiC and/or TiN. A close-up of a carbide from this sample can be seen in Figure 64 demonstrating the high density of Ti in the particles, with a Ti depleted zone surrounding the particles. No $M_{23}C_6$ carbides were found using the EDX scan, which may be due to them being either non-existent or too small to be detected.

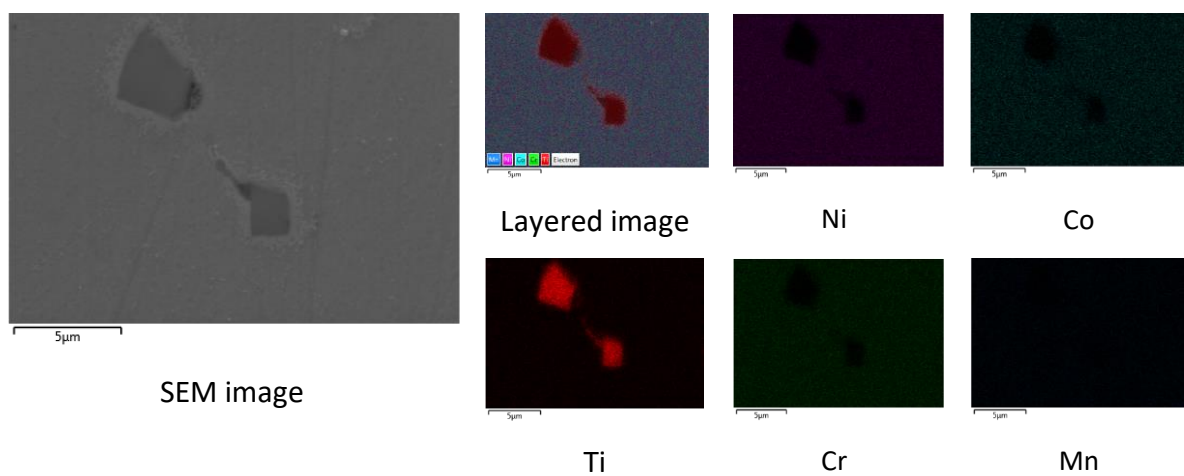


Figure 64: SEM and EDX images for Ni, Co, Ti, Cr and Mn in S+P sample.

SEM imaging of the S+P sample with the electro-etch shows the γ' particles at very high (240000x) magnification. It can be seen that the γ' is of approximately uniform size, of the scale of approximately 10 nm, as shown in the insert in Figure 65 and they appear spherical in nature. Similar morphologies have been found in René 88 under similar heat treatments with similarly sized nano-scale γ' particles [99].

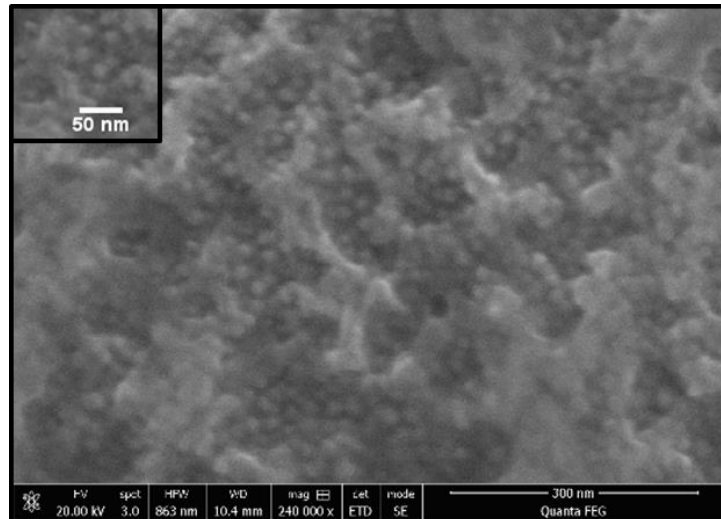


Figure 65: SEM image of S+P with the two-stage glycergia + electro-etch.

SEM summary

SEM and EDX study of the A.R and S+P samples has revealed that the heat treatments have significantly increased the grain size, and there appears to be an increased number of annealing twins in the heat treated sample. The presence of annealing twins can reduce fatigue and may even reduce corrosion, and are related to recrystallization within the microstructure. Recrystallization of grains would imply high dislocation density in that region, subsequently reduced by the build-up of dislocations that collapse into a new grain boundary, with a far lower density of dislocations. The susceptibility to recrystallization is related to the stacking fault energy of the material, and there is a relationship between pre-strain level and velocity of grain boundary migration leading to a higher annealing twin density [100], and so investigating the change in density of annealing twins utilising techniques such as EBSD allow one to infer strain history in the material during relaxation. This is accomplished in the following section. Both samples are found to contain blocky MC type carbides containing a high concentration of Ti, and overall uniform distribution of their component elements. The γ' appears to be of uniform spherical shape, and expected size (~ 10 nm) post heat-treatment.

10.2 Vickers Hardness Test

To investigate the effect of the thermomechanical process on the mechanical properties of the material a series of Vickers micro-hardness tests were completed on the surface edge of a coil spring and on the cross section of cut spring coil wire. The tests were accomplished on a Wilson Hardness Tester Tukon 1102 utilising the WIN-Control v.2.99.11 software for analysis. Indents were made at 500 g of pressure at each indent. The flattened end-coil of the spring samples were removed using a precision diamond-coated cutter. Samples were then mounted in resin and then prepared by grinding in five stages from 250p SiC grit paper to 1200p, followed by polishing with diamond suspensions at 6 μm 3 μm and 1 μm particle size increments. These tests were accomplished at room temperature. Hardness is proportional to the yield stress, and can be increased by both the dislocation density and a fine precipitate dispersion. It would be expected to have a complex interaction with the creep rate, as the creep rate is indeed also increased by the dislocation density, but reduced with the fine dispersion of precipitates. The grain size is assumed to be negligible in the current creep regime, however it is worth noting that a smaller grain size will also increase the hardness. While it is difficult to correlate the hardness with creep rate at high temperature, the change in the hardness during the testing will give an indication as to the micro-mechanical changes in the springs, such as dislocation multiplication, and possible recrystallization. As the dislocations are assumed to not annihilate during the higher temperature stress relaxation tests, due to being predominantly GND's and the temperature well below the annealing temperature, these tests are valid to predict the same behaviour while in the stress relaxation temperature regime.

10.21 Spring wire surface Vickers hardness test

The hardness is predicted to increase with the strain experienced by the material due to dislocation density, and possibly due to back-hardening. Maximum strain is expected to occur on the outside of the spring wire, and so the surface is considered first. A series of Vickers hardness tests were accomplished on the polished surface of the coil by cutting the bottom coil of a Nimonic 90 spring, mounting it in resin, and then grinding and polishing the surface to 0.1 μm .

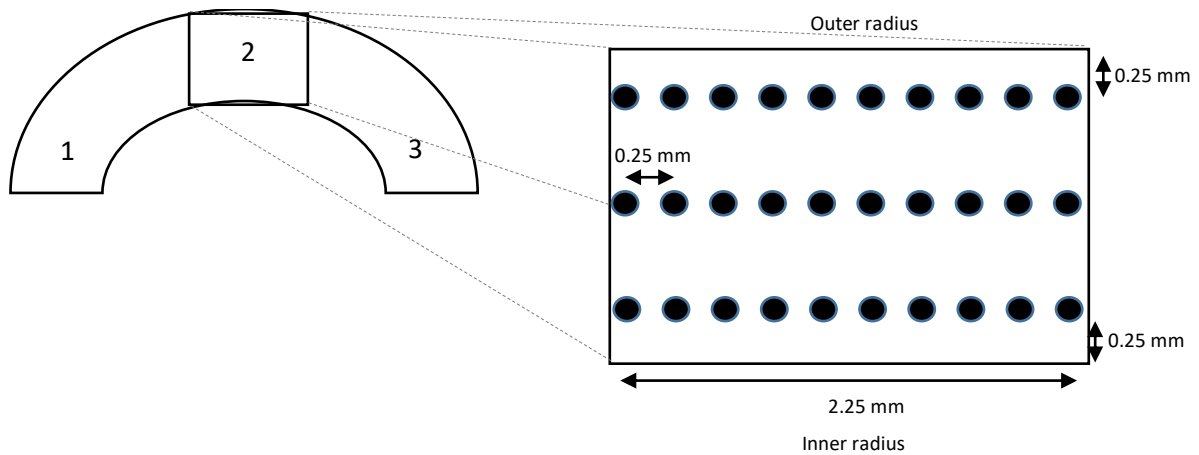


Figure 66: Top down view of end of coil, with three positions 1, 2, 3, where Vickers hardness tests are taken. Insert shows individual indents on position 2.

Three lines of ten indents were made at each position 1, 2 and 3, shown in Figure 66 with a line of ten indents at the outer radius, in the wire centre and at the inner radius, taken at 0.25 mm, 1.25 mm and 2.25 mm from the wire outer radius. The average value was then taken at each position.

Figure 67(a-e) demonstrates the effect of the thermomechanical process upon the Vickers hardness values in the stress relaxation tests, with the average values across sites 1-3 at each time period shown in Figure 68. The S+P only samples appear to have greater variation in hardness values, as can be seen in the 1 and 10 hour samples, where significantly larger deviation in values compared to the S+P+T samples are seen.

The 100 hour stress relaxation test showed the greatest increase in hardness from the S+P sample, with an increase in maximum hardness from 382 HV to 423 HV. The S+P sample increases in hardness as the stress relaxation time increases. The S+P+T data is more complex, softening within the first hour, but hardening to similar values at 10 and 100 hours. The 1000 hour SR data shows far less variation in the standard deviation error than 1, 10 and 100 hours, which could imply that the dislocation structure in the S+P sample is far more uniform after 1000 hours. There is not expected to be much, if any, variation between hardness values between positions 1, 2 and 3. However, there is some variation seen in some of the data in Figure 67. This may be explained by the fact that there was a small change in depth of the cut

across the sample due to the spring pitch. This led to position 1 and 2 being deeper into the sample than position 3, which was closer to the sample surface, where more strain could be expected, this may have led to position 3 having a slightly higher Vickers hardness than sites 1 and 2 in some cases.

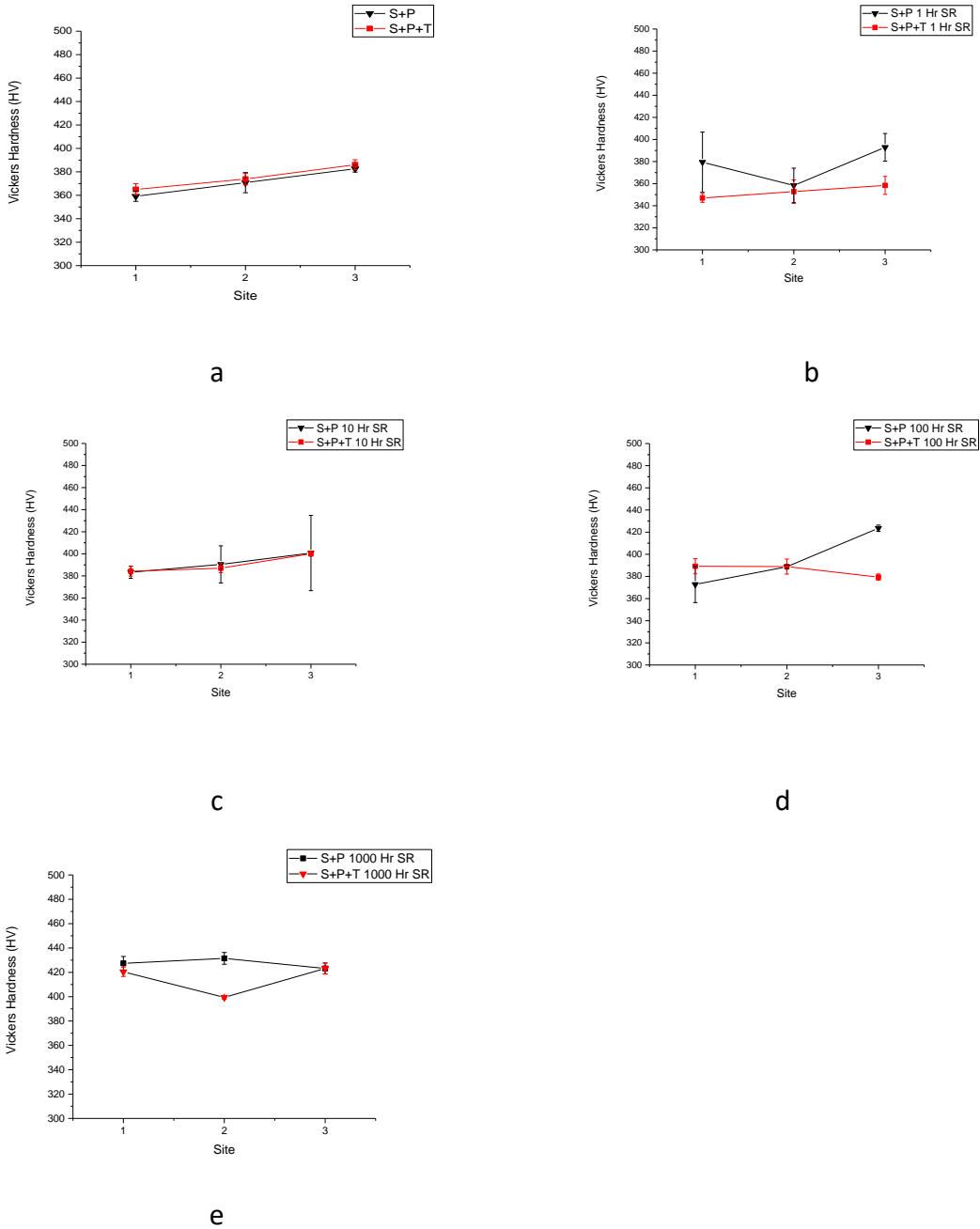


Figure 67: Vickers hardness test results for a) 0, b) 1, c) 10, d) 100, e) 1000 hour stress relaxation tests (6 mm displacement at 650 °C).

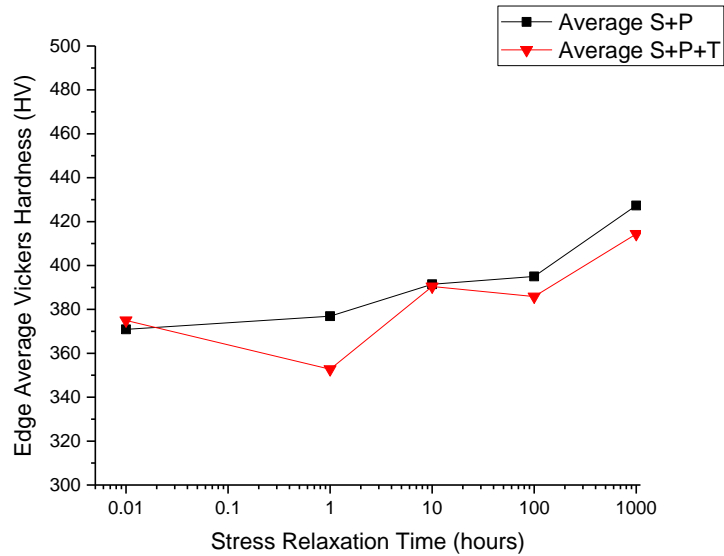


Figure 68: Average Vickers hardness on spring wire surface at each stress relaxation time on surface of spring wire for 6 mm displacement at 650 °C up to 1000 hours.

10.23 Cross-section Vickers hardness test

Hardness tests were also accomplished across the cross section of the coil wire, cut from the wire coil and mounted in resin. Vickers hardness tests were made along the centre diameter, from the outside radius to inside radius of the coil, as shown in Figure 69. Sample preparation was identical to the spring coil surface case. The wire is 2.5 mm in diameter, and so measurements were taken every 0.25 mm, from 0.25 mm to 2.25 mm, to avoid edge effects on the readings. Three sets of readings were taken on each sample, with the average used as the final value.

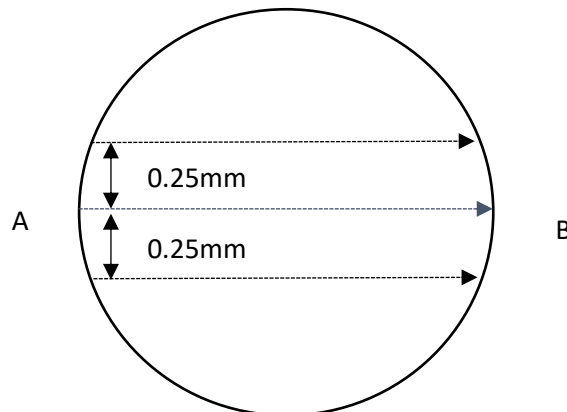


Figure 69 sketch of cross section of coil wire, showing Vickers hardness test lines. Scans begin from the outside radius, A, to the inside radius B.

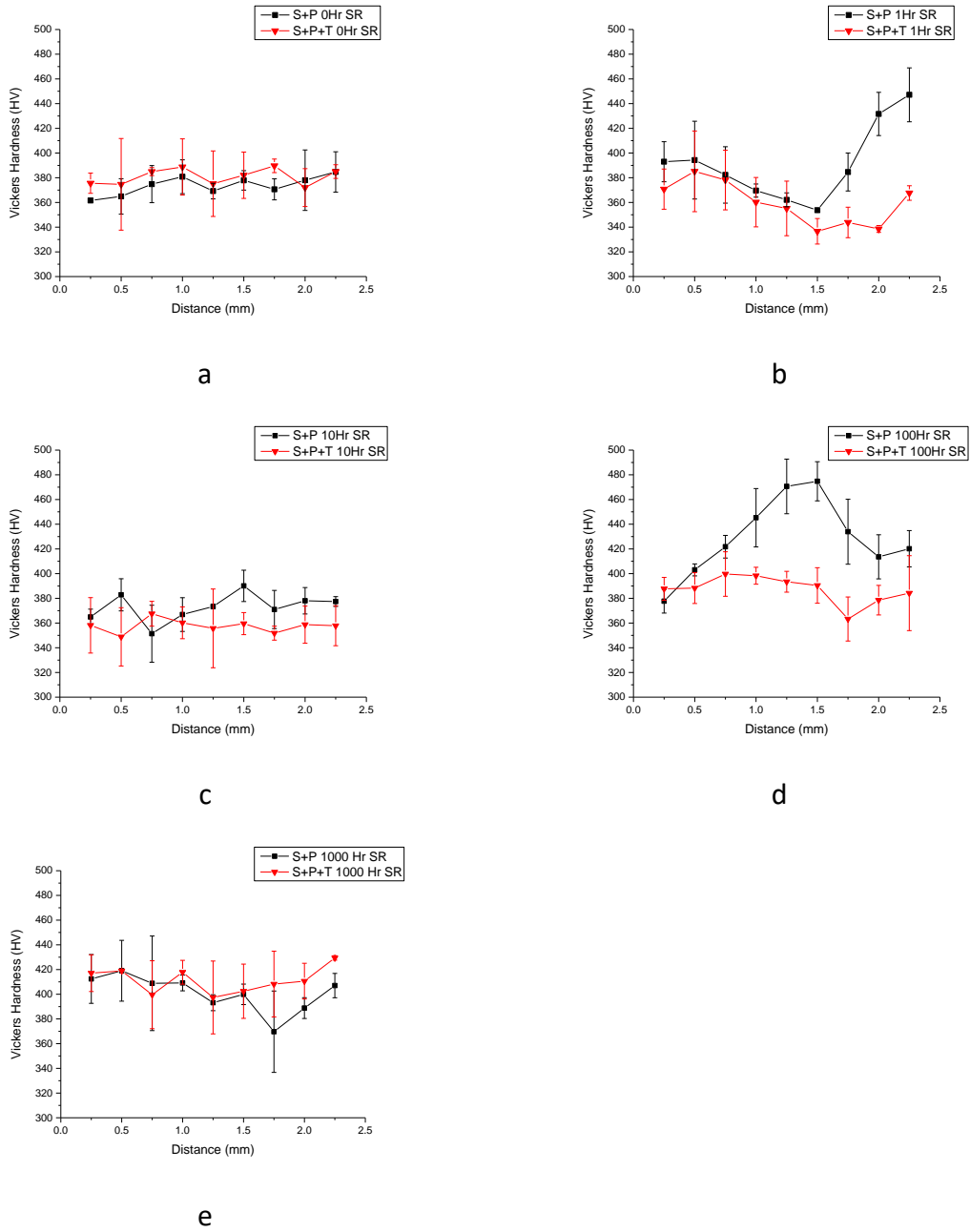


Figure 70: Cross-sectional Vickers hardness test results for a) 0, b) 1, c) 10, d) 100, e) 1000 hour stress relaxation tests (6mm displacement at 650°C).

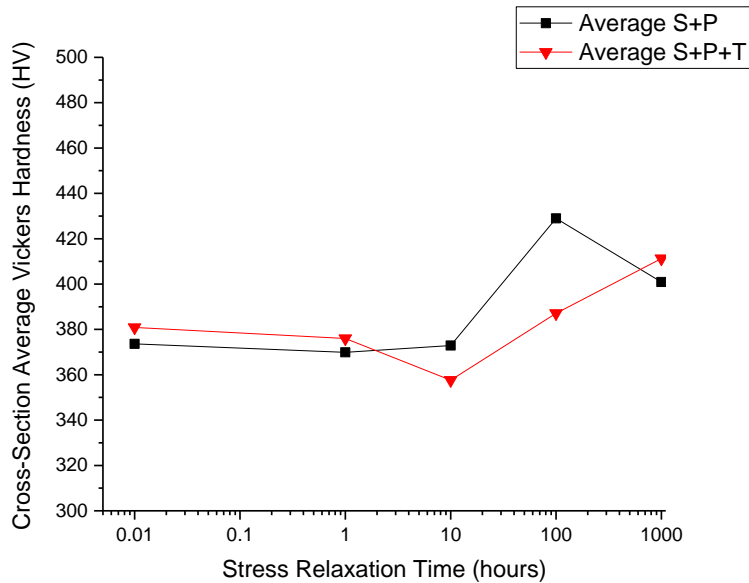


Figure 71: Average Vickers hardness on spring wire surface at each stress relaxation (SR) time for 6 mm displacement at 650°C up to 1000 hours.

The cross-sectional hardness values appear to generally increase from 0 hour SR to 1000 hour SR, as seen in Figure 70 and Figure 71. It would be expected that the inside and outside radius values of the hardness may be higher than the wire centre, as there less strain in the centre. The hardness results, however, show no clear trend of this, except in the case of 1 hour SR S+P, which approaches 447 HV at the inside radius. This large increase in hardness towards the inside radius is not seen in the 10 hour SR values, which demonstrates a more steady distribution of values, changing again at 100 hours SR in which the peak values are seen in the centre of the spring wire, 1.25mm-1.5mm. This central peak is not seen in the subsequent 1000 hour SR sample.

Observing the average Vickers Hardness against time for shows a general increase from the initial values to approximately 400-410 HV. There is very little change in the first hour for both S+P and S+P+T, with a slight decrease in the S+P+T between 1 and 10 hours. After 10 hours, both samples show a steady increase in hardness, with the S+P sample peaking at 100 hours. The 100 hour sample may be considered an anomalous result as the hardness in the centre of the spring would not be expected to be higher than the outside or inside surface. One explanation, however, may be that the spring has undergone an effective heat treatment in the ten hours of relaxation it has experienced at 650°C, this could have coarsened or

precipitated new γ' particles, leading to reduced hardness, providing the volume fraction remains the same or is reduced [2]. The values of the S+P and S+P+T hardness for the cross-section against surface values are demonstrated in Figure 72. It can be seen that the S+P values for the surface and cross-section are close up to 1 hour, but diverge greatly from 10-1000 hours. In this case the surface values are generally higher than the cross-section, except in the case of 100 hour relaxation, where the cross-sectional values are significantly higher. The S+P+T cross-section against surface graph shows that the surface values are slightly smaller than the cross-section hardness at first, and the hardness reduces up to an hour into the stress relaxation test. The cross-section values also follow the same pattern, albeit at a slower pace, between 1 and 10 hours. One would not expect to see softening effects within 1 to 10 hours, and so these values are surprising. The overall trend, however, is an increase in hardness over time for both samples, reaching equivalent values of hardness at 100 and 1000 hours.

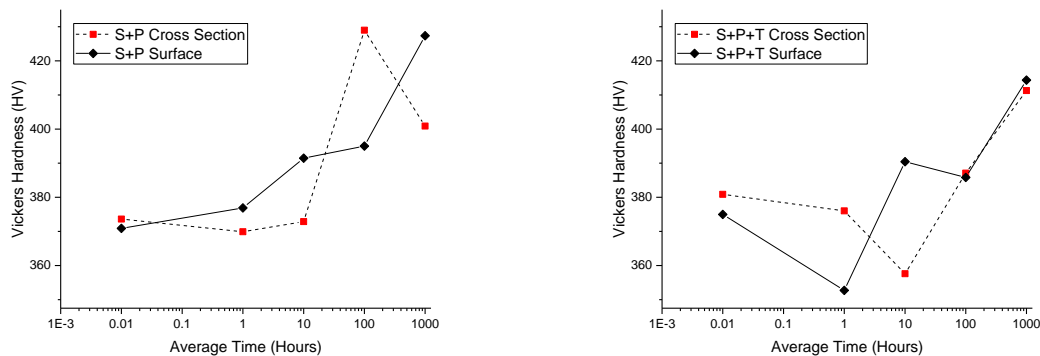


Figure 72: Left shows the average S+P Vickers hardness values for the cross-section against the surface values. Right shows the S+P+T Vickers hardness values under the same conditions.

10.24 Hardness test discussion

It would appear that the hardening effect across the cross section is greater than expected, compared to the surface hardness tests, as the cross-section would be expected to undergo significantly less strain during the tests. Vickers hardness is predicted to reduce with decreasing volume fraction of γ' , and over-coarsening of the particles [101], and so the hardness increase is likely due to strain hardening effects or smaller increase in particle size

into the optimal zone for hardness. Strain hardening is expected to occur as the dislocations within grains are locked on γ' particles or nucleated during the stress relaxation testing, creating dislocation tangles. It is predicted that the macro scale hardness will reach a saturation point, related to the increase in dislocation density and strain rate. The increase in dislocation density for 1000 hours stress relaxation tests is shown in Figure 73 predicted by the FE model utilising the equation $\rho(t) = \rho_0 \left(1 + \left(\frac{1}{\sqrt{3}} \right) K_0 \gamma_c \right)$, where $K_0=300$.

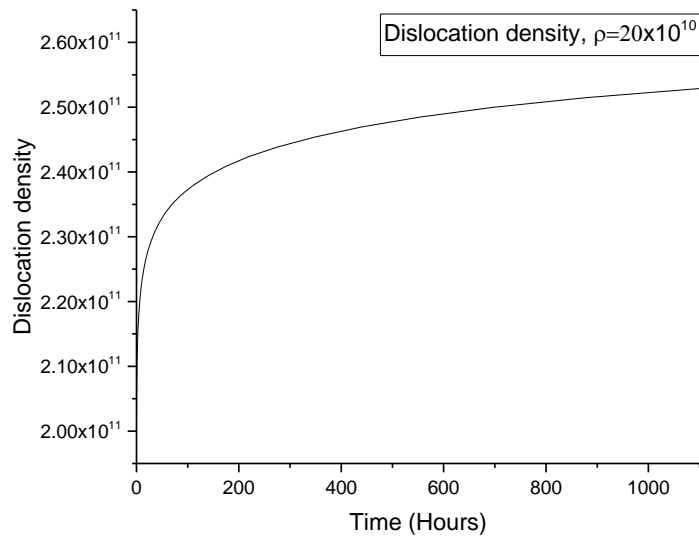


Figure 73: Dislocation density calculation in F.E model for $\rho(0) = 20 \times 10^{10} m^{-2}$.

Figure 74 (a) and (b) demonstrate the relative increase in hardness compared with change in particle volume fraction and size, and the dislocation density increase over the 1000 hours test period. It can be seen the volume fraction changes little from the values after 2 hours. The particle diameter increases continually throughout the 1000-hour test, with the values given by modelling the increase in particle diameter in JMatPro. The increase is non-linear, and the full values are given in Figure 75. As the rate of change varies the increase in diameter does not appear to match the change in hardness values. The dislocation density values, however, appear to share a good correlation of rate change with the hardness values, which may imply that it has the dominant effect on the sample hardness under the 650 °C condition. As the dislocation density increases the yield stress (and thus the hardness) of the samples

would be expected to increase according to $\sigma_Y = \sigma_0 + \alpha' \sqrt{\rho}$, where α' is a material constant. An increase of 25% of ρ would therefore be expected to lead to an increase in hardness of approximately 11-12%, which appears to be reflected in Figure 74 (a) and (b).

Work hardening, rather than particle coarsening, appears to be increasing the hardness. Investigation into measuring the dislocation densities during the stress relaxation testing would allow a more definite conclusion, as this prediction for dislocation density increase does not take into account recovery or recrystallization effects that could reduce the dislocation density in the material, in which case the γ' coarsening could be the dominant effect increasing the hardness. A method of calculating the dislocation density at each time period is introduced in section 10.54.

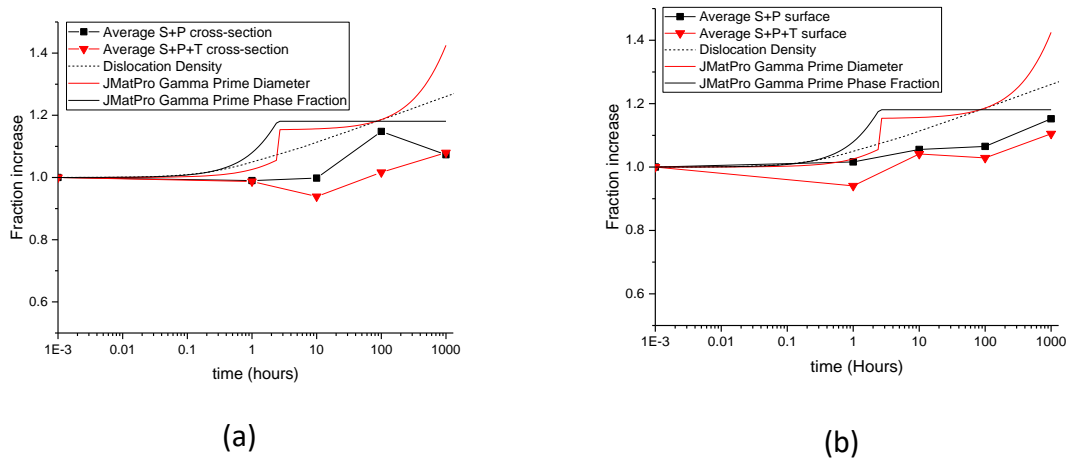


Figure 74: (a) shows the increase in normalised Vickers Hardness of S+P against calculated normalised dislocation density increase. (b) shows the normalised Vickers Hardness of S+P+T against dislocation density increase

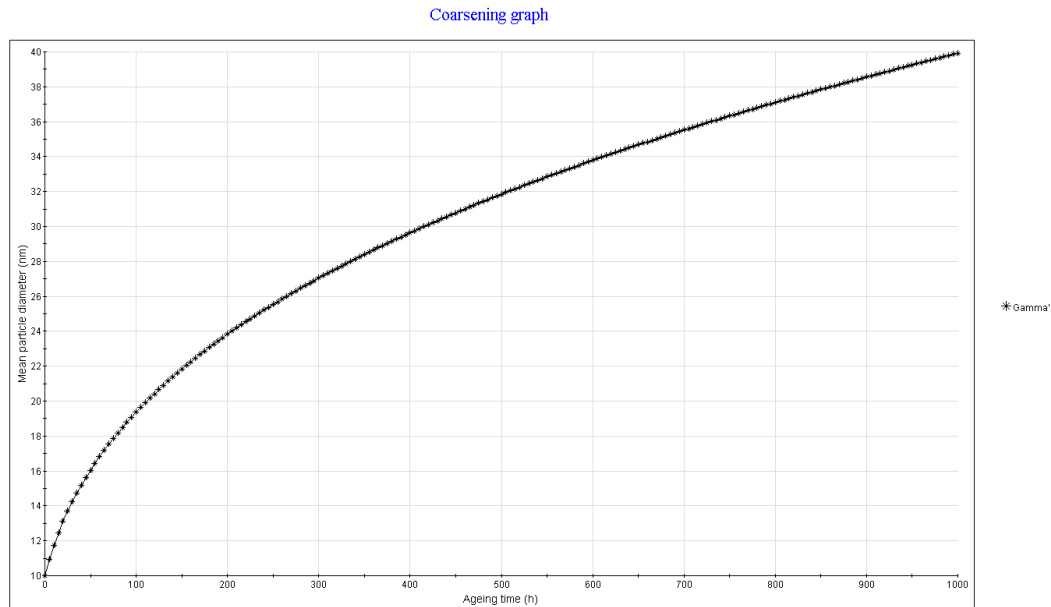


Figure 75: Coarsening of gamma prime at 650 °C taken from JMatPro, over a 1000 hours stress relaxation test full data.

10.3 EBSD operation

EBSD patterns are utilised to characterise the crystallographic orientation, grain boundary 'misorientation' and characterisation, texture, phase, strain and structure of polycrystalline samples. This data is obtained using a FEGSEM setup that has been equipped with a phosphor screen to generate a diffraction pattern from diffracted electrons, a Charged Couple Device (CCD) camera that can observe the diffraction patterns, known as Kikuchi patterns.

The setup for the system requires that the sample be tilted at 70°, after which an electron beam interacts with the sample and the diffracted electrons form a pattern characteristic of the orientation and crystallographic structure of the area in which is being impinged by electrons.

Some of the inelastic scatter of electrons from the sample will diffract at an angle that satisfies the Bragg equation [102]

$$n\lambda = 2d\sin\theta \quad (10.10)$$

where n is an integer, λ is the electron wavelength, d is the spacing of the diffracting plane and θ is the angle of the incident electrons on the sample plane. The diffracted electrons form sets of paired large-angle cones that correspond to the different diffracting planes. The electrons may then excite the phosphor screen, causing it to fluoresce, showing the Kikuchi bands. The Kikuchi pattern is then indexed, according to the Miller indices of the expected phases present in the sample.

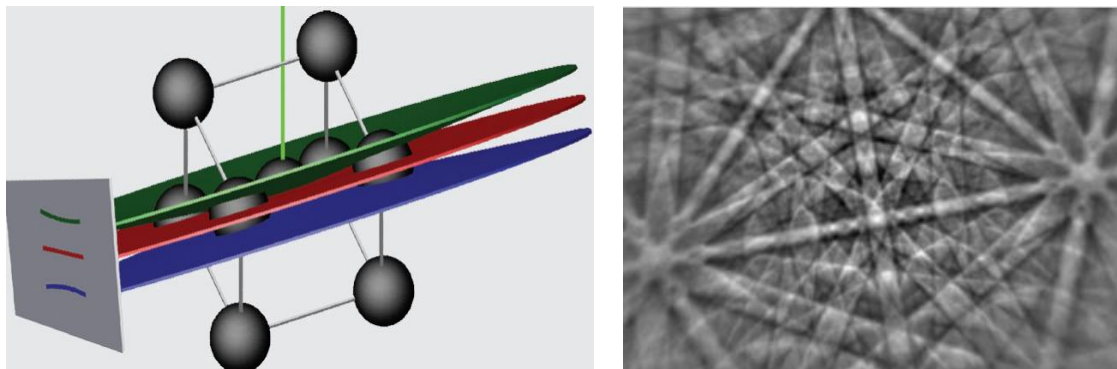


Figure 76: Left: cones, blue and green, created by electrons satisfying the Bragg equation on a BCC lattice plane. These cones are projected onto the phosphor screen, forming the Kikuchi bands, shown right [103].

The width, w , of the Kikuchi bands is given by

$$w \approx 2l\theta \approx \frac{n\lambda}{d} \quad [103] \quad (10.12)$$

where l is the distance between the sample and the phosphor screen. Samples with wider d spacing will give thinner Kikuchi bands, and vice versa. The diffraction pattern is dependent on the crystal structure, and so from the pattern, the crystal orientation may be deduced from the Kikuchi band positions.

Once the CCD obtains the Kikuchi pattern the computer applies a Hugh transform to the pattern, in order to determine the Kikuchi band position, allowing for the angles between detected bands to be calculated. These angles are then compared with a list of indexed interplanar angles for the predicted phase, after which the possible solutions are arranged to find the best-fit for the orientation of the crystal structure.

10.4 EBSD Sample Preparation and Methodology

Nimonic 90 samples utilised in the 1000 hours nut and bolt stress relaxation tests from in chapter 6 were cut using a diamond-coated precision cutter, in order to remove the end coil. As the coil had been flattened in formation, this was considered to be a suitable area for the surface EBSD. A diagram of the sample shape and scanning areas is given in Figure 77, with a scan at site A, B and C to ensure homogeneity of the sample microstructure and strains, while ensuring a suitable number of grains are sampled to give statistically significant results. The chosen samples for the EBSD are shown in Table 7. It is important to take great care in sample preparation for EBSD as the electrons diffracted to produce Kikuchi patterns only arise from the top 10-20 nm of the surface, and therefore a flat, deformation-free and highly polished surface is required [104]. Samples were mounted in resin and then the preparation of grinding in five stages from 250p SiC grit paper to 1200p, followed by polishing with diamond suspensions at 6 μm 3 μm and 1 μm particle size increments. A final colloidal silica solution of 0.2 μm was applied for 15 minutes to remove the final surface deformation left after diamond polishing. The samples were then broken out of the resin and mounted on small stubs with a glue.

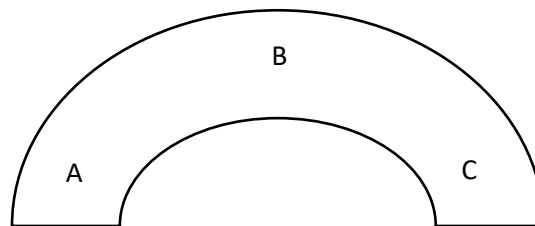


Figure 77: a top-down view of the sample surface with EBSD scanning areas A, B and C.

Sample relaxation	As-received	S+P	S+P+T
0 hr	Yes	Yes	Yes
1 hr	No	Yes	Yes
10 hr	No	Yes	Yes
100 hr	No	Yes	Yes
1000 hr	No	Yes	Yes

Table 7: work-scheme for EBSD analysis

The EBSD analysis in this thesis was carried out on a JEOL JSM-7800F FEGSEM, at tilt angle 70° and 20 KeV and working distance of 15mm. The probe current, which effects spot size, was 12 A. The 'binning', a method of measuring multiple pixels at once, and thus reducing the scan time, was set to 4x4, while gain was set to 8, with the system allowing a maximum of 12. Scans were completed at x250 magnification for areas on the sample of approximately $500 \times 500 \mu\text{m}^2$, this was chosen to give a significant amount of grains in the sample, while also covering a large enough area to be significant, as initial optical measurements had shown very large grains in the S+P and S+P+T condition. The drawback of this was the area was large enough that the step size was set to $1.0 \mu\text{m}$, making it unable to resolve γ' phase or many of the smaller carbides at grain boundaries. The Mean Angular Deviation (MAD), which represents the quality of fit between detected Kikuchi band width and the stored computer simulation, was considered acceptable at values at 1° or lower [105]. Analysis of EBSD imaging was accomplished in Flamenco using the Tango module to create suitable maps for grain boundaries, and strain.

10.5 EBSD Results

In this section the results will be divided into grain size and shape, grain boundary angles, strain measurement within a grain through misorientation, and finally a method will be presented to take the misorientation maps and calculate the assumed GND's utilising the strain gradient inserted into Nye's equation (8.21) within the sample at each time step of the stress relaxation tests. This will give an approximate value for the GND's, however will only

take data from a two-dimensional image, and thus will be an indicator and not a 'true' value of dislocation density.

10.51 Effect of heat treatments on microstructure

One of the most common maps that can be taken in EBSD is the Euler map. This map allows one to determine the orientation and shape of individual grains. The wire for the spring is cold-drawn, which can lead to longer, elongated grain structure, however it also undergoes a solution and precipitation treatment, which may create new grains, or grow grains to be much larger, therefore the grain structure of the spring wire is in question, and worth investigation. If the polycrystalline metal has clusters of similarly oriented grains, it is said to have 'texture' [106]. The orientation is calculated using the 'Euler angle' of the sample grain. This is accomplished by each crystal structure being given a particular reference orientation, and the angles required to rotate reference coordinate system into co-incidence with the sample orientation. The Euler angles are taken in order of φ_1 , ϕ and φ_2 , representing the rotations around the z-axis, followed by the x-axis and finally the rotation around the new z-axis, as shown in Figure 78.

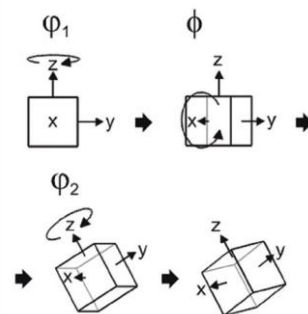


Figure 78: Euler angles and rotations [107]

The Euler maps utilise the 3 Euler angles represented by RGB colour scheme, where red corresponds to the [001] direction, the green corresponds to the [101] direction, and blue represents the [111] direction. This section contains qualitative analysis of the samples texture before and after the heat treatments applied to the post-coiled wire.

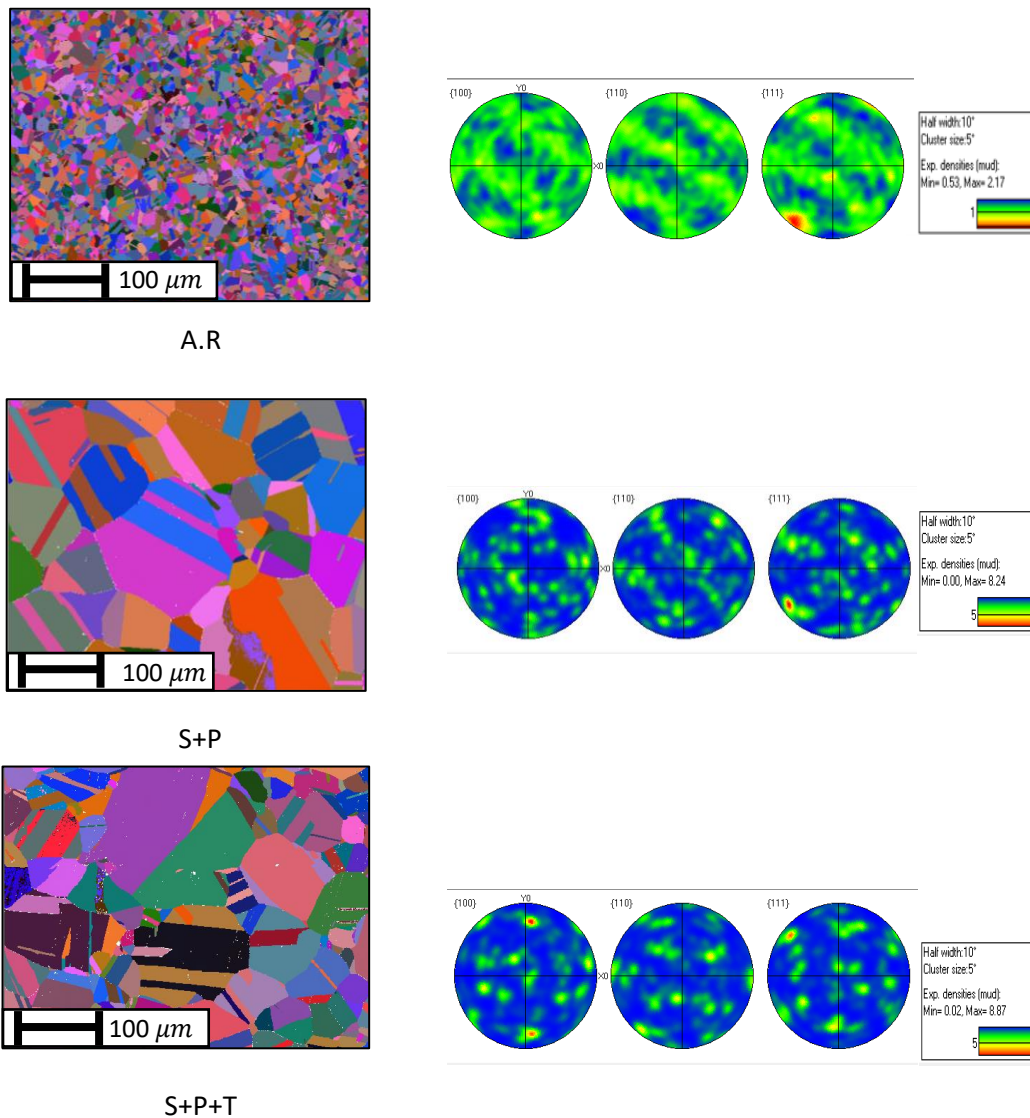


Figure 79: Euler maps and pole figures for the As-Received (A.R), Solution + Precipitation (S+P) and Solution + Precipitation + Thermomechanical Process (S+P+T) prior to stress relaxation testing.

It can be seen that the orientation of the samples for the 0 hour stress relaxation, the as-received sample appears to show a distinct preferred orientation along the {110} and {111} planes, which, after the solution and precipitation treatments, is greatly reduced. It is important to note, however, that the number of sampled grains after the heat treatments is reduced, due to grain growth. This may increase the Multiple of Uniform Distribution (MUD) in the pole figures. The scale is 1 for the A.R sample and 5 for S+P and S+P+T. this value is the mean of the range of the MUD. A value of 1 is considered to be perfectly uniform, and so the

higher the value, the less texture a sample has. Therefore, the number of sampled grains notwithstanding, the heat treatments can be seen to create a larger range of orientations, making them less textured. This agrees with the work of Detrois et al[108] which found that increased strain through cold rolling leads to a highly textured grain structure. A similar process of strain may be mirrored through the winding of the spring wire into a coil. The internal stresses are then reduced by applying the solution treatment 1150°C . It has been found that dynamic recrystallization may occur at around 1130°C [109], which leads to the reduction in dislocation density and new, strain-free grains.

10.52 Heat treatment effect on grain size and shape

Utilising the Tango module of the Flamenco software the maps for the grain size and shape can be created. The grain shape is determined by matching the grain shape aspect ratio to the aspect ratio of a given fitted ellipse. The maximum step size is considered suitable if it is less than 12% of the mean grain size for approximately 5% error in grain size and shape analysis [104], making the $1\ \mu\text{m}$ step size acceptable for accurate application. Grain area is determined by the line-intercept method, where a line is drawn across the scanned image and if where it intercepts two grain boundaries, the length between can be determined. The grain size shift between the A.R sample and the heat treated samples S+P and S+P+T can be seen in Table 8. These represent the average of all grains from scans taken at A, B and C on the sample surface, as in Figure 77. The average grain size changes considerably with the application of heat treatments to the as-received sample.

Sample	Grain size (μm)
A.R	74
S+P	785
S+P+T	644

Table 8: Grain size change with heat treatments

The grain aspect ratio

The fitted ellipse method was used in the Tango module of the Flamenco software to calculate values for the accentuated shapes of the grains in the microstructure. The distribution of values for the A.R, S+P, and S+P+T are displayed in Figure 80. The peak values for the aspect ratios are all found at 1.5, and decrease with increasing aspect ratio. No grains were found at aspect ratio 1 as this would imply a perfectly round shape. The as-received samples are more tightly correlated than the heat treated samples, with a smaller aspect ratio, while the heat treated samples are closer to one-another, with an appreciable fraction of the grains having an aspect ratio of 4 or more.

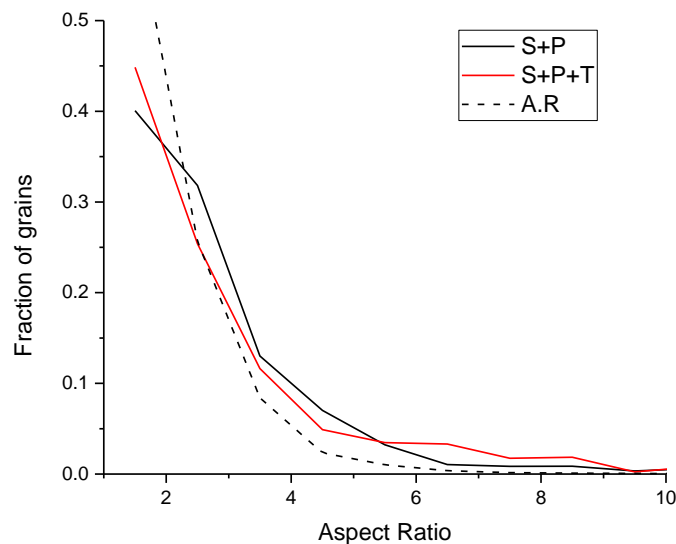


Figure 80: Distribution of aspect ratios of grains for S+P, S+P+T and A.R samples prior to stress relaxation testing.

Grain boundary misorientation

A grain boundary misorientation, also known as 'disorientation', is the crystallographic relationship between two neighbour grains, sharing the same phase. The grain boundary misorientation is important to analyse as the misorientation across a grain boundary has a large impact on the material properties; including the diffusivity and mobility [110]. Typically grain boundaries can be characterised as 'Low Angle Boundaries' (LAB's) which have total misorientation $< 15^{\circ}$. And Random High Angle Grain Boundaries (RAB's) which appropriately

have misorientations $>15^\circ$. Special grain boundary types, known as Coincident Site Lattice's (CSL's) may also be investigated, such as the $\Sigma 3$ annealing twins, which, along with a significant amount of RAB's, can be indicative of strain induced by cold working of a material. In FCC metals dislocation slip and twin deformation can be competing modes, both occurring simultaneously to accommodate plastic strain, interactions between the dislocations and twins can lead to the formation of high-angle grain boundary crystals, along with strain concentration at those boundaries [111].

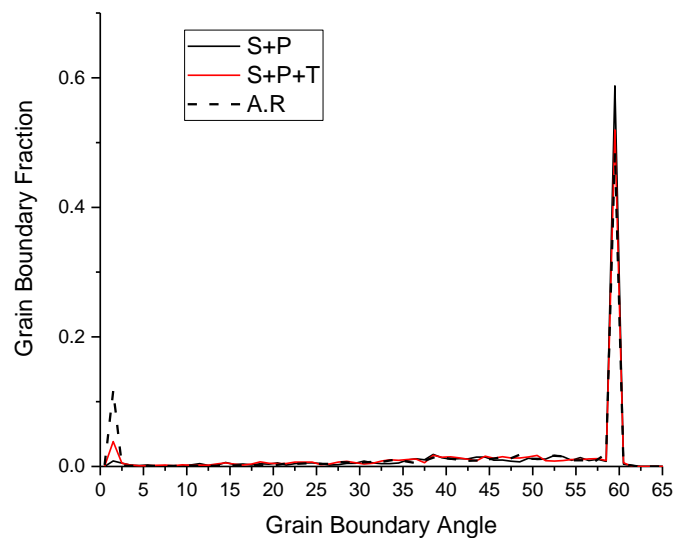


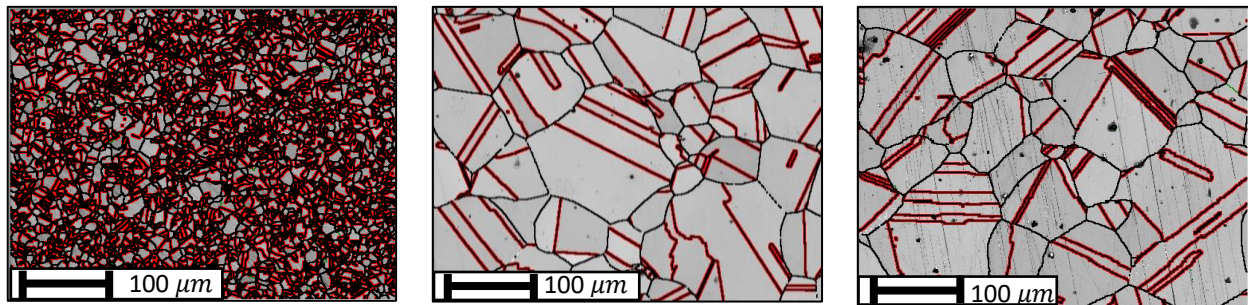
Figure 81: Grain boundary misorientation for S+P, S+P+T and A.R samples prior to stress relaxation testing.

The results in Figure 81 show the percentage of non-twin boundaries misorientation angles. There appears to be little major difference in the grain boundary angles as a result of the heat treatments. There is a gradual shift from LAB to RAB's in the amount with the S+P and S+P+T samples, compared with the A.R sample, which may be related to recovery processes, specifically recrystallization, leading to nucleation of new strain-free grains characterised as RAB's [112], which is likely the case here. The thermomechanically treated sample has a small amount of LAB's, which may be due to the dislocation movement within the grain during the thermomechanical process. It has been found that dislocations that glide, reaching the grain boundaries, where they may create large dislocation tangles, effectively act as LAB's, or they initiate the creation of sub-grains with the bulk grain, by arrangement of large dislocation

densities [111]. The strain caused by the 8mm displacement at 650 °C may be mirroring this effect, causing this small peak.

Twin boundaries

The twin boundaries are shown in red in Figure 82. The values for the average $\Sigma 3$ annealing twins percentage of grain boundaries is shown in Table 9



A.R

S+P

S+P+T

Figure 82: $\Sigma 3$ annealing twin boundaries shown in red for S+P, S+P+T and A.R samples.

Sample	Percentage of annealing twins (%)
A.R	26
S+P	58
S+P+T	52

Table 9: Annealing twin percentage for A.R, S+P and S+P+T samples prior to stress relaxation.

There appears to be a significant increase in the percentage of annealing twins. As the solution heat treatments may be inducing recrystallization, the formation of annealing twins is likely. The most common factors effecting the frequency that twins form are grain size, temperature/annealing time, grain boundary energy, prior deformation stacking fault energy and grain size [113]. As Nimonic 90 has a relatively low stacking fault energy and very large grains post-heat treatment, it would be expected that a large fraction of the grain boundaries may be annealing twins.

Microstructural strain

EBSD may be utilised to infer the plastic strain that a material has undergone by measuring the 'misorientation'. Plastic strain is known to degrade the quality of a diffraction pattern [114], this is a result of curvature of the crystal lattice due to the plastic deformation, leading to the crystal planes no longer being exactly parallel, as in Figure 83.

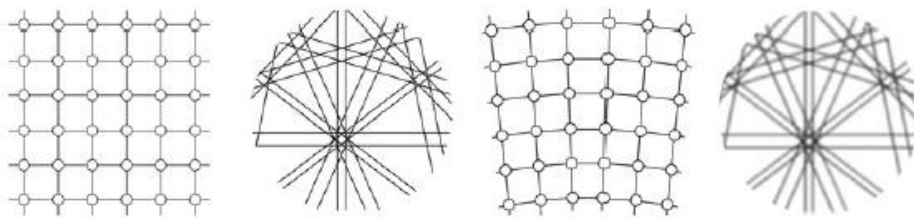


Figure 83: An unstrained crystal lattice with clear, sharp diffraction pattern, and a deformed crystal lattice resulting in degradation in pattern quality [114].

The Kikuchi pattern becomes a superposition of the patterns from each individual subgrain within the diffraction volume, giving a range of Bragg conditions within a range of angles, i.e. the contrast in the image is degraded, and this degradation is related to the amount of deformation in the diffraction volume. It is important to note that the lattice curvature is caused by the GND population, and that SSD's have been found to have little effect on the curvature and are thus not accounted for in misorientation mapping [115].

The method utilised to map the strain in this thesis is the Kernel Average Misorientation (KAM) method. The average deviation of the orientation within a 'kernel', which is a set of points around the scan point, typically selected as the neighbouring pixels. A map can then be created of this misorientation. The A.R, S+P and S+P+T samples misorientation maps are shown in Figure 84, where the misorientation it is observed that the A.R sample appears to have the greatest amount of misorientation, with some grain boundaries accommodating a relatively large amount. The S+P sample appears to have the most homogenous and lowest misorientation, while the S+P+T sample appears to have a slightly larger misorientation than the S+P. Misorientation in the heat treated samples does appear to be quite homogenous, as a graph of the fraction of total misorientation at each misorientation angle in Figure 85 shows.

It is clear from this that the heat treated samples have a smaller range of misorientation values, while the A.R sample is more spread, with a peak value at 0.25° . The S+P and S+P+T samples both have a peak fraction at the lower value of 0.15° , although it may be noted that the S+P+T sample has a higher fraction of its misorientation at the larger angle values, which is to be expected due to the small strains induced by thermomechanical process.

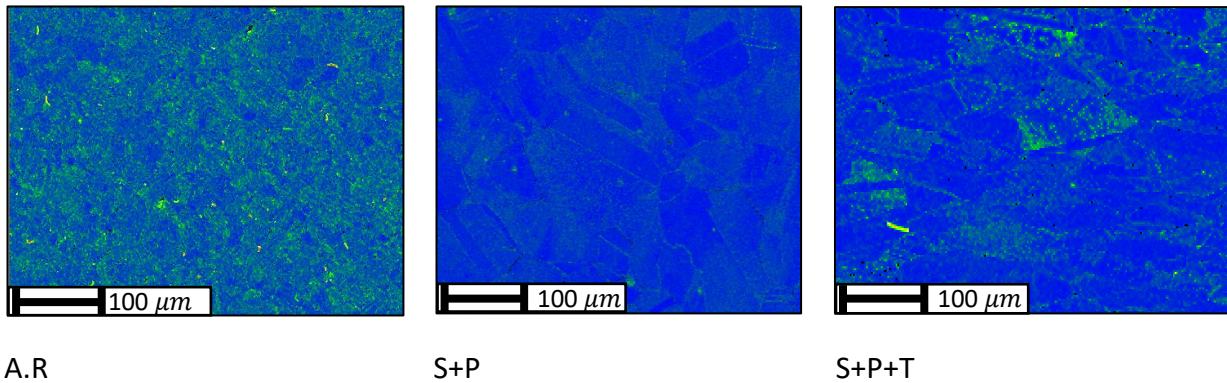


Figure 84: Misorientation maps for A.R, S+P and S+P+T samples.

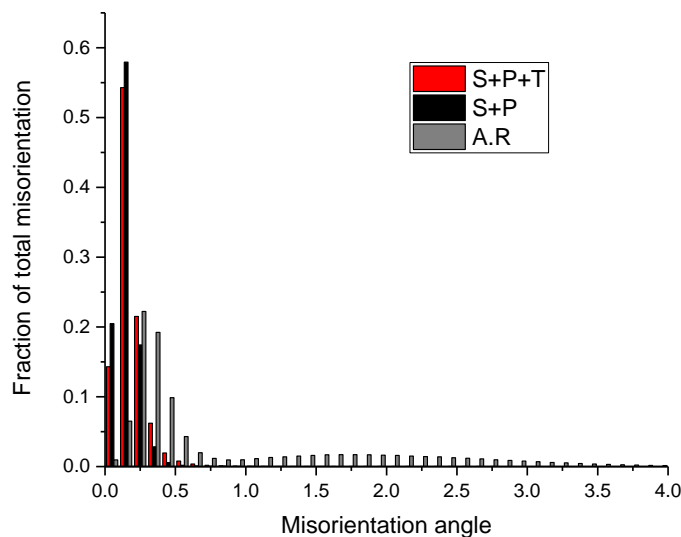


Figure 85: Fraction of total misorientation at increasing misorientation angle for A.R, S+P and S+P+T samples prior to stress relaxation testing.

Heat treatment summary

The effect of the solution treatment of 1150°C for 30 minutes, followed by 4 hours precipitation treatment at 750°C has been investigated using EBSD techniques, along with the effect the thermomechanical treatment of 8mm displacement at 650°C for 30 minutes has on the microstructure of the heat treated sample. First, it was found that the texture of the as-received sample was found to be reduced in the heat treated samples. It was shown that the solution and precipitation heat treatments cause a considerable increase in the grain size, of the order of 10 times the as-received sample size. The thermomechanical treatment has little effect on the grain size, being found on average to be 19% smaller than the heat treated sample, however this is still of the same order of magnitude. The grain shape was investigated, with the heat treated and thermomechanically treated samples noted to have a higher fraction of grains with increased aspect ratio of 3 and above, suggesting the grains have a more elongated shape post-heat treatment. It has been found that the heat treatment reduces the amount of LAB's, while increasing the number of RGB's and annealing twins significantly. Further straining by the thermomechanical process is seen to increase the amount of LAB's again, which may be dislocation arrangements acting leading to small low-angle sub-grains. Finally, the microstructural strain was investigated through the KAM method. It was found that the heat treatment leads to a lower average misorientation, with a more homogenous distribution, and the thermomechanical treatment was seen to have a small effect on the misorientation, with the peaks measurably higher at increased misorientation angle. The overall effect of the thermomechanical process appears to be a dislocation redistribution that leads to a higher proportion of low angle boundaries, while shifting the misorientation peaks slightly. There appears to be a greater intensity of misorientation within some grains of the S+P+T sample compared to the S+P sample, which may be indicative of the stress redistribution in the sample.

10.53 Stress relaxation effect on microstructure

The stress relaxation nut and bolt test samples from chapter 6 were prepared for EBSD using the same method as in section 10.52 and scans were taken at the same three areas on the sample surface as in Figure 77. The S+P and S+P+T samples are directly compared at each time

period held at 6mm displacement, at 650°C, for 1, 10, 100 and 1000 hours. The texture of the samples can be seen in Figure 86 and Figure 87. It appears that the texture does not change significantly during the stress relaxation tests. The grain size did appear to vary during the testing, however. The MUD values are found to vary only slightly between the S+P and S+P+T samples at 1 hour stress relaxation, with S+P at 12.97 and S+P+T at 10.2. Larger time scales, 10, 100 and 1000 hours also show that the texture is more closely corroborated between the S+P and S+P+T. As the stress relaxation time increases between 1 and 100 hours, it can be seen that the MUD values decrease, which may imply that the strain is causing homogenization of the grain texture across the sample.

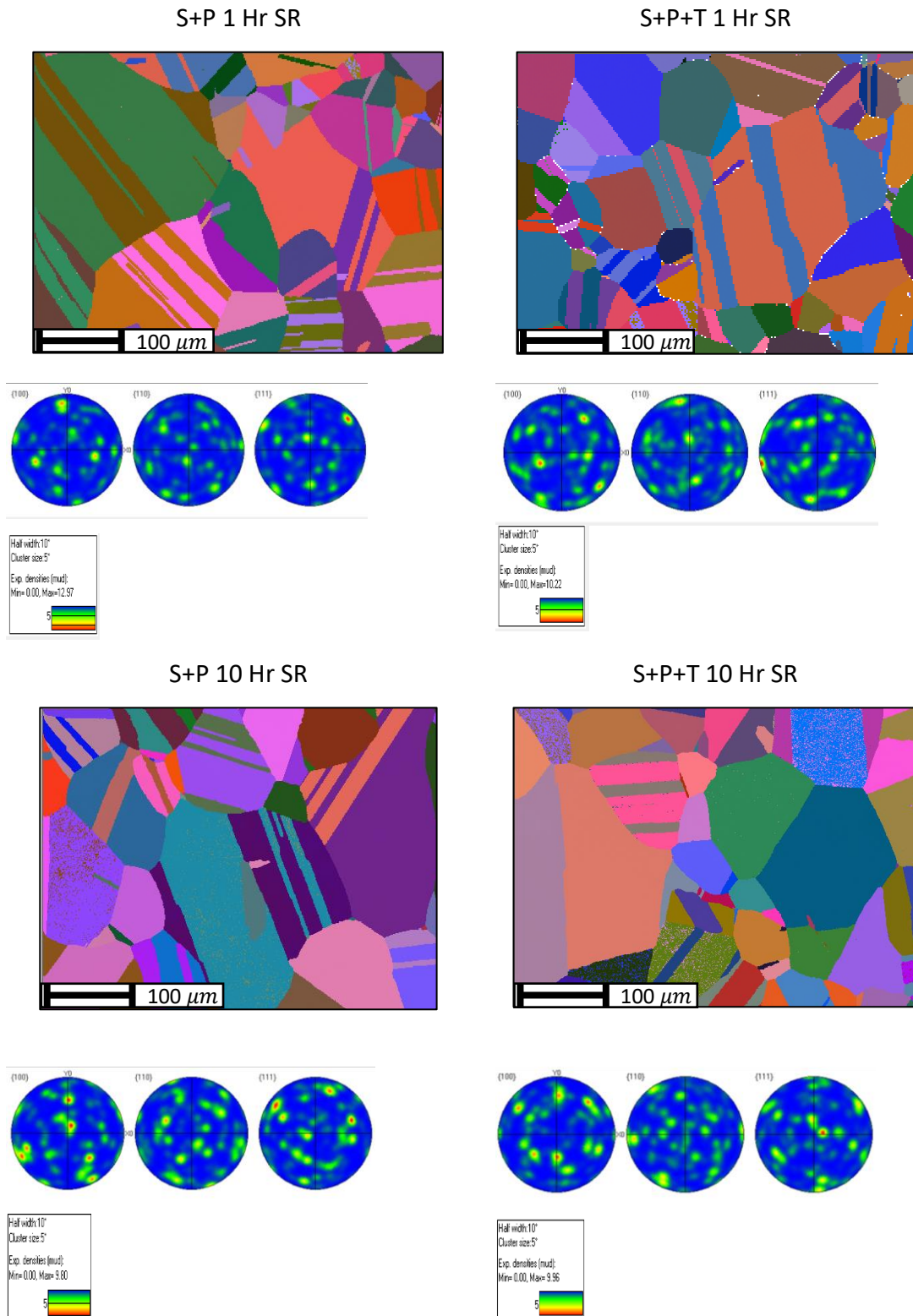


Figure 86: Orientation maps for S+P and S+P+T samples after stress relaxation tests at 6mm displacement, at 650°C for 1 and 10 hours.

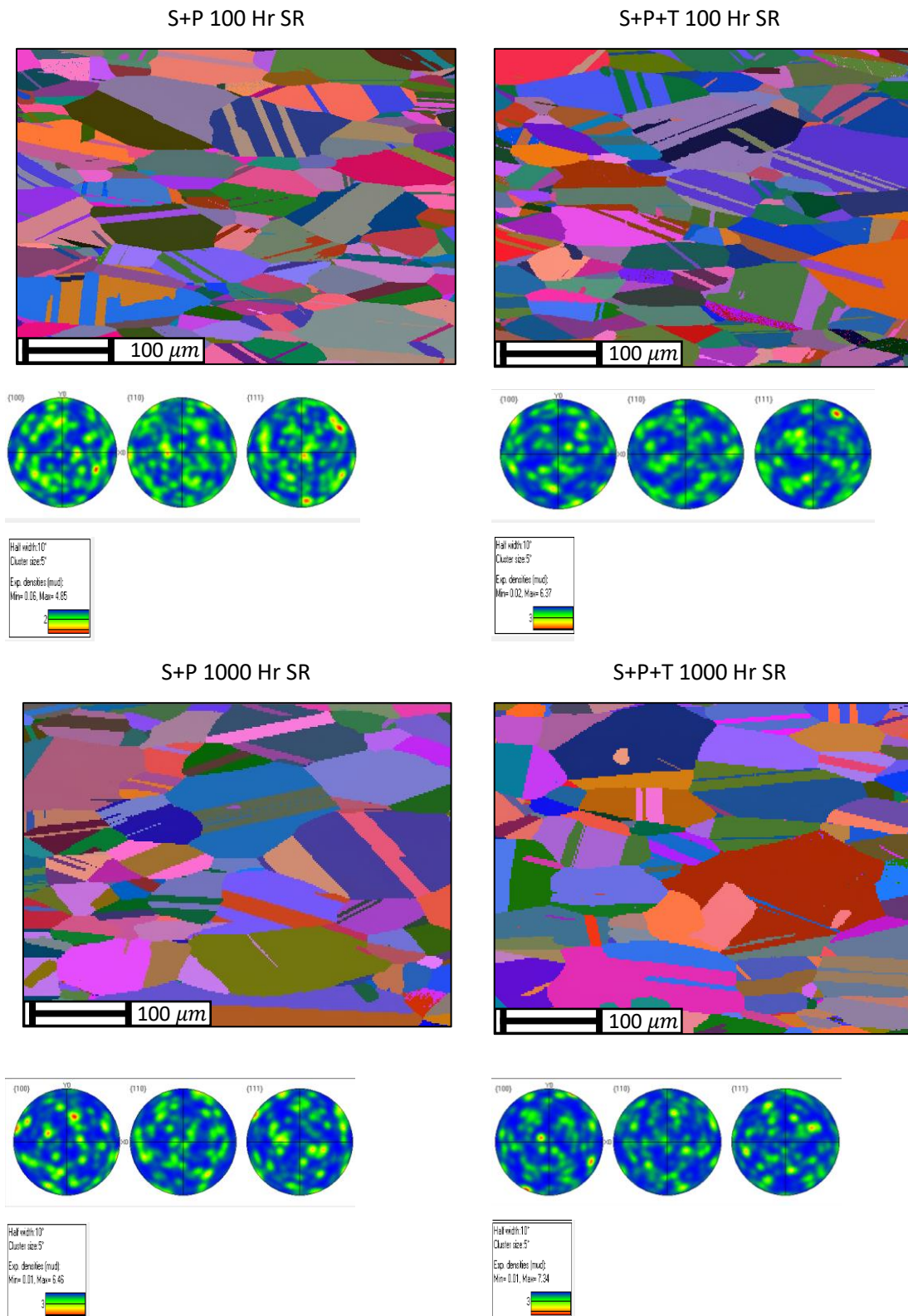


Figure 87: Orientation maps for S+P and S+P+T samples after stress relaxation tests at 6mm displacement, at 650°C for 100 and 1000 hours.

The average grain size across the 3 scanned areas for each sample at each stress relaxation time is given in Table 10. It can be seen that the grain size continues to increase during the stress relaxation testing, however the grain size appears to peak at 10 hours for both samples. The recrystallization temperature of Nimonic 90 is far higher than the temperature in the stress relaxation tests and so one would not expect a larger density of small grains to form as a result of this.

Sample	Grain size (μm^2)	
	S+P	S+P+T
0 Hr SR	785	644
1 Hr SR	1252	996
10 Hr SR	1693	1466
100 Hr SR	952	874
1000 Hr SR	1041	1004

Table 10: Grain size across stress relaxation samples, 6mm displacement at 650 °C from 1 to 1000 hours.

The average percentage of twin boundaries across the three scanned areas for each sample are shown in Figure 88. It can be seen that the fraction of annealing twins reduces significantly for both samples from the beginning of the test to the end is approximately equal. However during the test there is a definite reduction up to 100 hours and then increase between 100 and 1000 hours in the twin boundary fraction. Recovery processes can lead to the creation of small low angle subgrains, which may over time coarsen and be driven from low to high angle boundaries [116].

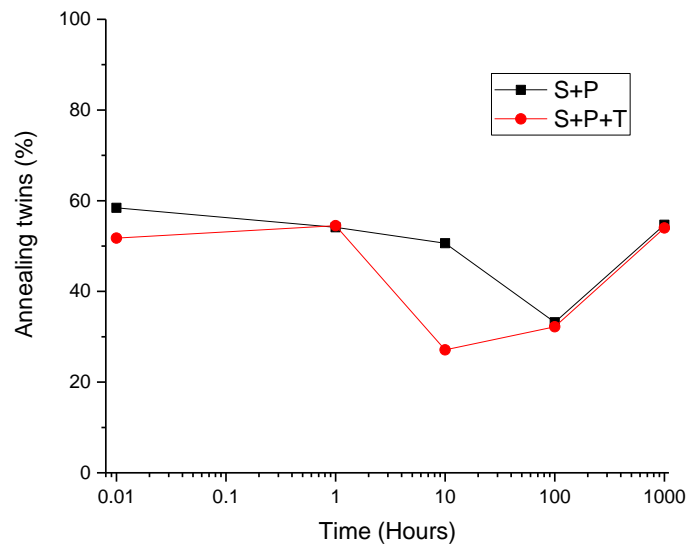


Figure 88: Percentage of $\Sigma 3$ annealing twins of total boundary length, for each time period of stress relaxation from nut and bolt test, 6mm compression at 650 °C.

Grain boundary misorientation

Observing the results for the grain boundary misorientation in Figure 89, it can be seen that the LAB's increase significantly during the first 10-100 hours of stress relaxation, before tending to uniform RGB fraction at 1000 hours. This lends support to the possibility that the formation of subgrains induced by dislocation re-arrangement during the stress relaxation tests is occurring during the first 100 hours. The annealing twin fraction reducing between 1 and 100 hours may be explained by the formation of subgrains, while the increase in the fraction may be due to some larger grains continuing to grow at the expense of the smaller subgrains, thus leaving a greater portion of the total grain boundary as twins.

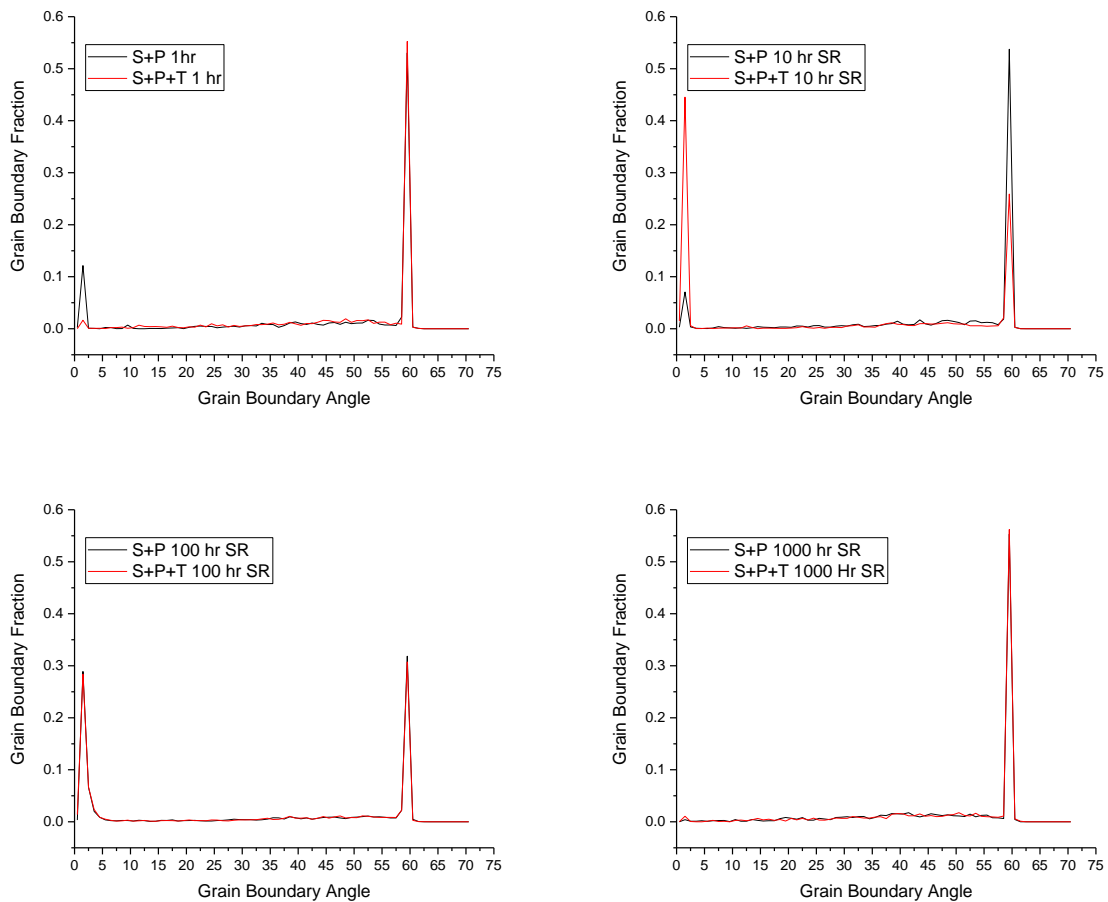


Figure 89: Grain boundary misorientation for S+P and S+P+T samples undergoing nut and bolt stress relaxation tests at 6mm compression, at 650 °C.

Grain Shape

Utilising the same methodology as in section 10.52 the grain shape was calculated using the fitted ellipse method. The results are shown in Figure 90. Peak values for the grain aspect ratio drop dramatically for the S+P sample from an aspect ratio of 1.5 making up 67% of grains, to an aspect ratio of 9.5, totalling 36% of grains, within the first 10 hours. It is clear that as the stress relaxation experiment is conducted, the aspect ratio of grains has a tendency to shift from a uniform, high concentration of low aspect ratio grains towards longer, more elliptical grains.

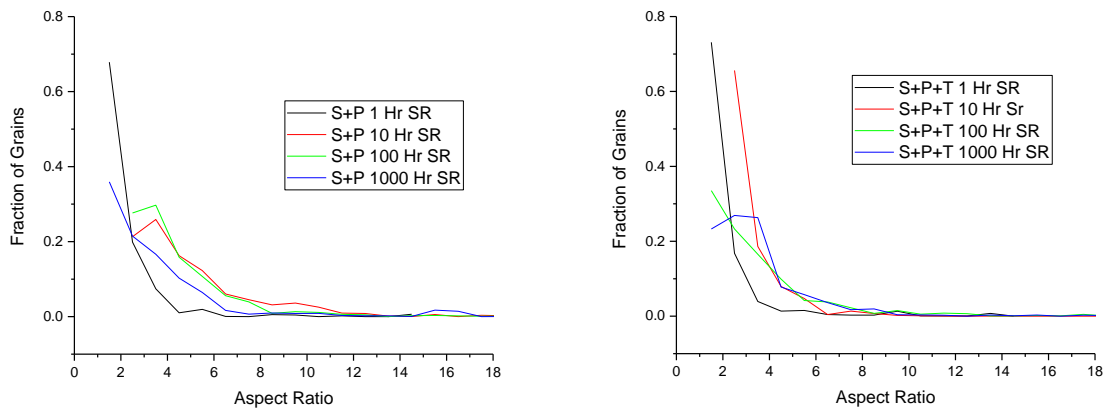


Figure 90: Aspect ratio of samples utilised in nut and bolt stress relaxation tests at 6mm displacement at 650 °C up to 1000 hours. Shown left-S+P sample, Right-S+P+T.

Grain misorientation

The misorientation during the stress relaxation tests is recorded here. The misorientation maps in Figure 91 and Figure 92 demonstrate the evolution of misorientation with time. The grain boundary map filters have been removed from these maps to allow for clearer imaging of the misorientation at the grain boundaries, which would be expected to be significantly higher than the bulk grain, and would be obscured with the grain filter on. The 1 hour stress relaxation maps appear to show grains with generally homogenous misorientation for the S+P sample, while the S+P+T sample has misorientation peaks accumulated at the grain boundaries. Moving to the 10 hour samples, both the S+P and S+P+T have very similar profiles. The grain boundaries appear to be clear for most grains, however bulk grain misorientation is also more clear and homogenous than in the 1 hour samples. The 100 and 1000 hours samples appear to have less misorientation within bulk grains, with some grain boundaries accommodating the majority of the misorientation. Observing the misorientation angle profiles in Figure 93 it can be seen that the misorientation have a trend of increasing the range of misorientation values up to 100 hours of stress relaxation, and then the 1000 hour values show a narrow band of small misorientation values.

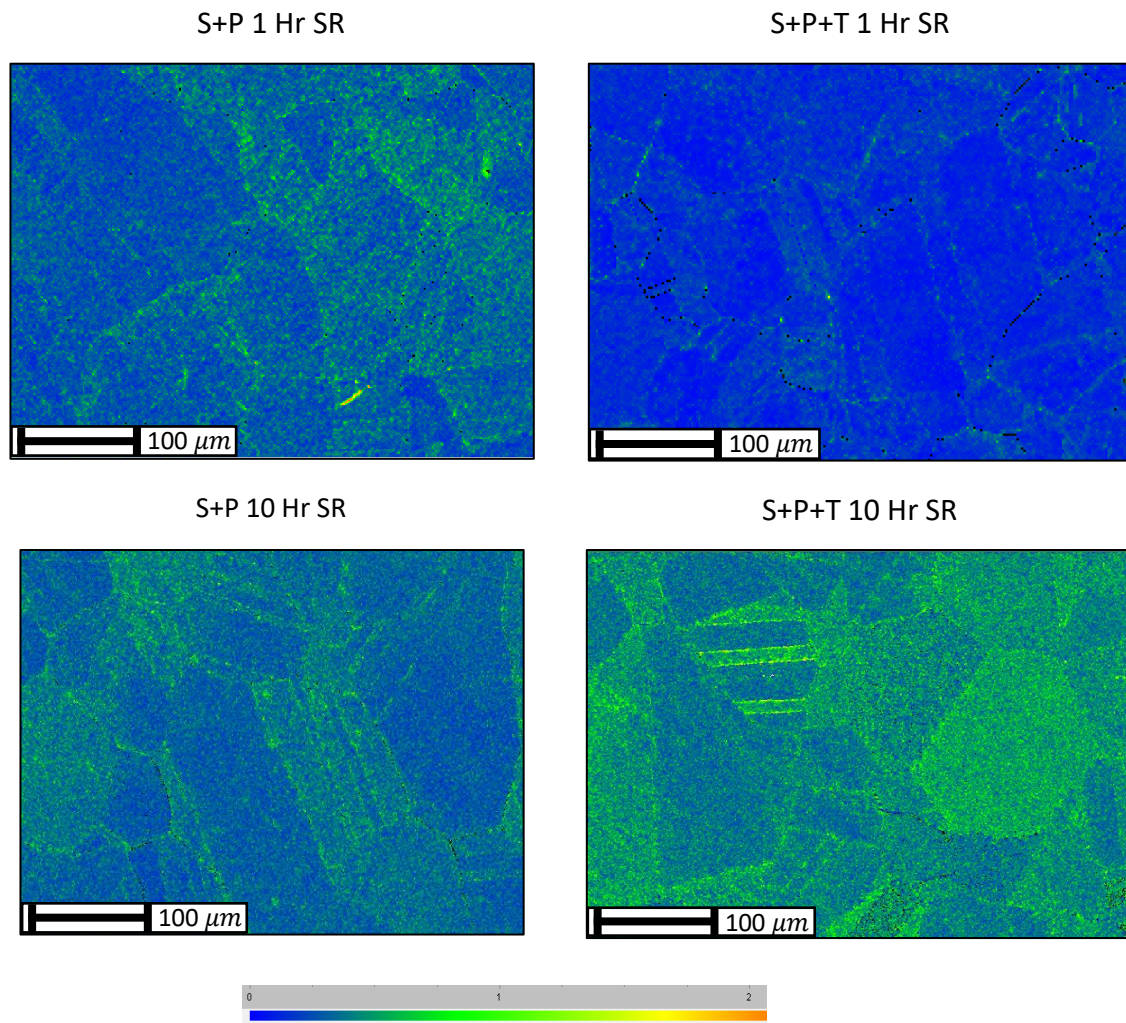


Figure 91: KAM maps for nut and bolt stress relaxation tests at 1 and 10 hours for S+P and S+P+T samples, compressed to 6mm and held at 650°C.

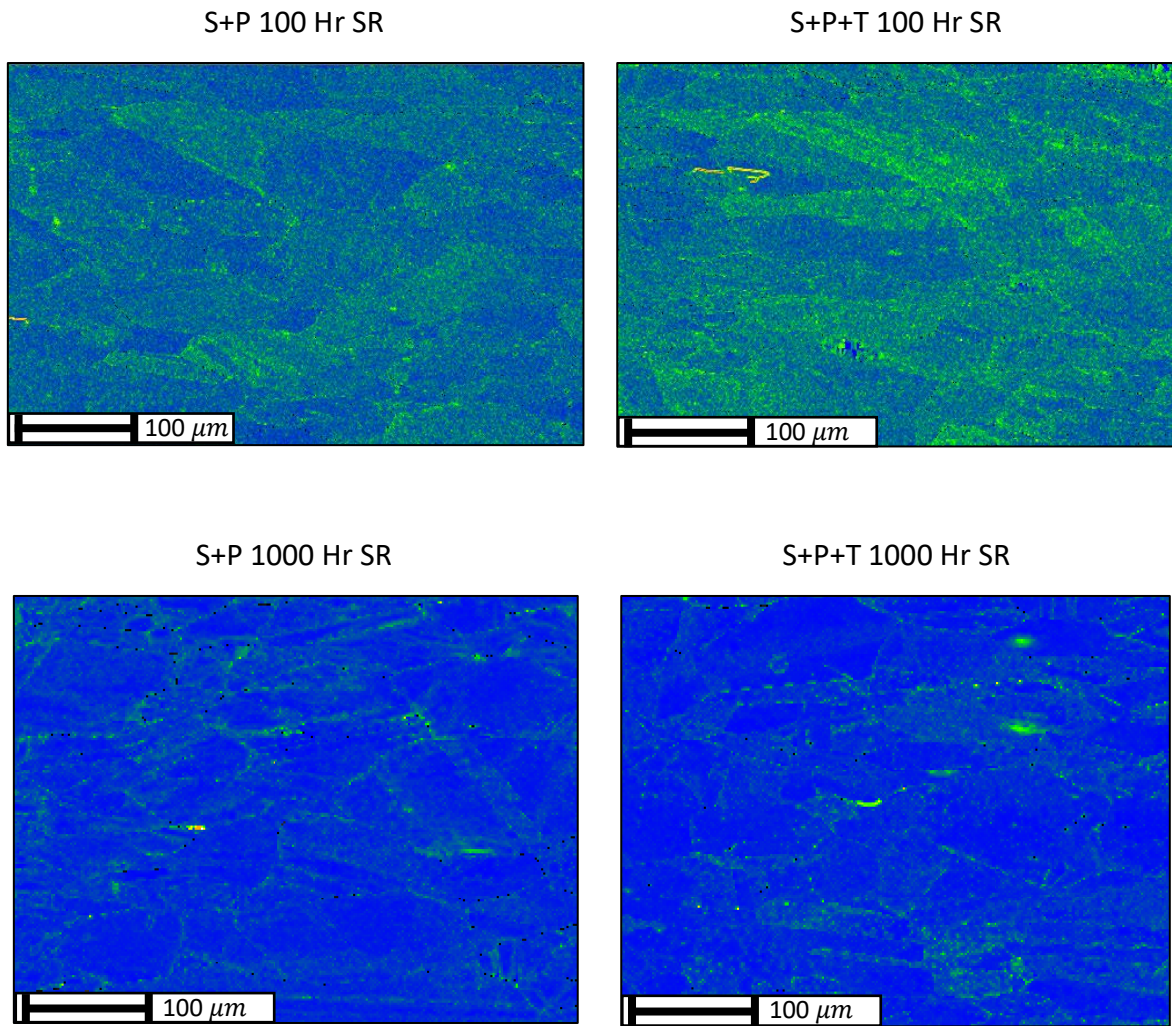


Figure 92: KAM maps for nut and bolt stress relaxation tests at 100 and 1000 hours for S+P and S+P+T samples, compressed to 6mm and held at 650°C.



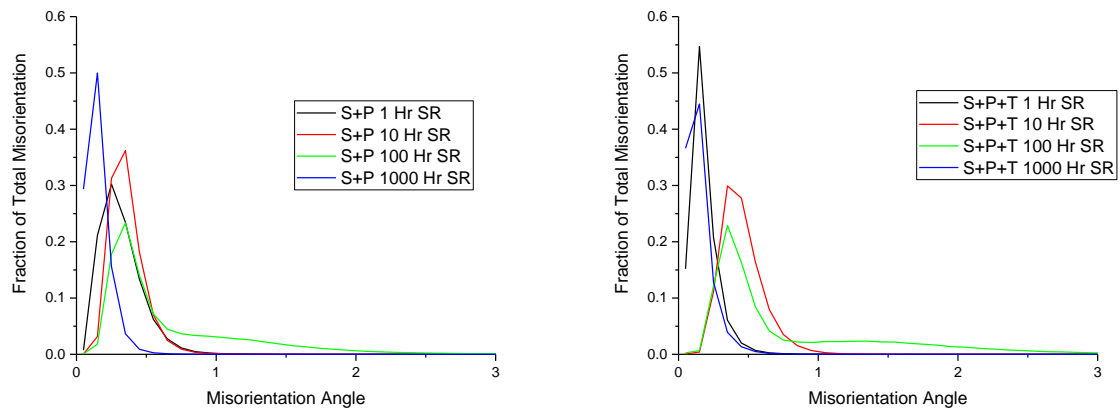


Figure 93: KAM misorientation profiles of samples utilised in nut and bolt stress relaxation tests at 6mm displacement at 650 °C up to 1000 hours. Shown left-S+P sample, Right-S+P+T.

10.54 Dislocation calculation from misorientation maps

The calculation of dislocation density has been attempted for the as-wound samples in section 8.24. In this section a method of calculating the dislocation density during stress relaxation and observing the evolution thereof during service is presented. Typically the dislocation density would be estimated utilising TEM imaging, however, these techniques have the shortcoming of only being able to image a small area at a time, which may not be representative of the local area within the material, let alone the material as a whole [117].

Calculation of dislocation density from KAM maps of metals under strain has been previously accomplished utilising an adapted two-dimensional Nye tensor for GND's [118] shown in equation (8.21), however information on dislocation densities during stress relaxation in polycrystalline nickel-superalloys utilising this technique is not readily available, and so performing this method here will allow for greater understanding of the microstructural evolution of Nimonic 90 and similar alloys under stress relaxation at 650 °C.

By utilising the Image Processing Toolbox in Matlab R2016A, the local misorientation maps were imported and converted to greyscale colour palette, an example given in Figure 94. This assigns each pixel a numerical colour value, which was scaled between 0 and 255, for 'minimum' strain and 'maximum' strain respectively.

The 'imgradientxy' function was utilised to obtain the value of the gradient in colour between a single pixel and its 8 neighbouring pixels. This gradient was then utilised as an approximation for the strain gradient at any one point in the sample image. By summing the x and y components of the strain gradients and inserting into the Nye model for dislocation density, one may calculate an estimated value of GND density. It is important to note that it is impossible to obtain values of the strain gradient in EBSD orthogonal to the surface of the sample and thus the Nye Tensor is simplified in this case to only 2 dimensions, instead of requiring advanced techniques, such as creating estimates of distortion fields orthogonal to the surface by utilising mechanical experimental data [119] or creating 3D voxel image maps in EBSD and 'stitching' them together [120]. As only the total strain is known, and not the individual strain components, the method must be viewed as approximate, although the magnitude of the result is expected to be reasonably accurate.

From chapter 3 the maximum value for the strain under 6 mm displacement is $\varepsilon_e^{max} = 0.41\%$, and thus the colour gradient was normalised to this value, where perfect black (0) was taken to be 0 strain, and the brightest gradient, 255, was taken to be associated with the strain of 0.0041.

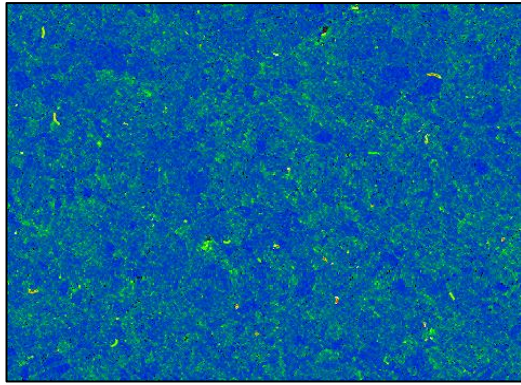
The calculation was therefore

$$\rho_G = \frac{1}{b} \nabla \varepsilon_{xy}^p \quad (10.13)$$

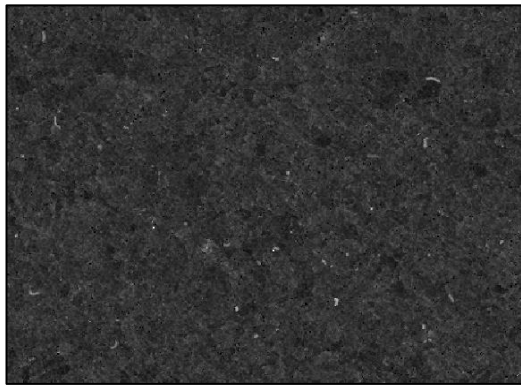
where

$$\nabla \varepsilon_{xy}^p = \frac{\nabla \varepsilon_{avg}^p \left(\frac{\varepsilon_{max}}{255} \right)}{\frac{d_{pix}}{8}} \quad (10.14)$$

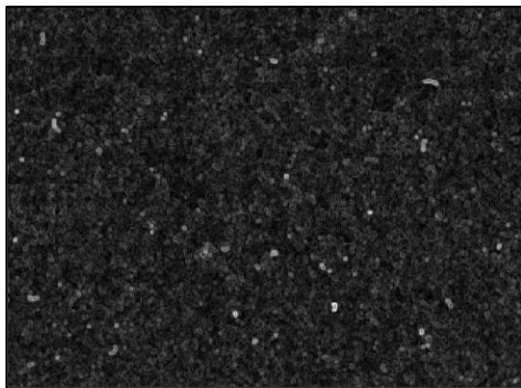
in which $\nabla \varepsilon_{xy}^p$ is the normalized summation of strain gradient in the x and y direction, $\nabla \varepsilon_{avg}^p$ is the average calculated strain gradient taken from the KAM map, and d_{pix} is the calculated distance each pixel represents, calculated by dividing the known distance of the scan size by the number of pixels.



Misorientation image



Misorientation image in grayscale



Gradient magnitude map

1) The original misorientation image from the EBSD scan is imported into MATLAB.

2) The image is converted to grayscale.

3) The magnitude of the x and y gradients for each pixel compared to its 8 neighbours are calculated and the values are exported to Microsoft Excel to average and calculate the $\nabla \varepsilon_{xy}^p$ according to (10.14).

Figure 94: Methodology of conversion of KAM misorientation map to a gradient magnitude map using MATLAB.

Sample	Dislocation density (average) (m^{-2})
A.R	46×10^{10}
S+P	11×10^{10}
S+P+T	11×10^{10}

Table 11 calculated dislocation density for A.R, S+P and S+P+T samples compressed 6mm, prior to relaxation.

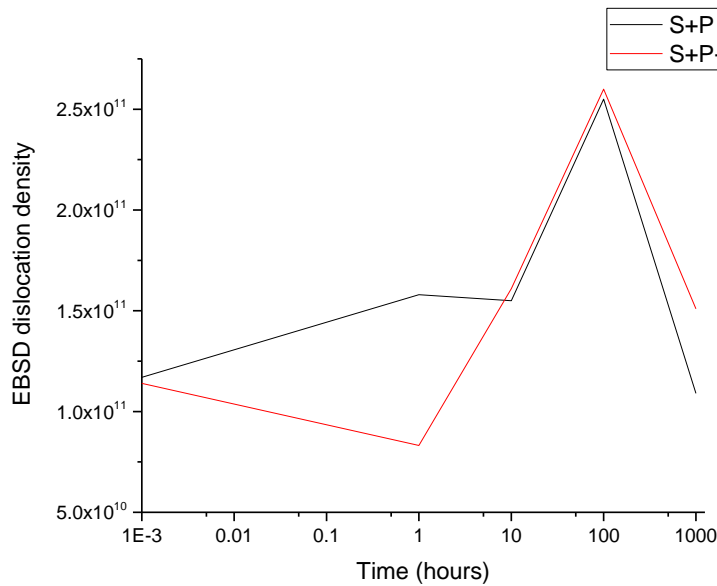


Figure 95: Values for dislocation density taken from KAM maps utilising adapted Nye equation.

It can be seen from Figure 95 that the expected dislocation density is calculated at about $1.1 \times 10^{11} m^{-2}$. This is smaller than the values calculated in section 8.24 from equations (8.17) and (8.21) giving $5.5 \times 10^{11} m^{-2}$ and the bending of a wire into a coil F.E model in section 8.24, also giving a value of $5.5 \times 10^{11} m^{-2}$ for the GND density. However, it is of the correct order of magnitude, and much large than the value of $0.03 \times 10^{11} m^{-2}$ derived for wire before

coiling. As with the misorientation calculations it is based upon (Figure 93), the values generally increase from 0 to a peak at 100 hours, with a significant decline between 100 and 1000 hours, which may be explained by dislocation multiplication due to applied stresses activating Frank-Read sources within the material. Once the stress is reduced, the effective shear stress is reduced below the critical point at which new dislocations may be generated. The existing dislocations may climb and glide, creating tangles and potentially annihilating one another. The total increase in dislocation density with the first 100 hours is shown in Figure 73, and is predicted to increase by a factor of 1.29 in 1000 hours. Plotting the dislocation densities increase from the misorientation maps against the predicted values gives the fractional increase shown in Figure 96.

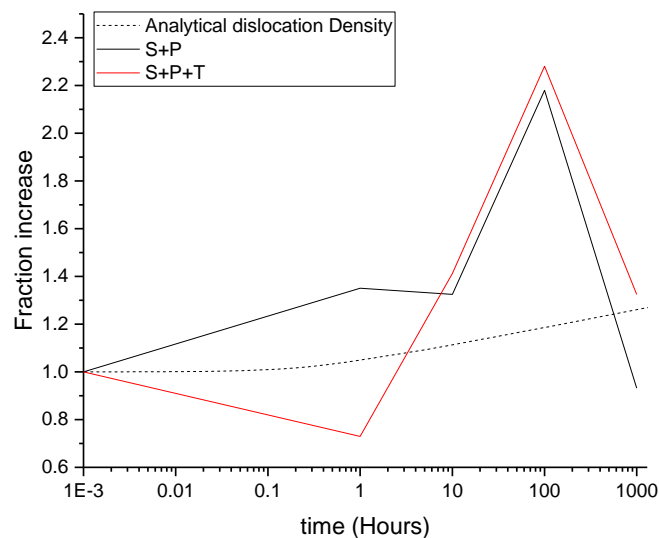


Figure 96: Analytical calculation of dislocation density against EBSD misorientation map dislocation densities.

It is clear there is a disparity between the analytical solution and the EBSD map solution, however, this difference is only larger than a factor of 1 at 100 hours of stress relaxation, which implies that there could well be some high level of strain accumulating during the first 100 hours, which is subsequently annihilated through recovery. It is interesting to note that while the EBSD dislocation densities drop between 100 and 1000 hours, the Vickers hardness was generally found to increase between the same time periods. This could imply that in fact particle coarsening could be the rate controlling aspect of the increase in hardness, as it is

expected to increase significantly between 100 and 1000 hours. Further experiments on the particle growth against hardness for Nimonic 90 could be carried out to find the optimal particle size beyond which softening occurs.

Microstructural change during stress relaxation summary

EBSD of the samples during stress relaxation has shown that no new texture is formed within the samples during the 1000 hours of relaxation. However the grain size was seen to vary rather significantly during the first 10 hours, then reducing slightly at 100 hours. This is possibly due to the formation of small subgrains that reduce the average grain size, which subsequently coarsen during the following 900 hours, leading to a slight increase at 1000 hours. The formation of low-angle boundaries gives further credence to this, as small dislocation-free subgrains tend to be of LAB in character [121]. The increase in number of grains reduces the total percentage of the grain boundaries that are $\Sigma 3$ twins, as seen at 10-100 hours in Figure 88. As these grains coarsen, and are put under strain from the stress relaxation testing, they show a greater range of higher aspect ratio's compared to the pre-stress relaxation samples, showing a tendency towards longer, more elliptical grains. The misorientation values of the samples follow the trend of larger range of misorientation angles from 0 to 100 hours, then a large reduction is seen at 1000 hours, with a thin, high peak at low misorientation angles in both the S+P and S+P+T samples. The increase in dislocation density calculated using the misorientation maps shows a similar trend of increase in dislocation density up to 100 hours, then decrease to 1000 hours, further indicating substantial recovery during the stress relaxation test.

10.6 Conclusions

In conclusion the microstructural and mechanical analysis utilising SEM, hardness testing and EBSD techniques has shown

- 1) The microstructure of the as-received and heat treated samples consists of small polycrystalline grains that on average increase in size by a factor of approximately 10 when heat treated. These grains are made up of a homogenous distribution of the component elements in the γ matrix, with Ti concentrations in blocky MC carbides.
- 2) High-resolution imaging of etched samples shows the γ' appears to be of uniform spherical shape, and expected size (~ 10 nm diameter) post heat-treatment.
- 3) The hardness of the samples increased significantly during the stress relaxation tests, except for between 1 and 10 hours of relaxation in the S+P+T case. After this reduction, however, substantial increase was then found. The trend of hardness increase matched the calculated values for the dislocation density from JMatPro well.
- 4) Heat treatments appeared to have a small effect on the shape of grains, increasing the fraction of grain boundaries at higher aspect ratios.
- 5) Heat treatments increase the percentage of annealing twins and reduce the number of LAB's significantly.
- 6) The as-received sample appeared highly textured, and the heat treatments reduced the measured texture. It is important to note, however, that the grain size difference leads one to be cautious with this, and further scans of larger numbers of grains are necessary to be certain.
- 7) The thermomechanical process had negligible effects on grain size and misorientation, but a small increase in LAB's can be seen after the process, which may indicate subgrain growth.
- 8) The overall effect of the thermomechanical process appears to be a dislocation redistribution that leads to a higher proportion of LAB's, and a small shift in the misorientation peaks towards higher angles.
- 9) EBSD performed on stress relaxation tests on the samples indicate that there is measurable recovery occurring during the tests, both dislocation annihilation reducing

the dislocation density after a substantive increase, and rearrangement into low angle subgrains boundaries, which subsequently coarsen.

10) The dislocation density from KAM maps of the samples increases by a factor of 2 up to 100 hours, and then reduces significantly by 1000 hours of testing. As the Vickers Hardness of the sample continue to increase up to 1000 hours, the question of where the effect of hardening is coming from is posed, as the new dislocation density values did not match the hardness well. It may be derived either from the dislocation multiplication in the samples, or from the coarsening of γ' , which is predicted to be significant. This would, however, imply the particles would eventually reach an optimal size, beyond which the hardness would reduce.

These findings inform the modelling work in this thesis as the models presented in this work assume dynamic micromechanical mechanisms to describe the creep rate. Understanding these mechanisms and proving they apply during the testing is therefore paramount to vindicate the model choice.

The Dyson model assumes homogenous deformation, it is important therefore to prove that the texture of grains is not too intense, as this could lead to isotropic behavioural effects on loading, which would render the use of the Dyson model for creep rate a questionable choice. However, the orientation is seen to be reduced after heat treatments.

Hardness is related to the growth of particles, such as γ' coarsening, along with the dislocation density, and as such is related to the creep rate. The measured hardness values again validate the model choice, as they imply substantial increase in the dislocation density over time, which is therefore included in the model.

There is no clear micromechanical change between the S+P and S+P+T samples beyond what is expected, it is therefore acceptable to utilise the same modelling effort for the thermomechanical process in this thesis.

Chapter 11: Discrete Dislocation Interaction Model

Throughout this thesis the physically-based nature of the Dyson creep model has been mentioned repeatedly. The model takes into account the particle size, distribution, and dislocation density, in order to create a climb-glide model under particular stress and temperature conditions, neglecting tertiary creep and under small strains. The dislocation interactions with particles and with each other are predicted to reduce the creep rate over time.

Although the effect of stress relaxation has been shown to be modelled acceptably by utilising creep rate equations, there are still a few remaining fundamental questions to answer with relation to stress relaxation:

- (1) Is there a difference between the mechanisms of creep and stress relaxation? The same constitutive laws are typically always used to model both processes.
- (2) Are creep and stress relaxation affected by the nature of the dislocation population, i.e. SSDs or GNDs? Being of similar Burgers vector, interactions between GNDs will all be repulsive, whereas SSDs will have a balance of repulsive and attractive forces.

A very basic discrete dislocation interaction model is developed in this chapter to address these questions. The simplified model means that the results are unlikely to be quantifiably correct. However, the objective is to see relative changes between the different models, and this should provide some insight into the mechanisms at work.

In the case of residual stresses being reduced over time, it has been suggested that stress relaxation may be a result of thermal effects, such as the temperature and stress dependant glide or climb of dislocations, leading to annihilation or arrangements of dislocations that lead to a change in stress distribution. It may also be purely mechanical, such as effectively cold-working a material during loading at high stresses (such as winding a wire into a coil spring), or shot peening among others, which may reduce the effective residual stress in the material, could potentially lead to reduced reaction force from the material at temperatures with which little or no creep would occur.

The behaviour of dislocations in the sample matrix during climb and glide can be complex, with dislocations of opposite sign annihilating upon contact with one-another, and dislocations generated by activation of Frank-Read sources. Dislocation pile-up on precipitates is the core component of the back-stress hardening effect, used to describe the load transfer from matrix to precipitate, and modelling this using distinct dislocation movements allows for greater understanding of the underlying principle by calculating an estimate for the reduction in effective stress within a grain as dislocations become slowed by the presence of other dislocations and precipitates acting as blockers to glide. The aim of this model is to demonstrate the principles behind the stress-relaxation and hardening effect presented in this thesis, and to create a reasonable core for further work on the behaviour of dislocations under applied stress.

First, the principles of dislocation motion under a force, known as the Peach-Koehler equation, is presented, after which the model is built up from a simple interaction between two distinct dislocations to scaling up to hundreds of dislocations and introducing dislocation multiplication through Frank-Read sources. Finally the creep rate within the grain is calculated utilising the Orowan equation (3.13) introduced in chapter 3, along with the reduction in effective stress over time.

11.1 Dislocation Interaction

The dislocation interaction model assumes that all dislocations are edge type and move under a force \vec{F} (per unit length) perpendicular to the glide plane, which is described as

$$\vec{F} = \tau \vec{b} \quad (11.10)$$

where τ is the shear stress resolved in the direction of \vec{b} , the burgers vector. As the dislocation moves within the glide plane, only the shear stress on this plane is considered, as stress components normal to the glide plane do not contribute to movement. The diagram in Figure 97 demonstrates the dislocation movement along a slip plane under applied stress σ_{yy} . The applied stress is resolved as a shear stress, and F is seen to be acting perpendicular to the dislocation line.

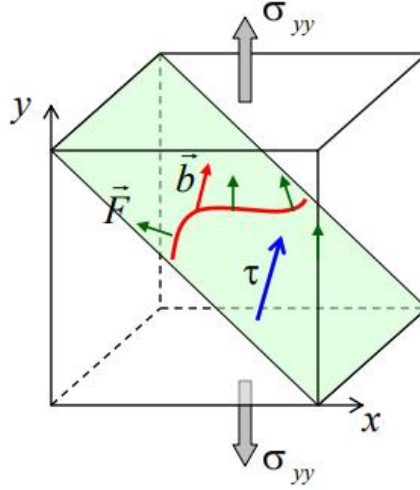


Figure 97 diagram describing dislocation movement along slip plane (in green). The red line dislocation travels normal to the resolved shear stress [122].

In general terms the Peach-Koehler equation describes the force at a given point as

$$\vec{F} = (\sigma \cdot \vec{b}) \times \vec{l} \quad (11.12)$$

where \vec{l} is the local line tangent direction at a given point and $\sigma \cdot \vec{b}$ is the local force per unit length acting on a plane of area b perpendicular to the \vec{b} direction. When taking the value of $\sigma \cdot \vec{b}$ one may segment the stress into the 3 principle directions

$$\vec{g} = (\sigma \cdot \vec{b}) = (g_x, g_y, g_z) \quad (11.13)$$

where the stress components σ_{xx} , σ_{yx} , and σ_{zx} define the traction on the surface normal to b , and \vec{F} , \vec{l} , \vec{g} are orthogonal to each other. Figure 98 shows a glide plane of (001) with the components $\vec{b} = (b_x, b_y, b_z) = (-b, 0, 0)$ and $\vec{l} = (l_x, l_y, l_z) = (0, 1, 0)$ with force components

- $g_x = \sigma_{xx}b_x + \sigma_{xy}b_y + \sigma_{xz}b_z = -\sigma_{xx}b$
- $g_y = \sigma_{yx}b_x + \sigma_{yy}b_y + \sigma_{yz}b_z = -\sigma_{yx}b$
- $g_z = \sigma_{zx}b_x + \sigma_{zy}b_y + \sigma_{zz}b_z = -\sigma_{zx}b$

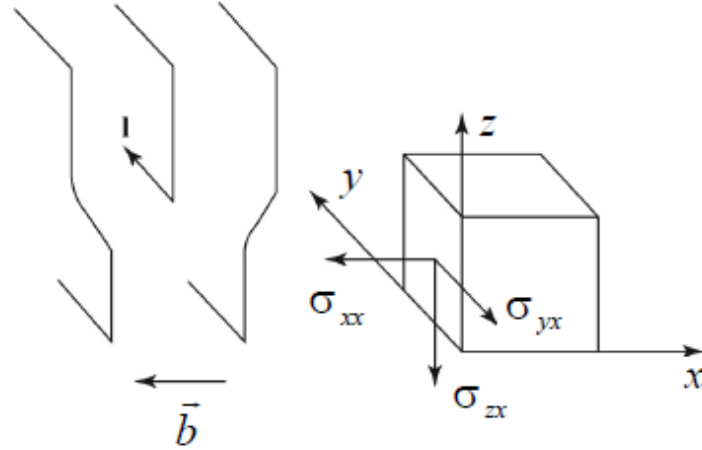


Figure 98 edge dislocation line along y axis with Burgers vector $\vec{b} = (-b, 0, 0)$ and line tangent direction $\vec{l} = (0, 1, 0)$.

In the example presented here the contributions of (g_x, g_y, g_z) and $(\sigma_{xx}, \sigma_{yx}, \sigma_{zx})$ are

- $g_x = -\sigma_{xx}b$ which is perpendicular to \vec{l} , leading to a climb force downwards of $|F| = \sigma_{xx}b$
- $g_y = -\sigma_{yx}b$ is parallel to \vec{l} , leading to σ_{yx} making zero contribution to F
- $g_z = -\sigma_{zx}b$ which is perpendicular to \vec{l} , leading to glide force along x-axis of $|F| = \sigma_{zx}b$

The models presented here are on a simple x-y plane, and so contributions from σ_{zx} are neglected, and \vec{l} is a unit vector into the paper. The force between two separate dislocations is equal to the sum of all Peach-Koehler forces between them. In the case of two parallel edge dislocations, the stress field from dislocation 1 acting upon dislocation 2 gives

$$\vec{F} = (\sigma_1 \cdot \vec{b}_2) \times \vec{l}_2 \quad (11.14)$$

In which the subscript values in equation (11.14) denote the dislocation in question, shown in Figure 99 a. The stresses generated by dislocation 1 can be described by

$$\sigma_{xx} = -\frac{Gb_1}{2\pi(1-\nu)} \frac{y(3x^2 + y^2)}{(x^2 + y^2)^2} \quad (11.15)$$

$$(11.16)$$

$$\sigma_{xy} = \frac{Gb_1}{2\pi(1-\nu)} \frac{x(x^2 - y^2)}{(x^2 + y^2)^2}$$

where x and y are the distance in the x and y planes between the two dislocations. The total force for dislocations of the same sign is therefore

$$\vec{F} = -\frac{Gb_1b_2}{2\pi(1-\nu)} \frac{x(x^2 - y^2)}{(x^2 + y^2)^2} \hat{x} - \frac{Gb_1b_2}{2\pi(1-\nu)} \frac{y(3x^2 + y^2)}{(x^2 + y^2)^2} \hat{y} \quad (11.17)$$

and the signs are reversed for dislocations of opposing sign. The first term in the x -direction represents glide, while the second term in the y -direction represents the climb force.

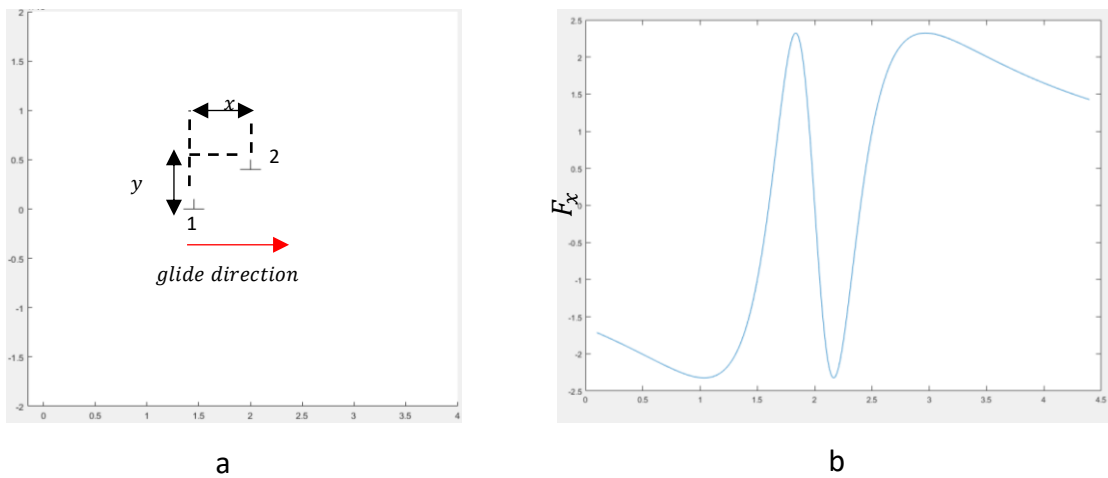


Figure 99 a) shows a demonstration of simple movement of dislocation 1, with dislocation 2 fixed in place. As dislocation 1 glides along the x axis the value of x will change, and the calculated force, F_x , between the dislocations will vary according the graph in b).

Initially a simple model was devised to move a dislocation along a line with a second dislocation placed in free space, as in Figure 99, as a preliminary model considering only the glide force. Dislocation 1 begins at coordinate (0,0) and is moved along the x -axis while dislocation 2 is kept in position at point (2, 0.5). The graph for the dislocation interaction force F_x as dislocation 1 is moved relative to dislocation 2 along the slip plane shows that the force between them has minima and maxima at different positions in the x plane. The graph in Figure 99b shows $F_x = 0$, and therefore at unstable equilibrium, where $x = y$, at an angle of 45° from one another, or with $x = 0$. It can be seen that the force is negative (attractive) as dislocation 1 approaches dislocation 2, where $x < y$, switching to a positive (repulsive) force

when $x > y$, in order tend towards the unstable equilibrium. When $x = 0$, and therefore dislocation 1 is directly below dislocation 2, $F_x = 0$. At this point, if $x < 0$, $F_x > 0$ and the force is attractive, similarly, if $x > 0$, $F_x < 0$, and the force is also attractive.

Setting the Burgers vector of dislocation 2 to negative gives the values for F_x in Figure 100 b), which are as expected opposite to the previous case, with the two dislocations attracted to one-another.

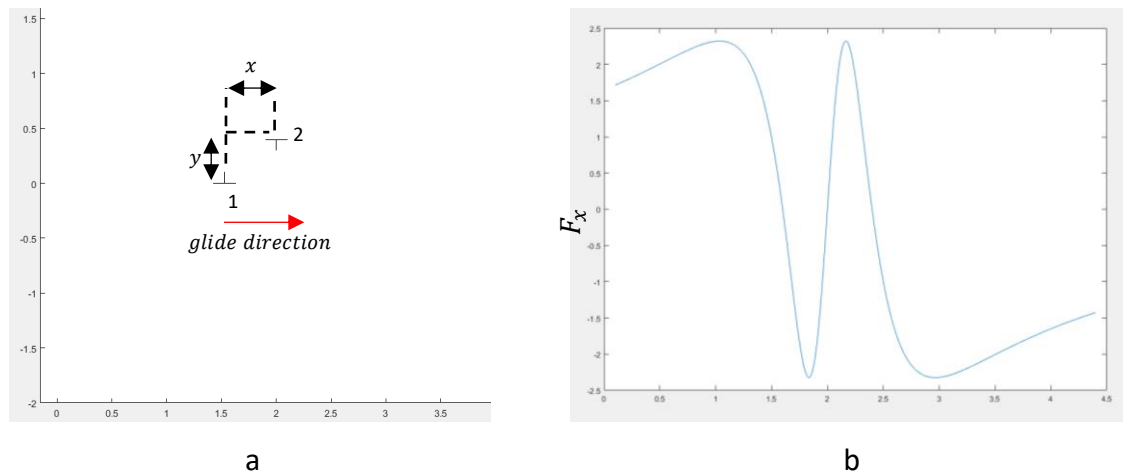


Figure 100 dislocation 1 and 2 with opposing Burgers vectors. As dislocation 1 glides along the x axis the value of x will change, and the calculated force, F_x , between the dislocations will vary according the graph in b).

11.2 Full model

The code for the full model is listed in Appendix 2. In order for the effect of multiple dislocations force to be accounted for on the behaviour of a single dislocation, a for-loop was designed to create initially randomly distributed dislocations within an area of $xlim \times ylim = (500 \times b)^2$, where b_0 , the burgers vector, was used as a scaling factor, equal to $2.5 \times 10^{-10} m$. The number of dislocations was set to $n=100$ initially, giving a dislocation density of $\rho_0 = 6.5 \times 10^{15} m^{-2}$, which is high but not unrealistic. They were randomly assigned a positive or negative burgers vector, to determine the dislocation sign. All dislocations initial positions are fully random in the x-axis and y-axis.

The forces between a dislocation and all others were calculated in the x and y directions by finding the instantaneous distance in the x and y directions between every dislocation at every

iteration of the model to calculate the force in the x and y planes. The summation of which was the total force components acting on a dislocation, f_x and f_y . This force was then used to calculate the velocity of the dislocation using $v_x = M_{glide}f_x$ and $v_y = M_{climb}f_y$, where the M_i are mobility's associated with glide and climb respectively. In this model the glide rate M_{glide} is set to 1 and the climb rate $M_{climb} = 0.001M_{glide}$, which has been used in DDD simulations on single-crystal nickel superalloys previously to represent temperatures of 900-1000 °C [123]. For creep simulations the applied stress is taken as constant, $\tau = G\gamma_0$, where γ_0 is the initial shear strain. For stress relaxation, the applied stress is $\tau = G(\gamma_0 - \gamma_c)$, where γ_c is the creep shear strain accumulated over the simulation. The shear modulus is chosen to be $G = 6.26 \times 10^{10} Pa$ [124]. Dislocations are moved each time step according to their velocity, with a maximum displacement of $\frac{1}{2}b_0$. Dislocations climb by the diffusion of vacancies and are therefore only allowed to climb in one direction. Dislocations of opposite sign annihilate if they come into contact, and are removed from the model. A simple sketch of the basic model is shown in Figure 101.

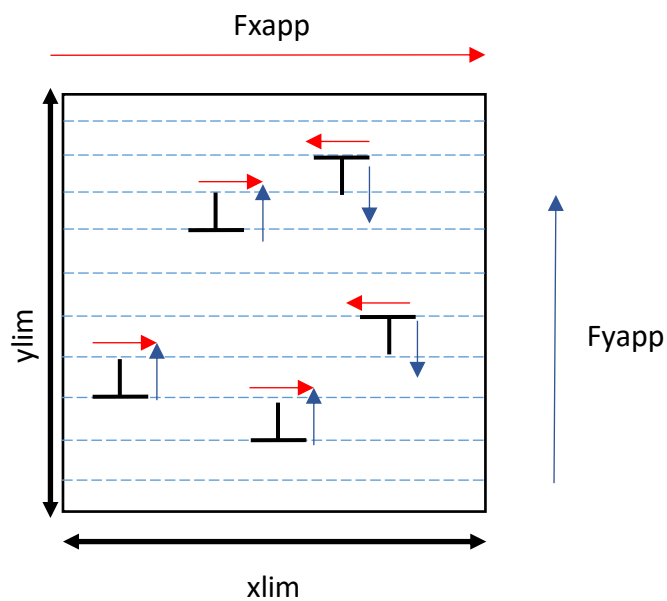


Figure 101 sketch of 5 dislocations with randomly assigned burgers vectors and slip plane. The resolved velocity in the x and y directions from the applied F_{xapp} and F_{yapp} only are denoted by the red and blue arrows for each dislocation respectively. Each dislocation also experiences a force from every other dislocation in the simulation, which will also affect the resolved velocity.

11.21 Boundary Conditions

Periodic boundary conditions were chosen. If a dislocation is displaced outside the area of interest defined by $xlim$ and $ylim$ then the dislocation is replaced at the opposite boundary edge, as shown in Figure 102 a) and b) where the dislocation is displaced beyond either $xlim$ or $ylim$. The dislocation is then placed on the opposing end of the area of interest to continue movement.

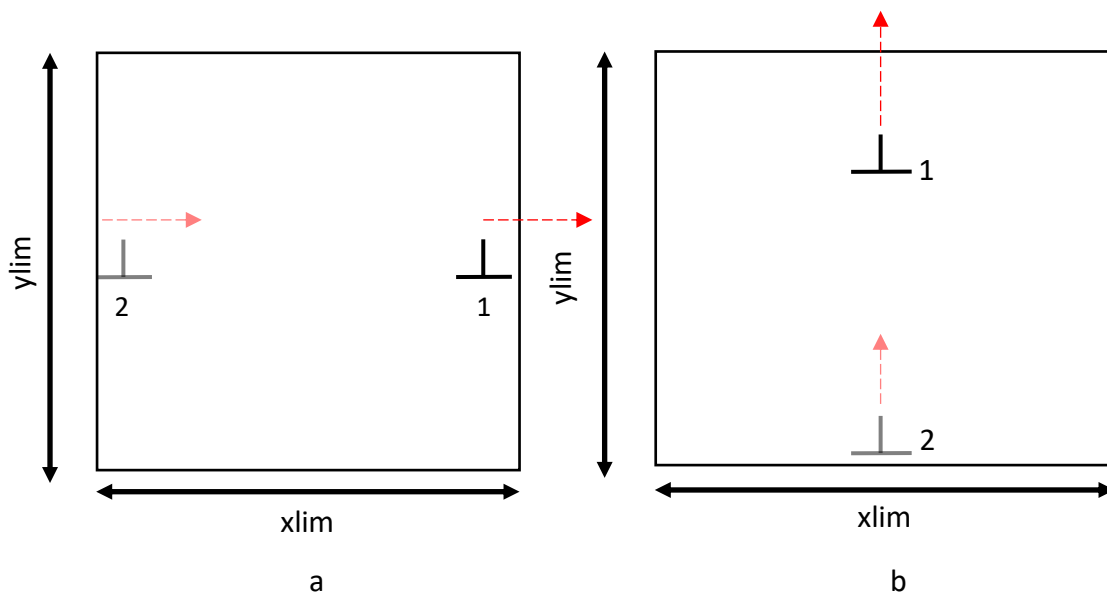


Figure 102 a) demonstrates the periodic boundary condition in the x-axis, as dislocation at position 1 is displaced outside of the area denoted as $xlim$, it is instead placed at position 2. This is the same case for the y-axis in b) where dislocation at position 1 is displaced beyond $ylim$.

For the calculation of force between any two dislocations, periodic boundary conditions were also utilised. To be consistent with this unit cell approach, multiple images of each dislocation should ideally be accounted for, but one of the assumptions here is that dislocations from neighbouring unit cells are neglected. If the distance x between two dislocations, 1 and 2, is greater than $xlim/2$ then the value of x is set to $x = x - xlim$, in effect setting the position of dislocation 2 to 2', allowing for force calculations to be made across the shorter distance between the area of interest or across boundaries. This is also applicable in the y-axis. A sketch of this in the x-axis is shown in Figure 103 where the calculation for the distance

between two dislocations is shown to be calculated as the distance between 1 and 2', rather than 1 and 2.

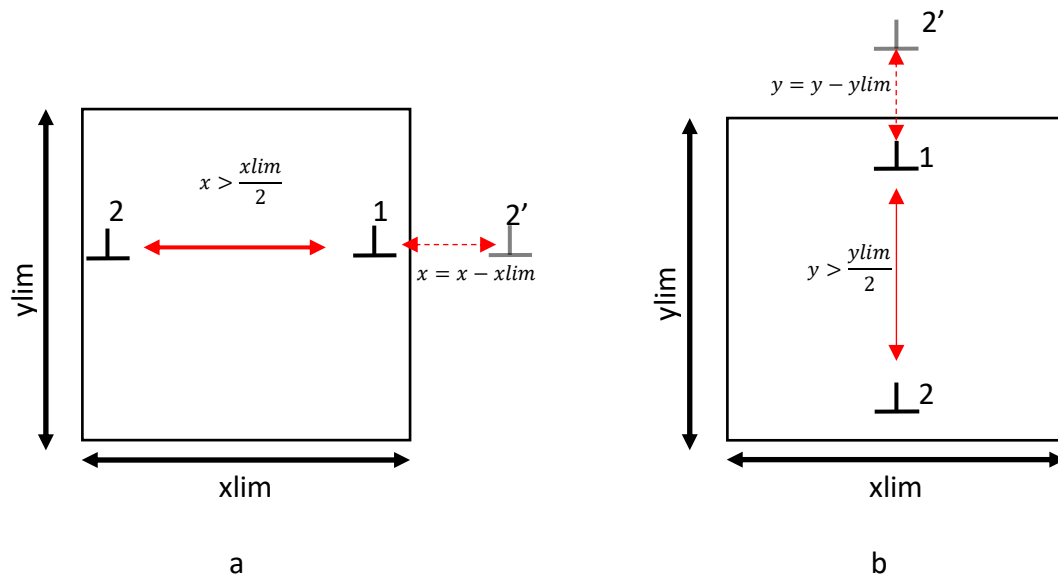


Figure 103 a demonstration of the symmetric boundary condition in a) the x-axis and b) the y-axis. In both cases a 'mirror' image of dislocation 2, known here as 2', is used for the calculation of distance for the force between dislocation 1 and 2.

11.22 Gamma Prime precipitates

The addition of γ' was achieved by creating circular particles of radius $r_p = 20 \times b_0$. The number of particles was calculated to take up 20% of the total area of the simulation, $xlim \times ylim$. The particles were randomly spaced, and prevented from making contact by having a minimum separation of r_p . The particles are placed so that there is no clear glide path across the simulation, i.e. so that no dislocation can cross the unit cell without climbing. Dislocations cannot enter particles in the model through glide or climb, and are prevented from doing so. If a dislocation would be displaced into a particle, it is replaced at the particle edge, and its velocity is set to zero so that it does not contribute to the overall strain rate. Dislocations may climb over the γ' particles, after which they are free to continue gliding in the x-axis.

11.23 Frank-Read Sources

Dislocation multiplication was added to the model through the implementation of Frank-Read sources. These are dislocations that are pinned within a slip plane. Under applied stress, τ , the dislocation may bow out. Under continual stress the dislocation may continue to bow out and around the original dislocation line, creating two new dislocations of opposing burgers vector, which may then go on to climb and glide through the sample matrix. Four sample Frank-Read sources were implemented by randomly placing them throughout the simulation area, and calculating the total force on that point from surrounding dislocations and the applied forces. The required shear stress to generate a new dislocation from the Frank-Read source is [124]

$$\tau_{fr} = \frac{2Gb_0}{l} \quad [125] \quad (11.25)$$

where l is the distance between pinning points.

The force between the Frank-Read source and all dislocations, and the applied force are calculated each iteration. The force required to separate the two positive and negative dislocations (F_{xcrit}) is calculated. This is inversely proportional to the distance between the two dislocations. In this model the new dislocations are placed a distance $30b_0$ apart such that $F_{xcrit}=0.12$. If the net force on the pair exceeds F_{xcrit} then they are created. They then behave as any other dislocation, climbing and gliding according to their assigned burgers vectors. The back stress from a newly introduced pair will prevent reactivation of the source until they move sufficiently far away. Eventually pile up stops the source completely until a dislocation at the front of the pile climbs past its obstruction and glides further away.

22.24 Strain rate calculation

The strain rate was calculated as a function of the dislocation glide and climb velocity. The sum of all gliding velocities in the x direction for all dislocations are taken and divided by total area to account for the dislocation density. The overall strain rate is adopted from the Orowan equation (3.17) reproduced here

$$\dot{\gamma} = \rho b_0 v_g \quad (11.26)$$

where v_g is the glide velocity. Note that this equation does not account for the climb as a creep process, instead in this model climb is implemented only to allow dislocations to pass γ' particles. As the particles come into contact with a γ' particle the velocity in the x-axis is slowed, reducing the overall glide velocity throughout the simulation, until the dislocation is able to climb past the particle, after which the dislocation may glide again and contribute to the creep rate. Stress relaxation is introduced into the model by taking the a maximum target strain of $\gamma_c=0.01$, which is of the order of maximum predicted strain in the stress relaxation tests for Nimonic 90 springs in this thesis.

11.3 Results

Shown in Figure 104, dislocations can be seen to glide onto particles, as a result of the applied force and interaction force between dislocations of opposing sign. The γ' particle highlighted in the black circle show a particular concentration of dislocations that demonstrate the mechanisms at work here. Dislocations '49' and '38' show strong attractive force to the opposing side of the particle, compared to others, due to the large density of opposite sign dislocations on the same slip plane. They are pinned on the particle and thus must climb over before continuing to glide. The dislocation pair '26' and '55' at the bottom of the black circle are about to annihilate, drawn towards each other, they will be removed from the simulation on contact.

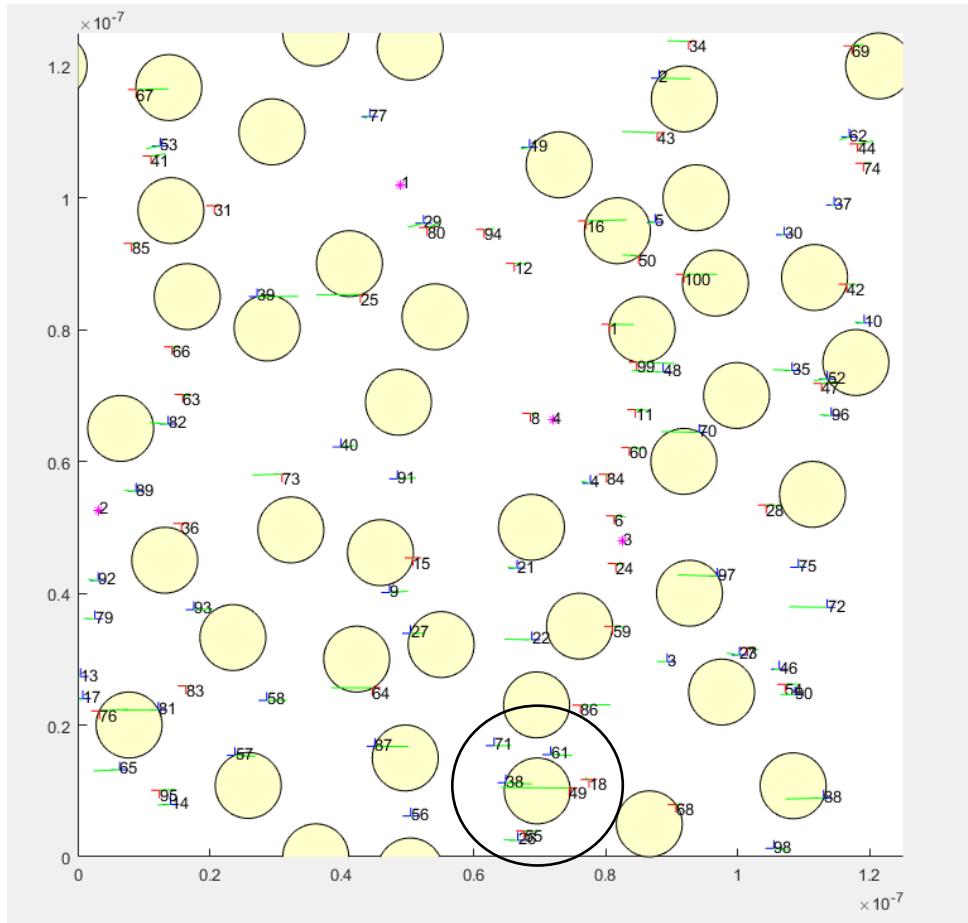


Figure 104: Dislocation interaction model under applied stress. Each dislocation is numbered, coloured blue for positive burgers vector, and red for negative burgers vector. The circles represent γ' particles, while the '*' icons represent the Frank-Read sources. The green lines forming from dislocations show the direction of force and the length is proportional to the intensity of force in the given direction.

Having determined that the dislocations were appearing to glide and climb according to the expected behaviour, a series of tests were carried out to record the difference in behaviour between stress relaxation and creep. One question that still needs to be answered is whether there is a difference between stress relaxation and creep. One of the potential differences is that during creep the load is maintained at a constant level, while in a stress relaxation test the reaction force can reduce over time. This may mean that the stress in a material may drop below that necessary for dislocation multiplication to occur, leading to a shortened or otherwise altered secondary creep state, in which the multiplication of dislocations is

approximately equal to the annihilation rate. The tests were taken further by considering the difference between SS and GND dominated materials. The dislocation calculations completed in this thesis utilising the Nye equation in previous chapters are all considered to be GND's. A large amount of SSD's are assumed to be annihilated during the heat treatments the samples undergo. Therefore, the difference between a GND-only sample and SSD sample is investigated for the stress relaxation case and the creep case. For the GND case, all the Burgers vectors of the initial dislocation population are the same (positive, say), whereas for the SSD case there are equal numbers of positive and negative dislocations. For the simulations shown here, the applied force, F_{xapp} was 0.157, and the separation force for the Frank-Read sources for a pair of dislocations introduced $30b_0$ apart was $F_{xcrit} = 0.12$. The data taken in these simulations is the average of three tests for each combination of dislocation and stress relaxation and creep tests. Each was run for 20000 iterations.

The first thing to notice in the simulations is that the net horizontal glide of the positive dislocations is to the left and the net migration of the negative ones is to the right. The positives therefore accumulate on the right side of precipitates and the negatives on the left side. In the GND case therefore, dislocations only decorate the right side of precipitates, whereas in the SSD case they are found on both sides. The precipitates have a diameter of $40b_0$ (10nm) so the interaction force on the glide plane between a single pair of dislocations on either side of the horizontal diameter is 0.09, of the order of the applied force of 0.15. The climb force between two dislocations separated by the vertical diameter is the same. Hence it is reasonable to expect that the nature of the interactions between the two types of dislocation population may play a significant role in the deformation rate of the samples.

11.31 Stress relaxation simulation

From the F_{xapp} plot in Figure 105, it can be seen that the GND case initially drops at a faster rate than the SSD simulation, with the minimum value of 0.03 reached while the SSD case takes significantly longer to reach its minimum value of 0.045. The GND case appears to 'overshoot' in relaxation of F_{xapp} and then increase slightly after the initial drop at $t = 40$. This is due to the effect of repulsion on GND's from each other after the initial drop in applied force. The repulsion force overcomes the driving force and dislocations will be pushed in the opposite direction, essentially creating a back-stress as the velocity of dislocations is reduced,

or even drops to 0 as dislocations become ‘trapped’ in low-energy configurations. Both the SSD and GND cases experience a back-stress, as neither cases drop to $F_{xapp}=0$, with the back-stress equal to the minimum value reached.

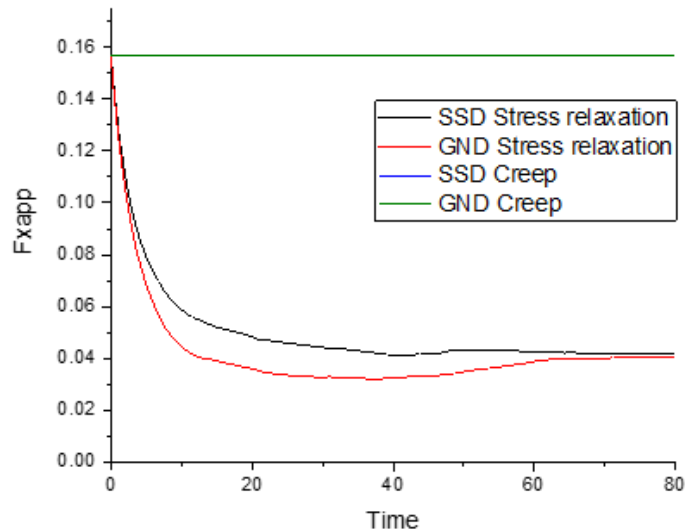


Figure 105: Reduction in applied force during creep and stress relaxation simulations for GND and SSD dominated samples. The creep values remain constant, while the applied load F_{xapp} reduces with accumulated strain.

Dislocation multiplication

The GND and SSD dislocation generation in the stress relaxation cases of Figure 104 are compared in Figures 105. Figure 105a shows that a similar amount of dislocations were generated by sources in both the GND and SSD cases. Both the SSD and GND cases generated 2 and 3 dislocation pairs respectively after F_{xapp} had dropped below F_{xcrit} . This must be due to local stresses generated by dislocations surrounding the Frank Read sources, leading to small areas with effective stress driving F_{xapp} above F_{xcrit} .

Figure 105b shows the total number of dislocations, including pairs created by Frank-Read sources and pairs which annihilated. Throughout the relaxation simulation, the GND dislocation total remained constant, except at small values of t where dislocations are likely to have been generated and then annihilated. The total number of dislocations for the GND

case stabilises after F_{xapp} drops below F_{xcrit} , and would be expected to remain constant as $t \rightarrow \infty$. However, the number of dislocations in the SSD simulations continued to reduce throughout. This is expected to continue to slow as the dislocation total becomes smaller, eventually reaching zero after a long time.

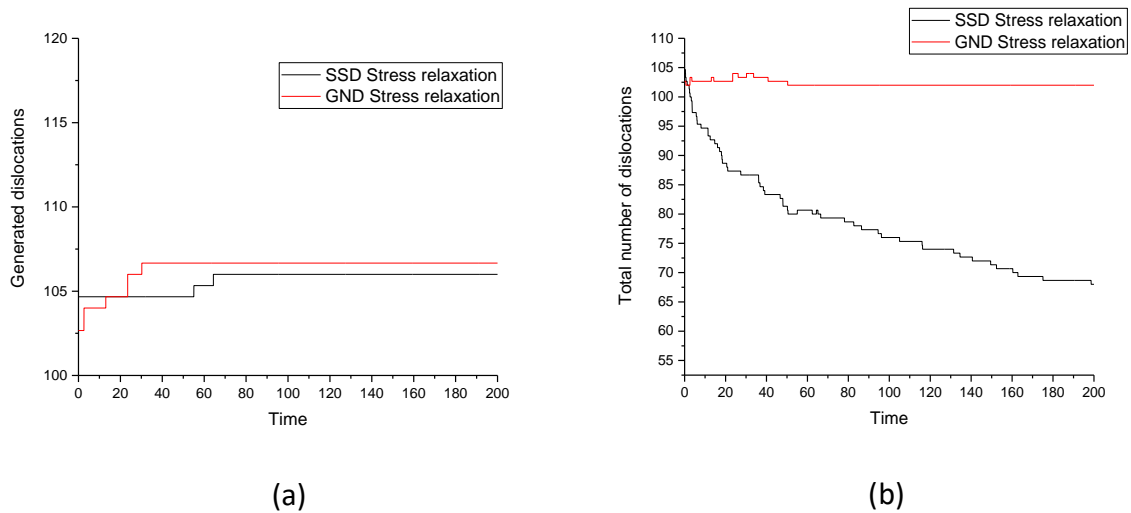


Figure 106: (a) The number of dislocations generated during the stress relaxation simulation, (b) the total number of dislocations accounting for generation and annihilation of dislocation pairs.

Strain

Observing the strain rate plot in Figure 107 (a), it is clear that the GND and SSD simulations show a rapid decrease in strain rate, with the majority of the drop occurring while $t < 10$, and reaching a minimum rate for SSD and GND cases while $10 < t < 20$. While the two cases appear to have a similar rate of reduction in strain rate, it is interesting to note that the SSD case is noisier than the GND case. This is due to the annihilation events occurring during relaxation.

The total accumulated strain in Figure 107 (b) for both simulations shows a corresponding rapid transition from primary to secondary creep within a similar time window. After the transition from primary to secondary creep, the GND and SSD simulations converge to a steady state that would be expected to tend towards the target strain of 0.01 as $t \rightarrow \infty$. Similarly to the stress relaxation plot in Figure 105, the GND case has a rapid increase in strain

that ‘overshoots’ the steady state strain rate, which then reduces due to repulsion and trapping by dislocations of the same sign.

It appears that there is very little difference between the GND and SSD cases in a stress relaxation test at large values of t , as the difference in total dislocation number, which would be expected to lead to a significantly higher strain accumulated by the GND case, is negligible when compared with the rapid decrease in the effective stress driving creep.

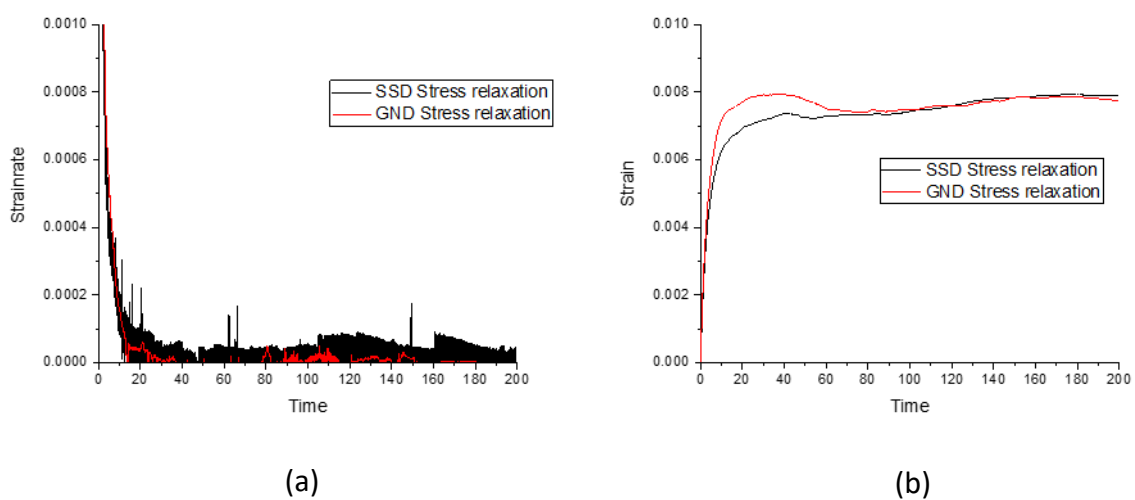


Figure 107: (a) The strain rate during the stress relaxation simulation, (b) the accumulated strain during the stress relaxation simulation.

11.32 Creep simulation

For the creep simulation both the SSD and GND case had F_{xapp} fixed at 0.15, to mirror a constant applied stress. This can be seen in Figure 105 with the stress relaxation data.

Dislocation multiplication

The data collected for the creep case in Figure 108 (a) for GND and SSD shows that the dislocation generation is far more active than the stress relaxation case, as expected given the applied force does not reduce over time. The SSD case has a rapid generation of

dislocations while $t < 50$, and begins to slow. The GND case slows similarly to the SSD case, In effect, the dislocation generation for both cases appears to be about the same. By observing the total dislocation plot in Figure 108 (b), it is apparent that the SSD case reduces in rapidly up to $t = 50$, and then at a reduced rate for the rest of the simulation. The GND case shows only a slight upward trend in the dislocation total despite the largest amount of generated dislocations, with the majority of generated dislocation pairs annihilating one-another. It can be expected that the strain rate for the GND case would therefore be higher than the SSD simulation.

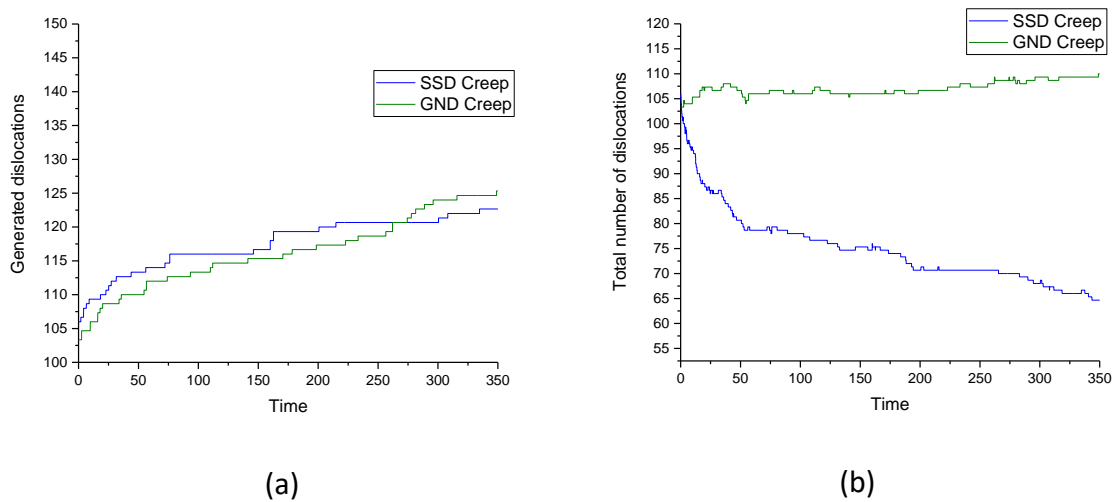


Figure 108: (a) The number of dislocations generated during the creep simulation, (b) the total number of dislocations accounting for generation and annihilation of dislocation pairs in creep.

Strain

The strain rate graph for the creep simulation in Figure 108a shows a rapid drop in the strain rate, reaching a minimum rate at approximately $t = 50$. The GND creep rate is generally higher than the SSD case, and this is due to the difference in the total number of dislocations. This is reflected in the accumulated strain plot, which shows the GND case creeps faster than the SSD case. Both the SSD and GND case move from primary to secondary creep as the dislocations pile up at obstacles. This is in stark contrast to the stress relaxation case, where there is less difference between the SSD and GND cases.

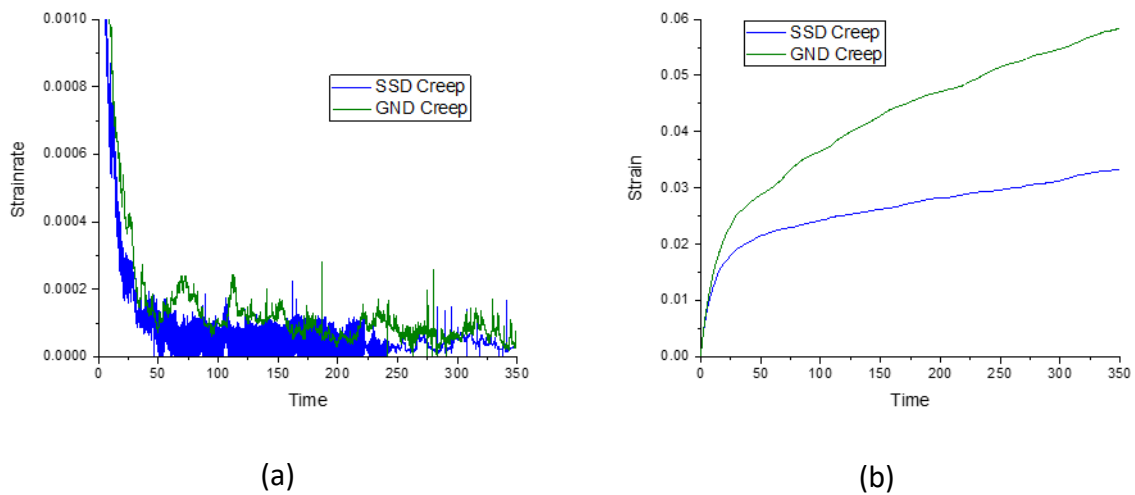


Figure 109: (a) Strain rate for SSD and GND simulations in creep simulation. (b) accumulated strain for GND and SSD simulations in creep simulation.

11.33 Stress relaxation and creep simulation summary

In summary, the model presented here shows that the difference in behaviour between the GND and SSD stress relaxation cases is noticeable initially but less obvious at longer times. Comparing stress relaxation with the creep case, it is evident that the behaviour at longer times for GND and SSD dominated simulations is significantly different. Whereas in the stress relaxation simulation the accumulated strain converges to the same value for both cases, the creep simulation shows the GND and SSD cases diverging, leading to the GND case accumulating a significantly larger amount of strain. The data from this model implies that the difference between a GND and SSD dominated sample is significant at high stresses but is not noticeable at lower stresses. To further investigate the difference between the GND and SSD effect on the stress relaxation and creep, the strain per dislocation was calculated. This was done by dividing the strain rate by the number of dislocations at that time. The strain per dislocation is then the accumulation of this strain over time. Figure 110 shows that for both cases the GND's have a greater effect on the accumulated strain compared with the SSD's, of approximately 20%. This is due to repulsive interactions between GNDs. This implies that the increased stress relaxation and creep is due to a combination of a higher number of total dislocations as GND's do not annihilate, and dislocation interactions.

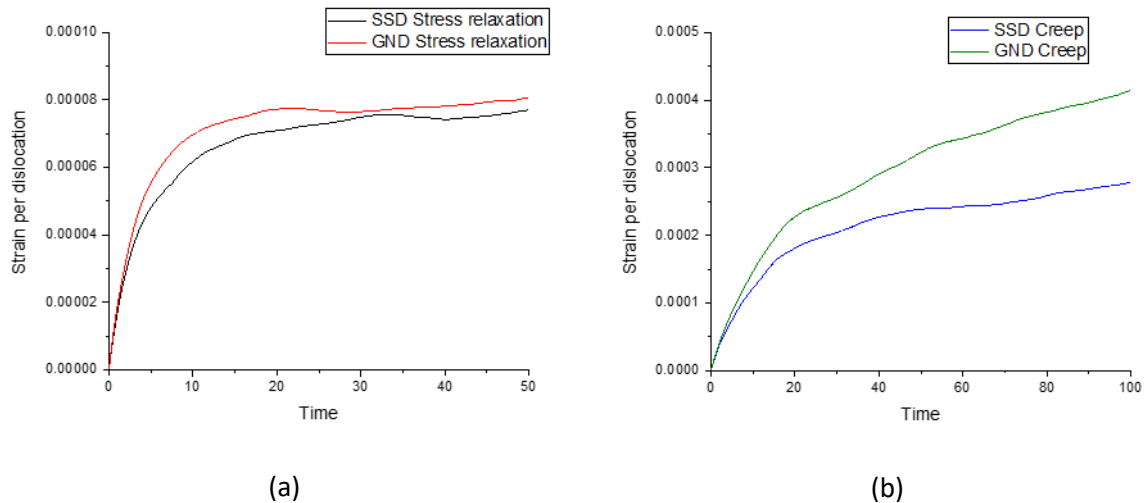


Figure 110: (a) Strain per dislocation for Stress relaxation case, (b) Strain per dislocation for creep case

11.34 Multiple stage thermomechanical processing

By reapplying the original applied force F_{app} at iterations 1000 and 2000 it is possible to recreate the three stage deformation back-stress hardening seen in chapter 9.1. The results are shown in Figure 109. The SSD and GND cases appear to relax at different rates, as expected from Figure 104. The SSD stress relaxation resistance improves significantly more than GND case. This is likely to be due to the annihilation of dislocations during the initial 1st deformation. The second and third deformations show a decreased stress relaxation rate in both cases, but with increased divergence between the SSD and GND cases. While this model should not be used to quantitatively measure the stress relaxation of a superalloy, it does imply that inducing large numbers of GND's in a spring during winding not only reduces the relaxation resistance but that GND dominated samples benefit less from a thermomechanical treatment, as the dislocation density is resistant to annealing, and dislocations repelling each other, producing a higher strain per dislocation.

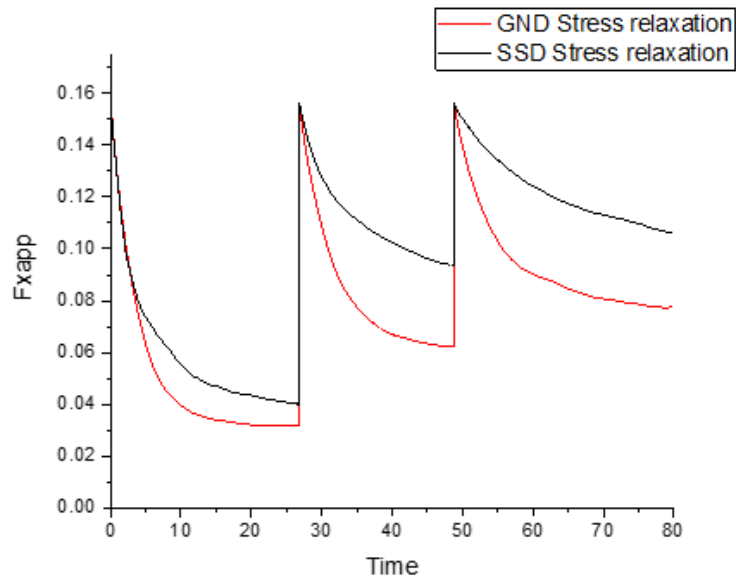


Figure 111: The thermomechanical multiple stage deformation for GND and SSD cases, with the original stress applied reapplied at two times.

11.4 Conclusions

By implementing a model to investigate the effect of dislocation interaction during stress relaxation, a series of tests were performed to investigate the effect of a GND dominated sample, which is the assumed condition of the Nimonic 90 springs in this thesis post-heat treatment. In answer to the question if there is any difference between creep and stress relaxation phenomena, this model must not be taken as a complete, thorough assessment of the two scenarios. It does, however, suggest that in answer to questions (1) and (2) at the beginning of this chapter

1. Stress relaxation is related to the creep mechanisms of dislocation climb and glide, as expected, but due to the nature of the difference between a stress relaxation test and creep test, the stress may drop during a stress relaxation test enough to prevent dislocation multiplication from occurring.
2. The model predicts strain rates significantly higher in creep in a GND dominated sample compared to SSD samples. This is primarily attributed to a combination of the lack of dislocation annihilation in the GND case, and repulsive interactions between the dislocations of the same sign.

Finally, the multiple stage thermomechanical creep hardening has been modelled, to recreate the predictions of the climb-glide dislocation-dislocation interactions on the overall stress relaxation rate, assumed by the physically based Dyson creep rate model. It was found that a sample that is GND dominated is less efficient to perform a thermomechanical treatment compared with an SSD sample. It may therefore be prudent to investigate thermomechanical treatments upon spring geometries that have less GND's as a result of forming processes.

Chapter 12: Conclusions and further work

12.1 Stress relaxation modelling

The effects of stress relaxation on nickel based superalloy springs has been modelled and discussed in this work. The main objective of this thesis was to create a microstructure-sensitive model for the stress relaxation behaviour of the springs in the temperature range of 600-700°C. This was accomplished by creating an FE model and analytical torsional model to compare with mechanical test results, based upon the physical parameters of the Dyson creep rate model, which assumes a climb-glide creep mechanism, and takes into account the γ' size and volume fraction, along with the dislocation density. The analytical model was improved with the implementation of a plastic creep zone parameter, which gave more physical results for the reaction force as $t \rightarrow 0$.

When compared with mechanical test results it was found that the models under-predicted the stress relaxation. This was determined to be due to the use of uniaxial data for the dislocation density in which GNDs were not present. By creating an FE model and comparing with analytical predictions for the GND's incurred by bending a straight wire into a coil, the dislocation density was calculated at $\rho_{GN} = 55 \times 10^{10}$, which is two orders of magnitude higher than the previously used value. Combined with the addition of back-stress hardening, the FE and analytical models were found to predict short and long-term stress relaxation data well.

Methods for improving the stress relaxation resistance of the coil springs were then considered, leading to the development of a thermomechanical process modelled using FE. By increasing the back-stress hardening prior to service, one can rearrange the dislocations onto precipitates and essentially increase the time taken to reach a given reaction force. The following conclusions were found:

- 1) A simple thermomechanical process of 8 mm compression at 650°C for 30 minutes can be modelled using FE and comparing with mechanical data it is found that the stress relaxation resistance of the spring can be increased by between 5 and 10 times.

- 2) Short thermomechanical processes are preferred due to cost and manufacturing time, and can also be shown to prevent over-coarsening of γ' .
- 3) Increasing the number of deformation stages, temperature and displacement have all been shown to have significant increases in the stress relaxation behaviour of the springs. In order to make the most efficient process, increasing the pitch/height of springs would allow for far better stress relaxation behaviour.

12.2 Microstructural and mechanical characterization

Prior to stress any stress relaxation the effects of the heat treatments and thermomechanical treatments were analysed using SEM, and EBSD methods. As-received, S+P and S+P+T samples were investigated, and the following conclusions were made

- 1) The microstructure of the as-received and heat treated samples consists of small polycrystalline grains that on average increase in size by a factor of approximately 10 when heat treated. These grains are made up of a homogenous distribution of the component elements in the γ matrix, with Ti concentrations in blocky MC carbides.
- 2) High-resolution SEM imaging of etched samples shows the γ' appears to be of uniform spherical shape, and expected size (~ 10 nm diameter) post heat-treatment.
- 3) Heat treatments appeared to have a small effect on the shape of grains, increasing the fraction of grain boundaries at higher aspect ratios.
- 4) Heat treatments increase the percentage of annealing twins and reduce the number of LAB's significantly.
- 5) The thermomechanical process had negligible effects on grain size and misorientation, but a small increase in LAB's can be seen after the process, which may indicate subgrain growth.
- 6) The overall effect of the thermomechanical process appears to be a dislocation redistribution that leads to a higher proportion of LAB's, and a small shift in the misorientation peaks towards higher angles.
- 7) The as-received sample appeared highly textured, and the heat treatments reduced the measured texture.

The stress relaxation samples utilised in the nut and bolt stress relaxation tests in chapters 10 and 11 were then investigated using SEM and EBSD, with Vickers hardness tests completed on the cross sections and surface of the wire at each time period. A method to calculate the GND density from the KAM misorientation maps was introduced. The following conclusions can be made

- 1) The hardness of the samples increased significantly during the stress relaxation tests, except for between 1 and 10 hours of relaxation in the S+P+T case. After this reduction, however, substantial increase was then found. The trend of hardness increase matched the calculated values for the dislocation density from JMatPro well.
- 2) EBSD performed on Stress relaxation tests on the samples indicate that there is measurable recovery occurring during the tests, both dislocation annihilation reducing the dislocation density after a substantive increase, and rearrangement into low angle subgrains boundaries, which subsequently coarsen.
- 3) The dislocation density from KAM maps of the samples increases by a factor of 2 up to 100 hours, and then reduces significantly by 1000 hours of testing. As the Vickers Hardness of the sample continue to increase up to 1000 hours, the question of where the effect of hardening is coming from is posed, as the new dislocation density values did not match the hardness well. It may be derived either from the dislocation multiplication in the samples, or from the coarsening of γ' , which is predicted to be significant.

12.3 Dislocation interaction model

A model was created to simulate the interactions between dislocations and precipitates within an SSD and GND dominated sample. It was found that

1. Stress relaxation does appear to be related to the creep mechanisms of dislocation climb and glide, but due to the nature of the difference between a stress relaxation test and creep test, the stress may drop during a stress relaxation test enough to prevent dislocation multiplication from occurring.

2. The model predicts strain rates significantly higher in creep in a GND dominated sample compared to SSD samples due to lack of dislocation annihilation, and dislocations repelling one another. In stress relaxation, however, an 'overshoot' effect is seen where the strain rate in a GND sample will initially increase followed by a small decrease as the dislocations arrange into lower energy formations.
3. A multiple stage thermomechanical creep hardening has been modelled, and it was found that a sample that is GND dominated is less efficient to perform a thermomechanical treatment on compared with an SSD sample. It may therefore be prudent to investigate thermomechanical treatments upon spring geometries that have less GND's as a result of forming processes.

12.4 Further work

By observing the objectives for the thesis given in chapter 1.2 it is clear that there has been some success at achieving at least in part the primary and secondary objectives. A working FE model that has been calibrated to the Nimonic 90 springs has been proposed, and tested against mechanical data, and a processing methodology has been proposed to increase the component lifetime at the increased temperatures required for more efficient turbine design. There are further experiments that can be carried out, however, and some examples are posed here:

- 1) Further mechanical testing at long time periods up to at least 1000 hours, at both 650 °C and 700 °C, to allow for further calibration of the stress relaxation models.
- 2) Perform thermomechanical processes at various temperatures and displacements on Nimonic 90 springs, to validate the predictions for reduction in height.
- 3) Design and test on Nimonic 90 springs with increased height, to fully implement the thermomechanical process with no loss in initial reaction force.
- 4) Calibrate the model to other, similar medium γ' nickel superalloys, to allow for comparison and optimal alloy choice for higher temperature use.
- 5) The Discrete Dislocation Interaction Model may be made more physical by incorporating a more physical number of Frank-Read sources, and be extended to

investigate larger numbers of dislocations, acting on different precipitate geometries such as the cuboidal γ' that is seen at larger volume fraction nickel superalloys.

- 6) The evolution of the dislocation density has been estimated using the Nye equation to give an indication from strain maps of the spring samples at various points during a stress relaxation test. It still remains to 'close the loop' on the Dyson model by linking $\dot{\rho}_{GND}$ back into the creep rate equation for $\dot{\gamma}$. The effect of this inclusion is expected to be small, due to the small calculated stain (analysis in section 3.31 predicts strain values of the order of 0.1%) and therefore the effect of dislocation multiplication arising from strain gradients may be negligible, however further investigation is worthwhile.

Finally, the choice of a helical spring for the proposed task has thus far not been taken into account. Helical coil springs are not the only design of spring used in surface control clearance systems. As the stresses have been shown to be very high due to the coiling of the wire into a helical spring, it is of worth to consider the stress relaxation behaviour of other spring designs, under similar conditions and made from the same alloy. Some early work was accomplished on this and is shown below in section 12.4.

12.4 Comparison of coil spring and leaf spring

As helical coil springs are not the only possible geometry possible for spring design, it is prudent to ensure that the current design efficient compared to other possibilities. The main other geometry used in surface control clearance systems to exert pressure against the steam turbine casing is the so-called 'Leaf-spring' design. This is named after its simple geometry, which is a simple Nickel-based superalloy plate slotted into a turbine casing with dimensions given in Table 12 and a schematic drawing of a leaf spring design given in Figure 112.

	Value	Units
INITIAL DEFLECTION (δ)	3.175	mm
PACKING RING RADIAL TRAVEL, IN.	6.35	mm
NUMBER OF RING SEGMENTS	8	-
NUMBER OF SPRINGS PER SEGMENT	1	-
SPRING THICKNESS	3.175	mm
SPRING WIDTH (< MAX WIDTH)	36.576	mm
RADIUS OF PACKING RING OUTSIDE DIAMETER, IN.	482.6127	mm
RADIUS OF TOP OF SPRING SLOT, IN .	497.5225	mm
WEIGHT OF EACH RING SEGMENT, LBS.	63.45373	N
YOUNG'S MODULUS FOR INCONEL X SPRING, PSI	179263.8	Mpa
SPRING ACTIVE LENGTH, IN.	241.7736	mm
NOM. SPRING STRESS FOR INITIAL DEFLECTION. ($\leq 50,000$ PSI)	185.487	Mpa

Table 12 leaf spring geometrical data [126]

A simple two-dimensional F.E model was designed to replicate the effect of compression on a leaf spring by creating a rectangular bar with the same mechanical properties as Nimonic 90 and compressing from the centre by indenting using a curved block to represent the casing of the turbine. This was designed to replicate the in-service compression. The casing of the turbine is indented into the centre of the leaf and the leaf has a reaction force that reduces with distance from this point.

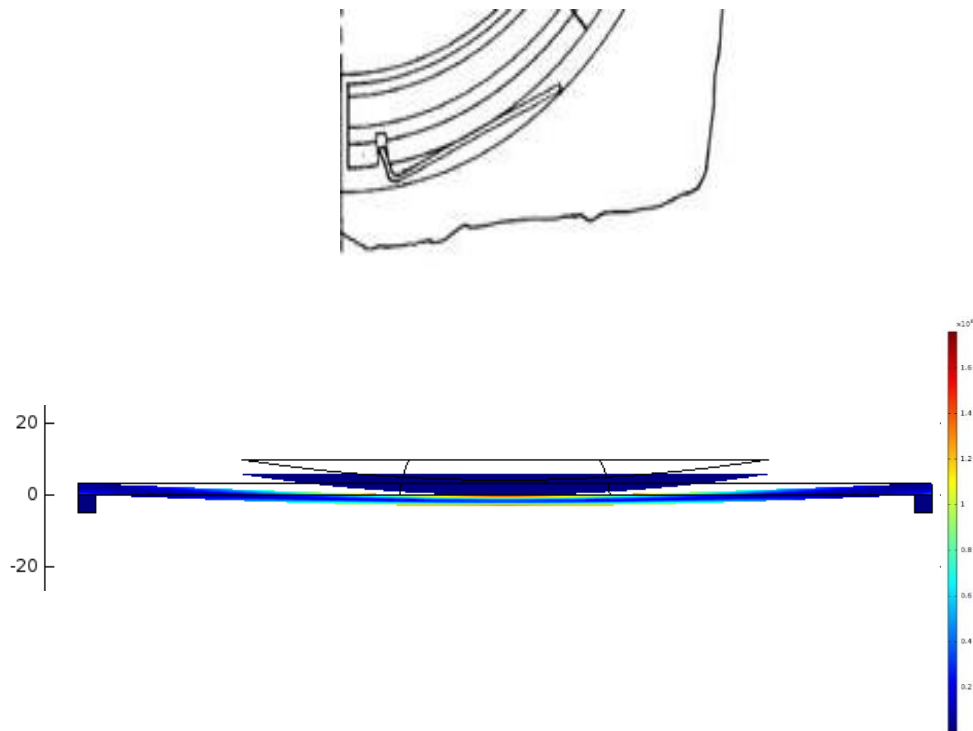


Figure 112: Above) leaf spring geometry sketch provided by GE of spring inserted into turbine surface clearance system [126]. Below) F.E model showing leaf spring under 3.175mm compression Von Mises stress concentration

Initial comparisons between the coil spring FE model and the leaf spring model found that the leaf spring could not be compressed 10 mm, and so the in-service displacement for the leaf spring, given as 3.175 mm, was utilised, along with the in-service temperature, 600°C for comparison of the models. This gives a reaction force of 165 N. The coil spring FE model was thus displaced to 12 mm in order to give 165 N reaction force. The reaction force for the leaf spring was calculated by performing a 'line integration' along the block moved into the leaf spring geometry. The contact pressure was then multiplied by the width of the leaf spring (36.576 mm) to give the contact pressure across the sample, demonstrated in Figure 113.

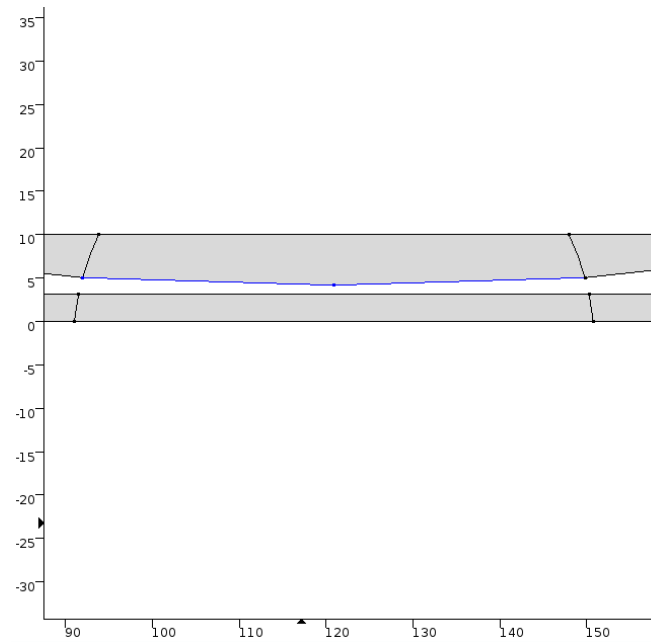


Figure 113 line shown in blue along which the contact pressure is calculated for the leaf spring model.

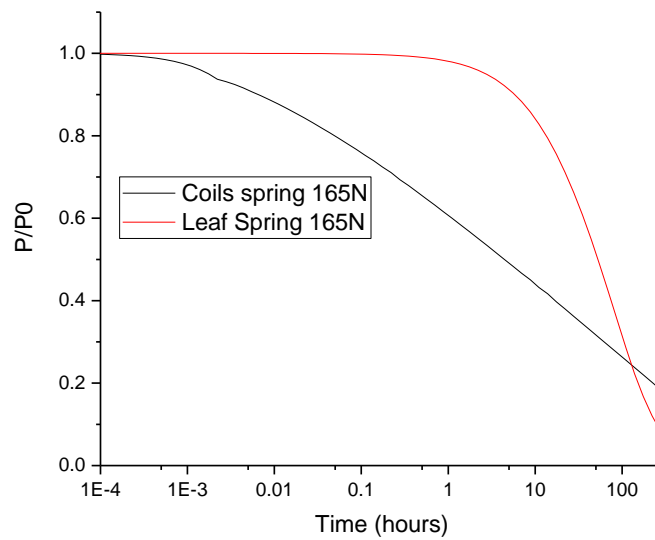


Figure 114 comparison of leaf spring and coil spring at given reaction force 165 N (coil spring displaced to 12mm and leaf spring displaced to 3.175 mm at 600°C).

It can be seen in Figure 114 that the leaf spring is better suited for short time periods, however at approx. 150 hour the coil spring becomes the more appropriate choice for stress-relaxation resistance, provided 0.2 of original reaction force is an operationally practical value. It is important to note that in reality the reaction force of the leaf spring at any given displacement is higher than that of the coil spring, and so it was necessary to compare the stress relaxation of the springs at both a given reaction force(165 N) , as in Figure 114. However, as a stress relaxation test is essentially a creep test at constant displacement, it is also of worth to directly compare stress relaxation curves for leaf and coil springs at the same displacement, which naturally gives different values of initial reaction force. This is shown in Figure 115 where a similar behaviour is seen on a smaller time-scale. The leaf spring is no longer relaxing significantly less than the coil spring. The curves are much closer than in the scenario in Figure 114. Analysis of the leaf spring using mechanical data, to determine the FE calculated values will help with understanding, and further development of the FE model.

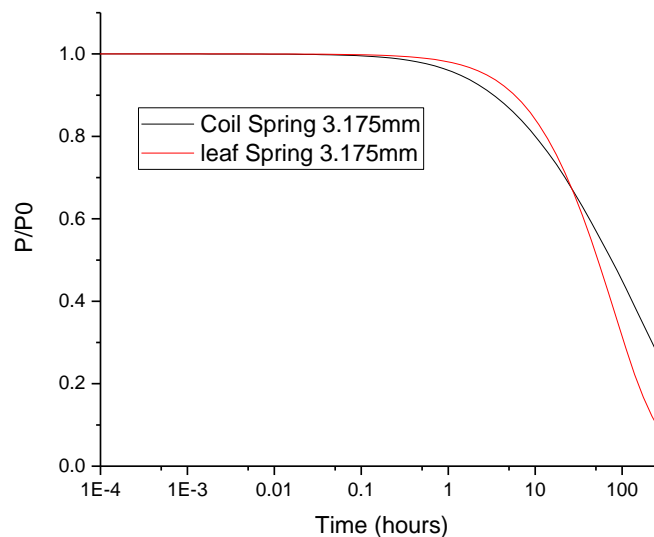


Figure 115 coil spring against leaf spring stress relaxation test, both springs at 3.175mm at 600°C.

12.11 Analytical prediction for number of coil springs to number of helix springs

As there are two wildly different geometries being compared, it is important to determine how many coil springs to leaf springs would be necessary to produce the same reaction force.

The derivation for maximum stress in the leaf spring is shown below

$$\delta = \frac{PL^3}{48EI} \quad (12.10)$$

such that

$$P = \frac{48EI}{L^3} \delta \quad (12.11)$$

where E is the Young's modulus, L is the length of the beam, $I = \frac{bd^3}{12}$ is the second moment of area, where b is the width of the beam and d is the thickness.

As reaction force, $P = k\delta$;

$$k_{leaf} = 4Eb \left(\frac{d}{L}\right)^3 \quad (12.12)$$

The maximum value for $\delta=3.175$ mm is calculated to be $\sigma_x=184.8$ MPa, which approaches the value given by G.E for the maximum stress at the same displacement (given as 188 MPa). Calculating the spring constant, k_{leaf} of the leaf spring and comparing with the spring constant of the coil geometry k_{coil} , will allow the calculation of expected ratio of reaction force at a given displacement of leaf to coil as $P = k\delta$ according to Hookes Law. This will infer the suitable number of coil springs in service to the number of leaf springs. Calculating the value of k_{leaf} gives $k_{leaf} = 59.1$ N/mm. Utilising simple elastic analytical modelling it can be shown that for a coil spring the spring constant $k_{helix} = \frac{Ga^4}{4R^3N} = 17.5$ N/mm. This gives $\frac{k_{leaf}}{k_{helix}} = 3.37$, which of course is higher than the ratio of coil springs to leaf springs in use, currently 2 coil springs for each leaf spring. This value would imply that the maximum reaction force value for a leaf spring at any given displacement would be approximately three times the value of the coil spring at the same displacement. Utilising the F.E model of the leaf spring and comparing values of reaction force at 3.175mm gives $\frac{P_{leaf}}{P_{helix}} = \frac{164.83N}{44.62N} = 3.69$ which

fits the predicted value of 3.37 well. This would suggest for that it is most efficient to utilise 3-4 coil springs in place of a single leaf spring, to produce the same reaction force.

12.2 Geometry Comparison Summary

A comparison of leaf springs and coil springs has been made utilising F.E modelling. The leaf spring is found to, at a given displacement, contribute over 3 times the reaction force of one coil spring, which is an advantage in isolation. However, if the number of coil springs is increased to three, and all 3 springs are compressed together with the amount of force as the leaf spring, it can be seen that the coil springs have superior long-term stress relaxation resistance. For example the coil springs arriving at 0.25 of the original force at 277 hours, compared to the leaf spring which arrives at 0.25 at 130 hours. For shorter term stress relaxation, i.e. under 100 hours, the two geometries have comparable stress relaxation properties, provided there is a 3:1 ratio of coil springs to leaf springs to maintain the same reaction force. As this is the case it is suggested that amount of material and cost of production of leaf springs and coil springs be investigated in order to obtain greatest efficiency in geometry selection.

References

1. Reed R. The Superalloys, Fundamentals and Applications. CAMBRIDGE UNIVERSITY PRESS.
2. Tancret F, Bhadeshia, H K D H, MacKay DJC. Design of a creep resistant nickel base superalloy for power plant applications: Part 1 - Mechanical properties modelling. *Materials Science and Technology*. 2003 Mar;19(3):283-90.
3. Krishna R, Hainsworth SV, Atkinson HV, Strang A. Microstructural analysis of creep exposed IN617 alloy. . 2009.
4. Gariboldi E, Cabibbo M, Spigarelli S, Ripamonti D. Investigation on precipitation phenomena of Ni–22Cr–12Co–9Mo alloy aged and crept at high temperature. *International Journal of Pressure Vessels and Piping*. 2008;85(1):63-71.
5. Jiang L, Feng G, Zhao J. Development of Superalloy GTD262 at GE. ; March 15, 2012.
6. Chang DJ. Prediction of Stress Relaxation for Compression and Torsion Springs. 1995 Nov 1,.
7. Dyson BF. Microstructure based creep constitutive model for precipitation strengthened alloys: theory and application. *Materials Science and Technology*. 2009 Feb;25(2):213-20.
8. Shenoy M, Tjiptowidjojo Y, McDowell D. Microstructure-sensitive modeling of polycrystalline IN 100. *International Journal of Plasticity*. 2008;24(10):1694-730.
9. Sims C.T, Stollof N.S, Hagel W.C. Superalloys: Genesis and Character, Superalloys II. 1st ed. John Wiley and Sons; 1987.
10. Davis JR. Nickel, cobalt and their alloys. 1. printing ed. Materials Park, OH: ASM Internat; 2000.
11. Jena AKC, M.C. Review The role of alloying elements in the design of nickel-base superalloys. *Journal of Materials Science*. 1984;19(1):3121-39.
12. Reed RC, Tao T, Warnken N. Alloys-By-Design: Application to nickel-based single crystal superalloys. *Acta Materialia*. 2009;57(19):5898-913.
13. S. Schlegel, S. Hopkins, E. Young, M. Frary, J. Cole, T.Lillo. Precipitate Redistribution during Creep of Alloy 617. United States: DOE - NE; 2009 Dec 1,.
14. Gessinger GH. Powder Metallurgy of Superalloys. 1st ed. Great Britain: Butterworth Monographs in Materials; 1984.
15. Á LVAREZ TEJEDOR T, Singh R, Pilidis P. Modern Gas Turbine Systems. 1st ed. Cambridge: Woodhead Publishing; 2013.
16. Durand-Charre M. The Microstructure of Superalloys. 1st ed. London: CRC; 1997.

17. Hughs H. Precipitation in alloyed steels containing chromium, nickel and titanium. J. Iron Steel Institute. 1965;203(1):1019-23.
18. Marsh A, inventor; UK Patent 2129. patent 2129. 1906 .
19. Imphy SA, inventor; French Patent 496930 . patent 496930.
20. Decker R. The evolution of wrought age-hardenable superalloys. JOM. 2006 Sep;58(9):32-6.
21. Pilling NB, Merica E, Merica PD, inventors; Inco US Patent 2 048 163 . patent 2 048 163. 1936 .
22. Betteridge W, Shaw SWK. Development of Superalloys . Materials Science and Technology. 1987;3(1):682-94.
23. Pearcey BJ, VerSnyder FL. A new development in gas turbine materials - The properties and characteristics of PWA 664. J. Aircraft. 1966;3(5):390-7.
24. McLean M. Directionally Solidified Materials for High Temperature Service . The Metals Society. 1983;1.
25. Winstone MR. Microstructure and Alloy Developments in Nickel-Based Superalloys; In: Strang A, Cawley J, Greenwood GW, editors. Microstructural stability of creep resistant alloys for high temperature plant applications. Cambridge: The University Press; 1998. p. 27-47.
26. Single Crystal Superalloys [Internet].; 2012 [cited 11/06/2018]. Available from: <https://makezine.com/2012/01/16/single-crystal-superalloys/>.
27. Courtney TH. Mechanical Behaviour of Materials. 2nd ed. Singapore: McGraw-Hill International Editions; 2000.
28. Campbell FC. Elements of Metallurgy and Engineering Alloys. 1st ed. Ohio, USA: ASM International; 2008.
29. Nickel Based Superalloys [Internet]. [cited 08/05/2018]. Available from: <https://www.phase-trans.msm.cam.ac.uk/2003/Superalloys/superalloys.html>.
30. Wilson B, Hickman J, Fuchs G. The effect of solution heat treatment on a single-crystal Ni-based superalloy. JOM. 2003 Mar;55(3):35-40.
31. Huron ES, Reed RC, Hardy MC, Mills MJ, Montero RE, Portella PD, et al. Superalloys 2012. 1. Aufl. ed. Somerset: Wiley-TMS; 2012.
32. Hazotte A, Grosdidier T, Denis S. γ' Precipitate splitting in Nickel-based superalloys: A 3-D finite element analysis. Scripta Materialia. 1996;34(4):601-8.

33. Del Llano-Vizcaya L, Rubio-Gonzalez C, Mesmacque G, Banderas-Hernández A. Stress relief effect on fatigue and relaxation of compression springs. *Materials and Design*. 2007;28(4):1130-4.
34. Callister WD. *Materials Science and Engineering*. 7th ed. USA: John Wiley and Sons; 2007.
35. Baldan A. Review Progress in Ostwald ripening theories and their applications to nickel-base superalloys Part I: Ostwald ripening theories. *Journal of Materials Science*. 2002 Jun;37(11):2171-202.
36. Pelachova T, Bajana O. *Key Engineering Materials*. Trans Tech Publishers; 2013.
37. Preuss M, Quinta da Fonseca J, Grant B, Knoche E, Moat R, Daymond M. The effect of γ' particle size on the deformation mechanism in an advanced polycrystalline nickel-base superalloy. In: Reed R, Green K, Caron P, Gabb T, Fahrman M, Huron E, et al, editors. *Superalloys 2008*. Elsevier Ltd; 2008. p. 405-14.
38. Völkl R, Glatzel U, Feller-Kniepmeier M. Measurement of the lattice misfit in the single crystal nickel based superalloys CMSX-4, SRR99 and SC16 by convergent beam electron diffraction. *Acta Materialia*. 1998;46(12):4395-404.
39. Müller L, Glatzel U, Feller-Kniepmeier M. Modelling thermal misfit stresses in nickel-base superalloys containing high volume fraction of γ' phase. *Acta Metallurgica Et Materialia*. 1992;40(6):1321-7.
40. Van Sluytman JS. *Microstructure and high temperature creep of platinum group metal modified nickel base superalloys [dissertation]*. University of Michigan; 2010.
41. CHEN Q, JONES C, KNOWLES D. The grain boundary microstructures of the base and modified RR 2072 bicrystal superalloys and their effects on the creep properties. *Materials Science and Engineering A*. 2004 Nov 15;;385(1-2):402-18.
42. Chen QZ, Jones N, Knowles DM. The microstructures of base/modified RR2072 SX superalloys and their effects on creep properties at elevated temperatures. *Acta Materialia*. 2002;50(5):1095-112.
43. Liu LR, Jin T, Zhao NR, Sun XF, Guan HR, Hu ZQ. Formation of carbides and their effects on stress rupture of a Ni-base single crystal superalloy. *Materials Science & Engineering A*. 2003;361(1):191-7.
44. Reed R, Jackson M, Na Y. Characterization and modeling of the precipitation of the sigma phase in UDIMET 720 and UDIMET 720Li. *Metall and Mat Trans A*. 1999 Mar;30(3):521-33.
45. NDT Resource Center- Linear Defects-Dislocations [Internet]. [cited 15/05/2018]. Available from: https://www.nde-ed.org/EducationResources/CommunityCollege/Materials/Structure/linear_defects.htm.

46. Tian S, Yu X, Jinghong Y, Nairen Z, Yongbo X, Zhuangqi H. Deformation features of a nickel-base superalloy single crystal during compression creep. *Materials Science and Engineering A*. 2004;379(1):141-7.
47. Ardell A. precipitation hardening. *Metallurgical and Materials Transactions A*. 1985;16(1):2131-65.
48. Nickel based superalloy: dislocation structure [Internet]. [cited 15/05/2018]. Available from: <http://www.phase-trans.msm.cam.ac.uk/2002/Zhang.html>.
49. R W Kozar, A Suzuki, W W Milligan, J J Schirra, M F Savage, T M Pollock. Strengthening Mechanisms in Polycrystalline Multimodal Nickel-Base Superalloys. *Metallurgical and Materials Transactions*. 2009 Jul 1;40A(7):1588-603.
50. 'Nimonic Alloy 90'- Special Metals [Internet].; 2004 [cited 30/05/2018]. Available from: <http://www.specialmetalswiggins.co.uk/pdfs/products/NIMONIC%20alloy%2090.pdf>.
51. Harrison GF, Evans WJ, Winstone MR. Comparison of empirical and physical deformation maps for Nimonic 90. *Materials Science and Technology*. 2009 Feb;25(2):249-57.
52. Ezugwu EO, Wang ZM, Machado AR. The machinability of nickel-based alloys: a review. *Journal of Materials Processing Tech*. 1999 Feb 15;86(1-3):1-16.
53. University of Cambridge DoITPoMS [Internet].; 2006 [cited 11/06/2018]. Available from: <https://www.doitpoms.ac.uk/tlplib/creep/intro.php>.
54. Courtney T. *Mechanical Behaviour of Materials*. 2nd ed. Singapore: McGraw Hill Book Co; 2000.
55. Shah D, Vega S, Woodard S, Cetel A. PRIMARY CREEP IN NICKEL-BASE SUPERALLOYS. In: Green KA, Pollock TM, Harada H, editors. *Superalloys 2004*. USA: The Minerals, Metals & Materials Society; 2004. p. 197-206.
56. Poirier JP. On the symmetrical role of cross-slip of screw dislocations and climb of edge dislocations as recovery processes controlling high-temperature creep. *Revue de Physique Appliquée*. 1976;11(6):731-8.
57. Jenkins WD, Digges TG, Johnson CR. Creep of High-Purity Nickel. *Journal of Research of the National Bureau of Standards*. 1954;53(6):329-52.
58. Rosler J, Arzt E. The kinetics of dislocation climb over hard particles--II. Effects of an attractive particle-dislocation interaction. *Acta materialia*. 1988;36(4):1053-60.
59. Chen JF, Jiang JT, Zhen L, Shao WZ. Stress relaxation behavior of an Al–Zn–Mg–Cu alloy in simulated age-forming process. *Journal of Materials Processing Technology*. 2014 Apr;214(4):775-83.

60. Zhang JX, Harada H, Ro Y, Koizumi Y, Kobayashi T. Thermomechanical fatigue mechanism in a modern single crystal nickel base superalloy TMS-82. *Acta Materialia*. 2008;56(13):2975-87.
61. Gupta I, Li JCM. Stress Relaxation, Internal Stress and Work Hardening in LiF and NaCl Crystals. *Materials Science and Engineering*. 1970;6(1):20-6.
62. Chaboche JL. Constitutive equations for cyclic plasticity and cyclic viscoplasticity. *International Journal of Plasticity*. 1989;5(3):247-302.
63. Zhan Z-, Tong J. A study of cyclic plasticity and viscoplasticity in a new nickel-based superalloy using unified constitutive equations. Part II: Simulation of cyclic stress relaxation. *Mechanics of Materials*. 2007;39(1):73-80.
64. Orowan E. Fracture and strength of solids. *Reports on Progress in Physics*. 1949;12(1):185-231.
65. Kassner ME, Perez-Prado MT. *Fundamentals of creep in metals and alloys*. 1st ed. London: Elsevier; 2004.
66. Norton eH. *The Creep of Steel at High Temperatures*. 1st ed. New York: McGraw Hill; 1929.
67. Méric L, Cailletaud G. Single Crystal Modeling for Structural Calculations: Part 2—Finite Element Implementation. *Journal of Engineering Materials and Technology*. 1991;113(1):171.
68. Nabarro FRN, de Villers F. *Physics Of Creep And Creep-Resistant Alloys*. 1st ed. London: Taylor and Francis; 1995.
69. Pollock TM, Argon AS. Creep resistance of CMSX-3 nickel base superalloy single crystals. *Acta Metallurgica et Materialia*. 1992;40(1):1-30.
70. McLean M, Dyson BF. Modeling the Effects of Damage and Microstructural Evolution on the Creep Behavior of Engineering Alloys. *Journal of Engineering Materials and Technology*. 2000;122(3):273.
71. BASOALTO HC, Wisbey A, Brooks JW. A Micromechanics Approach to Residual Life Assessment of Nickel-Based Superalloys. *ICF-12*. 2009;1(1):1-10.
72. Dyson B. Use of CDM in Materials Modeling and Component Creep Life Prediction. *Journal of Pressure Vessel Technology*. 2000;122(3):281.
73. Mustata R, Hayhurst RJ, Hayhurst DR, Vakili-Tahami F. CDM predictions of creep damage initiation and growth in ferritic steel weldments in a medium-bore branched pipe under constant pressure at 590° C using a four-material weld model. *Arch Appl Mech*. 2006 May;75(8):475-95.

74. Kobelev V. Some basic solutions for nonlinear creep. *International Journal of Solids and Structures*. 2014 Oct;51(19-20):3372-81.
75. Jiang WG, Henshall JL, Walton JM. A concise finite element model for three-layered straight wire rope strand. *International Journal of Mechanical Sciences*. 2000;42(1):63-86.
76. Gill SPA, McColvin G, Strang A. Stress relaxation of nickel-based superalloy helical springs at high temperatures. *Materials Science and Engineering: A*. 2014 Sep;613:117-29.
77. Lewthwaite GW, Smith RT. On the analysis of creep tests using helical spring specimens. *British Journal of Applied Physics*. 1967 Jul 1;18(7):1012-6.
78. Watanabe K, Hamamoto H, Ito Y, Isobe H. Proceedings of the Advanced Spring Technology, Japanese Society of Spring Engineers 60th anniversary International Symposium. 2007; Nagoya, Japan: .
79. Harrison GF, Evans WJ, Winstone MR. Comparison of empirical and physical deformation maps for Nimonic 90. *Materials Science and Technology*. 2009 Feb;25(2):249-57.
80. Werner BT, Antoun BR, Sartor GB. Thermal Degradation of Extension Springs. United States: USDOE National Nuclear Security Administration (NNSA); Mar 1, 2015.
81. Mulla TM, Kadam SJ, Kengar VS. FINITE ELEMENT ANALYSIS OF HELICAL COIL COMPRESSION SPRING FOR THREE WHEELER AUTOMOTIVE FRONT SUSPENSION. *International Journal of Mechanical and Industrial Engineering*. 2012;2(3):74-7.
82. Koutaro, WATANABE TAMA SPRING CO, LTD, 2-5-14 Oyamagaoka2Choume, Machida-city, Tokyo, 194-0215 Japan TEL:+ 81-42-798-5511 FAX:+81-42-798-5515 e-mail:research@tamaspring.co.jp. Simplified Stress Calculation Method for Helical Spring.
83. Gill SPA, Atkinson HV. *Structural Alloys for Power Plants*. In: ; 2012. p. chapter 21.
84. Arsenlis A, Parks DM. Crystallographic aspects of geometrically-necessary and statistically-stored dislocation density. *Acta Materialia*. 1999;47(5):1597-611.
85. Fleck NA, Muller GM, Ashby MF, Hutchinson JW. Strain Gradient Plasticity: Theory and Experiment. *Acta metall. mater*. 1994;42(2):475-87.
86. Article *Acta Metallurgica* · March 1953. Some Geometrical Relations In Dislocated Crystals.
87. Arsenlis A, Parks DM. Crystallographic aspects of geometrically-necessary and statistically-stored dislocation density. *Acta Materialia*. 1999;47(5):1597-611.
88. Kysar JW, Gan YX, Morse TL, Chen X, Jones ME. High strain gradient plasticity associated with wedge indentation into face-centered cubic single crystals: Geometrically necessary dislocation densities. *Journal of the Mechanics and Physics of Solids*. 2007;55(7):1554-73.

89. Fleck NA, Hutchinson JW. Strain Gradient Plasticity. *Advances in Applied Mechanics*. 1997;33(1):295-361.
90. Yang M, Pan Y, Yuan F, Zhu Y, Wu X. Back stress strengthening and strain hardening in gradient structure. *Materials Research Letters*. 2016 Jul 2;;4(3):145-51.
91. Swieskowski HP. *Heat Setting Procedures for Helical Coiled Springs*. Illinois, USA: 1976.
92. Slingsby RG. A new heat-treatment process overcomes temperature relaxation problems for spring users. *shotpeener.com*; 1979.
93. Srinivasa N, Prasad YVRK. Hot working characteristics of nimonic 75, 80A and 90 superalloys: a comparison using processing maps. *Journal of Materials Processing Tech*. 1995;51(1):171-92.
94. Saunders N, Guo U, Li X, Miodownik A, Schillé J. Using JMatPro to model materials properties and behavior. *JOM*. 2003 Dec;55(12):60-5.
95. Li X, Saunders N, Miodownik A. The coarsening kinetics of γ' particles in nickel-based alloys. *Metall and Mat Trans A*. 2002 Nov;33(11):3367-73.
96. Kruml T. From dislocation cores to strength and work-hardening: a study of binary Ni3Al. *Acta Materialia*. 2002 Dec 3;;50(20):5091-101.
97. Lin YC, Wu X, Chen J, Chen X, Wen D, Zhang J, et al. EBSD study of a hot deformed nickel-based superalloy. *Journal of Alloys and Compounds*. 2015 Aug 15;;640:101-13.
98. Wusatowska-Sarnek AM, Blackburn MJ, Aindow M. Techniques for microstructural characterization of powder-processed nickel-based superalloys. *Materials Science & Engineering A*. 2003 Nov 15;;360(1-2):390-5.
99. Hwang JY, Banerjee R, Tiley J, Srinivasan R, Viswanathan GB, Fraser HL. Nanoscale Characterization of Elemental Partitioning between Gamma and Gamma Prime Phases in René´ 88 DT Nickel-Base Superalloy. *METALLURGICAL AND MATERIALS TRANSACTIONS A*. 2009;40A(24):24-35.
100. Jin Y, Bernacki M, Rohrer GS, Rollett AD, Lin B, Bozzolo N. Formation of Annealing Twins during Recrystallization and Grain Growth in 304L Austenitic Stainless Steel. *Materials Science Forum*. 2013 Mar;753:113-6.
101. Lapin J, Pelachova T, Bajana O. Microstructure and Mechanical Properties of CMSX-4 Single Crystals Prepared by Additive Manufacturing. *22nd International Conference on Metallurgy and Materials (METAL)*. 2013:1277-82.
102. Dingley DJ, Field DP. Electron backscatter diffraction and orientation imaging microscopy. *Materials Science and Technology*. 1997;13(1):69-78.

103. From data acquisition to advanced analysis. EBSD Explained.
104. Mingard KP, Roebuck B, Bennett EG, Thomas M, Wynne BP, Palmiere EJ. Grain size measurement by EBSD in complex hot deformed metal alloy microstructures. *Journal of Microscopy*. 2007;227(3):298-308.
105. Prior D, Mariani E, Wheeler J. EBSD in the Earth Sciences: Applications, Common Practice, and Challenges. In: Schwartz AJ, editor. *Electron Backscatter Diffraction in Materials Science 2nd Ed.* USA: Springer Science+Business Media; 2009. p. 345-60.
106. Bachmann F, Hielscher R, Schaeben H. Texture Analysis with MTEX – Free and Open Source Software Toolbox. *Solid State Phenomena*. 2010 Feb;160:63-8.
107. EBSD Explained [Internet].; 2015 [cited 17/07/2018]. Available from: <https://nano.oxinst.com/products/ebsd/>.
108. Detrois M, Goetz R, Helmink R, Tin S. The role of texturing and recrystallization during grain boundary engineering of Ni-based superalloy RR1000. *J Mater Sci*. 2016 Jun;51(11):5122-38.
109. Srinivasa N, Prasad YVRK. Hot working characteristics of nimonic 75, 80A and 90 superalloys: a comparison using processing maps. *Journal of Materials Processing Tech*. 1995;51(1):171-92.
110. Randle V, Davies H, Cross I. Grain boundary misorientation distributions. *Current Opinion in Solid State & Materials Science*. 2001;5(1):3-8.
111. Hou J, Peng QJ, Lu ZP, Shoji T, Wang JQ, Han E-, et al. Effects of cold working degrees on grain boundary characters and strain concentration at grain boundaries in Alloy 600. *Corrosion Science*. 2011;53(3):1137-42.
112. Vandermeer RA, Juul Jensen D. The Migration of High Angle Grain Boundaries during Recrystallization. *Interface Science*. 1998 Feb 1;;6(1):95.
113. Imam MA, Pande CS. NUCLEATION AND GROWTH OF TWIN INTERFACES IN FCC METALS AND ALLOYS. *Materials and Physical Mechanics*. 2000;1(2):61-6.
114. Wright SI, Nowell MM, Field DP. A Review of Strain Analysis Using Electron Backscatter Diffraction. *Microscopy and Microanalysis*. 2011 May 23;;17(3):316-29.
115. Moussa C, Bernacki M, Besnard R, Bozzolo N. About quantitative EBSD analysis of deformation and recovery substructures in pure Tantalum. *Institute of Physics Publishing*; Aug 2015.
116. Humphreys FJ. A unified theory of recovery, recrystallization and grain growth, based on the stability and growth of cellular microstructures—I. The basic model. *Acta Materialia*. 1997;45(10):4231-40.

117. Calcagnotto M, Ponge D, Demir E, Raabe D. Orientation gradients and geometrically necessary dislocations in ultrafine grained dual-phase steels studied by 2D and 3D EBSD. *Materials Science & Engineering A*. 2010;527(10):2738-46.
118. Ruggles TJ, Fullwood DT. Estimations of bulk geometrically necessary dislocation density using high resolution EBSD. *Ultramicroscopy*. 2013 Oct;133:8-15.
119. Hardin TJ, Adams BL, Fullwood DT, Wagoner RH, Homer ER. Estimation of the full Nye's tensor and its gradients by micro-mechanical stereo-inference using EBSD dislocation microscopy. *International Journal of Plasticity*. 2013 Nov;50:146-57.
120. Wilkinson AJ, Britton TB. Strains, planes, and EBSD in materials science. *Materials Today*. 2012 Sep;15(9):366-76.
121. Gourdet S, Montheillet F. A model of continuous dynamic recrystallization. *Acta Materialia*. 2003;51(9):2685-99.
122. Defects and Microstructure in Materials [Internet].; 2015 [cited 15/08/2018]. Available from: <http://people.virginia.edu/~lz2n/mse6020/>.
123. Haghghat SMH, Eggeler G, Raabe D. Effect of climb on dislocation mechanisms and creep rates in $[\gamma]$ '-strengthened Ni base superalloy single crystals: A discrete dislocation dynamics study. *Acta Materialia*. 2013 Jun 1,;61(10):3709.
124. Haghghat SMH, Eggeler G, Raabe D. Effect of climb on dislocation mechanisms and creep rates in $[\gamma]$ '-strengthened Ni base superalloy single crystals: A discrete dislocation dynamics study. *Acta Materialia*. 2013 Jun 1,;61(10):3709.
125. Szajewski BA, Chakravarthy SS, Curtin WA. Operation of a 3D Frank–Read source in a stress gradient and implications for size-dependent plasticity. *Acta Materialia*. 2013 Mar;61(5):1469-77.
126. Dimensions of a leaf spring. 2016.
127. All about circuits [Internet].; 2015 [cited 24/08/2015]. Available from: www.allaboutcircuits.com/vol_1/chpt_9/7.html.
128. Weertman, J. Creep Deformation of ice. *Annual Reviews, Earth Planet. Sci*, 1983, 11, 215-40

Appendices

Appendix 1 finite difference equations

The finite difference equations for the creep rate equation involving back stress hardening are summarised here. The general form for the finite difference method is

$$f_{n+1} = f_n + (f(x)_n * \Delta t) \quad (9.10)$$

where $\Delta t = 0.001 \times t$.

From equation (6.22) the rate of change of H is defined as

$$\dot{H} = \left[\frac{Ef}{3(1-f)} \left(1 - \frac{H}{H^*} \right) + HG \right] \frac{1}{G(gr\phi - \gamma_c)} \dot{\gamma}_c \quad (9.10)$$

The solution for H_{n+1} is therefore

$$H_{n+1} = H_n + \left(\left[\frac{Ef}{3(1-f)} \left(1 - \frac{H}{H^*} \right) + HG \right] \frac{1}{G(gr\phi - \gamma_c)} \dot{\gamma}_c \right) \times \Delta t \quad (9.12)$$

From equation (6.24) the creep rate $\dot{\gamma}_c$ is written as

$$\dot{\gamma}_c = \sqrt{3}A \sinh[\sqrt{3}\alpha G b \phi (1 - H(t))] \quad (9.13)$$

The solution for $\gamma_{c,n+1}$ is therefore

$$\gamma_{c,n+1} = \gamma_{c,n} + (\sqrt{3}A \sinh[\sqrt{3}\alpha G b \phi (1 - H_n)]) \times \Delta t \quad (9.14)$$

The finite difference model calculates the stress relaxation using equation (5.32) which uses $b(t)$ as a parameter. $b(t)$ may be defined from equation (5.29) as $\dot{b} = \frac{-A \sinh(\alpha G b \phi)}{\phi}$. The

solution for b_{n+1} is

$$b_{n+1} = b_n - \left(\left(\frac{\gamma_{c,n}}{\phi} \right) \times \Delta t \right) \quad (9.15)$$

Inserting b_n and $b_0 = a = 0.00125$ into equation (5.32) allows for calculation of the stress relaxation with the back-stress hardening parameter, H .

Appendix 2 Discrete dislocation interaction model

```

clear;
tic; % start timer

% Set up
N =100; % number of dislocations
b0=2.5e-10; % magnitude of the Burgers vector
XLim = 500*b0; % width of sample
YLim = 500*b0; % height of sample
tmax = 100; % maximum time to run simulation for
itmax = 20000; % maximum number of iterations
itinterval=[1:100:itmax]; % interval of iterations for dislocation
multiplication
%dt=tmax/itmax; % change in time for each iteration
%Fapp=(2.75E5/400E-6); % applied shear stress
Fapp=6E8;
G=6.26E10; % shear modulus
tau=G/100; % applied shear stress
nu=0.33; % Poisson ratio
Mx=1;
My=0.0001; % mobility in y-direction (assume cclimb in y)
dmax=XLim/1000; % maximum distance a dislocation can move
%g=44; % number of gamma prime particles
r=20*b0; %radius of gamma prime
primearea=pi()*(r^2); %gamma prime area
%f=0.0 %volume fraction of gamma prime
f=0.2;
gvalue=((XLim*YLim)/primearea)*f; %area fraction of gamma prime giving
number of gamma prime particles
g=(round(gvalue));
mindisdist=b0; %minimum dislocation distance
ddensity=N/(XLim*YLim); %Dislocation density
Nfr=4; %number of Frank Read Sources
frdx=15*b0; % initial (half) spacing between newly
generated dislocations
b02=b0^2;
A=G/(2*pi*(1-nu))*b02; % stress constant
fxcrit=A/(2*frdx); % attractive force between two new FR dislocs
which must be exceeded if they are not to immediately annihilate
alpha=3.92E-8; %stress constant
Yslip=[b0:50*b0:500*b0]; %Slip planes
Fcrit=max(fxcrit,0.0); % force to activate FR sources (should be greater
than fxcrit)
mu=0.33; %poisson ratio
Hstar=(2*f)/(1+(2*f)); %max back stress
a=2*((1+mu)*f)/(3*(1-f)); %back stress a
b1=((1+mu)*(1+(2*f)))/(3*(1-f))-1; %back stress b
Nneg=0; %number of annihilated dislocations
Nneg1=0;

% Generate dislocations
x(1:N)=0;
y(1:N)=0;
vx(1:N)=0;
vy(1:N)=0;
b(1:N,1:2)=0;
for i = 1:N
    x(i)=random('unif',0,XLim);

```

```

y(i)=random('unif',0,YLim);
angle = random('unif',0,2*pi);
if (angle<pi)
    b(i,1)=+1.0;
    b(i,2)=0.0;
else
    b(i,1)=-1.0;
    b(i,2)=0.0;
end;
end;
for i=1:N
    D(i,1:2)=[x(i),y(i)];
end

% Generate Gamma Prime
k=1;
dmin=2*r;           %minimum distance between dislocations
p=1;
n=g;
k=1;
xvalue=zeros(1,n);
yvalue=zeros(1,n);

ncover=round(YLim/(1.0*r)); % number of particles required to block whole
vertical section spaced r apart
xc(k)=random('unif',0,XLim);
yc(k)=0.0;           %random('unif',0,YLim);
xvalue(1,1)=xc(k);
yvalue(1,1)=yc(k);
k=k+1;
while k<n+1
    xc(k)=random('unif',0,XLim);
    if (k<=ncover)
        yc(k)=(k-1)*1.0*r;           % ensure 1st ncover particles
completely cover vertical section
    else
        yc(k)=random('unif',0,YLim);
    end
    if k>1
        mindistance=1e10;
        for i=1:k-1           % check distances between particles
(taking periodic boundaries into account)
            dx=xc(k)-xc(i);
            dy=yc(k)-yc(i);
            if dx>(XLim/2)           %boundary condition in x direction
                dx=dx-XLim;
            end
            if dx<(-XLim/2)           %boundary condition in x direction
                dx=dx+XLim;
            end
            if dy>(YLim/2)           %boundary condition in y direction
                dy=dy-YLim;
            end
            if dy<(-YLim/2)           %boundary condition in y direction
                dy=dy+YLim;
            end
            dist2=dx^2+dy^2;
            if dist2<mindistance mindistance=dist2; end
        end
        if sqrt(mindistance)>=2.5*r   % leave space around particles so no
touching

```

```

        xvalue(1,k)=xc(k);
        yvalue(1,k)=yc(k);
        k=k+1;
    end
end
end

%*****Frank-Read Sources*****

k=1;
while k<Nfr+1;
    xfrc=random('unif',0,XLim);
    yfrc=random('unif',0,YLim);
    mindistance=1e10;
    for i=1:n+k-1 % check distances between particles
        (taking periodic boundaries into account)
        dx=xfrc-xc(i);
        dy=yfrc-yc(i);
        if dx>(XLim/2) %boundary condition in x direction
            dx=dx-XLim;
        end
        if dx<(-XLim/2) %boundary condition in x direction
            dx=dx+XLim;
        end
        if dy>(YLim/2) %boundary condition in y direction
            dy=dy-YLim;
        end
        if dy<(-YLim/2) %boundary condition in y direction
            dy=dy+YLim;
        end
        dist2=dx^2+dy^2;
        if dist2<mindistance mindistance=dist2; end
    end
    if sqrt(mindistance)>2.5*r
        xfr(k)=xfrc;
        yfr(k)=yfrc;
        xc(n+k)=xfrc;
        yc(n+k)=yfrc;
        k=k+1;
    end
end

% ***** Main loop *****
t=0;
it=0; % number of iterations
sc=XLim/sqrt(N)/10;
dxmax=(XLim/2);
dymax=(YLim/2);
while (it<itmax)
    it=it+1;
    My=(1E-10);
    Mx=My*100;

    if it>1 %for
        constant stress and Fxapp in simulation
        % tau(it)=(tau(it-1));
        tau(it)=G*(0.01-strain(it-1)); % stress relaxation
        % if (it>1000) tau(it)=G*(0.01+strain(1000)-strain(it-1)); end
        % reapply original load after 10000 iterations
    end
end

```

```

%         if (it>2000) tau(it)=G*(0.01+strain(2000)-strain(it-1)); end
% reapply original load after 10000 iterations
else
    tau(1)=G*0.01;
end

if it>1
    Fxapp=tau(it)*b0;           %applied force x axis
    Fyapp=tau(it)*b0;           %applied force y axis
else
    Fxapp=tau(1)*b0;           %applied force x axis
    Fyapp=tau(1)*b0;           %applied force y axis
end

Nneg=0; %reset Nneg every iteration

%*****FRANK READ SOURCE DISLOCATION GENERATION*****
if ismember(it,itinterval)    % limits dislocation generation
every interval
    % calculate forces on frank read sources
    Fxfrp(1:Nfr)=0;           % a pair of dislocs produces
    (p=+ and m=-)
    Fxfm(1:Nfr)=0;
    for i=1:Nfr
        for j=1:N
            dyfr=y(j)-yfr(i);
            if dyfr>(YLim/2)           %boundary condition in y
direction
                dyfr=dyfr-YLim;
            end
            if dyfr<(-YLim/2)           %boundary condition in y
direction
                dyfr=dyfr+YLim;
            end
            dxfr=x(j)-(xfr(i)+frdx);    % 1st (+ive) disloc in FR pair
            if dxfr>(XLim/2)           %boundary condition in x
direction
                dxfr=dxfr-XLim;
            end
            if dxfr<(-XLim/2)           %boundary condition in x
direction
                dxfr=dxfr+XLim;
            end
            dist2=dxfr^2+dyfr^2;
            Ab=-A*(1.0)*b(j,1)/dist2^2; % assumes burgers vector
only has x-component
            fxfr=Ab*dxfr*(dxfr^2-dyfr^2);
            Fxfrp(i)=Fxfrp(i)+fxfr;    % force acting on i due to
j
            dxfr=x(j)-(xfr(i)-frdx);    % 2nd (-ive) disloc in FR
pair
            if dxfr>(XLim/2)           %boundary condition in x
direction
                dxfr=dxfr-XLim;
            end
            if dxfr<(-XLim/2)           %boundary condition in x
direction
                dxfr=dxfr+XLim;
            end
        end
    end
end

```

```

        end
        dist2=dxfr^2+dyfr^2;
        Ab=-A*(-1.0)*b(j,1)/dist2^2;           % assumes burgers vector
only has x-component
        fxfr=Ab*dxfr*(dxfr^2-dyfr^2);
        Fxfrm(i)=Fxfrm(i)+fxfr;               % force acting on i
due to j
    end
end

for i=1:Nfr
    if (Fxfrp(i)+Fxapp*(+1.0)>Fcrit)&&(Fxfrm(i)+Fxapp*(-1.0)<=-
Fcrit) % force on +ive FR dislocation must be positive to activate
        b(N+1,1)=+1.0;
        b(N+1,2)=0.0;
        b(N+2,1)=-1.0;
        b(N+2,2)=0.0;
        x=[x xfr(i)+frdx xfr(i)-frdx];      % introduce a pair of
dislocs 2*frdx apart
        y=[y yfr(i) yfr(i)];
        N=N+2;
    end
end
end

%*****Calculate forces with dislocations*****
Fx(1:N)=0;           % zero forces
Fy(1:N)=0;
for i = 1:N
    for j=1:i-1
        dx=(x(j)-x(i));
        dy=(y(j)-y(i));
        if dx>(XLim/2) %boundary condition in x direction
            dx=dx-XLim;
        end
        if dx<(-XLim/2) %boundary condition in x direction
            dx=dx+XLim;
        end
        if dy>(YLim/2) %boundary condition in y direction
            dy=dy-YLim;
        end
        if dy<(-YLim/2) %boundary condition in y direction
            dy=dy+YLim;
        end
        dist2=dx^2+dy^2;
        if (dist2<b02) % minimum separation allowed between dislocations
            dist2=b02;
            if (b(i,1)+b(j,1)==0) % opposite sign so annihilate
                b(i,1)=0;
                b(j,1)=0;
            end
        end
        Ab=-A*b(i,1)*b(j,1)/dist2^2; % assumes burgers vector only has x-
component
        fx=Ab*dx*(dx^2-dy^2);
        fy=Ab*dy*(3*dx^2+dy^2);
        Fx(i)=Fx(i)+fx; % force acting on i due to j
        Fx(j)=Fx(j)-fx; % force acting on j due to i
        Fy(i)=Fy(i)+fy; % force acting on i due to j
        Fy(j)=Fy(j)-fy; % force acting on j due to i
    end
end;

```

```

end;

% calculate dislocation velocities
for i=1:N
    vx(i)=(Mx)*(Fxapp*b(i,1)+(Fx(i)));
    vy(i)=(My)*(Fyapp*b(i,1)+(Fy(i)));
    if b(i,1)*vy(i)<0 vy(i)=0; end
end;

% calculate time step
vxmax=max(abs(vx));
vymax=max(abs(vy));
dt(it)=(dmax/max([vxmax,vymax]));

hold on;

% Move dislocations
for i=1:N
    x(i)=x(i)+vx(i)*dt(it);
    y(i)=y(i)+vy(i)*dt(it);
end;

% Plot dislocations
if (mod(it,25)==0) % plot every 25 iterations
    figure(1);
    axis([0 XLim 0 YLim]);
    daspect([1 1 1]);
    hold on

    for k=1:g %gamma prime circle
        rectangle('Position',[xvalue(1,k)-r yvalue(1,k)-r 2*r
2*r],'FaceColor',[1 1 .8],'Curvature',[1 1]);
        if (xvalue(1,k)-r<0) rectangle('Position',[xvalue(1,k)-r+XLim
yvalue(1,k)-r 2*r 2*r],'FaceColor',[1 1 .8],'Curvature',[1 1]); end
        if (yvalue(1,k)-r<0) rectangle('Position',[xvalue(1,k)-r
yvalue(1,k)-r+YLim 2*r 2*r],'FaceColor',[1 1 .8],'Curvature',[1 1]); end
        if (xvalue(1,k)+r>XLim) rectangle('Position',[xvalue(1,k)-r-
XLim yvalue(1,k)-r 2*r 2*r],'FaceColor',[1 1 .8],'Curvature',[1 1]); end
        if (yvalue(1,k)+r>YLim) rectangle('Position',[xvalue(1,k)-r
yvalue(1,k)-r-YLim 2*r 2*r],'FaceColor',[1 1 .8],'Curvature',[1 1]); end
    end
    for i = 1:N
        if b(i,1)<0
            plot([x(i)-sc*b(i,1),x(i)+sc*b(i,1)],[y(i)-
sc*b(i,2),y(i)+sc*b(i,2)], 'color', 'red');
            plot([x(i),x(i)-sc*b(i,2)],[y(i),y(i)+sc*b(i,1)], 'color',
'red');
        plot([x(i),x(i)+Mx*Fx(i)*dt(it)*100],[y(i),y(i)+My*Fy(i)*dt(it)*100],
'color', 'green');
            text(x(i), y(i)+(b(i,1)*(0.05E-8)),num2str(i));
        elseif b(i,1)>0
            plot([x(i)-sc*b(i,1),x(i)+sc*b(i,1)],[y(i)-
sc*b(i,2),y(i)+sc*b(i,2)], 'color', 'blue');
            plot([x(i),x(i)-sc*b(i,2)],[y(i),y(i)+sc*b(i,1)], 'color',
'blue');
        plot([x(i),x(i)+Mx*Fx(i)*dt(it)*100],[y(i),y(i)+My*Fy(i)*dt(it)*100],
'color', 'green');

```

```

        text(x(i), y(i)+(b(i,1)*(0.05E-8)),num2str(i));
    end
end
for i=1:Nfr                                     %Frank Read sources
    plot(xfr(i), yfr(i), '*', 'color', 'magenta');
    text(xfr(i), (yfr(i)+(0.05E-8)),num2str(i));
end
drawnow;
refresh;
hold off;
title('Dislocation Movement')
end
% *****BOUNDARY CONDITIONS*****%
%Periodic boundaries
for i=1:N
    if x(i)>XLim;
        x(i)=x(i)-XLim;
    end
    if x(i)<0;
        x(i)=x(i)+XLim;
    end
    if y(i)>YLim;
        y(i)=y(i)-YLim;
    end
    if y(i)<0;
        y(i)=y(i)+YLim;
    end
end

%*****contact with gamma prime*****%
for i=1:N
    for k=1:g
        dx=x(i)-xvalue(1,k);
        dy=y(i)-yvalue(1,k);
        if dx>(XLim/2)                               %boundary condition in x direction
            dx=dx-XLim;
        end
        if dx<(-XLim/2)                             %boundary condition in x direction
            dx=dx+XLim;
        end
        if dy>(YLim/2)                               %boundary condition in y direction
            dy=dy-YLim;
        end
        if dy<(-YLim/2)                             %boundary condition in y direction
            dy=dy+YLim;
        end
        distance=sqrt(dx^2+dy^2);
        if distance<r
            Xr2origin=sqrt((r^2)-(dy^2));
            if (dx<0)
                x(i)=xvalue(1,k)-Xr2origin;
            else
                x(i)=xvalue(1,k)+Xr2origin;
            end
            if (x(i)<0) x(i)=x(i)+XLim; end
            if (x(i)>XLim) x(i)=x(i)-XLim; end
            vx(i)=0.0;                               % particles velocity is
effectively zero
        end
    end
end
end

```

```

% calculate strain rate
bxdot=0;
btot=0;
for i=1:N
    bxdot=bxdot+b(i,1)*vx(i)+b(i,2)*vy(i);
    btot=btot+abs(b(i,1)); % total non-zero burgers
vector dislociotns
end;
strainrate(it)=bxdot*b0/(XLim*YLim);
strainrateperdisloc(it)=bxdot/btot*b0/(XLim*YLim);
if (it>1)
    strain(it)=strain(it-1)+strainrate(it)*dt(it);
    strainperdisloc(it)=strainperdisloc(it-
1)+strainrateperdisloc(it)*dt(it);
else
    strain(it)=0.0;
    strainperdisloc(it)=0.0;
end

%***time value***
if it>1;
    t(it)=t(it-1)+dt(it);
end

%*****number of annihilated dislocations*****
Nneg=0;
for i=1:N
    if b(i,1)==0
        Nneg=Nneg+1;
    end
end
Nneg1(it)=Nneg;
Ntot(it)=N;
Ntot2(it)=Ntot(it)-Nneg1(it);
clf;
end

% ***** End of main loop *****

toc % output time since program started

A(1:it,1)=t;
A(1:it,2)=strainrate;
A(1:it,3)=strain;
A(1:it,4)=tau;
A(1:it,5)=Ntot;
A(1:it,6)=Ntot2;
A(1:it,7)=strainrateperdisloc;
A(1:it,8)=strainperdisloc;
xlswrite('srlp0ssd.xlsx',A);

```